

**Biomaterials Science: Studies on Polymer Nanogels for  
Theranostic Applications**

A THESIS PRESENTED BY

**Vineeth V.M**

TO

SREE CHITRA TIRUNAL INSTITUTE FOR MEDICAL  
SCIENCES AND TECHNOLOGY  
THIRUVANANTHAPURAM  
INDIA

IN PARTIAL FULFILMENT OF THE REQUIREMENTS  
FOR THE AWARD OF  
**DOCTOR OF PHILOSOPHY**

January 2017

## **DECLARATION**

I, Vineeth V.M, hereby certify that I had personally carried out the work depicted in the thesis entitled, “Biomaterials Science: Studies on Polymer Nanogels for Theranostic Applications”, except where due acknowledgment has been made in the text. No part of the thesis has been submitted for the award of any other degree or diploma prior to this date.

Thiruvananthapuram

12-01-2017

Vineeth V.M

Reg No: Ph.D/2014/03

Roll No: 6656

**SREE CHITRA TIRUNAL INSTITUTE FOR MEDICAL  
SCIENCES & TECHNOLOGY, TRIVANDRUM**

Thiruvananthapuram – 695011, INDIA  
(An Institute of National Importance under Govt. of India)  
Phone-(91)0471-2520248 Fax-(91)0471-2341814  
Email: jayabalan@sctimst.ac.in Web site – www.sctimst.ac.in



**CERTIFICATE**

This is to certify that **Mr. Vineeth V.M**, in the Polymer Division, BMT Wing of this institute has fulfilled the requirements prescribed for the Ph.D. degree of the Sree Chitra Tirunal Institute for Medical Sciences and Technology, Thiruvananthapuram. The thesis entitled, “**Biomaterials Science: Studies on Polymer Nanogels for Theranostic Applications**” was carried out under my direct supervision. No part of the thesis was submitted for the award of any degree or diploma prior to this date.

\* Clearance was obtained from the Institutional Ethics Committee/ Institutional Animal Ethics Committee for carrying out the study wherever it is required.

Thiruvananthapuram  
12-01-2017

Dr. M Jayabalan Ph.D, D.Sc  
(Research Supervisor)  
Scientist - G & Head  
Polymer Division, BMT wing  
SCTIMST, Thiruvananthapuram

The thesis entitled

*“Biomaterials Science: Studies on Polymer Nanogels for  
Theranostic Applications”*

Submitted by

**Vineeth V.M**

for the degree of

**Doctor of Philosophy**

Of

**SREE CHITRA TIRUNAL INSTITUTE  
FOR MEDICAL SCIENCES AND TECHNOLOGY,  
THIRUVANANTHAPURAM - 695011**

is evaluated and approved by

.....  
Dr. M Jayabalan. Ph.D, D.Sc.  
(Research Supervisor)

.....  
Examiner

Dedicated to  
My family, teachers & friends.....

## A C K N O W L E D G E M E N T

*I would like to express my heartfelt gratitude and respect to my supervisor Dr. M. Jayabalan, Scientist-G, Polymer Science Division-BMT wing, SCTIMST for providing me with unfailing support, guidance and continuous encouragement throughout my years of study and through the process of researching and writing this thesis. His dynamism, vision, sincerity and motivation have deeply inspired me. He has taught me the methodology to carry out the research and to present the research works as clearly as possible.*

*I am grateful to the former and present Director of SCTIMST and the present Head and the previous Heads, BMT Wing for all support provided during the course of my work.*

*I thank members of the Doctoral advisory committee, Dr. H K varma, (Scientist-G, Head BMT Wing) and Dr. Rekha M R (Scientist-E, Division of Biosurface Technology) for their timely suggestions and critical comments.*

*I am thankful to Dr. George A.V, Registrar, Dr. Sundar Jayasingh, former Deputy Registrar, Dr. Santhosh Kumar, Deputy Registrar, Dr.Kumari T.V, Associate Dean for Ph.D affairs, Dr. Kalliyanakrishnan V, Dean, and all members of academic division and Director's office for their administrative support.*

*I thank all my friends from our laboratory Dr. Sunitha Prem Victor, Dr. Shivaram Selvam, Remya, Shamon , Jibin, Adarsh , Reesha, Girija and Gayathri for their help and support.*

*I am thankful to Dr.Prabha.D.Nair, Rakhi, Rahul (Fluorescence spectroscopy), Dr.K.Sreenivasan , P.R.Hari (GPC analysis), Dr.Ansar, Nishad KV (Magnetic Hyperhermia and EDAX analysis), Dr. Jayasree RS, Dr. Lekshmi V Nair, Ms. Resmi V Nair, Ms. Parvathy (Fluorescence bioimaging facility), Dr.Sachin J Shenoy (Animal experiments), Dr.TV Anilkumar,Dr. Geetha (Histopathology analysis), Dr. Lizzy K Krishnan, Dr. Anugya Bhatt, Priyanka A, Anilkumar V (Hemolysis studies).*

*Thanks to the staff of various administrative departments and library of the Institute and fellow students in the campus for their lively companionship.*

*I thank The Director, NIIST, TVPM (NMR and VSM analysis) for extending their research facilities.*

*I am thankful to SCTIMST for JRF/SRF fellowships.*

*I am thankful to my parents (Vijayan, Maheswari), brother (Vipin V.M), family, friends and teachers for their, blessings, prayers, support and encouragements. This accomplishment would not have been possible without them.*

*My immense gratefulness to the Lord Almighty for showering immeasurable blessings with ever loving family, caring supervisor, supporting friends.*

**Vineeth V.M**

# CONTENTS

	<b>Page Number</b>
<b>SYNOPSIS</b>	xx
<b>Chapter 1 INTRODUCTION</b>	
1.1 Therapeutic strategies used in theranostic application	3
1.2 Diagnostic strategies used in theranostic applications	9
1.3 Polymer based theranostic agents	13
<b>Chapter 2 REVIEW OF LITERATURE</b>	
2.1 Nanogels based theranostic agents	26
2.2 Nanogels with innate imaging capability for theranostic application	31
2.3 Objectives of the present study	32
<b>Chapter 3 MATERIALS AND METHODS</b>	
3.1 Materials	37
3.2 Synthesis of photoluminescent comacromers	38
3.3 Structural characterization of the photoluminescent comacromers	41
3.4 Determination of photoluminescent properties of comacromers	42
3.5 Synthesis of nanogels from photoluminescent comacromers	42
3.6 Analyses of morphology, size and surface charge of nanogels	45
3.7 In vitro drug loading and release profiles of nanogels	46
3.8 Magnetic Hyperthermia Experiments of C-SPION-NG	47

3.9	Evaluation of cytocompatibility and therapeutic capability of the nanogels	48
3.10	Evaluation of haemolytic potential of the nanogels	52
3.11	Evaluation of cellular uptake of the nanogels	53
3.12	Studies on in vivo bioimaging and biodistribution nanogels in mice	54
3.13	Histopathological evaluation of nanogels on different organs	56
3.14	Statistical analysis	56

## **Chapter 4 RESULTS**

4.1	Studies on passively targeted nanogels for theranostic applications	58
4.1.1	Synthesis of photoluminescent PPF-PEG-glycine (PLM) and PPF-PEG-citric acid-glycine (C-PLM) comacromers	58
4.1.2	Structural evaluation of PLM and C-PLM comacromers	60
4.1.3	Evaluation of the photoluminescence properties of the PLM and C-PLM comacromers	63
4.1.4	Investigation on the photoluminescence properties of analogues of PLM and C-PLM comacromers	69
4.1.5	Preparation of PLM-NG and C-PLM-NG nanogels and evaluation of size, morphology and surface charge of nanogels	72
4.1.6	Evaluation on cytocompatibility, hemolytic potential and cellular uptake and imaging capability of PLM and C-PLM-NG	78
4.1.7	Evaluation of the therapeutic potential of C-PLM-NG	81
4.1.8	Evaluation of the bioimaging capability of C-PLM-NG	82
4.1.9	Evaluation of the bioimaging, biodistribution and biocompatibility of C-PLM-NG	85
4.2	Studies on magneto-fluorescent nanogel for theranostic applications	90

4.2.1	Synthesis of photoluminescent PEG-Maleic acid-Glycine (PMG) comacromer	90
4.2.2	Structural evaluation of PMG comacromer	91
4.2.3	Evaluation of the photoluminescence properties of the PMG comacromer	92
4.2.4	Synthesis of magneto-fluorescent nanogel (C-SPION-NG)	95
4.2.5	Evaluation of size,morphology and surface charge of C-SPION-NG	97
4.2.6	Evaluation of the magneto-fluorescent characteristics of C-SPION-NG	99
4.2.7	Evaluation of the cyto compatibility,hemolytic potential and cellular uptake of C-SPION-NG	103
4.2.8	Evaluation of the theranostic potential of C-SPION-NG	107
4.2.9	Evaluation of the bioimaging, biodistribution and biocompatibility of C-SPION-NG	111
4.3	Studies on actively targeted nanogel for theranostic applications	114
4.3.1	Preparation and structural characterization of photoluminescent comacromer PEG-Maleic acid-Benzoic acid (PMB) and octreotide conjugated nanogel (PMB-OctN)	114
4.3.2	Evaluation of the photoluminescence properties of the PMB comacromer	118
4.3.3	Evaluation of size,morphology and surface charge of PMB-OctN	121
4.3.4	Evaluation of drug release, therapeutic capability and hemolytic potential of PMB-OctN	122
4.3.5	Evaluation of the targetting capability of PMB-OctN	126
4.3.6	Evaluation of the bioimaging capability of PMB-OctN	127
4.3.7	Evaluation of the biodistribution and biocompatibility of PMB-OctN	128

## **Chapter 5 DISCUSSION**

5.1	Studies on passively targeted nanogels for theranostic applications	
5.1.1	Synthesis of photoluminescent PPF-PEG-glycine (PLM) and PPF-PEG-citric acid-glycine (C-PLM) comacromers	131
5.1.2	Structural evaluation of PLM and C-PLM comacromers	132

5.1.3	Evaluation of the photoluminescence properties of the PLM and C-PLM comacromers	133
5.1.4	Investigation on the photoluminescence properties of the analogues of the comacromers	135
5.1.5	Preparation of PLM-NG and C-PLM-NG nanogels and evaluation of size,morphology and surface charge of nanogels	136
5.1.6	Evaluation on cytocompatibility, hemolytic potential and cellular imaging capability of PLM and C-PLM-NG	138
5.1.7	Evaluation of the therapeutic potential of C-PLM-NG	139
5.1.8	Evaluation of the bioimaging, biodistribution and biocompatibility of C-PLM-NG	140
5.2	Studies on magneto-fluorescent nanogel for theranostic applications	
5.2.1	Synthesis and characterisation of photoluminescent PEG-Maleic acid-GlycinePMG comacromer	142
5.2.2	Evaluation of the photoluminescence properties of the PMG comacromer	142
5.2.3	Preparation of magneto-fluorescent nanogel C-SPION-NG and evaluation of size,morphology and surface charge of nanogels	143
5.2.4	Evaluation of the magneto-fluorescent characteristics of C-SPION-NG	145
5.2.5	Evaluation on cytocompatibility, hemolytic potential and cellular uptake of C-SPION-NG	145
5.2.6	Evaluation of the theranostic potential of C-SPION-NG	147
5.2.7	Evaluation of the bioimaging, biodistribution and biocompatibility of C-SPION-NG	148
5.3	Studies on actively targeted nanogel for theranostic applications	150
5.3.1	Synthesis and characterisation of photoluminescent comacromer PEG-Maleic acid-Benzoic acid (PMB) and octreotide conjugated nanogel (PMB-OctN)	150

5.3.2	Evaluation of the photoluminescence properties of the PMB comacromer	151
5.3.3	Preparation and evaluation of size,morphology and surface charge of PMB-OctN	152
5.3.4	Evaluation of drug release, therapeutic capability and hemolytic potential of PMB-OctN	152
5.3.5	Evaluation of the targetting capability of PMB-OctN	154
5.3.6	Evaluation of the bioimaging, biodistribution and biocompatibility of PMB-OctN	155
<b>Chapter 6</b>	<b>SUMMARY AND CONCLUSIONS</b>	<b>157</b>
6.1	Future prospects	163
	References	164
	List of publications	178
	Conference proceedings	179
	Curriculum vitae	180

## List of Figures

<b>Figure-1:</b> Components of a theranostic polymer nanocarrier	14
<b>Figure-2:</b> Components of a theranostic polymeric micelle	16
<b>Figure-3:</b> Components of a theranostic polymeric liposome	19
<b>Figure-4:</b> Components of a theranostic polymeric dendrimer	22
<b>Figure-5:</b> Components of a theranostic polymeric nanogel	25
<b>Figure-6:</b> Synthesis of photoluminescent PLM comacromer	58
<b>Figure-7:</b> Synthesis of photoluminescent C-PLM comacromer	57
<b>Figure-8:</b> FTIR Spectral analyses of PLM comacromer (a), C-PLM comacromer (b)	61
<b>Figure-9:</b> <sup>1</sup> H NMR Spectral analyses of PLM comacromer (a), C-PLM comacromer (b)	62
<b>Figure-10:</b> Photoluminescence spectra of PLM comacromer under aqueous conditions at different excitations on visible region (400nm-540nm)	64
<b>Figure-11:</b> Photoluminescence spectra of PLM comacromer under aqueous conditions at different excitations on visible region (400nm-640nm)	64
<b>Figure-12:</b> The three dimensional photoluminescent contour plots of PLM	65
<b>Figure-13:</b> The three dimensional photoluminescent contour plots of C-PLM	65
<b>Figure-14:</b> Photo stability graph of PLM	66
<b>Figure-15:</b> Photo stability graph of C-PLM	67
<b>Figure-16:</b> Photoluminescence life time of PLM comacromer	67
<b>Figure-17:</b> Photoluminescence life time of C-PLM comacromer	68
<b>Figure-18:</b> Excitation & emission spectra of PLM comacromer	68
<b>Figure-19:</b> Excitation & emission spectra of C-PLM comacromer	69
<b>Figure-20:</b> Photoluminescence properties of PEG-Glycine(a) PEG-PPF(b)	70

<b>Figure-21:</b> UV-VIS absorption spectrum of comacromer analogues (a) and fluorescent spectrum of PEG-Maleic acid comacromer (b)	71
<b>Figure-22:</b> Crosslinking of PLM comacromer to form nanogel	72
<b>Figure-23:</b> Crosslinking of C-PLM comacromer to form nanogel	73
<b>Figure-24:</b> TEM images of PLM-NG (a), DLS histogram of PLM-NG (b)	74
<b>Figure-25:</b> Morphology and size of nanogel C-PLM-NG at pH 7.4 (a) at pH 5.5 (b)	75
<b>Figure-26:</b> DLS measurement of C-PLM-NG at pH 7.4 (a) at pH 5.5 (b)	76
<b>Figure-27:</b> Surface charge analysis of PLM	77
<b>Figure-28:</b> Surface charge analysis of C-PLM	77
<b>Figure-29:</b> MTT assay showing the cell viability of the PLM-NG at different concentrations (500-6000 $\mu\text{g/ml}$ )	78
<b>Figure-30:</b> MTT assay showing the cell viability of the C-PLM-NG at different concentrations (500-6000 $\mu\text{g/ml}$ )	79
<b>Figure-31:</b> Cellular uptake of PLM-NG in L929 cells (a) HeLa cells (b)	80
<b>Figure-32:</b> Cellular uptake of C-PLM-NG in HeLa cells	80
<b>Figure-33:</b> pH Sensitive release of doxorubicin from C-PLM-NG	81
<b>Figure-34:</b> Cell viability C-PLM-NG and doxorubicin-loaded C-PLM-NG	82
<b>Figure-35:</b> Images of the subcutaneously injected nanogel on mice for different excitations	83
<b>Figure-36:</b> Processed near IR fluorescent images of mice using C-PLM-NG	84
<b>Figure-37:</b> Biodistribution of intravenously injected nanogel in mice	85
<b>Figure-38:</b> <i>Ex vivo</i> imaging of carcass of mice after 3 h and 24 h post injection depicting biodistribution	86
<b>Figure-39:</b> <i>Ex vivo</i> imaging of different organs of mice after 3 h and 24 h post injection depicting biodistribution	87

<b>Figure-40:</b> H&E stained images of organs of mice at 24 h and 48 h post injection	88
<b>Figure-41:</b> Lymph node imaging of a mice using C-PLM-NG	89
<b>Figure-42:</b> Synthesis of the photoluminescent PMG comacromer	90
<b>Figure-43:</b> FTIR spectral analyses of the photoluminescent PMG comacromer	91
<b>Figure-44:</b> <sup>1</sup> H NMR spectral analyses of the photoluminescent PMG comacromer	92
<b>Figure-45:</b> Excitation wavelength dependent photoluminescent spectra of the PMG comacromer under aqueous conditions at different excitations (480-800nm)	93
<b>Figure-46:</b> Three dimensional photoluminescence contour plot of the PMG comacromer	93
<b>Figure-47:</b> Photoluminescence life time of PMG comacromer	94
<b>Figure-48:</b> Photostability graph of the comacromer	95
<b>Figure-49:</b> Synthesis scheme of magneto-fluorescent nanogel (C-SPION-NG)	96
<b>Figure-50:</b> DLS histogram of C-SPION (a), C-SPION-NG (b)	97
<b>Figure-51:</b> TEM images of C-SPION (a) C-SPION-NG (b)	98
<b>Figure-52:</b> Zeta potential measurement of C-SPION-NG	99
<b>Figure-53:</b> EDAX spectrum of C-SPION-NG	100
<b>Figure-54:</b> C-SPION and C-SPION-NG in the absence of magnetic field (i), in the presence of magnetic field (ii)	100
<b>Figure-55:</b> VSM graph of C-SPION (a) and C-SPION-NG (b)	101
<b>Figure-56:</b> Excitation wavelength dependent photoluminescent spectra of the C-SPION-NG under aqueous conditions at different excitations (500-800nm)	102
<b>Figure-57:</b> C-SPION-NG under normal light (i), under UV light (ii), C-SPION-NG under magnetic field (iii), C-SPION-NG under UV light and magnetic field (iv)	102

<b>Figure-58:</b> Cellular viability of SPION and C-SPION-NG having different concentrations (250-4000 $\mu$ g)	103
<b>Figure-59:</b> Live dead assay of C-SPION-NG. HeLa cells as control (a), cells treated with 500 $\mu$ g of C-SPION-NG (b), cells treated with 1000 $\mu$ g of C-SPION-NG (c)	104
<b>Figure-60:</b> Cell cycle analysis of C-SPION-NG. HeLa cells as control (a), cells treated with 500 $\mu$ g of C-SPION-NG (b) cells treated with 1000 $\mu$ g of C-SPION-NG (c)	105
<b>Figure-61:</b> Hemolysis assay of C-SPION-NG	106
<b>Figure-62:</b> Prussian blue staining of HeLa cells incubated with C-SPION-NG. Control HeLa cells (a), cells treated with 500 $\mu$ g of C-SPION-NG (b) cells treated with 1000 $\mu$ g of C-SPION-NG	106
<b>Figure-63:</b> Fluorescent microscope images showing uptake in HeLa cells with C-SPION-NG. Observed with FITC filter and Texas red filter	107
<b>Figure-64:</b> Magnetic hyperthermia curves of distilled water(a), 2 mg/ml C-SPION-NG (b), 4mg/ml C-SPION-NG (c)	108
<b>Figure-65:</b> Live dead assay of magnetic hyperthermia treated HeLa cells Control HeLa cells(a), HeLa cells incubated with C-SPION-NG without alternating magnetic field (b), HeLa cells incubated with C-SPION-NG with alternating magnetic field (c)	109
<b>Figure-66:</b> Phase contrast microscope images of control HeLa cells (a), HeLa cells treated with alternating magnetic field (b)	110
<b>Figure-67:</b> <i>In vivo</i> fluorescence bioimaging capability of mice using different excitation and emission wavelengths	111
<b>Figure-68:</b> Biodistribution of intravenously injected C-SPION-NG in mice at different time points	112
<b>Figure-69:</b> H&E stained images of organs of mice at 48h post injection	113
<b>Figure-70:</b> Synthesis scheme of photoluminescent comonomer(PMB) and octreotide-conjugated nanogel (PBM-OctN)	115
<b>Figure-71:</b> FTIR Spectral analyses of the PMB comonomer	116
<b>Figure-72:</b> $^1\text{H}$ NMR spectra Spectral analyses of the PMB comonomer	117

<b>Figure-73:</b> FTIR spectra of the octreotide and PMB-OctN	118
<b>Figure-74:</b> Excitation wavelength dependent photoluminescent spectra of the PMB under aqueous conditions at different excitations on visible region (460-800nm)	119
<b>Figure-75:</b> Three dimensional photoluminescent contour plot of the PMB	119
<b>Figure-76:</b> Photoluminescence life time of PMB	120
<b>Figure-77:</b> Photostability graph of the PMB	120
<b>Figure-78:</b> TEM image of PMB-OctN (a), DLShistogram of PMB-OctN (b)	121
<b>Figure-79:</b> Zeta potential measurement of PMB –OctN	122
<b>Figure-80:</b> Doxorubicin release profile from PMB–OctN	123
<b>Figure-81:</b> Cell viability of PMB-OctN and doxorubicin-loaded PMB–OctN	123
<b>Figure-82:</b> Live dead assay of PMB -OctN and doxorubicin-loaded PMB-OctN. Untreated Hela cells as control (a), Hela cells treated with PMB -OctN (b), Hela cells treated with doxorubicin-loaded PMB -OctN (c)	124
<b>Figure-83:</b> Flow cytometric analysis of PMB -OctN. Hela cells as control (a), cells treated with PMB -OctN (b) cells treated with doxorubicin-loaded PMB -OctN (c)	125
<b>Figure-84:</b> Hemolysis assay of PMB-OctN	126
<b>Figure-85:</b> Fluorescent microscope images showing uptake comparison in Hela cells with PMB -N and PMB-OctN. Hela cells as control (i) cells treated with PMB-N (ii), cells treated with PMB-OctN (iii)	127
<b>Figure-86:</b> <i>In vivo</i> fluorescence bioimaging capability of PMB-OctN in mice using different excitation and emission wavelengths	128
<b>Figure-87:</b> Biodistribution of intravenously injected PMB-OctN in mice	129
<b>Figure-88:</b> H&E stained images of organs of mice at 96h post injection	130

## List of tables

**Table-1:** Photoluminescence properties of PLM and C-PLM comacromers 69

## Abbreviations

C-PLM	Citrated photoluminescent comacromer
C-SPION	Citrated Superparamagnetic ironoxide
C-SPION-NG	Citrated Superparamagnetic ironoxide nanogel
DLS	Dynamic Light Scattering
DMEMA	Dimethyl aminoethyl methacrylate
EDAX	Energy Dispersive X ray
FTIR	Fourier Transform Infrared
GPC	Gel Permeation Chromatography
H&E	Hematoxylin and Eosin
MRI	Magnetic Resonance Imaging
NG	Nanogel
NIR	Near Infra Red
NMR	Nuclear Magnetic Resonance
Oct	Octreotide
Oct-N	Octreotide conjugated nanogel
PBS	Phosphate Buffer Saline
PEG	Polyethylene Glycol
PLM	Photoluminescent Comacromer
PPF	Polypropylene fumarate
QD	Quantum Dots
SPION	Superparamagnetic ironoxide
TEM	Transmission Electron Microscope
TSCPC	Time Correlated Single Photon Counting
VSM	Vibrating Sample Magnetometry

## SYNOPSIS

### **Biomaterials Science: Studies on polymer nanogels for theranostic applications**

Multifunctional nanoparticles that can perform different functions such as therapeutic and diagnostic are becoming promising candidates in nanomedicine. Diagnosing tumors is equally important similar to treating them. Hence, the developments of nanoformulations that combine both therapeutic and diagnostic functions are highly relevant in cancer therapy. Combination of therapeutic and diagnostics (theranostics) was first termed by Funkhouser, which started a new era in nanomedicine where researchers have started working on this emerging and challenging area. Nanomaterials and near IR emitting fluorophores are highly preferred for bioimaging applications. The near IR emissions have the highest tissue penetration with lowest autofluorescence, which makes bioimaging more efficient. Different types of nanomaterials such as iron oxide nanoparticles, gold nanoparticles and carbon nanotubes and near IR emitting fluorophores such as quantum dots, organic dyes and lanthanides are explored for theranostic applications, as all of these materials are endowed with different therapeutic and imaging capabilities. However, these nanoparticles and near IR emitting fluorophores have some major drawbacks such as toxicity, non-biodegradability and short circulation half-life *in vivo*. Hence these issues have to be tackled efficiently for the use in theranostic applications. Nanogels are chemically or

physically cross linked hydrophilic or amphiphilic polymeric nanostructures. They are endowed with properties such as high water absorptivity, rapid response to external stimuli, high biocompatibility and availability of versatile functional groups for conjugation with imaging and therapeutic agent. These properties make it appropriate for executing theranostic applications. However, the imaging function is usually accomplished by conjugating imaging agents on the surface of nanogel such as quantum dots, organic dyes and iron oxide nanoparticles which do possess toxicity issues. Hence the leakage of these imaging agents from the surface of the nanogel causes significant toxicity issues. Hence the development of nanogels with innate near IR imaging capability which does not require any external imaging agents is of crucial importance in the area of theranostic nanomedicine. The current study focuses on biocompatible polymeric nanogels with innate fluorescence characteristics that can be used for potential theranostic applications. These biocompatible nanogels with innate near IR fluorescence characteristics can efficiently execute theranostic functions without causing any toxicity issues.

The thesis comprises of 6 chapters. Chapter 1 deals with introduction about theranostic nanomedicine and the different types of polymeric carriers such as liposomes, dendrimers, micelles and nanogels used for theranostic applications. The advantages and disadvantages of these polymer based theranostic systems are also discussed.

Chapter 2 deals with the literature review about the different polymer based nanocarriers currently explored for theranostic applications. The major

challenges associated with these carriers are also presented. The objectives and scopes of the present study are also presented in this chapter.

Chapter 3 deals with the materials and methods. It deals with the synthesis and characterization of different photoluminescent comonomers and nanogels. Four different types of comonomers were synthesized and crosslinked with different vinyl monomers to prepare nanogels. The first photoluminescent comonomer (PLM) was synthesized by polycondensation reaction of polyethylene glycol (PEG), polypropylene fumarate (PPF) and glycine. The nanogel (PLM-NG) was prepared using PLM by crosslinking the unsaturated double bonds of the comonomer with acrylic acid. The second photoluminescent comonomer (C-PLM) was synthesized by polycondensation reaction of polyethylene glycol (PEG), polypropylene fumarate (PPF), citric acid and glycine. The nanogel (C-PLM-NG) was prepared using C-PLM comonomer by crosslinking it with a pH sensitive tertiary amino groups bearing crosslinker N,N dimethylaminoethylmethacrylate (DMEAMA). The third photoluminescent comonomer (PMG) was synthesized by polycondensation reaction of polyethylene glycol (PEG), maleic acid and glycine. Further, citric acid capped super paramagnetic iron oxide nanoparticles (C-SPION) was synthesized by coprecipitation method. A magneto-fluorescent nanogel (C-SPION-NG) was prepared by the *in situ* incorporation of C-SPION during the crosslinking of PMG comonomer with DMEAMA crosslinker. The fourth comonomer (PMB) was synthesized by polycondensation reaction of polyethylene glycol (PEG), maleic acid and 4-aminobenzoic acid. The nanogel (PMB-N) was prepared by crosslinking the PMB comonomer with diethyleneglycoldiacrylate (DEGDMA).

A targeted nanogel (PMB-OctN) was prepared by conjugating the PMB-N with a targeting ligand octreotide through EDC/NHS coupling reaction. The structure of the synthesized comacromers was evaluated using FTIR and proton NMR spectroscopy. The molecular weight analysis of the comacromers was determined using gel permeation chromatography (GPC) analysis. The fluorescence properties of the comacromers were evaluated through fluorescence spectroscopy and time-correlated single photon count analysis (TSCPC). The hydrodynamic size of the nanogel was measured through dynamic light scattering (DLS) analysis. The surface charge of the nanogels was measured through zeta potential measurement. The shape and size of the nanogel was studied through transmission electron microscopy (TEM) analysis. The cytocompatibility of the nanogels was studied using MTT assay. The hemolytic potential of the nanogels were studied using hemolysis assay according to ISO standards (10993:4). The therapeutic capabilities of the nanogels were evaluated using MTT assay, live-dead cell assay and flowcytometry. The *in vitro* and *in vivo* imaging capabilities of the nanogels were evaluated using fluorescence microscopy and IVIS *in vivo* bioimaging system respectively. The biocompatibility evaluation of the nanogels was studied using histopathology analysis.

Chapter 4 and 5 deals with results and discussion respectively. These chapters are divided in to 3 different sections.

Section-1 deals with the studies on PLM and C-PLM comacromers and nanogels (PLM-NG and C-PLM-NG). The comacromers PLM and C-PLM exhibited excitation wavelength dependent fluorescence properties (EDF). PLM and C-PLM comacromers when excited at different wavelengths in visible region

from 400 nm to 600 nm exhibits fluorescent emissions from 520 nm to 700 nm in aqueous condition. The fluorescence lifetime of PLM and C-PLM was 6 and 7 nanoseconds respectively. The Stokes shift values of PLM and C-PLM was 120 nm revealing the appreciable Stokes shift. These comonomers have good photostability of 30 min. The EDF characteristics exhibited by PLM and C-PLM comonomers can be attributed to the presence of  $n-\pi^*$  interactions of the hydroxyl oxygen atoms of PEG with carbonyl groups of the ester linkages present in the comonomers. The nanogels synthesized from the PLM and C-PLM comonomers (PLM-NG and C-PLM-NG) has shown spherical morphology with particle size around 180 and 85 nm. The studies on *in vitro* cytotoxicity and hemolytic potential with MTT assay and hemolysis revealed that the PLM-NG and C-PLM-NG is non-toxic. The hemolytic studies of PLM-NG and C-PLM-NG have shown low hemolytic percentages (0.12 and 0.03) which were lower than the acceptable limit of 5% according to ISO standards. The inherent EDF characteristics associated with PLM-NG and C-PLM NG enable cellular imaging of HeLa cells. The C-PLM-NG which was prepared with the pH sensitive crosslinker N, N dimethyl amino ethylmethacrylate (DMEMA) has shown pH responsive swelling with particle size around 100 nm and 180 nm at pH 7.4 (physiological) and 5.5 (intracellular acidic condition of cancer cells) respectively. The C-PLM-NG nanogel undergoes pH responsive swelling and release around 50% doxorubicin (DOX) at pH 5.5 in comparison with 15% observed at pH 7.4. The DOX-loaded C-PLM-NG encapsulated in HeLa cells induces lysis of cancer cells. The studies on biodistribution and clearance mechanism of C-PLM-NG from the body of mice reveal bioimaging capability and safety of the present nanogel.

Section-2 deals with the studies on hybrid magneto-fluorescent nanogel (C-SPION-NG). Magneto-fluorescent nanogel was based on photoluminescent comonomer [PEG-maleic acid-glycine] (PMG), N, N Dimethyl amino ethylmethacrylate (DMEAMA) and citrate capped superparamagnetic iron oxide nanoparticles (C-SPION) endowed with near IR fluorescence and superparamagnetic properties. The comonomer PMG exhibited EDF properties with different excitations (480 nm-800 nm) and different fluorescent emissions (520 nm- 860 nm) in aqueous condition. The magneto-fluorescent nanogel (C-SPION-NG) synthesized from PMG, DMEAMA and C-SPION was found to have core-shell morphology (C-SPION core and PEG shell) with average particle size of 80 nm. VSM analysis showed that the designed nanogel exhibited superparamagnetic properties. The cytocompatibility of the synthesized nanogel studied using MTT, live dead assays and flow cytometry revealed the excellent cytocompatibility of the nanogel. The hemolysis studies of C-SPION-NG have shown low hemolytic percentage (0.03) which was lower than the acceptable limit of 5% according to ISO standards. The cellular uptake of the nanogel on cervical cancer cell line Hela evaluated through Prussian blue staining and fluorescence microscopy have revealed good cellular internalization and cancer cell imaging capability. Magnetic hyperthermia experiments have shown that the synthesized nanogel generated significant heat required for the lysis of cancer cells. The lysis of cancer cells were demonstrated through live dead assay with significant cell death which suggests the good therapeutic potential of the nanogel. The studies on biodistribution and clearance mechanism of C-PLM-NG from the body of mice reveal bioimaging capability and safety of the present nanogel.

Section-3 deals with the studies on a targeted octreotide conjugated nanogel. The targeted octreotide conjugated fluorescent nanogel (PMB-OctN) was based on photoluminescent comacromer [PEG-maleic acid-4 aminobenzoic acid] (PMB), diethylene glycoldimethacrylate (DEGDMA) and octreotide. The comacromer PMB exhibited EDF properties with different excitations (460 nm- 800 nm) and different fluorescent emissions (520 nm- 780 nm) in aqueous condition. The targeted octreotide conjugated nanogel (PMB-OctN) synthesized from PMB, DEGDMA and octreotide has spherical morphology with average particle size of 40 nm. The PMB-OctN nanogel can load 78 % of anticancer drug and release for 5 days and beyond in sustained way. The studies on drug delivery of doxorubicin from PMB-OctN nanogel carried out with cervical cancer cells Hela revealed appreciable therapeutic capability. The hemolysis studies of PMB-OctN has shown low value of hemolytic percentage (0.06) which was lower than the acceptable limit of 5% according to ISO standards. The studies on cellular uptake of the nanogel revealed increased cellular uptake when compared to the nontargetted nanogel. The study on fluorescence bioimaging of the PMB-OctN nanogel in mice has demonstrated near IR imaging capability. Then biodistribution studies of the PMB-OctN nanogel in mice have also revealed longer *in vivo* circulation lifetime. The histopathology analysis has suggested the safety of the PMB-OctN nanogel. Comparative analysis of all of the synthesized nanogels shows that the octreotide conjugated nanogel shows better properties for theranostic applications, such as longer circulation lifetime, active targeting capability, good near IR imaging capability, sustainable drug release profile and good therapeutic capability.

The chapter 6 deals with the summary, conclusions and future perspectives of the present study. The most promising nanogel and further exploration of product safety evaluation and clinical translation of the designed nanogels for theranostic nanomedicine are emphasized.

## CHAPTER-1

### INTRODUCTION

*This chapter presents an overview of the different therapeutic and diagnostic strategies used to construct theranostic system. The importance of polymer based theranostic carriers are presented in this chapter. The different types of polymeric carriers such as micelles, liposomes, dendrimers and nanogels explored for theranostic applications are also presented.*

Cancer is the leading cause of death globally, different types of cancers such as colorectal, breast, lung and liver causes significant mortalities all around the world (Rushton *et al.*, 2015). Lack of proper diagnostics and treatment is the major cause for this kind of increased number of mortalities. Even though different types of anticancer drug formulations are available in the market, this scenario continues. The major reasons behind this phenomenon are poor aqueous solubility of anticancer drugs and nontargetted distribution of anticancer drugs inside the body and subsequent toxicity hazards created by these anticancer drugs. In order to increase the efficacy of these anticancer drugs and reduce toxicity, nanomedicine has contributed immensely. Development of nanotherapeutics has

addressed most of these challenges faced by the anticancer drugs. It has improved the cancer therapy in many aspects such as dose reduction, specificity and improved pharmacokinetics (Devadasu *et al.*, 2013). The diameters of the smallest capillary of the body are in the range of 5-6  $\mu\text{m}$ ; hence the nanosized carriers can be conveniently administered through the intravenous route. First generation nanomedicine is focused on the development of passively targeted nanoparticles which exploited the enhanced permeability and retention effect of nanoparticles on leaky vasculature tumor tissues (Riehemann *et al.*, 2009), (Greish *et al.*, 2010). Some of the important classes of these first generation nanoformulations available in the market are based on polymers and liposomes (Torchilin., 2005), (Farokhzad *et al.*, 2009). Diagnosing tumors is equally important as treating them. Hence, the development of nanoformulations that combine both therapy and diagnostics are very important in cancer therapy. Combination of therapy and diagnostics (theranostics) was first termed by Funkhouser in 2002, which started a new era in nanomedicine (Kelkar *et al.*, 2011). Development of nanoparticles having both imaging and therapeutic capabilities offers several advantages such as noninvasive monitoring of disease progression with therapeutic efficacy, visualization biodistribution real time, analysis of drug distribution at target site and facilitation of triggered drug release (Lammers *et al.*, 2010). Hence theranostic nanoparticles can significantly reduce the gap between therapy and diagnostics which can ultimately results in optimal therapeutic time window to diseases like cancer (Wang *et al.*, 2014). Designing a theranostic agent is quite challenging because many important biological factors such as circulation lifetime, excretion rate and tissue specificity should be considered while designing a theranostic agent. For example, the molecular

imaging component which is used for diagnostics purposes should be eliminated rapidly after performing its intended function. At the same time, the loaded therapeutic component inside the theranostic agent should get sufficient circulation life time to accumulate in the tumor region. Hence careful design strategy is required for meeting these requirements for the success of these theranostic agents. Different types of therapeutic and diagnostics modalities are combined together in a single nanoparticles frame work to design a theranostic agent. The commonly employed therapeutic strategies used for the construction of a theranostic agent are summarized as follows

### ***1.1. Therapeutic strategies used in theranostic applications***

#### **1.1.1. Drug delivery**

Efficient drug delivery is important therapeutic strategy adopted in the design of a nanotheranostic agent. Anticancer drugs such as Doxorubicin, paclitaxel, 5 Fluorouracil etc are conjugated or entrapped with the theranostic nanoparticles to accomplish the desired therapeutic response (Singh *et al.*, 2009). These theranostic nanoparticles by virtue of its enhanced permeability and retention effect accumulates on the tumor tissues and releases the loaded drug in a slow and sustainable manner (Fang *et al.*, 2011). The properties of theranostic agents such as surface charge, size, biodegradability and hydrophobicity are tailored to get the optimal therapeutic response (Moghimi *et al.*, 2001), (Panyam *et al.*, 2003), (Panyam *et al.*, 2003). The nanosize of these carriers favors good cellular uptake and targeted distribution of drugs. Non-targeted distributions of anticancer drugs are one of the major concerns in cancer therapy. These

nanotheranostic agents can be incorporated with stimuli responsive units. Different types of stimuli responsive strategy are investigated for drug delivery.

### **1.1.2. pH responsive drug delivery**

pH is one of the most important stimuli used for drug delivery applications. There is a natural existence of pH gradient inside the body among different organs and tissues such as stomach lumen (pH 1-3), duodenum and ileum (pH 6.6-7.5), normal tissues (7.4) and tumor tissues (5.7-7.8) (Gao *et al.*, 2010), (Rajput *et al.*, 2010), (Davis *et al.*, 1993). The acidic environment around the tumor tissues can be attributed to high levels of production of lactic acid owing to increased rate of glucose uptake by tumor cells. This effect is termed as Warburg's effect (Kim., 2006). Hence this natural existence of pH difference among different organs and tissues can be exploited for the construction of smart responsive drug reservoirs. They act as programmable drug delivery vehicles where the release of the loaded drug can be controlled by the external pH (Asokan *et al.*, 2002), (Vaupel *et al.*, 2004), (Gerweck *et al.*, 2006). The pH sensitivity can be imparted to a nanocarrier by the incorporation of pH sensitive groups such as amino or carboxylic acid on the structural units of these nanocarriers. pH sensitivity arises due to the ionization of these pendant carboxylic acid or amino groups present in the carrier with pKa values ranging from 3-11. Depending on the type of drug delivery, pH sensitivity can be tuned such as for tumor therapy. Usually the protonating amino groups in the nanocarriers undergo ionization and induce subsequent release of the loaded drug upon reaching the tumor site (lower pH) (Schmalijohann *et al.*, 2006). On the other hand for drug delivery applications such as insulin delivery, the drug should be protected from the harsh

acidic environments of stomach. Hence, the nanocarriers are modified with carboxylic acid groups which undergo ionization only at higher pH and provide site specific drug delivery.

### **1.1.3. Redox responsive drug release**

Redox potential is another important stimulus used for drug delivery applications. Redox responsive nanocarriers disassemble inside the cytosol which has high level of glutathione concentration (2-10 mM) when compared to extracellular fluids (2-20  $\mu$ M) (Cheng *et al.*, 2011), (Schafer *et al.*, 2001). The disassembly of the carrier in the high glutathione reducing environment causes the release of the encapsulated drug. It is a widely used stimulus for gene delivery applications. Gene delivery faces the big challenge of limited cytoplasmic delivery; this can be effectively addressed with the help of redox responsive nanocarriers. The high reducing environment inside the cytosol ensures the site specific delivery of the loaded therapeutic agent which in turn increases the therapeutic performance. Hence, polymeric nanoparticles with reduction sensitive disulfide (-S-S) linkages are widely used for gene delivery applications. These disulfide containing carriers will be internalized via endocytosis pathway and got disassembled in the lysosomal compartments having high reducing environment and causes the release of the therapeutic agent (Bauhuber *et al.*, 2009), (Candiani *et al.*, 2010), (Meng *et al.*, 2009).

### **1.1.4. Photodynamic therapy**

Photodynamic therapy is an emerging therapeutic modality used for cancer treatment. Unlike the conventional chemotherapy which has more systemic side

effects, photodynamic therapy offers several advantages such as minimal invasiveness, repeatability without cumulative toxicity and effective ablation of tumor cells without harming the surrounding normal cells (Lucky *et al.*, 2015). Photodynamic therapy was first demonstrated by Dougherty *et al.* in 1975 (Dougherty *et al.*, 1975); afterwards much important advancement has taken place to increase the efficacy of this treatment modality. The primary action mechanism of photodynamic therapy involves the administration of a photosensitizer into the tumor site followed by the irradiation of the tumor site with light having specific wavelength. This irradiation of light excites the photosensitizer to excited singlet state and generates cytotoxic reactive oxygen species which can lead to cancer cell ablation (Castano *et al.*, 2005). The tumor cell destruction capability of photodynamic therapy depends on several factors such as concentration of the administered photosensitizer, the type of tumor and the level of oxygenation produced after light irradiation.

Photosensitizer is the most important component which governs the efficacy of photodynamic therapy. An ideal photosensitizer should possess characteristics such as near IR excitation capability, high quantum yield of triplet state formation and sufficient excited state lifetime to interact with substrates to generate reactive oxygen species required for the destruction of cancer cells (Henderson *et al.*, 1992), (Dolmans *et al.*, 2003), (Oleinick *et al.*, 2015). Biological molecules present inside the body such as hemoglobin have stronger absorption profile below 700nm which can significantly hinder the action of the photosensitizer. Hence, the excitation of the photosensitizer is always accomplished by the usage of near IR wavelength light having higher tissue

penetration (Luan *et al.*, 2013), (Oleinick *et al.*, 1998). Porphyrins are the first generation photosensitizers widely used for photodynamic therapy. They possess several advantages such as effective destruction of tumors, easy clearance from the body and water solubility enabling the convenient intravenous delivery (Dougherty *et al.*, 1998), (Ormond *et al.*, 2013). In spite of these advantages, they still suffer from major drawbacks such as lack of tumor selectivity, oxygen depletion, hydrophobicity, aggregation and improper biodistribution (Allison *et al.*, 2014), (Konan *et al.*, 2002). Developments of nanocarriers have tremendously contributed to alleviate the major drawbacks that the conventional photosensitizers have encountered. The photosensitizer which is conjugated or loaded with the nanoparticles has shown more efficacies towards photodynamic therapy when compared to the conventional photosensitizers. As nanoparticles are endowed with large surface area to volume ratio, they can significantly increase the delivery of photosensitizer to tumor cells (Davis *et al.*, 2008), (Maeda *et al.*, 2000). They exhibit more specificity towards tumor cells by virtue of the enhanced permeability and retention effect of nanoparticles on tumor cells and thereby reducing the chance of adverse side effects to normal cells. More importantly, nanoparticles which impart amphiphilicity to the photosensitizer, favour easy travel through the blood stream and localize in cancer cells (Allison *et al.*, 2010).

For drug delivery applications, the drug should be released from the nanoparticles to exert the therapeutic effect. But for a photosensitizer, it is not mandatory that the photosensitizer should be released from the nanoparticles for performing the intended therapeutic function. The molecular oxygen and singlet

oxygen generated by the photosensitizer is able to diffuse from the carrier it is sufficient to perform the therapeutic function in cancer cells. Hence usually biodegradable nanoparticles based on natural or synthetic polymers are used for synthesizing these nanoparticles based photosensitizers. These biodegradable nanoparticles are highly susceptible towards enzymatic or hydrolytic degradation which ensures the removal of these nanoparticles after performing its intended function without causing any long term toxicological concerns. Phthalocyanine was the first photosensitizer encapsulated within the degradable cyanoacrylic nanospheres (Labib *et al.*, 1991). Afterwards many important developments have taken place in this area to address the challenges associated with the photodynamic therapy.

#### **1.1.5. Magnetic hyperthermia**

Magnetic hyperthermia is a treatment modality widely used to destroy cancer cells. Even though the major intention of magnetic hyperthermia is to kill cancer cells, it is also used to make cancer cells more sensitive to radiation and certain anticancer drugs (Banobre *et al.*, 2013), (Chichel *et al.*, 2007). Magnetic hyperthermia uses electromagnetic radiation in radiofrequency region which is safer and ensures high penetration to inner organs and tissues. The magnetic nanoparticles used in hyperthermia treatment converts electromagnetic energy into heat energy sufficient to kill cancer cells under an oscillating magnetic field. Cancer cells are highly sensitive towards temperature variations when compared to normal healthy cells. When the temperature is increased beyond 42<sup>0</sup>C, the natural enzymatic process which is responsible for retaining the cells in live condition becomes inactive and will lead to cell death (Andra *et al.*, 1998). Even

though hyperthermia treatment can increase the intracellular temperature and kill cancer cells, it still has some major issues such as ionization of genetic material and lack of selectiveness in radiation. Iron oxide nanoparticles are widely used for hyperthermia treatment due to its excellent properties such as size dependent magnetism, ease of surface functionalization and biocompatibility (Campbell *et al.*, 2007). For performing effective magnetic hyperthermia, the nanoparticles should possess a high magnetic saturation which is mostly observed with iron oxide nanoparticles. Superparamagnetism is highly preferred for biomedical applications since superparamagnetic material prevent the possible aggregation of the magnetic particles during circulation time which prevents the formation of clots in the blood stream (Xu *et al.*, 2013). The superparamagnetism offers zero corecivity and retentivity to magnetic particles which prevents the magnetic dipole interaction between the particles which can lead to aggregation.

## ***1.2. Diagnostic strategies used in theranostic applications***

### **1.2.1. Fluorescence bioimaging**

Fluorescence bioimaging is defined as acquisition of images of biological tissues by employing the fluorescence properties of fluorescent moieties and nanoparticles. Fluorescence imaging offers several advantages such as high sensitivity, selectivity and low cost. Fluorescence imaging can be accomplished using the long spectral range from 400-2500 nm (Pansare *et al.*, 2012), (Wolfbeis *et al.*, 2015). Tissue autofluorescence is one of the major obstacles in fluorescence bioimaging. Because, the components such as water, melanin and proteins have very strong absorption in the spectral range of 400-650 nm. Hence,

the fluorophores or nanomaterials having emissions in the near IR range 650-1450 are highly preferred for fluorescence bioimaging (Boppart *et al.*, 2005), (Billinton *et al.*, 2001), (Ballou *et al.*, 2005). Imaging in the near IR window can totally eliminate the autofluorescence of the biological tissues. Moreover the near IR wavelength light can penetrate more deeply in the biological tissue which favors deep tissue imaging such as tumor tissue imaging. The efficacy of fluorescence bioimaging depends on several important factors of the fluorophores used such as absorption coefficient, quantum yield, photostability and stability under different environments (Mason *et al.*, 1999). Different types of nanoparticles such as quantum dots, gold nanoclusters and carbon dots are extensively explored for fluorescence bioimaging. These nanoparticles are used to construct multifunctional nanoparticles that can be used for theranostic applications (Xie *et al.*, 2010). Indocyanine green (ICG) is the only FDA approved dye for the direct intravenous administration in medical NIR imaging of hepatic clearance, cardiac function and retinal angiography. Hence ICG is extensively used to construct theranostic probes. Even though these conventional fluorescent nanoparticles have excellent fluorescent properties, they suffer from many serious drawbacks including toxicity, high cost and non biodegradability (Wu *et al.*, 2013).

### **1.2.2. Magnetic resonance imaging (MRI)**

Magnetic resonance imaging is one of the versatile molecular imaging techniques used in biomedical imaging. MRI offers advantageous properties such as high resolution and good tissue contrast. The working principle of MRI relies on the proton gradient between different biological molecules such as water, lipid and proteins that are present in the different organs of the body (Busquets *et al.*,

2015), (Lam *et al.*, 2013). MRI uses large magnetic fields and radio frequencies to generate images at molecular level. Magnetic field strength ranging from 1.5-3T is usually used for imaging; the applied magnetic field aligns the randomly oriented magnetic moments of the protons present in the biological tissues. This application of magnetic field produces a net equilibrium magnetization along the longitudinal axis (Mornet *et al.*, 2004). Radiofrequency waves are applied which matches the energy difference between the different states of the magnetic moment this process is termed as magnetic resonance and the frequency used is known as resonance frequency. Application of resonance frequency radio pulse (5-100 MHz) which matches the energy difference between the states transfer energy to the protons and flip the magnetic moments from the longitudinal direction by specific angle known as flip angle. This process of resonance repeats several times during this process of imaging. The time taken for the magnetic moments to return to their ground state is termed as magnetic relaxation time. Different tissues have different magnetic relaxation times which can be exploited for imaging different tissues. The magnetic relaxation process is classified in to two types, longitudinal relaxation or T1 relaxation and transverse relaxation or T2 relaxation.

#### ***1.2.2.1. Longitudinal relaxation or T1 relaxation***

Longitudinal relaxation measures how fast a magnetization which is parallel to the applied magnetic field strength relaxes to the ground state. Protons that relax very fast to the ground state (short T1) produces high signal intensities when compared to protons that take more time (long T1) to relax and produces low intensity signals. Longitudinal relaxation is also termed as spin-lattice

relaxation because there is energy transfer from the spin states of the protons with the ground lattice sites (Rumenapp *et al.*, 2012).

#### ***1.2.2.2. Transverse relaxation or T2 relaxation***

Transverse relaxation measures how fast a magnetization which is perpendicular to the applied magnetic field strength relaxes to the ground state. During the process of magnetic resonance, the magnetic spins are aligned in phase but once the radiofrequency pulse is removed the magnetic field of the different nuclei interact with each other and transfer energy between them hence it is also known as spin-spin relaxation (Stephen *et al.*, 2011).

Local difference in proton density among different tissues results in different values of T1 and T2 generates endogenous MRI contrast to tissues that can be used for imaging. This inherent image contrast can be further enhanced with the help of exogenous contrast agents such as gadolinium chelates and iron oxide nanoparticles (Caravan *et al.*, 1999), (Gerald *et al.*, 2009). These contrast agents affect the relaxation time of protons and provide more contrast to tissue images which is very useful for diagnosis of diseases such as cancer.

#### **1.2.3. Ultrasound imaging**

Ultrasound imaging is a molecular imaging technique which uses ultrasound waves to image the body. Initially ultrasound waves are sent to the patient's body. This wave after interacting with the various tissues of the body produces reflections and scattering. These scattering and reflections are received by a transducer which converts them to a gray scale image of the tissue cross-section. Ultrasound imaging is mainly used for intravascular, ophthalmic and

skin imaging applications (Foster *et al.*, 1993), (Mallidi *et al.*, 2009). The contrast in ultrasound imaging is attributed to the acoustic contrast between different tissues. The contrast of ultrasound imaging can be enhanced with the help of external contrast agents such as perfluorocarbon nanoparticles and silica nanoparticles (Lanza *et al.*, 2001), (Liu *et al.*, 2006). These nanoparticles based contrast agents can preferentially accumulate on the leaky vasculature of tumor region and provide more details about the stage and progression of tumor.

### ***1.3. Polymer based theranostic agents***

All of the above discussed therapeutic and diagnostic modalities are combined together in a single nanoparticle platform to construct a theranostic agent. Different types of nanomaterials such as iron oxide nanoparticles, quantum dots, gold nanoparticles and carbon nanotubes are explored for theranostic applications (Xie *et al.*, 2010). As all of these materials are endowed with different imaging capabilities such as magnetic resonance and fluorescence imaging, they can be efficiently used for imaging tumors. But it has been reported that theranostic materials such as carbon nanotubes and ironoxide nanoparticles can cause oxidative stress and membrane damage which can lead to apoptosis of cells (Elsabahy *et al.*, 2015). The remedy for this problem is to link these theranostic probes to a polymeric material. Polymer based theranostic agents have received considerable interest in the area of theranostic nanomedicine. A polymer component offers many benefits for a theranostic probe such as biocompatibility of the probe and reduction of toxicity of the nanoformulations, water solubility to these probes, (iii) presence of functional groups for conjugation of the theranostic

probes to targeting agents to ensure site specific delivery of payloads (Krasia *et al.*, 2013).

A polymer based theranostic construct consists of 3 important components (i) a polymer back bone to act as a carrier for the therapeutic components (ii) An imaging component such as dyes, quantum dots, iron oxide nanoparticles etc for imaging tumors (iii) a targeting agent such as antibodies, aptamers, transferrin etc to ensure targeted delivery of the payload (Figure-1). Different classes of polymeric materials such as micelles, liposomes, dendrimers and nanogels are used to construct theranostic probes.

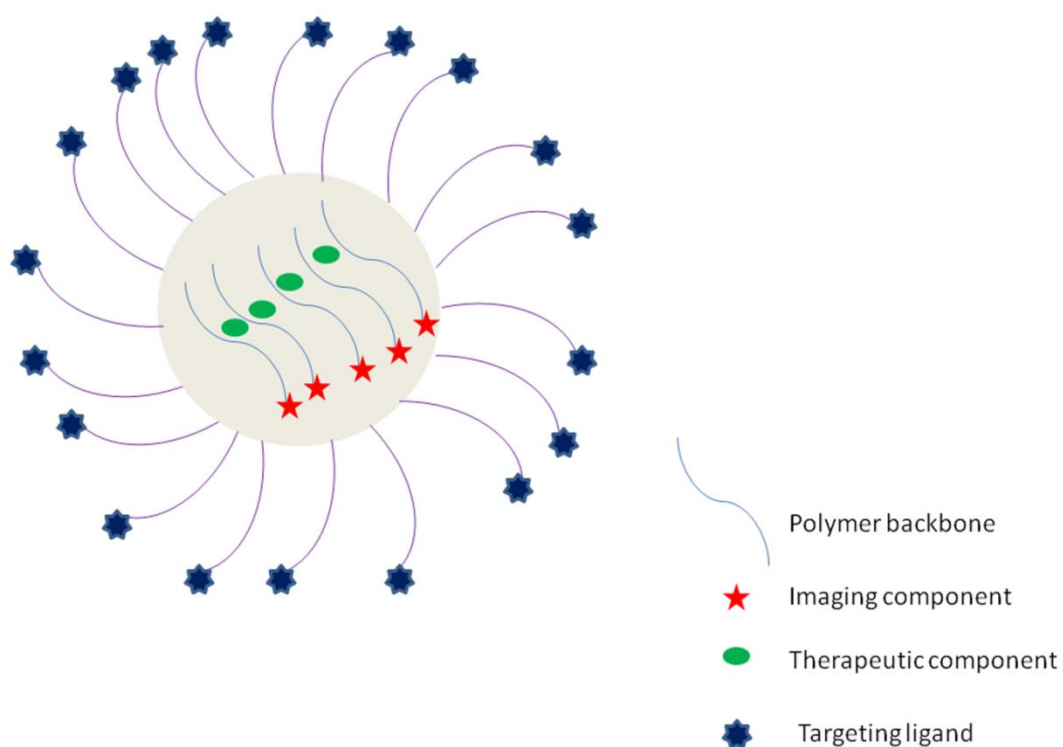


**Figure-1.Components of a theranostic polymer nanocarrier**

### 1.3.1. Micelles based theranostic agents

Micelles are polymeric structures formed by the self assembly of amphiphilic polymers which contains both hydrophilic and hydrophobic units linked together. Amphiphilic polymers self assemble above the critical micellar concentration to form a self assembled structure with hydrophobic core and hydrophilic chains projected outside like bristles of brushes (Jones *et al.*, 1999), (Xu *et al.*, 2013). An example of this type is PEG-PCL block copolymer, which self assemble above CMC to form micelles having PCL core and PEG shell. Most of the anticancer drug formulations are hydrophobic in nature. Hence, a hydrophilic carrier cannot encapsulate the anticancer drug efficiently. In the case of micelles, since it has hydrophobic interior compartments it can efficiently load the hydrophobic anticancer drug. Moreover, the stimuli responsive bonds present in these micelles facilitate smart stimuli responsive drug release from micelles. A micelle based theanostic probe comprises of the following components (i) a hydrophobic core with therapeutic component (ii) a fluorescent imaging probe inside the hydrophobic core (iii) a targeting ligand in the outer most hydrophilic shell (Figure-2).

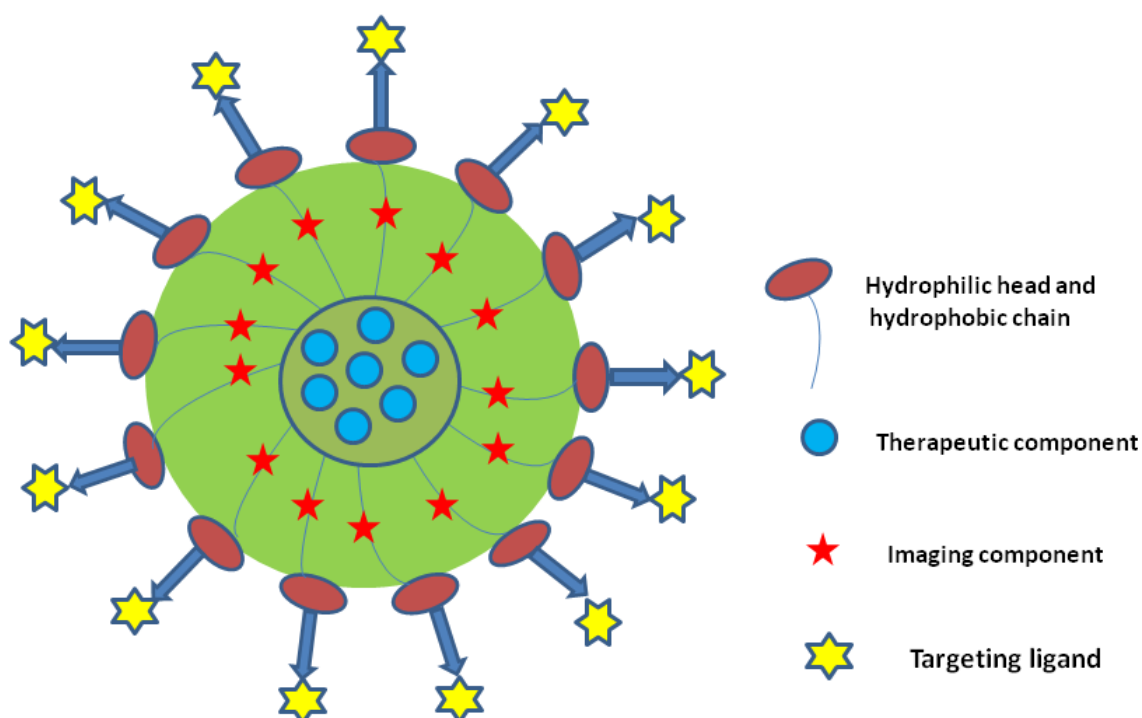


**Figure-2. Components of a theranostic polymeric micelle**

Different types of micelle based theranostic probes are reported.

Different types of micelle based theranostic probes are reported. Lie *et al* has reported a theranostic micelle based on hyaluronidase (HA) conjugated with a fluorescent photo sensitizer chlorine ce6 (ce6) (Li *et al.*, 2016). These theranostic micelles can perform tumor imaging through NIR/photo acoustic dual imaging. Guo and Hong *et al* has reported a theranostic micelle based on mPEG-b-polyaspartate, NIR emitting cyanine dye cypate and a photosensitizer ce6 (Guo and Hong *et al.*, 2014) for imaging (NIR/PA) tumor in mice. Guo and Mao *et al* has also reported a theranostic micelle based on poly(2-hydroxyethylmethacrylate),  $^{64}\text{Cu}$  radio chelator, doxorubicin and monoclonal antibody TRC105 (Guo and Mao *et al.*, 2014). The theranostic micelles have displayed pH sensitive release of doxorubicin. The *in vivo* tumor accumulation of these micelles conjugated with and without TRC 105 receptors were studied in

4T1 breast tumor bearing model has revealed higher accumulation of TRC 105 conjugated micelle. These micelles have also shown tumor imaging capability through positron emission tomography (PET) imaging.

Lee et al has reported a theranostic micelle based on poly (isopropyl acrylamide)-block-poly(caprolactone), NIR emitting cyanine dye DiR and anticancer drug carboplatin (Lee *et al.*, 2015). These theranostic micelles have shown temperature sensitive release of carboplatin due to the presence of the temperature sensitive isopropyl acrylamide unit of the micelle.

Wang et al has reported a theranostic magnetic micelles based on block polymer polylactide-mPEG and super paramagnetic iron oxide nanoparticles (SPION) and chitosan (Wang *et al.*, 2012). These cationic theranostic micelles can accomplish therapeutic function through gene delivery and imaging can be done with the help of magnetic resonance imaging. They exhibited good MRI imaging capability in mice model.

### **1.3.2. Liposome based theranostic agents**

Liposomes are vesicular system made up of phospholipids which will form a bilayer structure when dispersed in water. Liposomes can be classified based on several parameters such as no of lamellarity, size and preparation method. They were discovered by A.D. Bangham, which later becomes a promising candidate in drug delivery for the last 40 years (Luk *et al.*, 2012). Liposomes are ideal carriers for drug molecules since it is made up of natural phospholipids and is found to be biologically inert and nonimmunogenic. Moreover, different types of drugs such as hydrophilic and hydrophobic drugs can be incorporated inside the liposomes. The

hydrophobic drug can be entrapped inside the bilayer membranes of liposome and the hydrophilic drug can be entrapped inside the aqueous interior region. These types of liposomes are known as first generation liposomes. However the major drawback associated with these first generation liposomes are rapid removal by the mononuclear phagocyte system (MPS). This reduces the chance of reaching target tissues like cancer. Hence these first generation micelles cannot perform their function efficiently. This has led to the development of surface modified liposomes known as second generation micelles. This surface modification is usually done using molecules such as glycolipid and polyethylene glycol (PEG) (Malam *et al.*, 2009), (Sharma *et al.*, 1997). This surface modification significantly improve the circulation life time of liposomes, they prevent the opsonization process of liposome and thereby escape from the MPS system. This increased circulation lifetime significantly increases the therapeutic index of liposomes based drug formulations inside the body. As liposomes are already established as an excellent drug carrier, recent attempts are going on the construction of multifunctional liposomes which can perform various functions such as therapy and diagnostic (theranostic) functions together. A theranostic liposome will be very useful for early detection and treatment of deadly diseases like cancer. A theranostic liposome consists of the following components (i) a therapeutic component encapsulated in between the bilayer membrane (ii) a imaging component such as organic dyes, quantum dots inside the bilayer membrane for accomplishing imaging (iii) a stealth property imparting polymeric component like PEG on the outer shell (iv) a targeting ligand such as folic acid, transferrin, aptamer to ensure site specific delivery of payload (Figure-3).

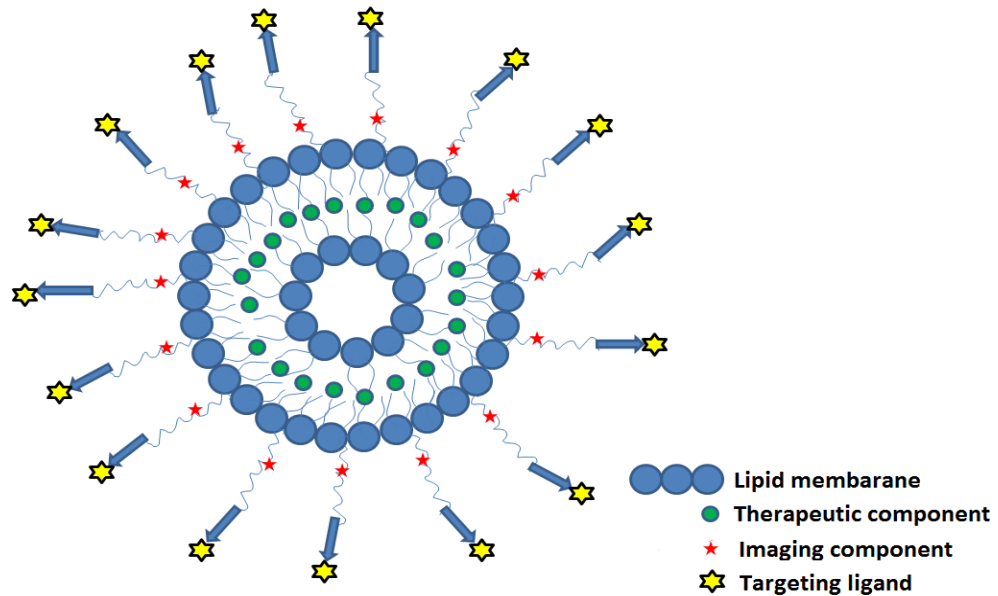


**Figure-3. Components of a theranostic polymeric liposome**

Portnoy et al. has reported a theranostic liposome for cerebral malaria. The liposome was based on phospholipon, PEG, indocyanine green (ICG) and artemisone (antimalarial drug) (Portnoy *et al.*, 2016). The developed theranostic liposome has shown good stability, modified pharmacokinetics and circulation life time when compared to free ICG. The efficacy of the developed liposome loaded with artemisone on cerebral malaria mice model has shown greater deposition in the cerebral areas of the brain infected mice when compared to normal mice. In another study Rizzitelli et al. has designed a theranostic liposome which can monitor the anticancer drug doxorubicin release through magnetic resonance imaging (MRI) (Rizzitelli *et al.*, 2015). The drug release from this theranostic liposome can be triggered with the assistance of pulsed low intensity nonfocused ultrasound (pLINFU). The theranostic capability of the liposome was further demonstrated with a murine breast cancer model. It was found that ultrasound stimulated mice have shown a remarkable enhancement in MRI signal which can be correlated to the ultrasound triggered drug release from the liposomes. Cho et al. has reported a

theranostic immunoliposome for osteoarthritis applications (Cho *et al.*, 2014). The distal ends of the liposomes that are conjugated with antibodies that can target the type II collagens present on the osteoarthritis affected cartilages. Hence the designed liposome can specifically bind to the receptors present on diseased area when compared to the normal cartilage. The *in vivo* imaging and histopathology analysis has revealed that these immunotheranostic liposomes mostly accumulated in the osteoarthritis region. Fang *et al.* has reported a theranostic liposome for brain targeting and bioimaging (Fang *et al.*, 2012). The quantum dot (imaging component) and apomorphine (therapeutic component) was incorporated inside the inner core of the liposome to confer theranostic property. The theranostic capability of the designed liposome tested in mice model has revealed increased fluorescence intensity from the brain of the mice in comparison to the free quantum dot. Murgia *et al.* reported a different class of theranostic liposome termed as cubosomes which are lipid based nanoparticles that are stabilized by pluronics (Murgia *et al.*, 2013). This theranostic cubosome has demonstrated live cell imaging capability along with good drug loading potential.

### **1.3.3. Dendrimers based theranostic agents**

Dendrimers are hyper branched polymer network used for different biomedical applications such as drug delivery and gene delivery applications. Dendrimers have low polydispersity and versatile surface functionality. The two important components of a dendrimer are a core which further generates the different branches of the dendrimer, the generations which are the branching layers attached to the core and a shell (Ma *et al.*, 2016), (Wang *et al.*, 2015). Dendrimers can be synthesized by two different methodologies known as

divergent synthesis and convergent synthesis. In divergent synthesis method, the dendrimer will be built from the core and it will start growing outside in to different branches or generations. Usually divergent method is used to synthesize lower generation dendrimers. In the convergent method the branches of the dendrimer will be built first and will converge towards the centre to generate the core of the dendrimer (Grayson *et al.*, 2001), (Hawker *et al.*, 1990). Dendrimers as a drug carrier possess so many advantageous properties such as higher drug loading, stimuli responsiveness and targeted delivery of the drugs. Drug loading can be accomplished via conjugating the drugs to the terminal branches or by encapsulating the drug inside the interior cavity of the dendrimer. The availability of multiple numbers of functional groups at the terminal ends of the dendrimer can be exploited for the conjugation with imaging agents and targeting ligands to construct multifunctional theranostic dendrimers. A theranostic dendrimer consists of the following components (i) a therapeutic component encapsulated in between the branches of the dendrimer (ii) a imaging component such as organic dyes, quantum dots inside for accomplishing imaging (iii) a stealth property imparting polymeric component like PEG on the outer shell (iv) a targeting ligand such as folic acid, transferrin, aptamer to ensure site specific delivery of payload (Figure-4).

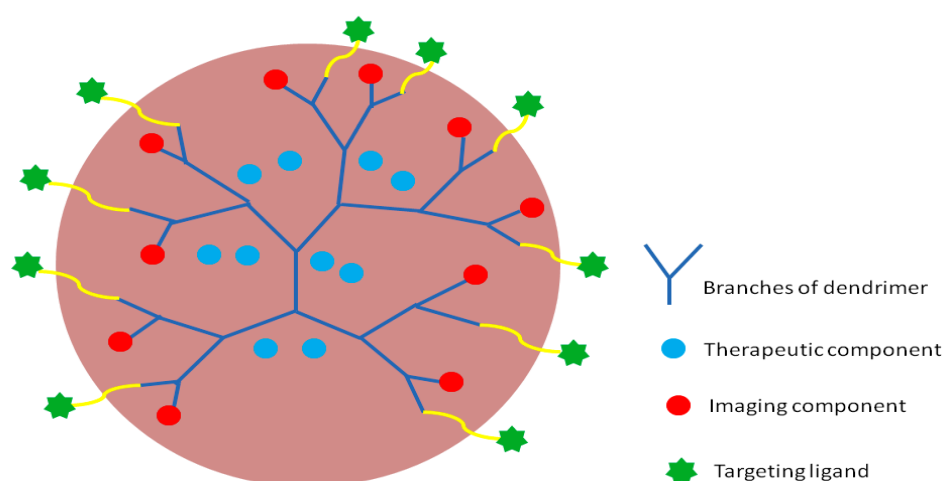


**Figure-4.Components of a theranostic polymeric dendrimer**

Li et al has reported a theranostic PEGylated dendrimers for cisplatin delivery and NIR imaging (Li *et al.*, 2016). The synthesized dendrimers are sensitive towards pH and redox potential variations. The *invitro* cancer imaging capability of the dendrimers evaluated in A549 cells have revealed good cellular internalization and cancer cell imaging capability. The anticancer activity of the theranostic dendrimers in A549 xenograft tumor bearing mice has revealed good pharmacokinetics, NIR tumor imaging capability and platinum distribution. In another study matai et al has reported a theranostic dendrimer based on carbon dots and epirubicin (Matai *et al.*, 2015). The designed theranostic dendrimer has shown dual emission imaging capability on MCF-7 breast cancer cells. The theranostic dendrimer also exhibited good therapeutic capability in MCF-7 cells by the generation of reactive oxygen species generation which leads to the apoptotic cell death. Xu et al has reported a theranostic dendrimer for gene delivery and biological tracking (Xu *et al.*, 2014). The designed dendrimer exhibited excellent gene delivery efficiency both *invitro* and *in vivo*. The designed

dendrimers showed potential for intracellular tracking, protein expression monitoring and bioimaging. These multifunctional characteristics of the dendrimer enables to understand the major pathways involved in gene delivery which helps to design efficient gene delivery systems. Zhu et al reported another class dendrimer for targeted cancer theranostics. (Zhu *et al.*, 2014). The gold nanoparticles present in the dendrimer confer it computed tomography imaging (CT) and the tocopheryl succinate confers the therapeutic capability to the designed dendrimer. The folic acid present in the dendrimer imparts active targeting capability to the dendrimers. The dendrimer also enhanced the water solubility of the therapeutic component tocopheryl succinate which resulted in good therapeutic response both invitro and invivo. The designed dendrimer also exhibited good CT imaging capability in tumor model. Zhang et al has reported a theranostic DNA based dendrimer for bioimaging and drug delivery (Zhang *et al.*, 2015). The designed dendrimer exhibited some interesting properties such as high stability and biocompatibility, high cellular internalization efficiency and high drug loading. The designed dendrimer exhibited good anticancer activity on human T cell acute lymphoblastic leukemia cell line with aptamer receptors. The intracellular distribution of the drug was studied using the self fluorescence of doxorubicin

#### **1.3.4. Nanogels based theranostic agents**

Nanogels are chemically or physically cross linked polymeric nanostructures endowed with properties such as high water absorptivity, rapid response to external stimuli, stimuli responsive swelling, high dispersion stability, network structure permeability, mechanical strength and biocompatibility. These

properties make it appropriate for executing both drug delivery and imaging. Nanogels have very high drug loading capacity which makes it one of the favorite candidates for drug delivery applications (Kabanov *et al.*, 2009), (Vinogradov *et al.*, 2002). The high drug loading capacity of nanogels can be attributed to the presence of high water content which makes more space for the loaded cargo inside the nanogels. The high water content present on this material also makes it more biocompatible when compared to all of the other polymeric carriers such as micelles, dendrimers and liposomes. Nanogels can be loaded with drugs via different methodologies such as physical entrapment, covalent conjugation and self assembly. The loaded cargo or drug can be released via different processes such as diffusion, degradation and variations in pH, temperature and ionic strength. These properties help to carry out the programmable delivery of drugs from the interior networks of nanogels. The versatile functional groups that are present outside the surface of the nanogels can be exploited for conjugating with imaging agents and targeting ligands to construct theranostic nanogels. A theranostic nanogel consists of the following components (i) a therapeutic component encapsulated inside the nanogel (ii) a imaging component such as organic dyes, quantum dots inside the nanogel for accomplishing imaging (iii) a stealth property imparting polymeric component like PEG on the outer shell (iv) a targeting ligand such as folic acid, transferrin, aptamer to ensure site specific delivery of payload (Figure-5).

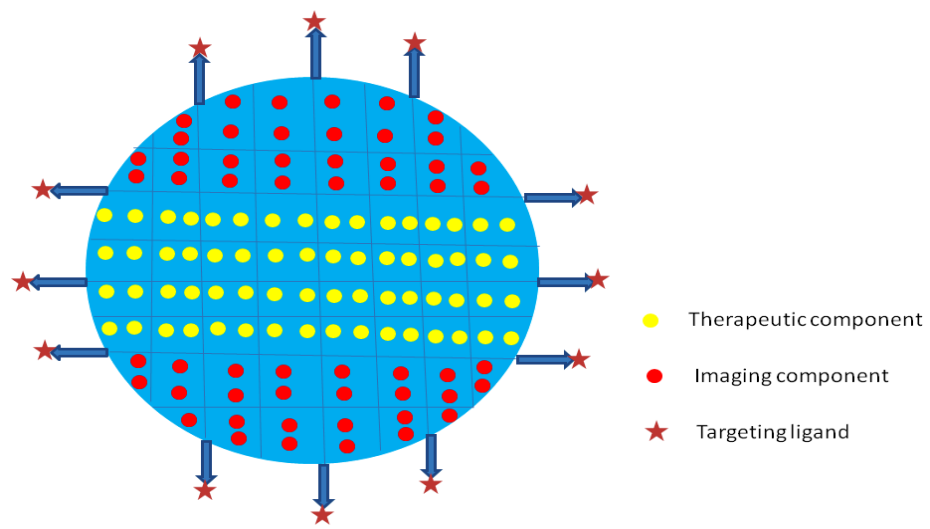


**Figure-5.Components of a theranostic polymeric nanogel**

## **Chapter-2**

### **Literature review**

*Nanocarriers have greater role in the area of theranostic nanomedicine. In this chapter, the research and developments on different nanogels that are explored for theranostic applications are presented.*

#### ***2.1. Nanogel based theranostic agents***

Nanogels are the most important polymer based theranostic agent due to its superior characteristics such as high biocompatibility, water content, drug loading capability, stimuli responsive nature and presence of versatile functional groups to conjugate the imaging moieties. There are many different reports available on nanogels as a theranostic carrier.

Recently Park et al has reported a theranostic sunflower type nanogel based on heparin modified pluronics, quantum dots and polyethyleneimine (PEI) for gene delivery and tracing of human mesenchymal stem cells (Park *et al.*, 2016). The heparinized nanogel was complexed with amino groups bearing quantum dots which were further coated with PEI to form the theranostic construct. The nanogel was further complexed with DNA to form the gene delivery vehicle. The

mesenchymal cellular internalization studies have shown that the nanogel entered to the nucleus of mesenchymal cells in a time dependent fashion. The transplanted mesenchymal stem cells modified with the nanogels was tracked with the fluorescence of the nanogel. However, the fluorescence emission of the quantum dot component of the nanogel is at visible region (650 nm) which cannot be used for imaging efficiently due to the auto fluorescence observed in this region.

Birjand et al has reported a theranostic nanogel based on thermo responsive polyglycerol and NIR absorbing dye IR806 using radical precipitation reaction (Birjand *et al.*, 2016). The synthesized nanogel exhibited responsiveness towards both temperature as well as NIR light. The designed nanogel has also shown a preferential accumulation in mitochondrial compartment of cancer cells. The nanogel has shown therapeutic capability by generating heat around 50<sup>0</sup>C upon irradiation with laser light. However, the poor photostability of the IR806 dye and leakage of the dye from the nanogel may limit the practical utility of this nanogel.

Nagahama et al has reported a theranostic nanogel based on dextran and curcumin synthesized by the self assembly of dextran-curcumin conjugate in water with curcumin loading content of 21.6 wt% (Nagahama *et al.*, 2015). The cellular internalization studies of the nanogel on Hela cells reveal significant cellular uptake and entry into the intracellular compartments via clathrin-mediated endocytosis. The green fluorescence characteristics of the curcumin fragment present on the nanogel was used for cell imaging. Even though, this curcumin based nanogel displayed good therapeutic capability, the visible green fluorescence of curcumin cannot be considered as efficient for imaging.

Quan et al. has reported a thermoresponsive galactose based nanogel as a theranostic agent in hypoxia hepatocellular carcinoma (Quan *et al.*, 2015). The nanogel was synthesized using reversible addition-fragmentation chain transfer polymerization of 2-lactobionamidoethyl methacrylamide, thermo sensitive diethylene glycol methyl ethyl methacrylate and iodoazomycin arabinofuranoside. It was found that the nanogel is hydrophobic at 37 °C and becomes collapsed for the entrapment of iodoazomycin arabinofuranoside inside the core of the nanogel. However, at low temperatures the nanogel core swells and releases the loaded iodoazomycin arabinofuranoside in a controllable manner. The drug release studies have shown that the nanogels can release the drug through passive diffusion over 10h. However, this nanogel is comprised of a green fluorescence emitting FITC dye for imaging, which is not an efficient fluorophore for NIR bioimaging.

Chiang et al. has reported a theranostic hollow hybrid nanogel endowed with MRI imaging and drug loading capability (Chiang *et al.*, 2013); the nanogel was prepared with citric acid coated superparamagnetic iron oxide nanoparticles and graft polymer of acrylic acid and 2-methacryloyloethyl acrylate. The nanogel maintained a high level (44wt %) of superparamagnetic iron oxide nanoparticles in the outer region of the hollow nanogel. The nanogel also exhibited higher doxorubicin loading efficiency (88%) with pH and temperature dependent drug release profile. However, the presence of high level of iron oxide nanoparticles in the outer layer of the nanogel can induce significant amount of reactive oxygen species in cells and subsequent toxicity issues.

Su et al. has reported a theranostic nanogels based on poly(N-isopropyl acrylamide-co-acrylic acid) and bovine serum albumin encapsulated-gold

nanocluster and iRGD peptide (Su *et al.*, 2013). Cationic drug doxorubin was introduced inside the anionic nanogel through electrostatic interaction. It was found that the nanogel displayed both temperature as well as pH responsive drug release profile of doxorubicin suitable for cancer therapy. The fluorescence of the gold nanoclusters of the nanogel enables the tracking of the nanogels *in vitro*. However, the fluorescence emission of the gold nanocluster of the nanogel is at visible region (640nm). Park *et al.* has reported a theranostic nanogel synthesized by the self assembly of Poly (N-isopropylacrylamide-co-acrylic acid), amine functionalized iron oxide nanoparticles and fluorescent carbocyanine dye (Park *et al.*, 2013). The nanogel exhibited temperature and pH dependent size variation. The cellular internalization of the nanogel in hMSC occurred through endocytosis. The hMSC loaded-nanogels were transplanted in to nude mice and visualized through the dual imaging (fluorescence and magnetic resonance imaging). Xing *et al.* has also reported a theranostic reduction sensitive nanogel for directly imaging reduction sensitive drug release (Xing *et al.*, 2012). The nanogel was synthesized by the copolymerization of nepsilon-carbobenzoxy-L-lysine, L-lysine and amino terminated Mpeg and coupled with aminocyanine dye. Doxorubicin was loaded inside the core of the nanogel to construct a NIR emitting prodrug nanogel. Under reduction sensitive environment, 88% of the drug released within 10h, whereas under reduction-insensitive environment only 68% of the drug released within the same time period. These hydrogels having carbocyanine dye is associated with issue of poor photostability and aggregation behavior of the carbocyanine in physiological fluid which may limit the practical utility of these nanogel for theranostic applications.

Wu et al. has reported a core-shell hybrid nanogel with tunable magnetic and fluorescent properties (Wu *et al.*, 2011). The nanogel was synthesized by growing Ag layer over magnetic nickel (Ni) nanoparticles to form bimetallic core-shell nanoparticles. This hybrid nanoparticle was further coated with a pH responsive gel shell of poly (ethylene glycol-co-methacrylic acid) to construct the theranostic hybrid nanogel. The nanogel exhibited stability with pH responsive drug release profile. Wu et al. has also reported a nanogel based on Ag/Au bimetallic nanoparticle, curcumin, polystyrene and polyethylene glycol (Wu *et al.*, 2011). The hydrophobic polystyrene was used as the inner core of the nanogel to augment curcumin loading in the nanogel. The hydrophilic PEG was used as the outer coating of the nanogel to confer hydrophilicity and biocompatibility to the nanogel. The bimetallic Ag/Au core of the nanogel confers fluorescence bioimaging and photothermal therapy capability to the designed nanogel. The nanogel responds to pH variations and near infrared light and releases the loaded drug curcumin in a controllable and sustainable way. However, the fluorescence emission of the Ag nanoparticles of these nanogels is confined with only visible region (550nm).

Rejinold et al. has reported a theranostic nanogel based on chitin and Cdse quantum dots (Rejinold *et al.*, 2011). The nanogel was further loaded with bovine serum albumin (BSA) to confer therapeutic capability to the nanogels. The nanogel synthesized was monodisperse with particle size around 100 nm favorable for theranostic applications. The nanogel has displayed controlled and sustainable release kinetics of BSA for 3 days. However, the fluorescence emission of the Cdse quantum dots of these nanogels is at visible region (590nm). Zhu et al. has

reported a temperature sensitive theranostic nanogel based on Bi<sub>2</sub>O<sub>3</sub> quantum dots and polyvinyl alcohol (PVA) (Zhu *et al.*, 2012). The designed nanogel can respond to temperature variations and will undergo volume phase transition over physiological temperature change of 37-40<sup>0</sup>C. A model anticancer drug temozolomide was used to study the temperature sensitive release properties of the designed nanogel. The nanogel has displayed fluorescence imaging capability in mouse melanoma B16F10 cells. However, the fluorescence emission of the Bi<sub>2</sub>O<sub>3</sub> quantum dots of this nanogel is at visible region (438nm).

## ***2.2. Nanogels with inherent imaging capability for theranostic applications***

Nanogels with inherent fluorescence (NIR) capability are considered as most promising candidates for theranostic purposes. Very few reports are available on nanogels with inherent fluorescence capability. Manry *etal* has reported a nanogel with innate blue fluorescence capability (Manry *et al.*, 2011). The designed nanogel was synthesized from biodegradable photoluminescent polymers (BPLP) by crosslinking with vinyl crosslinkers. The BPLP polymer synthesized was based on citric acid, diol and amino acid. The fluorescent property of the nanogel arises from the reaction of citric acid with amino acid forming cyclic ring structures. The BPLP nanogel synthesized was spherical in shape with particle size around 100nm. Chen *etal* has reported a self fluorescent nanogel based on abietane (a natural resin acid) (Chen *et al.*, 2013). The designed abietane based nanogel was conjugated with PEG and folic acid to confer biocompatibility and targeting capability to the abietane based nanogel. Doxorubicin was loaded inside the

nanogel to achieve the therapeutic capability and tested in MCF-7 cell lines. It was found that the abietane based nanogel mainly located at the cytoplasm of the cells and could be visualized with innate green fluorescence of the nanogel. However, the fluorescence emission of these nanogels is also confined with only visible region (550nm) which cannot be considered for NIR imaging.

### ***2.3. Objectives of the present study***

Nanocarriers with innate imaging capability have greater role in theranostic nanomedicine especially for the treatment of cancer. In this context, nanogels with innate imaging capability can be a better choice to perform the imaging and therapeutic functions. However, the reports on nanogels with innate imaging capability are quite rare. Even though BPLP nanogel reported by Manry *et al.*, (Manry *et al.*, 2011) and abietane based nanogel reported by Chen *et al.*, (Chen *et al.*, 2013) have inherent fluorescence; their fluorescence is confined only with visible region. Fluorescence at visible region is not appropriate for bioimaging due to its low tissue penetration which can interfere with the auto fluorescence from the body. On the other hand, near IR (NIR) light has the maximum tissue penetration with minimal auto fluorescence from the body. Therefore, efficient bioimaging can be accomplished only with the help of NIR emitting nanocarriers.

Excitation wavelength dependent photoluminescence (EDF) is an interesting phenomenon which show color tunable photoluminescent properties with different excitation and emission from visible to near IR region. Unlike the conventional fluorophores such as organic dyes and quantum dots in which

fluorescence tuning can be accomplished only through composition or size change, fluorophores exhibiting EDF can be tuned from visible to near IR region without the change of composition or size (Cushing *et al.*,2014). Hence, polymeric nanogels with inherent excitation wavelength dependent photoluminescence in NIR region are more promising therapeutic agent.

Therapeutic agents with the capability of drug delivery at the targeted tumor site are essential to ensure the safety and efficacy of the therapeutic agent. For safer therapeutic agent, it is mandatory that the therapeutic agents reach the targeted site, perform the therapeutic function and undergo metabolism or excretion from the body. Targeting of a therapeutic agent to the required site can be accomplished either by passive or active mode. The passive mode of targeting the tumor site and tumor-specific accumulation of drug (enhanced permeability and retention (EPR) effect), is mediated by stimuli responsive character of the nanocarrier. The stimuli responsive nanocarriers which are sensitive to pH and redox potential are therefore important as targeted nanocarriers for executing the therapeutic function. Nanogels with the presence of numerous functional groups such as carboxyl or amino groups enable conjugation with targeting ligands and render them with stimuli responsive nature. Therefore nanogel with stimuli responsive moiety is also more promising as passively targeted therapeutic agent.

Magneto-fluorescent nanocarriers have great scope for theranostic applications as they can combine the advantage of both optical and magnetic properties. Magneto-fluorescent nanocarriers comprising fluorophores such as quantum dots and organic dyes with magnetic iron oxide nanoparticles have excellent physico-chemical properties. However, their application is limited due

to reasons such as toxicity, non specific cell/tissue-polymer interaction, non-biodegradability and high cost. In order to address these issues, self fluorescent polymers are alternative to the toxic quantum dots and organic dyes to construct magneto-fluorescent nanocarriers. Therefore biocompatible polymeric magneto-fluorescent nanocarriers have great scope for theranostic applications.

The surface functionalization of nanocarriers with active targeting ligands such as antibody, antibody fragment, peptide, aptamer, polysaccharide, saccharide and folic acid are now receiving considerable amount of interest in biomedical research. These active ligands can enhance accumulation of the nanocarriers in tumor and internalization of the nanocarriers by cancer cells. Octreotide is a somatostatin analogue (natural growth hormone analogue) based octapeptide that has a high affinity with the somatostatin receptors (SST) that are over expressed on endocrinal cells and many types of solid tumors. Since octreotide does not have sites which are cleavable by enzymes, it is relatively more stable with half life of around 90 min. These characteristics favor octreotide as a targeting agent for anticancer drug delivery. Octeroscan and neotect are the two octreotide based formulations labeled with radioactive indium-111 and approved by FDA for treating tumors (Virgolini *et al.*,2002 and David *et al.*,2015). Therefore octreotide based targeted polymeric nanogels may ensure the site-specific delivery of the drug molecule at the target site and thereby avoids the toxic side effects of anticancer drug formulations.

One of the essential requirements for the theranostic nanocarrier is the optimum particle size and shape to favour prolonged blood circulation and to avoid renal clearance and also to avoid capture by the reticuloendothelial system (RES)

and surface chemistry required to avoid the systemic-level processes (such as opsonisation) and to enhance the cellular-level processes (such as cell uptake).

Based on this background, the present studies were designed with the major objectives of (i) Development of biocompatible comonomers with inherent excitation wavelength dependent photoluminescence in NIR region, polymeric nanogels with stimuli responsive and EDF characteristics for passive targeted delivery, polymeric magneto-fluorescent nanogels and octreotide based targeted polymeric nanogels with EDF characteristics for the site-specific delivery for the treatment of cancer, (ii) Studies on the therapeutic capability and imaging capability of the newly developed nanogels, (iii) Studies on the biocompatibility, bioimaging, biodistribution and clearance of newly prepared nanogels in rodents and (iv) Identification of most promising nanogel as theranostic agent for the treatment of cancer.

The detailed objectives of the studies include

1. (i) The synthesis and characterization of self fluorescent comonomers with EDF near IR character using carboxyl terminated polypropylene fumarate, PEG citric acid and glycine.  
  
(ii) Preparation and evaluation of self fluorescent pH sensitive nanogels as passively targeted theranostic nanocarrier.
2. (i) The synthesis and characterization of photoluminescent comonomer using PEG, maleic acid and glycine for magneto-fluorescent nanogel.  
  
(ii) Preparation and evaluation of magneto-fluorescent nanogel.

3. (i) The synthesis and characterization of photoluminescent comonomer using PEG, maleic acid and 4-aminobenzoic acid for octreotide conjugated nanogel.  
(ii) Preparation and evaluation of octreotide conjugated nanogel as targeted nanogel.
4. Evaluation of the fluorescence properties, fluorescence emission, photostability and fluorescence lifetime of the comonomers.
5. Evaluation of the size, surface charge, shape and morphology of the nanogels.
6. Evaluation of the therapeutic capability of the nanogels.
7. Evaluation of the biocompatibility, bioimaging, biodistribution and clearance of newly prepared nanogels in rodents.

## **Chapter -3**

### **Materials and methods**

*This chapter presents the materials and methods used to synthesize and characterize different photoluminescent comonomers and nanogels. The details regarding the synthesis of photoluminescent comonomers and nanogels are presented. The methodologies used for the structural characterization of the comonomers are presented in this chapter. The methodology used to study the fluorescent properties of the comonomers is presented. The methods used to study the properties of the nanogels such as size; shape and surface charge are presented in this chapter. The methodology used to evaluate the cytocompatibility; therapeutic capability and cellular imaging capability of the nanogels are presented in this chapter. The methodology used to evaluate the in vivo bioimaging capability, biodistribution and histopathology analysis of the nanogels are also presented in this chapter.*

#### **3.1. Materials**

Maleic anhydride, maleic acid, 1,2- propylene glycol, polyethylene glycol (PEG,MW:300,1000,2000), Ferrous chloride tetrahydrate, Ferric chloride

anhydrous, 4-amino benzoic acid, citric acid acetone and methanol were purchased from Merck (India). Ammonium persulfate (APS), Tetra methyl ethylene diamine (TEMED), Diethylene glycoldimethacrylate (DEGDMA), N,N Dimethyl aminoethyl methacrylate (DMEMA), acrylic acid, octreotide, propidium iodide, acridine orange, ethidium bromide and glycine were obtained from Sigma (Bangalore, India). Dialysis bag (500 and 1000D molecular weight cut-off), Dulbecco's modified eagle's medium (DMEM) and Fetal bovine serum (FBS) were purchased from Invitrogen (India). MTT (3-(4,5-dimethyl thiazol-2-yl)-2,5-diphenyl tetrazolium bromide) assay kit and live dead assay kit was purchased from Hi Media (India).

### ***3.2. Synthesis of photoluminescent comacromers***

#### **3.2.1. Synthesis of photoluminescent comacromers for passively targeted nanogels**

##### ***3.2.1.1. Synthesis of photoluminescent PPF-PEG-glycine comacromer (PLM)***

The photoluminescent comacromer (PLM) was synthesized using carboxy-terminated polypropylene fumarate (CT-PPF), PEG and glycine. CT-PPF was synthesized according to our previously published protocols [25]. Briefly maleic anhydride (1 M) and 1,2-propyleneglycol (0.5 M) were condensed with morpholine and sodium acetate as catalyst to produce CT-PPF. Afterwards 0.05 M CT-PPF (molecular weight 1389 D) and 0.1 M PEG (molecular weight 300 D) were refluxed under nitrogen atmosphere for 10 min at 180 °C. Once the constituents in the reaction mixture were melted 0.05 M glycine was added and the reaction was continued for another 100 min. The comacromer formed was a

brownish yellow coloured resin. The comacromer was then subjected to dialysis through a dialysis membrane (500 D) against deionised water for 3 days to completely remove the unreacted monomers to get the purified comacromer. The comacromer is coded as PLM.

### **3.2.1.2. Synthesis of PLM comacromer analogues**

The analogue of PLM coded as PEG-G was synthesized using PEG and glycine. Briefly 0.1 M PEG (molecular weight 300 D) was melt condensed with 0.05 M glycine under nitrogen atmosphere for 2 h at 180 °C. Two more analogues of PLM coded as PEG-M and PEG-P were also synthesized by replacing glycine in PEG-G with maleic acid and CT-PPF respectively. The analogues were then subjected to dialysis through a dialysis membrane (500D) against deionised water for 3 days to completely remove the unreacted monomers.

### **3.2.2. Synthesis of photoluminescent PPF-PEG-citric acid-glycine comacromer (C-PLM)**

A modified citric acid containing photoluminescent comacromer (C-PLM) was synthesized as follows. Briefly, PEG-300 (7.5 g) was refluxed with 0.05 M carboxy terminated poly (propylene fumarate) (CT-PPF) ( 12.5 g) and citric acid (2.62 g) under nitrogen atmosphere for 15 min at 180 °C. After melting of the reaction mixture, glycine (1g) was added and the reaction was continued for further 100 min. The comacromer formed was a brownish coloured resin. The comacromer was then subjected to dialysis through a dialysis membrane (500 D) for 3 days to completely remove the unreacted monomers. The comacromer was then lyophilized and stored at 4 °C.

### **3.2.3. Synthesis of photoluminescent PEG-maleic acid-glycine comacromer (PMG) for magneto-fluorescent nanogel**

Initially a photoluminescent comacromer was synthesized as follows. In a round bottom 3 neck flask, PEG-1000 (12.5g, 0.1 M) and maleic acid (1.5g, 0.05M) was condensed under nitrogen atmosphere at 180 °C. Once the complete melting of the reaction mixture has taken place, glycine (1.13g, 0.05M) was added and the reaction was continued for another 6h. The resulting brown coloured solution was dissolved in distilled water and then dialysed with a dialysing membrane for 3 days to completely remove the unreacted monomers. A brownish yellow coloured solution was isolated as the product. The comacromer was then lyophilised and stored at 4<sup>0</sup>C. The comacromer was coded as PMG.

### **3.2.4. Synthesis of photoluminescent PEG-maleic acid-aminobenzoic acid comacromer (PMB) for actively targeted nanogel**

Initially a photoluminescent comacromer was synthesized as follows. In a round bottom 3 neck flasks, PEG-2000 (12.5 g, 0.1 M) and maleic acid (1.5 g, 0.05 M) was condensed under nitrogen atmosphere at 180 °C. Once the complete melting of the reaction mixture has taken place, 4 aminobenzoic acid (1.13 g, 0.05 M) was added and the reaction was continued for another 6h. The resulting brown coloured solution was dissolved in distilled water and then dialysed with a dialysing membrane for 3 days to completely remove the unreacted monomers. A brownish yellow coloured solution was isolated as the product. The comacromer was then lyophilised and stored at 4<sup>0</sup> C. The synthesized comacromer was coded as PMB.

### ***3.3. Structural characterization of the photoluminescent comacromers***

The presence of different functional groups and structural evaluations of the comacromers were done using Fourier transform infrared (FT-IR) spectral and nuclear magnetic resonance spectrum (NMR) analyses.

#### **3.3.1. FTIR and Proton NMR analysis of the photoluminescent comacromers**

FT-IR spectra were obtained in the region of 400 to 4000  $\text{cm}^{-1}$  using a spectrometer (Jasco, FT/IR-4200, Easton, USA), with resin smear placed between KBr plates. Data acquisition and analysis was performed using JASCO's proprietary Spectra Manager TM II cross-platform software. The nuclear magnetic resonance spectrum of the comacromers was recorded using a Bruker 500 MHz spectrometer (Bruker Biospin, Billerica, MA) with DMSO and  $\text{CDCl}_3$  as solvents.

#### **3.3.2. Molecular weight determination of the photoluminescent comacromers**

The macromeric natures of the synthesized comacromers were evaluated using Gel permeation chromatography.

The molecular weight of comacromers was determined using a gel permeation chromatography (GPC) system (Waters) equipped with a 600 series pump, refractive index detector (Waters 2414) and styragel columns (HR-5E/4E/2/0.5) connected in series. Briefly, 20  $\mu\text{l}$  of 1% polymer solution in THF was injected into the system with the mobile phase (THF) set at a flow rate of 1 ml/min. Polystyrene standards (Mp: 100000, 9130 and 162) were used for relative calibration.

### ***3.4. Determination of photoluminescent properties of comacromers***

The photoluminescence evaluations of the comacromers were done to assess the excitation dependent fluorescence (EDF) characteristics of the comacromer.

The photoluminescence of the comacromers under aqueous condition was studied using CARY-40 spectrofluorimeter at room temperature. Comacromer solutions (1 mg/ml) were loaded inside a quartz cuvette having a path length of 10 mm. The excitation and emission slit width were kept at 1.5 nm. The photostability of the comacromers was evaluated under aqueous condition by continuously exciting the comacromers at the excitation wavelength of 420 nm in a spectrofluorimeter and monitored the change in emission intensity at 525 nm. The time resolved fluorescence experiments of the comacromers were performed using an IBH nanosecond single-photon counting employing a 440 nm Nano-LED excitation source and a Hamamatsu C4878-02 micro channel plate (MCP) detector.

### ***3.5. Synthesis of nanogels from photoluminescent comacromers***

#### **3.5.1. Preparation of passively targeted nanogel from PLM comacromer (PLM-NG)**

A nanogel was prepared from PLM comacromer as follows. Briefly, 0.8% (w/v) of PLM was dissolved in 5ml water to form a uniform homogenous solution. To this solution, 0.05% (v/v), of acrylic acid was added followed by  $1 \times 10^{-3}$  M of ammonium per sulfate and TEMED. The beaker containing the above

solution was then sonicated for 30 min. After sonication a slight turbidity was observed indicating the crosslinking into nanogel. The nanogel was coded as PLM-NG.

### **3.5.2. Preparation of passively targeted nanogel from C-PLM comonomer (C-PLM-NG)**

Nanogel was prepared using C-PLM as follows; briefly 40 mg of C-PLM was dissolved in 5 ml water to form a uniform homogenous solution. To this solution, DMEMA (10  $\mu$ l), was added followed by APS (30  $\mu$ l) and TEMED. The beaker containing the above solution was then sonicated for 30 min. After sonication a slight turbidity was observed indicating the crosslinking into nanogel. The nanogel was coded as C-PLM-NG.

### **3.5.3. Synthesis of magneto-fluorescent nanogel (C-SPION-NG)**

#### ***3.5.3.1. Synthesis of citrate capped superparamagnetic iron oxide nanoparticles (C-SPION)***

Citrate capped superparamagnetic iron oxide nanoparticles were synthesized. Initially SPION was synthesized as reported by cheraghipour et al [22]. Briefly, 50ml of  $\text{Fe}^{2+}$  and  $\text{Fe}^{3+}$  salts (1:2 molar ratios) were dissolved in 50 ml deionised water in two beakers. Further, the salt solutions were transferred in to 3 neck round bottom flask equipped with nitrogen atmosphere. Vigorous stirring of the reaction mixture was taken place at 80<sup>0</sup> C to avoid the chances of formation of large polycrystalline particles. Afterwards  $\text{NH}_4\text{OH}$  (25 wt %) was added drop wise to the reaction mixture with continuous monitoring of reaction pH. Once the pH value reached 12, formation of black precipitate has been taken

place indicating the formation of SPION. The reaction mixture was cooled in to room temperature. Afterwards the particles were centrifuged at 2000 rpm for 5 times to completely remove the impurities. Further, the particles were subjected for magnetic separation to get the purified SPION particles

The synthesized SPION was modified to get C-SPION using citric acid as follows, briefly SPION were treated with 0.5 mg/ml of citric acid and the reaction was carried out at 90<sup>0</sup>C for 1 hr under nitrogen atmosphere. The precipitate was formed after cooling the reaction mixture in to room temperature. Afterwards the particles were centrifuged at 2000 rpm for 5 times to completely remove the impurities. Further, the particles were subjected for magnetic separation to get the purified C-SPION particles.

#### ***3.5.3.2. Synthesis of magneto-fluorescent nanogel (C-SPION-NG) from PMG comacromer and C-SPION***

Magneto-fluorescent nanogel was prepared using PMG comacromer and C-SPION as follows; briefly, 40 mg of PMG comacromer was dissolved in 40 ml distilled water inside a round bottom flask and stirred for 15 minutes under nitrogen atmosphere. Further, C-SPION (15 mg) was added to the reaction mixture with stirring followed by the addition of 10 µl of DMEMA, ammonium per sulfate and TEMED (30µl, 1×10<sup>-3</sup> M). The solution was then sonicated for 30 min to disperse the synthesized nanogels. The nanogel was then dialysed against distilled water for 3 days to remove the unreacted reactents. The solution was then lyophilized; a brownish colored semisolid was isolated as the product and stored at 4<sup>0</sup>C. The nanogel was coded as C-SPION-NG.

#### **3.5.4. Synthesis of octreotide conjugated nanogel (PMB-OctN) from photoluminescent PMB comacromer and octreotide**

Octreotide conjugated nanogel was prepared as follows; briefly, 30 mg of PMB-N nanogel was dissolved in 10 ml distilled water inside a round bottom flask and stirred for 20 min under nitrogen atmosphere. Further, octreotide (50  $\mu$ l) was added to the reaction mixture with stirring at 1000 rpm followed by the addition of 40  $\mu$ l of EDC (4  $\mu$ M) and 40  $\mu$ l of NHS (10  $\mu$ M) and stirred for 24 h. The octreotide conjugated nanogel was then dialysed against distilled water for 3 days to remove the unreacted reactants. The solution was then lyophilized and stored at 4<sup>0</sup> C. The octreotide conjugated nanogel was coded as PMB-OctN.

A nanogel without octreotide conjugation was also prepared using comacromer, PMB, as follows; briefly, 45 mg of comacromer was dissolved in 40 ml distilled water inside a round bottom flask and stirred for 15 min under nitrogen atmosphere. Further, 30  $\mu$ l of diethyleneglycoldimethacrylate was added followed by ammonium per sulfate and TEMED (30  $\mu$ l,  $1 \times 10^{-3}$  M). The solution was then sonicated for 30 min to disperse the newly formed nanogel. The nanogel was then dialysed against distilled water for 3 days to remove the unreacted reactants. The solution was then lyophilized; a brownish colored semisolid was isolated as the product and stored at 4<sup>0</sup> C. The synthesized nanogel was coded as PMB-N.

#### ***3.6 Analyses of morphology, size and surface charge of nanogels***

The size, surface charge and morphology of the nanogels (PLM-NG, C-PLM-NG, C-SPION-NG and PMB-OctN) was investigated by using dynamic light

scattering, zeta potential and transmission electron microscopy. Nanogels were dispersed in distilled water (1mg/ml) and measured the hydrodynamic size and surface charge using Malvern Zeta sizer equipment. For TEM analysis (TEM, Philips CM12 STEM, Netherlands), the nanogels were deposited on the carbon-coated copper grid, the grid was dried for 2 days at room temperature and then examined.

### ***3.7. In vitro drug loading and release profiles of nanogels***

The drug loading and release profiles of the C-PLM-NG were studied using anticancer drug doxorubicin (DOX) as a model drug. For drug loading, DOX (1 mg) was dissolved in the aqueous phase and added to the reaction mixture containing C-PLM (40 mg) and DMEMA (10  $\mu$ l). The nanogel loaded with DOX was prepared by adding DOX along with C-PLM and DMEMA during the preparation of PLM-NG. The DOX-loaded nanogel dispersion (pH 7.4) was then subjected to dialysis through a 500D MW cut-off dialysis bag for 72 h to completely remove the unloaded DOX from the nanogel. A small portion of DOX-loaded nanogel was taken and measured the fluorescent emission using a fluorescent microplate reader (Tecan) with ex: 460 nm and em: 595 nm. The drug loading level was determined using a concentration versus fluorescence emission calibration curve of DOX.

$$\text{Drug loading efficiency (\%)} = \frac{\text{Weight of loaded DOX}}{\text{Weight of DOX in the nanogel suspension}} \times 100$$

Drug release profile was evaluated at different pH through dialysis method. DOX-loaded nanogel suspension (5 ml) was placed within a dialysis bag (MW cut-off 1000 D), followed by dialysis against phosphate buffer saline (PBS) solution (50 ml) having different pH values. At prescribed time intervals, 1 ml of

external buffer solution was withdrawn and replaced with fresh equivalent volume of medium. Concentration of DOX was determined using a calibration curve concentration versus fluorescence emission of DOX.

The drug release study of PMB-OctN was also carried out with doxorubicin as model drug. Initially, PMB-OctN (3 mg/ml) was dispersed in 10 ml distilled water and stirred at 1000 rpm for 10 min. Subsequently, DOX (1000 µg/ml) dissolved in the aqueous phase was added to the reaction mixture and stirring was continued for 24 h. Dialysis technique was employed to evaluate the drug release profile of PMB-OctN loaded with DOX. 5 ml of DOX-loaded PMB-OctN solution was added to a dialysis membrane and dialyzed against 50 ml of phosphate buffer saline solution (pH 7.4). 1 ml of external PBS solution was taken out at different time and replaced with fresh volume of PBS solution. Concentration of DOX released was calculated from the calibration curve of concentration versus fluorescence emission of DOX.

### ***3.8. Magnetic Hyperthermia Experiments of C-SPION-NG***

The therapeutic capability of the C-SPION-NG was evaluated by conducting the magnetic hyperthermia studies. Hyperthermia studies were done in accordance with the protocol of (Beeran *et al.*, 2015). Briefly, C-SPION-NG was subjected to alternating magnetic field and temperature was measured as function of time. The Ambell Easy Heat laboratory induction system was used for the studies. A solenoid coil with a 4 cm diameter , 2.6 cm length and total turns of 6 was set at a magnetic frequency of 275KHz. The induction coil was thermalized to room temperature with a closed circuit water chiller. The temperature change in the sample was monitored with a non-contact mode IR thermometer (Fluke 572,

Germany). The C-SPION-NG (2mg & 4mg) was dispersed in 1ml distilled water in a 1.5 ml centrifuge tube insulated with ceramic wool. The entire assembly was placed in the centre of a water- cooled copper coil and the temperature change was monitored for 15 min. The heat generation of C-SPION-NG was studied using different alternating magnetic field strengths and concentrations. Distilled water was used as control for hyperthermia measurements.

### ***3.9. Evaluation of cytocompatibility and therapeutic capability of the nanogels***

#### **3.9.1. Evaluation of cytocompatibility and therapeutic capability of the C-PLM-NG**

The cytocompatibility and therapeutic capability of C-PLM-NG were evaluated using MTT assay.

##### ***3.9.1.1. MTT assay***

Cells were seeded at a density of  $1 \times 10^5$  cells/well (200  $\mu$ l, 96-well tissue culture plate) and cultured in complete DMEM medium at 37 °C in 5% CO<sub>2</sub> for 24 h. The cultured cells were treated with different concentrations of PLM-NG (1000-4000  $\mu$ g/ml) and PLM-NG loaded with doxorubicin. After 24 h incubation, 20 $\mu$ l MTT solution was added to each well and incubated for further 4 h. To dissolve the formazan crystals formed, 200  $\mu$ l of DMSO was added to each well and placed in an orbital shaker for 15 min at 200 rpm. UV/Vis microplate reader (Tecan) was used to measure the absorbance at 570 nm. The percentage of viable cells was calculated using the equation given below

$$\text{Cell Viability} = \frac{[\text{Abs}]_{\text{sample}}}{[\text{Abs}]_{\text{Control}}} \times 100$$

### **3.9.2. Evaluation of cytocompatibility and therapeutic capability of the C-SPION-NG**

The cytocompatibility and therapeutic capability of C-SPION-NG were evaluated using MTT assay, flow cytometry analysis and live dead assay.

#### **3.9.2.1. MTT assay**

The cytocompatibility of C-SPION and C-SPION-NG was measured after incubating the HeLa cells with different concentrations of C-SPION and C-SPION-NG (250-4000  $\mu\text{g/ml}$ ) and the cell viability was measured. The details of MTT assay are given above in section 3.9.1.1.

#### **3.9.2.2. Cell cycle analysis**

The cytocompatibility of C-SPION-NG on HeLa cells were demonstrated using cell cycle analysis. Briefly, cells were seeded at a density of  $1 \times 10^5$  cells/well (50  $\mu\text{l}$ , 12-well tissue culture plate) and cultured in complete DMEM medium at 37 °C in 5% CO<sub>2</sub> for 24 h. The nanogel dissolved in media was added to HeLa cells and incubated for 24 h at 37 °C. The cells were then trypsinised and suspended in 1 ml PBS and transferred to a tube. The cell suspension was then centrifuged at 6000rpm for 10 min. The supernatant solution was removed and the resuspended cell pellet were added into the tube containing 1ml of ice cold 70% ethanol while vortexing at medium speed. The tube was then capped and frozen the cells at -20°C. After the overnight incubation, the supernatant ethanol was removed and washed the cells with 250 $\mu\text{l}$  PBS. The cells were again centrifuged and the pellet was taken after discarding the supernatant; 250 $\mu\text{l}$  of propidium iodide was added. This was incubated at dark for 30 minutes (which is light

sensitive). After this it was analyzed using a Flow Cytometer. Gating was performed with reference to untreated control cells and samples were analyzed. C-SPION-NG dissolved in media with 500 and 1000  $\mu\text{g}/\text{ml}$  was used.

### ***3.9.2.3. Live dead cell assay***

The cytocompatibility of C-SPION-NG on HeLa cells were demonstrated using lived dead cell assay. Briefly, cells were seeded at a density of  $1 \times 10^5$  cells/well (50  $\mu\text{l}$ , 12-well tissue culture plate) and cultured in complete DMEM medium at 37 °C in 5%  $\text{CO}_2$  for 24 h. After 24 h. C-SPION-NG dissolved in media (500 and 1000  $\mu\text{g}$ ) was added and incubated for another 24 h at 37 °C. The media was then carefully removed and washed the cells with sterile PBS with 3 times and incubated the cells with equal volumes of ethidium bromide and acridine orange (100  $\mu\text{M}$ , 500  $\mu\text{l}$ ) for 5 minutes. The cells were washed with sterile PBS 3 times and then observed the cells under a fluorescent microscope (optica, ITALY).

The therapeutic capability of C-SPION-NG on HeLa cells using the magnetic hyperthermia capability were carried out as follows. Briefly, cells were seeded at a density of  $1 \times 10^5$  cells/well (Polystyrene petri dish (100mm $\times$ 15 mm) mounted with a coverslip ) and cultured in complete DMEM medium at 37 °C in 5%  $\text{CO}_2$  for 24 h. C-SPION-NG suspended in media (1 mg) was added and placed the cells in the centre of a water- cooled copper coil and alternating magnetic field of 33.8 MT and 275 KHz was applied to the cells and the temperature change was monitored for 30 min. After 1 hr incubation of the cells, media was then carefully removed and washed the cells with sterile PBS with 3 times and incubated the cells were co-stained with equal volumes of ethidium bromide and

acridine orange (100  $\mu$ M, 500  $\mu$ l) for 5 minutes. The cells were washed with sterile PBS 3 times and then observed the cells under a fluorescent microscope (optica, ITALY).

### **3.9.3. Evaluation of cytocompatibility and therapeutic capability of the PMB-OctN**

The cytocompatibility and therapeutic capability of PMB-OctN were evaluated using MTT assay, flow cytometry analysis and live dead assay. The therapeutic capability of PMB-OctN was evaluated by incubating the Hela cells with bare PMB-OctN and PMB-OctN loaded with doxorubicin.

#### **3.9.3.1. MTT assay**

The cytocompatibility of PMB-OctN was evaluated by incubating the Hela cells with different concentrations of PMB-OctN (1000-4000  $\mu$ g/ml) and the cell viability was measured. The details of MTT assay are given above in section 3.9.1.1.

#### **3.9.3.2. Live dead cell assay**

Lived dead cell assay was carried out as described above in section 3.9.2.3. PMB-OctN loaded with doxorubicin and without doxorubicin with the concentration, 4000  $\mu$ g/ml was used. The therapeutic capability of bare PMB-OctN and PMB-OctN loaded with doxorubicin was evaluated with cell apoptotic activity and compared.

### **3.9.3.3. Cell cycle analysis**

The therapeutic capability of bare PMB-OctN and PMB-OctN loaded with doxorubicin was evaluated by cell cycle analysis. The details of cell cycle analysis are given above in section 3.9.2.2. The therapeutic capability was evaluated by the cell population in the G2/M phase and compared.

### **3.10. Evaluation of haemolytic potential of the nanogels**

The hemocompatibility of the synthesized nanogel was evaluated by measuring the hemolytic potential of the nanogels. *In vitro* hemolytic potential of the nanogels (PLM-NG, C-PLM-NG, C-SPION-NG and PMB-OctN) was investigated according to ISO 10993-4:2002 standards. Blood from the human volunteer was collected into the anticoagulant, CPD-A. The test sample (1 ml) was taken into the three wells of six well polystyrene dish in triplicates and 2 ml blood was added. One ml solution was aspirated immediately for initial analysis and the remaining solution was agitated using an Environ shaker thermo stated at  $35 \pm 2$  °C for 30 min at  $75 \pm 5$  rpm. Four wells of empty polystyrene culture dishes were exposed with blood as reference. The blood samples were centrifuged at 4000 rpm for 15 min and platelet poor plasma was aspirated. Percentage of hemolysis was calculated by measuring the total hemoglobin using automatic haematology analyser (Sysmex-K 4500). The free hemoglobin liberated in to the plasma before and after exposure to blood was measured in each sample using diode array spectrophotometer. Hemolysis (%) was calculated using the formula.

$$\text{Hemolysis (\%)} = \frac{\text{Free Hb}}{\text{Total Hb}/1000} \times 100$$

### ***3.11. Evaluation of cellular uptake and imaging capability of the nanogels***

The cellular internalization and imaging capability of the prepared nanogels were evaluated by evaluating the cellular uptake using fluorescence microscopy. Cellular uptake of the nanogels (PLM-NG, C-PLM-NG, C-SPION-NG and PMB-OctN) was evaluated by using L929 fibroblast and HeLa cell line. Briefly, the cells were seeded at a density of  $1 \times 10^5$  cells/well (200  $\mu$ l, 96-well tissue culture plate) and cultured in complete DMEM medium at 37 °C in 5% CO<sub>2</sub> for 24 h. The medium was removed and the cells were incubated with nanogels (2mg/ml) in PBS for 4 h at 37 °C. The cells were then washed with PBS twice and observed under a fluorescent microscope (optica, ITALY) at a magnification of 20X and 40X.

#### ***3.11.1. Evaluation of cellular uptake and imaging capability of the C-SPION-NG using Prussian blue staining***

The iron oxide nanoparticles present in the C-SPION-NG was detected inside the cells using Prussian blue staining. Cellular uptake of C-SPION-NG was evaluated by using HeLa cell line through Prussian blue staining. Briefly, the cells were seeded at a density of  $1 \times 10^5$  cells/well (50  $\mu$ l, 12-well tissue culture plate) and cultured in complete DMEM medium at 37 °C in 5% CO<sub>2</sub> for 24 h. The medium was then removed and added with 2 different concentrations of C-

SPION-NG (500 and 1000  $\mu\text{g}$ ) in media and incubated for 24 h at 37 °C. Cells were then washed with 500  $\mu\text{l}$  ice cold methanol for fixing and incubated for 5 min. Methanol was then removed and washed the cells with sterile PBS and added with Prussian blue reagent (1ml) and incubated for another 20 min. The cells were washed with sterile PBS to remove the Prussian blue reagent and then added with 1 ml of nuclear red solution to counter stain the nucleus and incubated for another 20 min. Further, the cells were washed to remove the nuclear red dye solution and observed the cells with a light microscope.

### ***3.12. Studies on in vivo bioimaging and biodistribution of nanogels in mice***

The efficacy of the prepared nanogels for bioimaging was evaluated using fluorescence bioimaging studies on mice model. For studies on bioimaging and biodistribution, Swiss albino mice with body weight range of 35-40 g were anesthetized with xylazine and ketamine. The back of the mice was clipped and epilated for subcutaneous injection. 0.25 ml of nanogel prepared in PBS solution with concentration 2 mg/ml was injected subcutaneously in the back of mice and then imaged with Xenogen IVIS spectrum optical imaging system.

#### **3.12.1. Studies on in vivo bioimaging and biodistribution of C-PLM-NG**

0.25 ml of C-PLM-NG prepared in PBS solution was injected subcutaneously in the back of mice and then imaged. Initially to choose the excitation wavelength which offers the emission at near IR region with relatively higher intensity, different excitations (430, 465, 505 and 535 nm) were used and emission wavelengths ranging from visible to near IR (540, 580, 610, 660, 680

and 700 nm) were collected using filters. As the emission at near IR region has relatively higher intensity for the excitation wavelength of 535 nm, capturing of broad Near IR emission was carried out with the excitation wavelength, 535 nm using different emission filters.

For biodistribution studies, 0.25 ml of C-PLM-NG in PBS solution (2 mg/ml) was injected through the lateral tail vein of the mice and then imaged at 3 h and 6 h with Xenogen IVIS spectrum optical imaging system with the excitation wavelength, 535 nm. Also *ex vivo* imaging of organs, urinary bladder, liver, kidney and heart etc from the carcass of the mice was carried out at 3 h and 24 h post injection after opening the abdomen and thorax. The application of the PLM-NG for lymph node imaging was also studied. For this studies, the back of the mice was clipped and epilated before imaging. Then, 0.1 ml of C-PLM-NG was injected into the ipsilateral foot pad of the mice. After 3 h, the animal was imaged.

### **3.12.2. Studies on in vivo bioimaging and biodistribution of C-SPION-NG**

0.25 ml of C-SPION-NG prepared in PBS solution was injected subcutaneously in the back of mice and then imaged. Different excitations (640,675 and 710 nm) were used and emission wavelengths ranging from visible to near IR (780,800,820 and 840nm) were collected using different filters. For biodistribution studies, 0.25 ml of C-SPION-NG prepared in PBS solution (2 mg/ml) was injected through the lateral tail vein of the mice and then imaged at different time points with Xenogen IVIS spectrum optical imaging system using excitation/emission wavelength of 675/800 nm respectively.

### **3.12.3. Studies on in vivo bioimaging and biodistribution of PMB-OctN**

PMB-OctN (0.25 ml) dispersed in PBS solution was injected subcutaneously in the back of mice and then imaged. Imaging was accomplished using excitations, 640 and 675 nm and emission wavelengths, 700 and 720 nm. The biodistribution in mice were assessed by injecting the PMB-OctN (0.25 ml) through the lateral tail vein of the mice and imaged at different time from 1 h to 96 h. All the animal experiments were conducted after getting permission from Institutional Animal Ethics Committee (IAEC).

### **3.13. *Histopathological evaluation of nanogels on different organs***

The histopathological evaluations were done to assess the toxicity profile of the synthesized nanogel. Histopathological evaluation of the nanogels (C-PLM-NG, C-SPION-NG and PMB-OctN) loaded organs such as heart, liver and kidney was carried out. For histopathology studies, formalin-fixed tissue samples were dehydrated through ascending grades of alcohol, cleared in xylene and impregnated with paraffin wax. Leica RM2255<sup>TM</sup> microtome was used for making tissue sections of 4  $\mu$ m thickness from paraffin tissue blocks. The sections were then stained with haematoxylin and eosin dyes (H&E) for microscopic observation.

### **3.14. *Statistical analysis***

All experimental data were analyzed by Student's *t* tests to evaluate the significance of differences between the sub groups considered. *P* values <0.05 were statistically significant.

## **Chapter 4**

### **Results**

*This chapter presents the results dealing with the synthesis and characterisation of three different photoluminescent comonomers and nanogels, and studies on near IR emission characteristics, cytocompatibility, therapeutic capability and cellular imaging capability of the nanogels. The first section deals with the results generated with the studies on passively targeted nanogel. The second section deals with the results generated with the studies on magneto-fluorescent hybrid nanogel endowed with innate near IR emissions and magnetic properties. The third section deals with the results generated with the studies on actively targeted octreotide conjugated nanogel endowed with innate near IR emissions. The results of the studies on fluorescent properties of the comonomers and physico-chemical properties of the nanogels are presented in this chapter. The results of the studies on cytocompatibility, therapeutic capability and cellular imaging capability of the nanogels are also presented in this chapter. The results on the studies on in vivo bioimaging, biodistribution and histopathology analysis of the nanogels are also presented in this chapter.*

#### 4.1. Studies on passively targeted nanogels for theranostic applications

##### 4.1.1. Synthesis of photoluminescent PPF-PEG-glycine (PLM) and PPF-PEG-citric acid-glycine (C-PLM) comacromers

Photoluminescent comacromer, PLM was synthesized by condensation polymerization of carboxyl terminated polypropylene fumarate (CT-PPF) with PEG and glycine. The reaction scheme is shown in given in Figure-6.

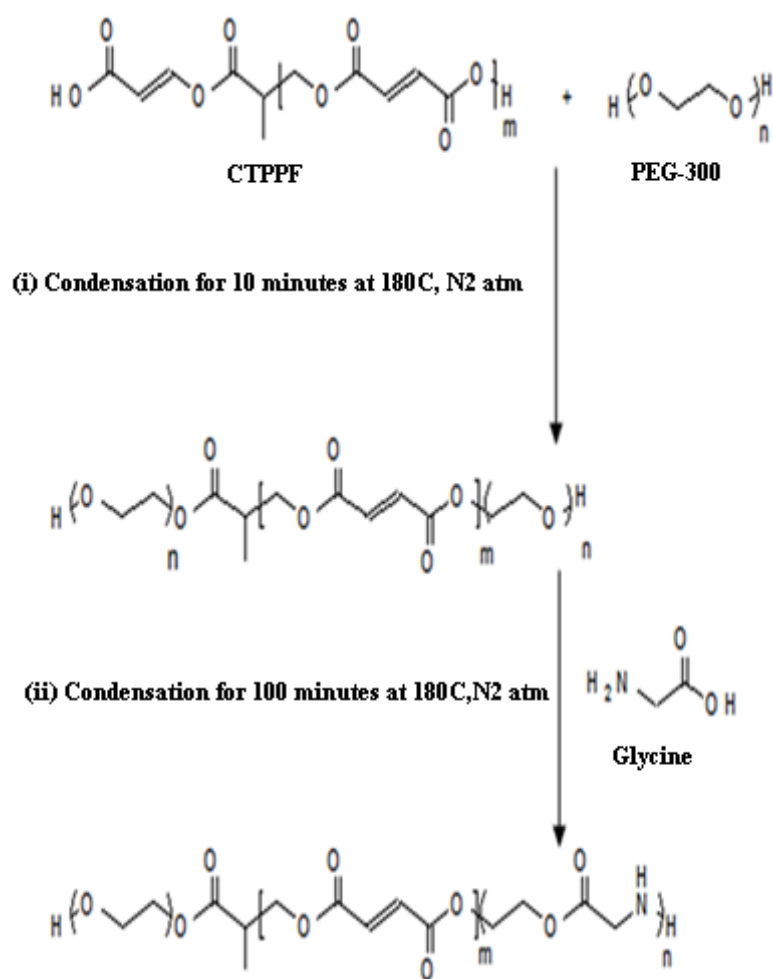
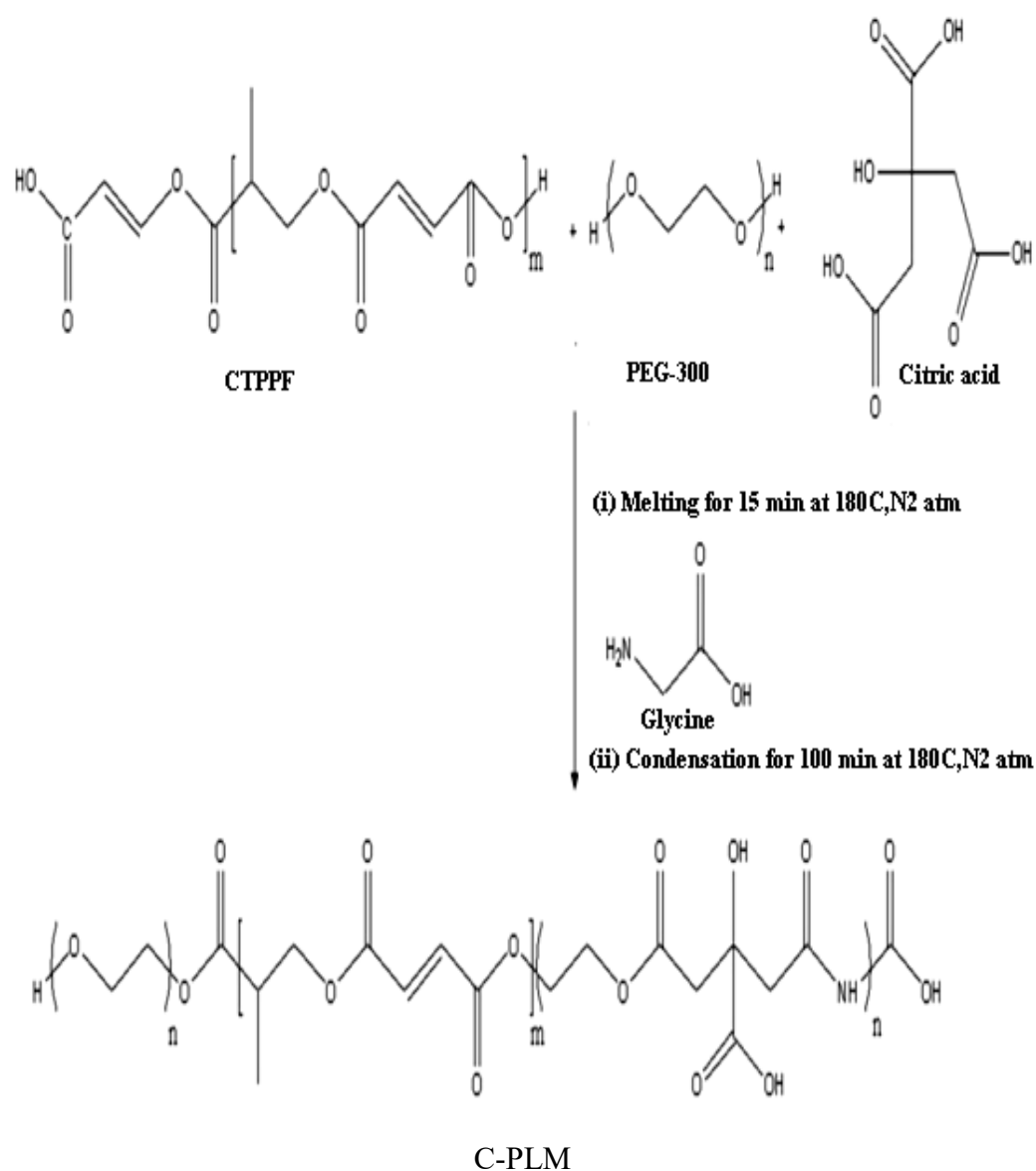


Figure-6. Synthesis of photoluminescent PLM comacromer

PLM

Photoluminescent comacromer, C-PLM was synthesized by condensation polymerization of carboxyl terminated polypropylene fumarate (CT-PPF) with PEG, citric acid and glycine. The reaction scheme is shown in given in Figure- 7

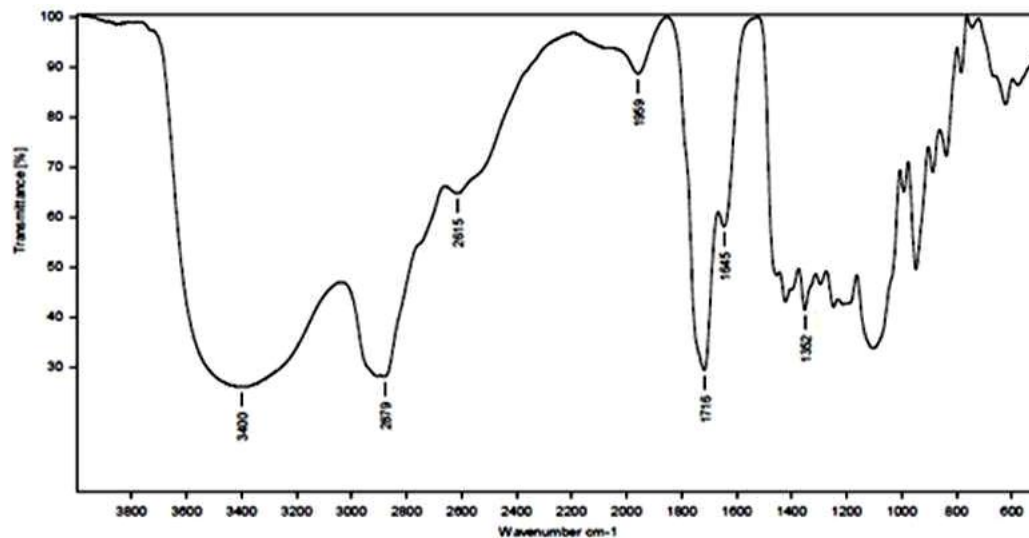


**Figure-7. Synthesis of photoluminescent C-PLM comacromer**

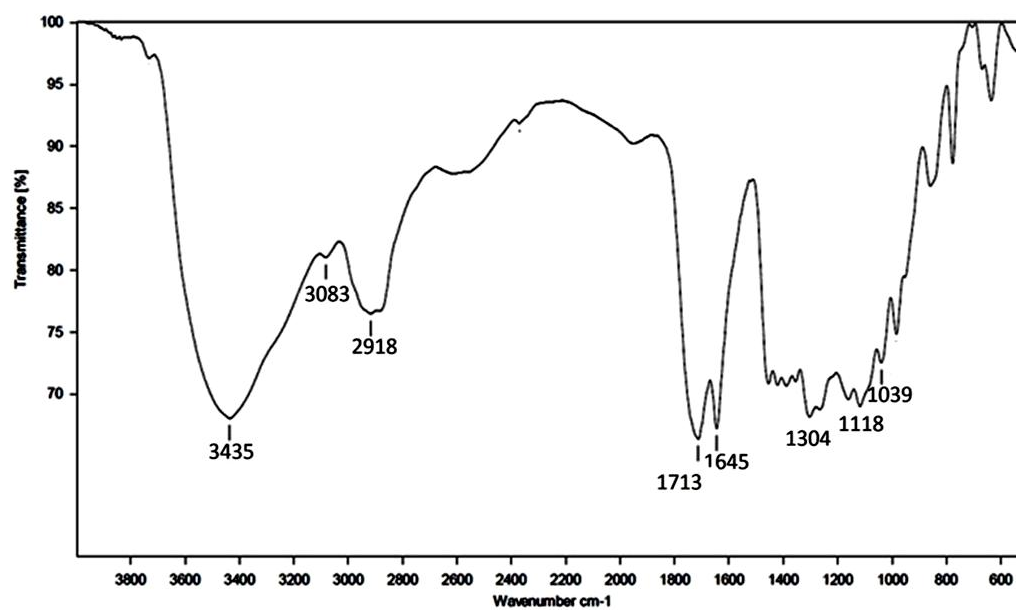
#### 4.1.2. Structural evaluation of PLM and C-PLM comacromers

The structures of the synthesized comacromers were evaluated using FTIR and proton NMR spectroscopy.

FT-IR spectrum of PLM (Figure-8a) exhibited peaks at  $3400\text{ cm}^{-1}$  (-OH stretching vibrations of PEG),  $2879\text{ cm}^{-1}$  (C-H stretching vibrations of  $\text{CH}_2$  groups PEG),  $1036\text{ cm}^{-1}$  (C-N stretching vibrations of glycine)  $1716\text{ cm}^{-1}$  (ester bonds of CT-PPF),  $1645\text{ cm}^{-1}$  (C=C stretching of CH=CH- bond of CT-PPF),  $1352\text{ cm}^{-1}$  (C-H bending vibrations of CT-PPF),  $1256\text{ cm}^{-1}$ , (C-O stretching of OH and ester linkages of CT-PPF), and  $976\text{ cm}^{-1}$  (C-H bending of trans CH=CH bond of CT-PPF). Thus IR spectral analysis clearly suggests the successful completion of the condensation of CTPPF, PEG and glycine to form the photoluminescent comacromer. FTIR spectrum of C-PLM (Figure- 8b) reveals peaks at  $3435\text{ cm}^{-1}$  (-OH stretching vibrations of PEG),  $3083\text{ cm}^{-1}$  (C-H stretching vibrations of -CH=CH bonds of CT-PPF),  $2918\text{ cm}^{-1}$  (C-H stretching vibrations of  $\text{CH}_2$  groups PEG and citric acid),  $1713\text{ cm}^{-1}$  (ester bonds of CT-PPF),  $1645\text{ cm}^{-1}$  (C=C stretching of CH=CH- bond of CT-PPF),  $1304\text{ cm}^{-1}$  (C-C and C-O stretching of ester linkages of CT-PPF),  $1118\text{ cm}^{-1}$  (ether C-O group stretching for PEG) and  $1039\text{ cm}^{-1}$  (C-N stretching vibrations of glycine). The FTIR analysis confirmed the formation of C-PLM.



(a)



(b)

**Figure-8. Spectral analyses of comacromers. PLM comacromer (a), C-PLM comacromer (b)**

The structure of the synthesized PLM was further evaluated using NMR analysis. Proton NMR spectrum of the PLM (Figure-9a) shows peaks at 6.8 ppm (fumarate double bonds CH=CH of polypropylene fumarate), 4.3 ppm (-CH<sub>2</sub> groups of PEG), 3.4 ppm (-CH<sub>2</sub>NH from glycine) which proves the formation of PLM.

$^1\text{H}$  NMR spectrum of C-PLM (Figure- 9b) shows peaks at 6.8 ppm (from the fumarate double bonds  $\text{CH}=\text{CH}$  of polypropylene fumarate), 4.7 ppm ( $-\text{NH}$  groups of glycine), 3.4 ppm ( $-\text{CH}_2$  groups from PEG) and peaks at 2.75 ppm ( $-\text{CH}_2$  from citric acid). The FT-IR and NMR analyses substantiate the structure of the C-PLM as given in figure 7.

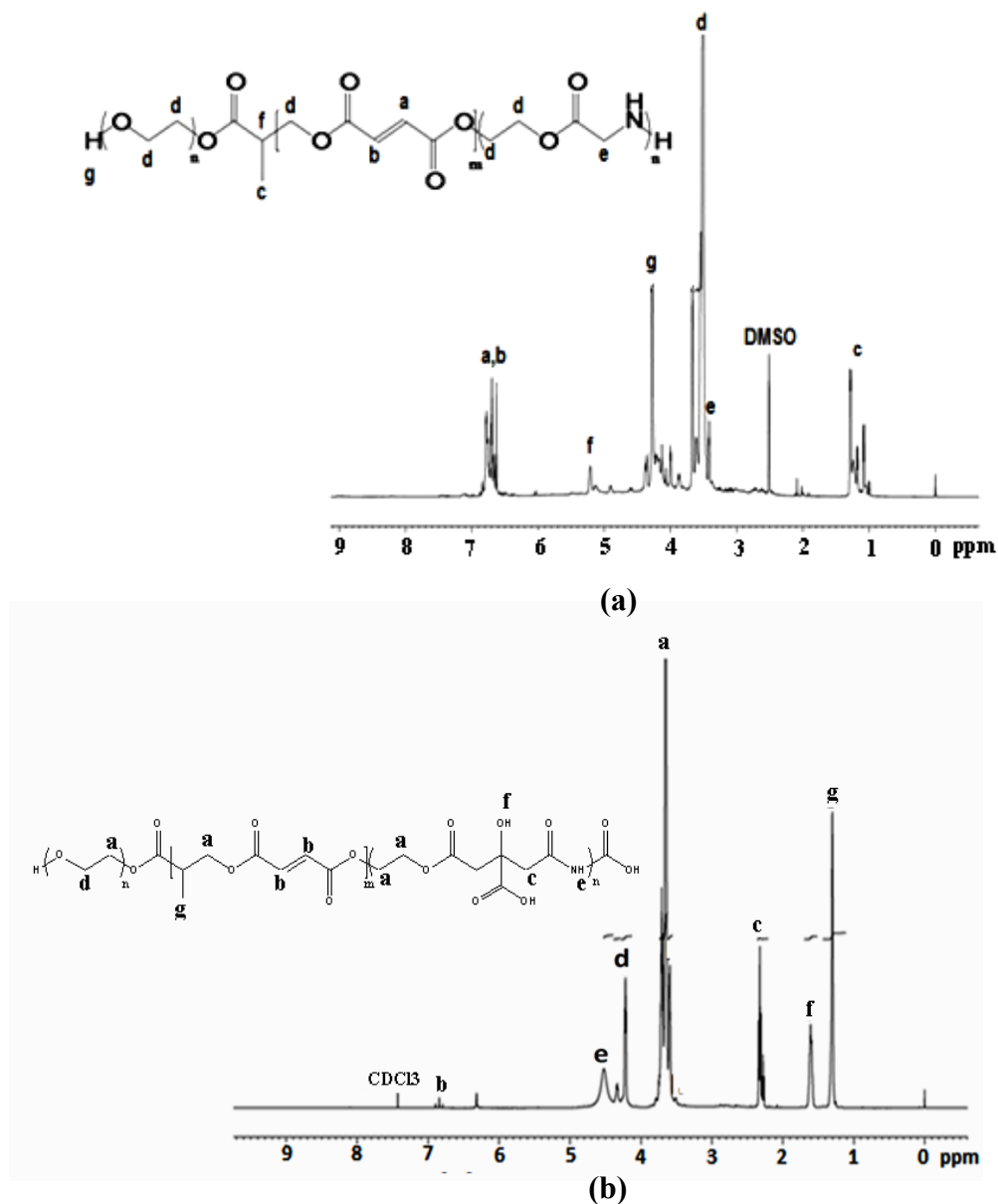


Figure-9.  $^1\text{H}$  NMR Spectral analyses of PLM comacromer (a), C-PLM comacromer (b)

The analysis of molecular weight of PLM using gel permeation chromatography revealed Mn 1225, Mw 3071 and polydispersity index 2.60. The molecular weight data of C-PLM are Mn 1335, Mw 3171 and polydispersity index 2.38.

#### **4.1.3. Evaluation of the photoluminescence properties of the PLM and C-PLM comacromers**

The photoluminescent behavior of PLM was investigated under aqueous condition. PLM exhibited photoluminescent properties with different range of excitations and emissions (Figure-10). When PLM was excited in the visible range from 400-540 nm, multiple emission peaks were appeared in the spectrum ranging from 480-590 nm, which demonstrated the excitation wavelength dependent fluorescence (EDF) phenomena. The photoluminescence spectra of the C-PLM comacromer in aqueous condition reveals emissions ranging from visible to near IR range, 510-718 nm for excitations in the range of 400-640 nm in aqueous condition (Figure-11).

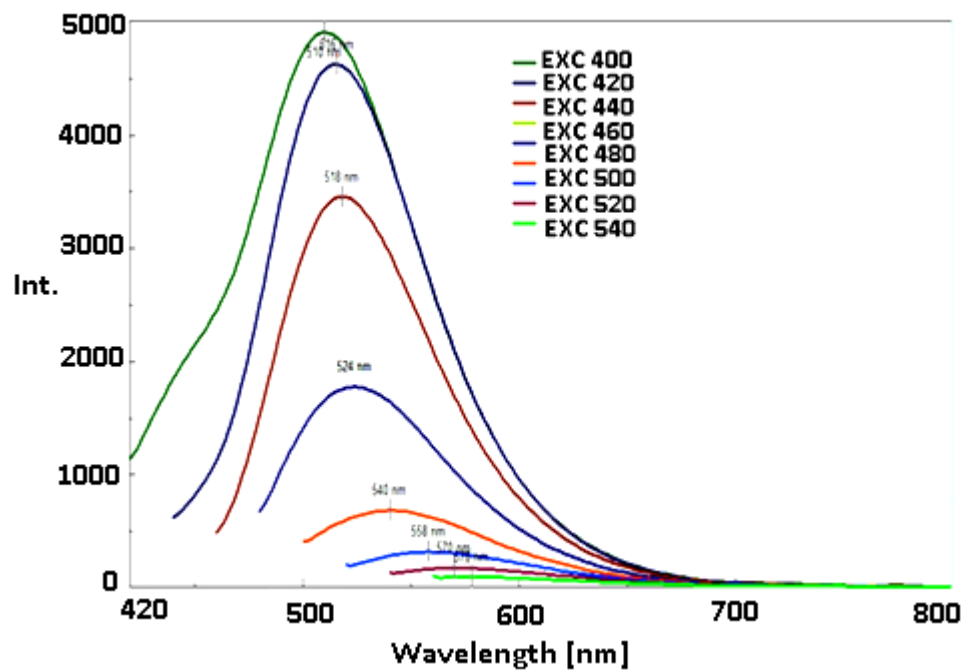


Figure-10. Photoluminescence spectra of PLM comacromer under aqueous conditions at different excitations on visible region (400nm-540nm)

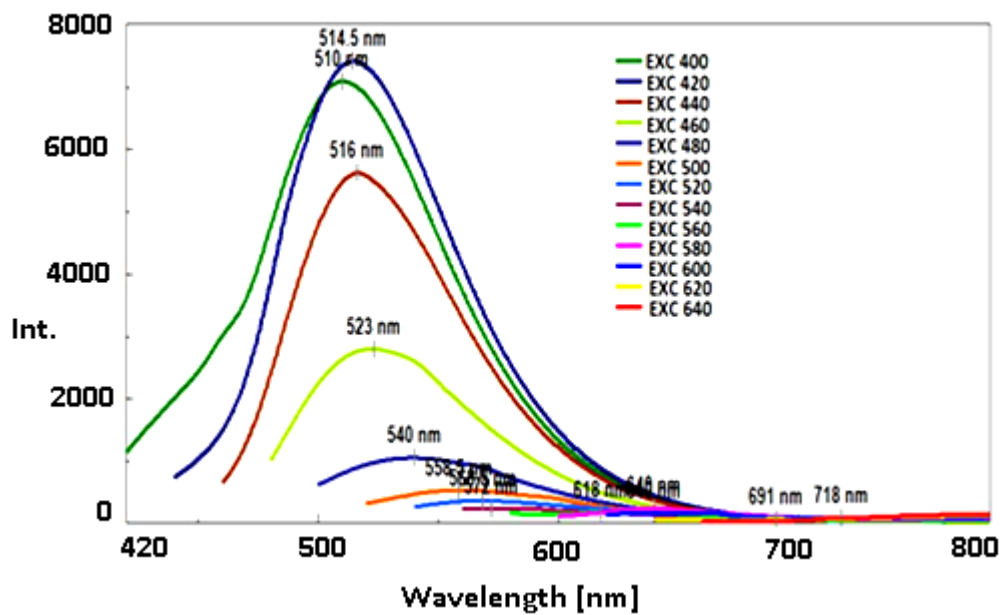


Figure-11. Photoluminescence spectra of C-PLM comacromer under aqueous conditions at different excitations on visible region (400nm-640nm)

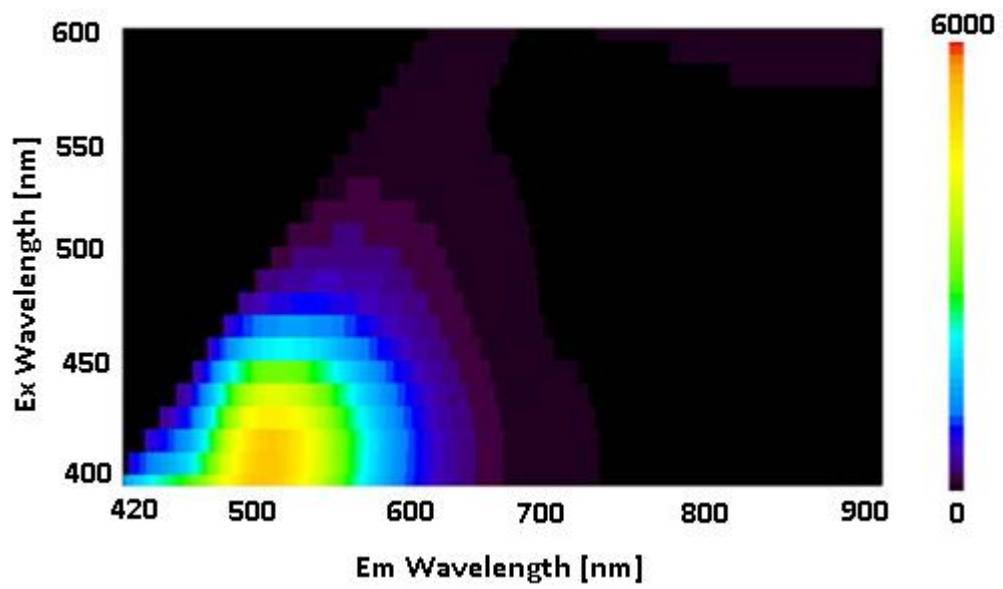


Figure-12. The three dimensional photoluminescent contour plots of PLM

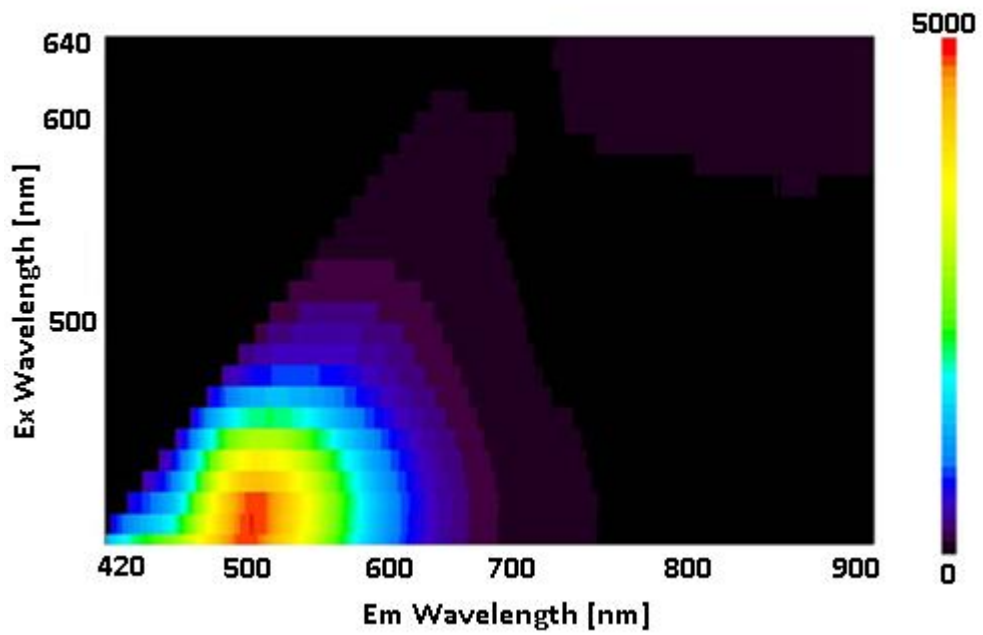


Figure-13. The three dimensional photoluminescent contour plots of C-PLM

The three dimensional photoluminescent contour plots of PLM and C-PLM comacromers substantiated the EDF characteristics exhibited by both the comacromers (Figure- 12 and 13). The PLM and C-PLM comacromers exhibited

visible to near IR fluorescence characteristics. Photostability and photoluminescence lifetime are two critical parameters, which determines the efficiency of any fluorophores for imaging applications. PLM exhibited photostability without quenching even under continuous irradiation for a period of 30 min without photo bleaching (Figure-14). C-PLM also exhibited photostability without quenching for a period of 30 min (Figure-15). PLM and C-PLM exhibited fluorescent lifetime of 7 nanoseconds (Figure-16 and 17).

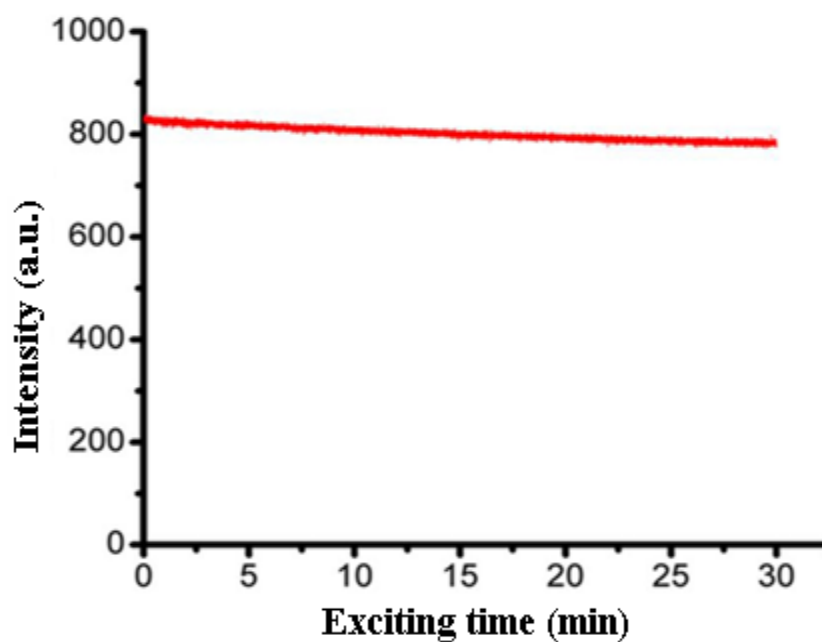


Figure-14. Photo stability graph of PLM ( $\lambda_{\text{ext}}$  : 420 nm &  $\lambda_{\text{emiss}}$  : 525 nm)

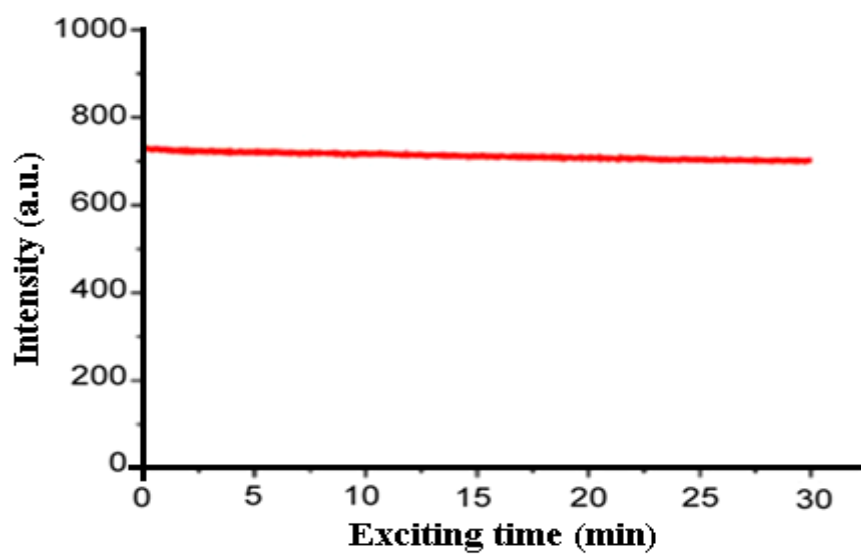


Figure-15. Photo stability graph of C-PLM ( $\lambda_{\text{ext}}$  : 420 nm &  $\lambda_{\text{emiss}}$  : 525 nm)

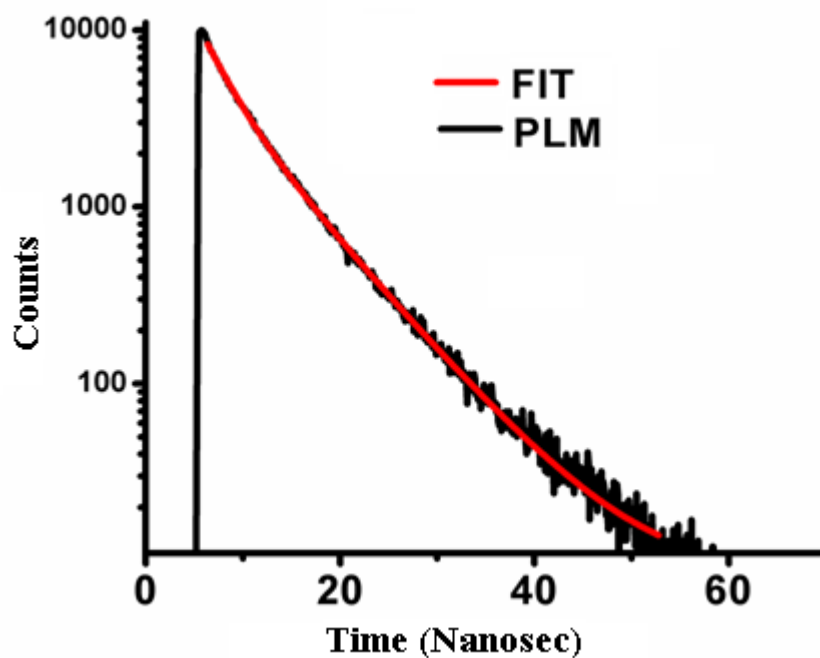


Figure-16. Photoluminescence lifetime of PLM comacromer

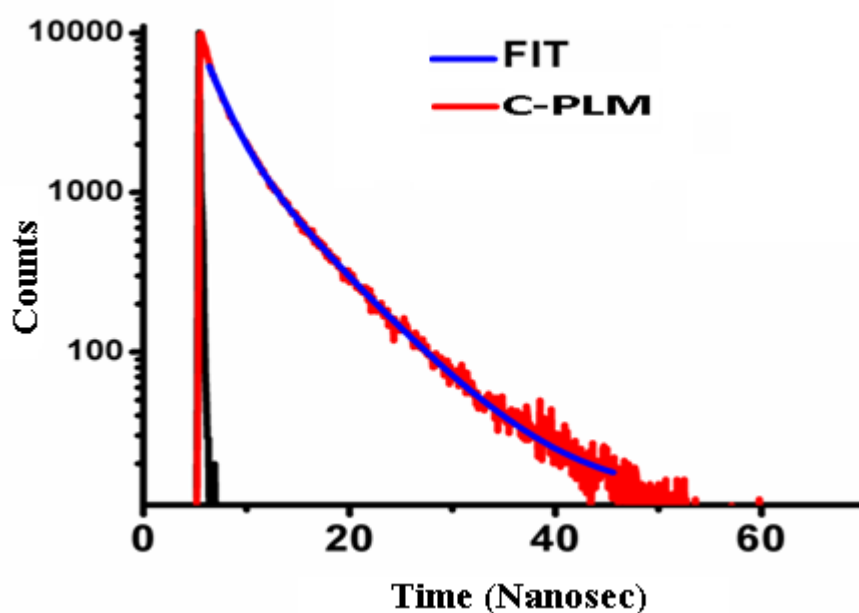


Figure-17. Photoluminescence life time of C-PLM comacromer

The excitation-emission spectra of PLM and C-PLM comacromers reveal stokes shift of around 120 nm (Figure-18 and 19). The photoluminescent characteristics of the comacromers are summarized in table-1

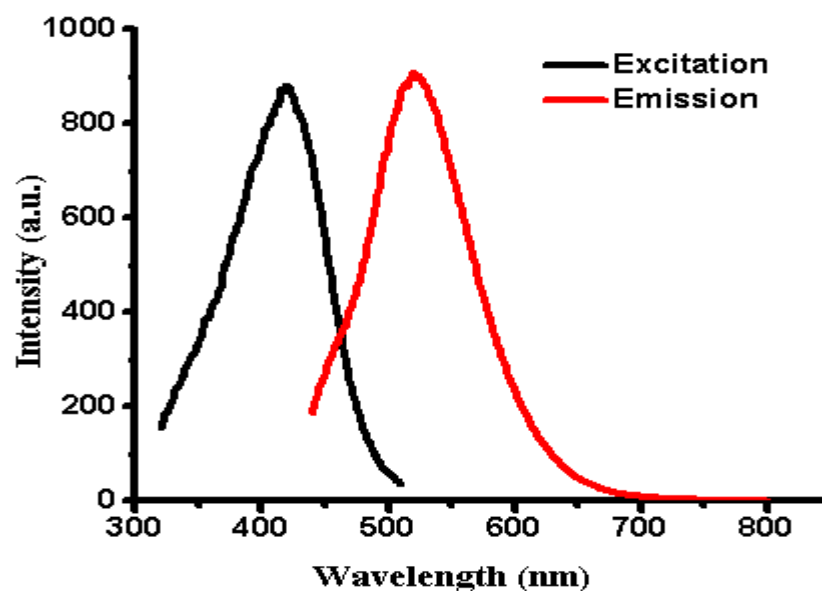


Figure-18. Excitation & emission spectra of PLM comacromer

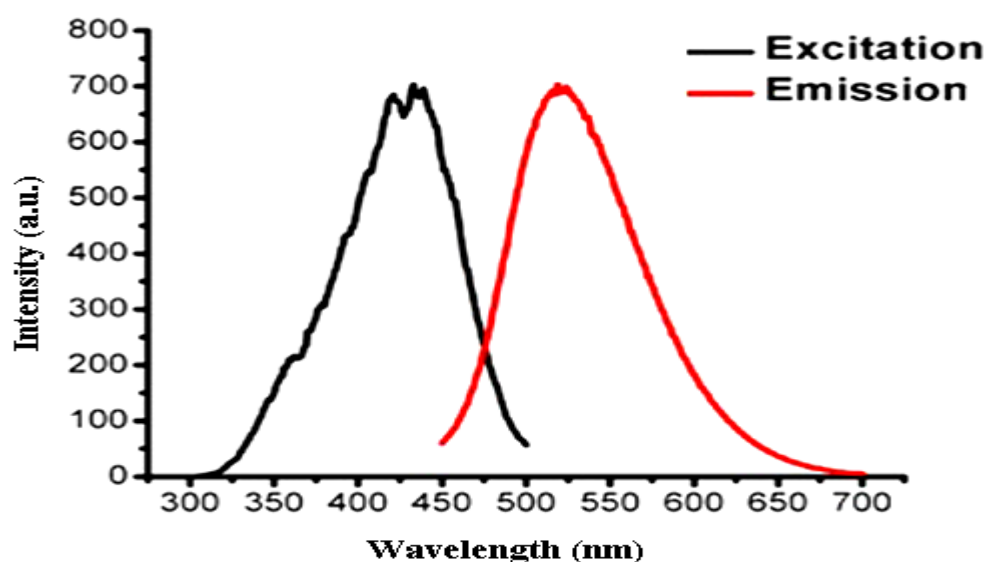


Figure-19. Excitation & emission spectra of C-PLM comacromer

Table- 1: Photoluminescence properties of PLM and C-PLM comacromers

Comacromer	Fluorescence Emission (nm)	Fluorescence Lifetime (nm)	Photo stability (min)	Stokes shift (nm)
PLM	480-590	7	30	120
C-PLM	510-718	7	30	120

#### 4.1.4. Investigation on the photoluminescence properties of analogues of PLM and C-PLM comacromers

To unravel the photoluminescence behavior of the PLM, the photoluminescent property of the analogues of PLM viz PEG-PPF and PEG-Glycine was investigated. Interestingly, both the PEG-PPF and PEG-Glycine exhibited photoluminescent characteristics. PEG-G excited from 380-500 nm had corresponding emissions between 470-560 nm (Figure 20a). Similarly, PEG-PPF also exhibited photoluminescent activity (Figure-20 b). The UV absorption spectra of the comacromer and its analogues revealed a sharp peak at 300 nm and a shoulder peak originating from 350 nm and it extended till 700 nm (Figure 21a).

As fluorescence activity was observed with the condensation product of PEG and CTPPF (PEG-P) the fluorescence activity for the condensation product between PEG and maleic acid (PEG-M) was investigated. PEG-M also exhibited fluorescent characteristics (Figure 21b). PEG-M, excited in the range of 380-500 nm, generated corresponding emissions between 470-560 nm.

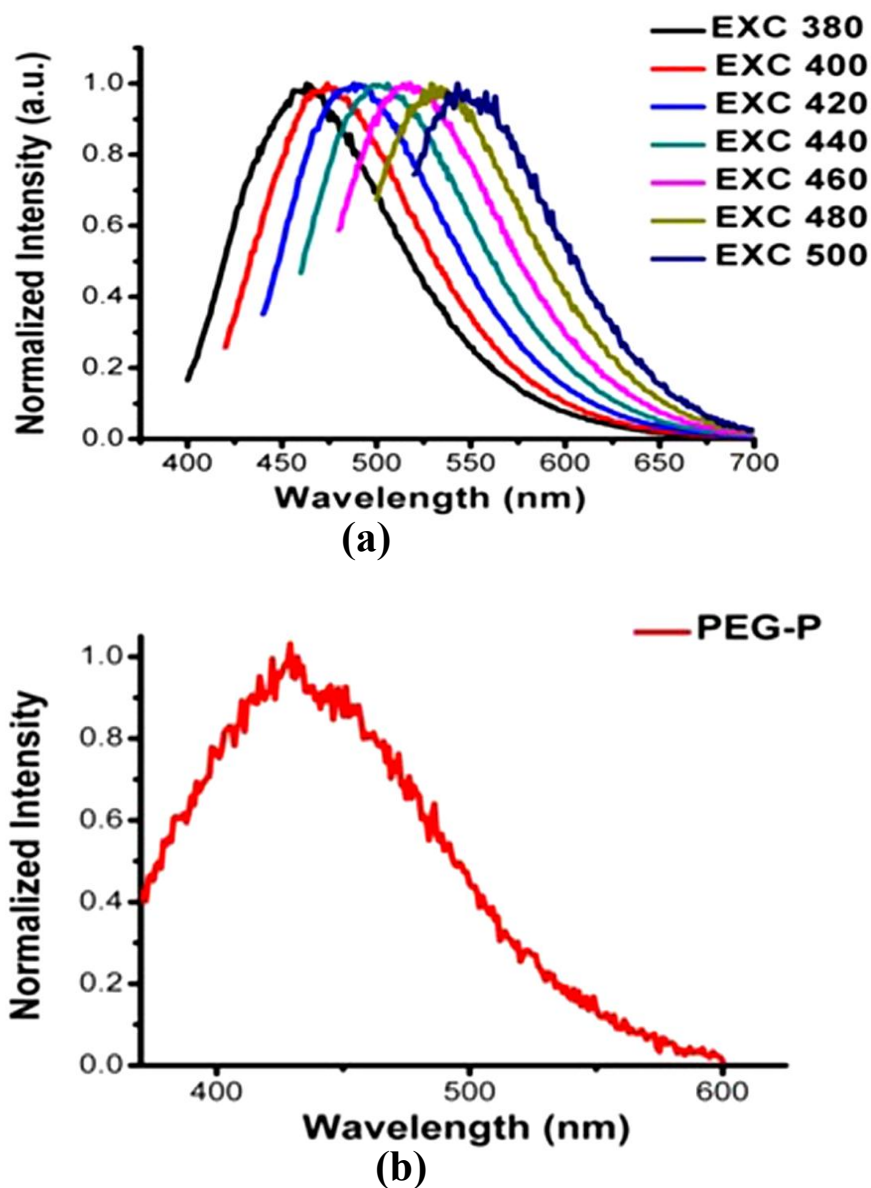
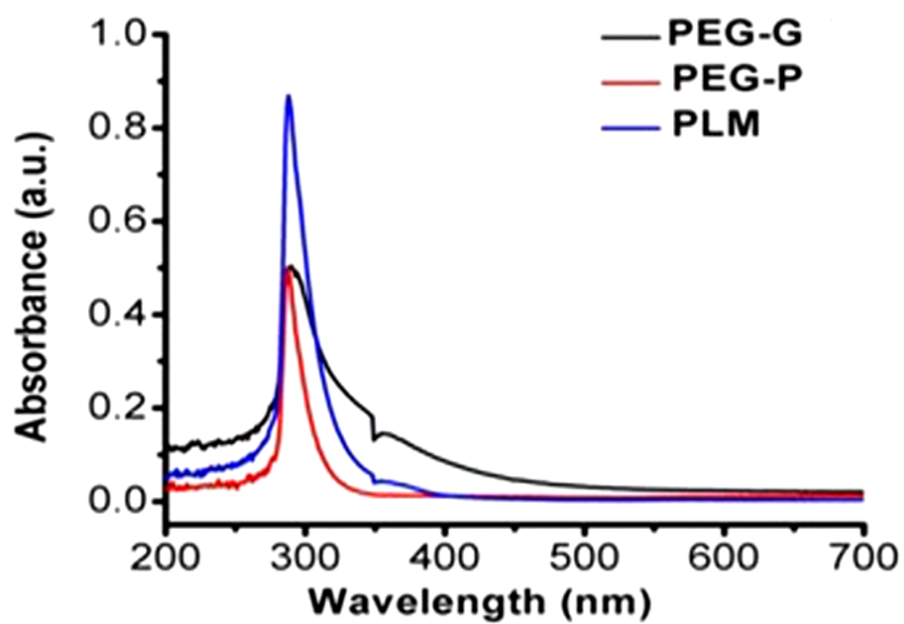
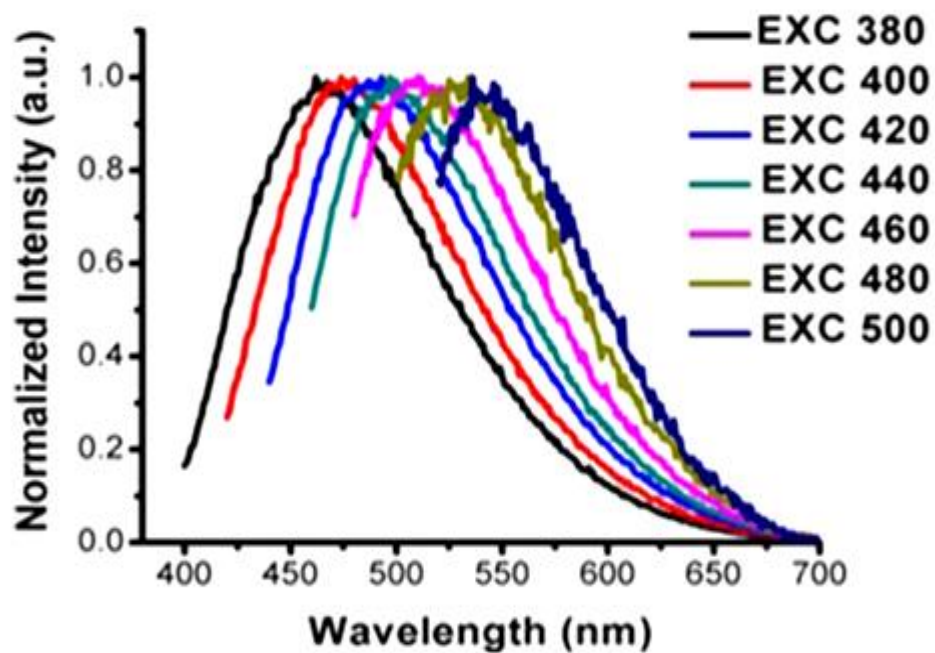


Figure-20. Photoluminescence properties of PEG-Glycine(a),PEG-PPF (b)



(a)



(b)

Figure-21. UV-VIS absorption spectrum of comacromer analogues (a) and fluorescent spectrum of PEG-Maleic acid comacromer (b).

#### 4.1.5. Preparation of PLM-NG and C-PLM-NG nanogels and evaluation of size, morphology and surface charge of nanogels

Nanogels were synthesized from PLM and C-PLM comacromers by crosslinking the unsaturated double bonds of the comacromer with vinyl crosslinkers acrylic acid and N, N dimethylaminoethylmethacrylate respectively. The reaction scheme is given in Figure-22 and Figure-23.

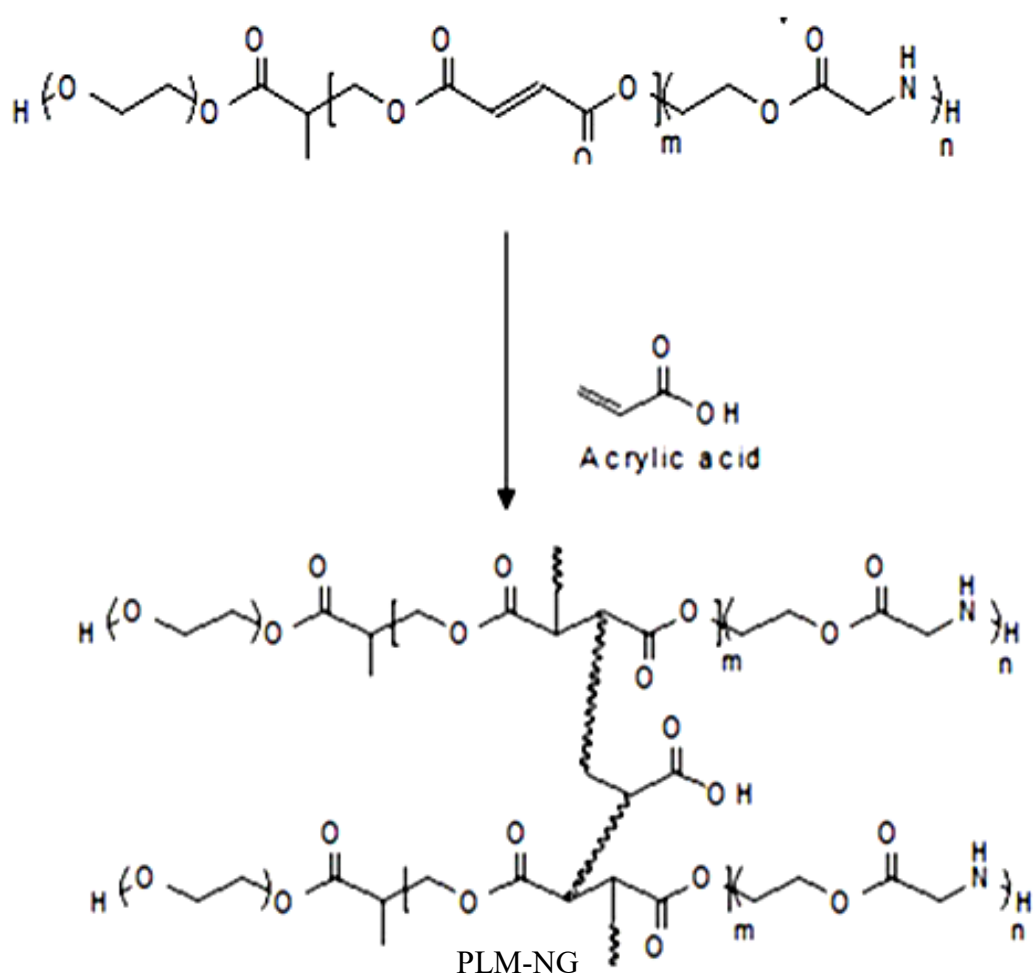
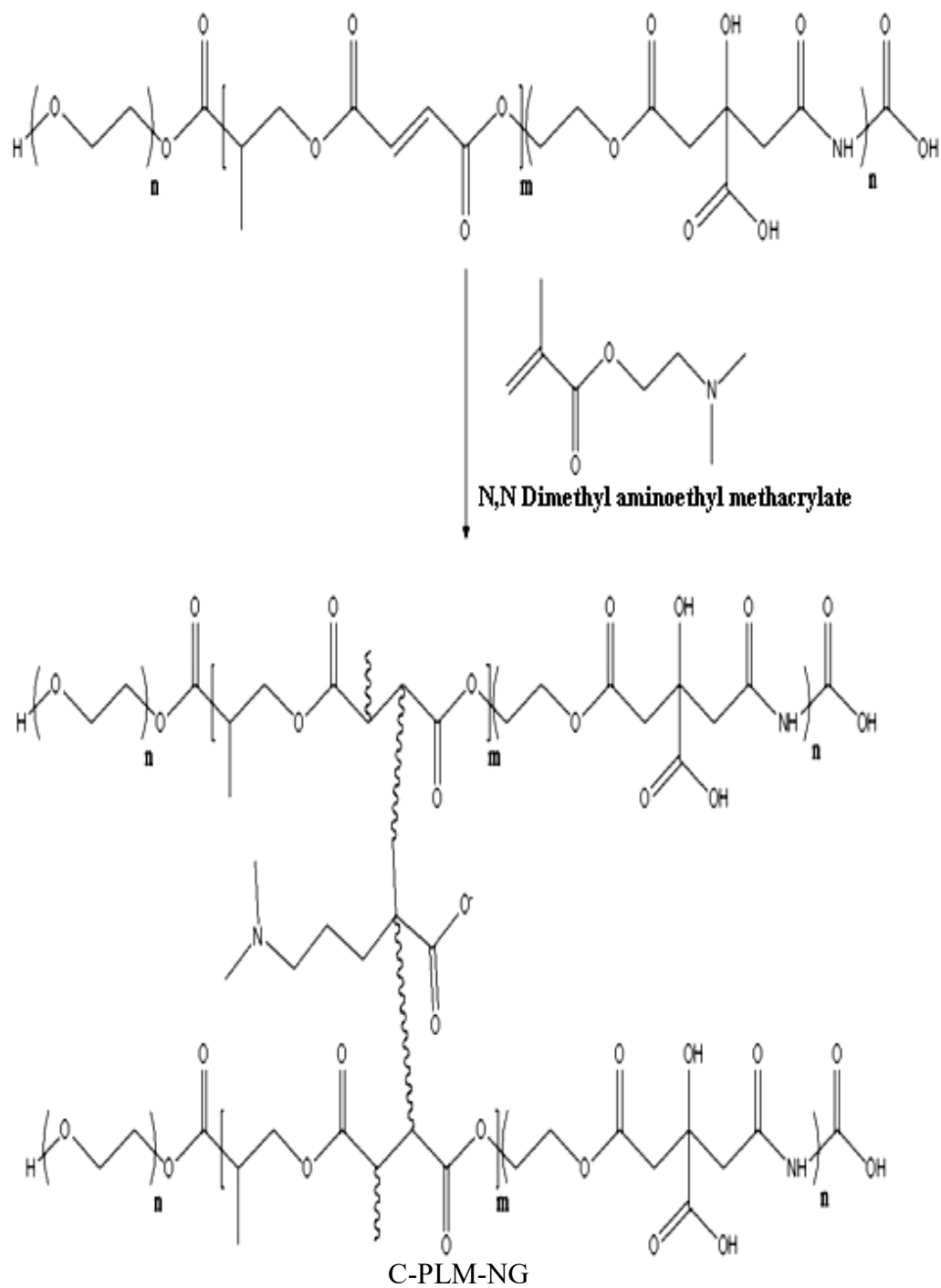


Figure-22. Crosslinking of PLM comacromer to form nanogel



**Figure-23. Crosslinking of C-PLM comonomer to form nanogel**

The TEM images of the PLM-NG reveal smooth spherical geometry with particle size around 180 nm (Figure-24a). The dynamic light scattering measurements has shown that the average particle size of the synthesized PLM-NG was around 210 nm (Figure-24b).

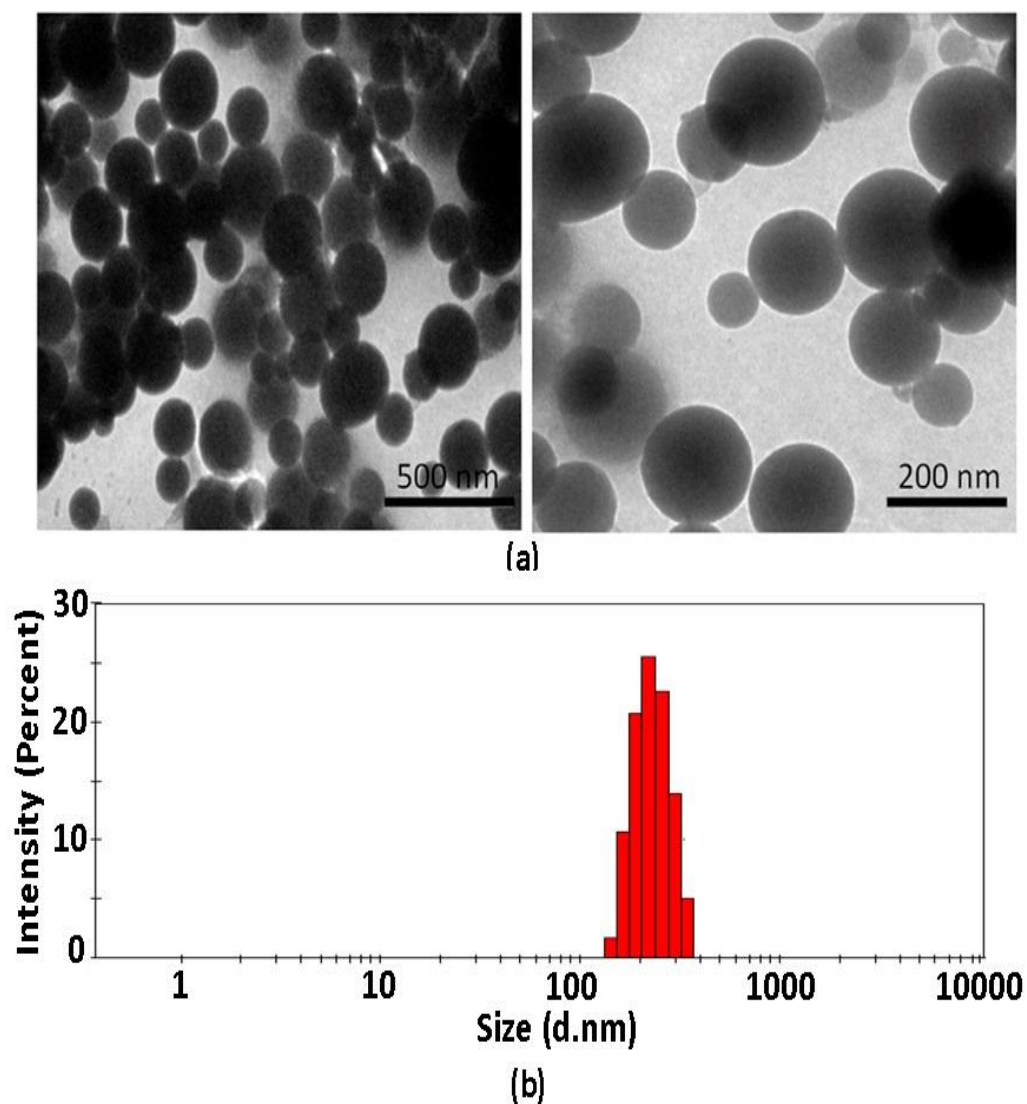
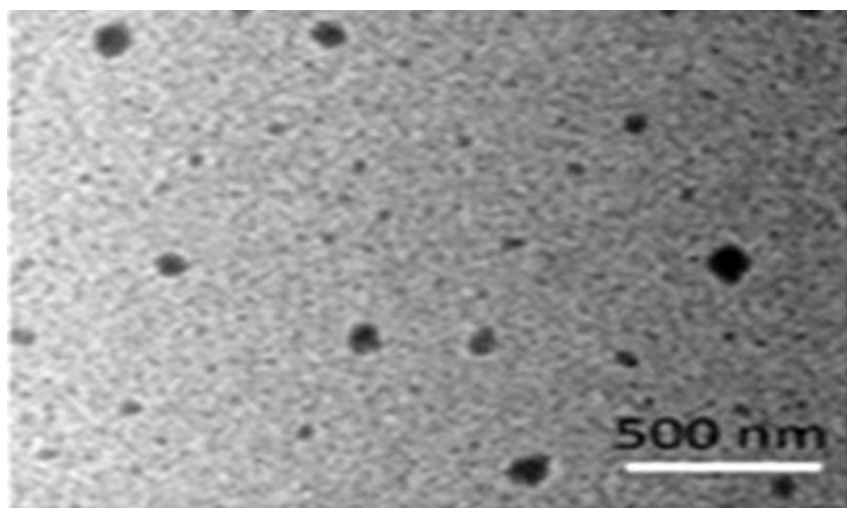


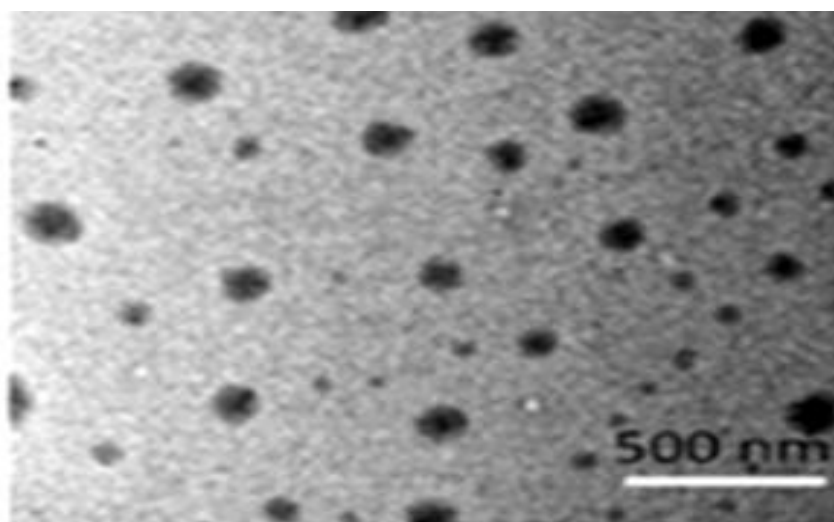
Figure-24. TEM images of PLM-NG (a), DLS histogram of PLM-NG (b).

The nanogel prepared from the C-PLM comacromer (C-PLM-NG) has exhibited pH sensitive swelling property. TEM analysis of C-PLM-NG exhibited different size depending on the pH of the solution. The C-PLM-NG has particle

size around 100 nm and 180 nm at pH 7.4 (physiological) and 5.5 (intracellular acidic condition of cancer cells) respectively (Figure-25).



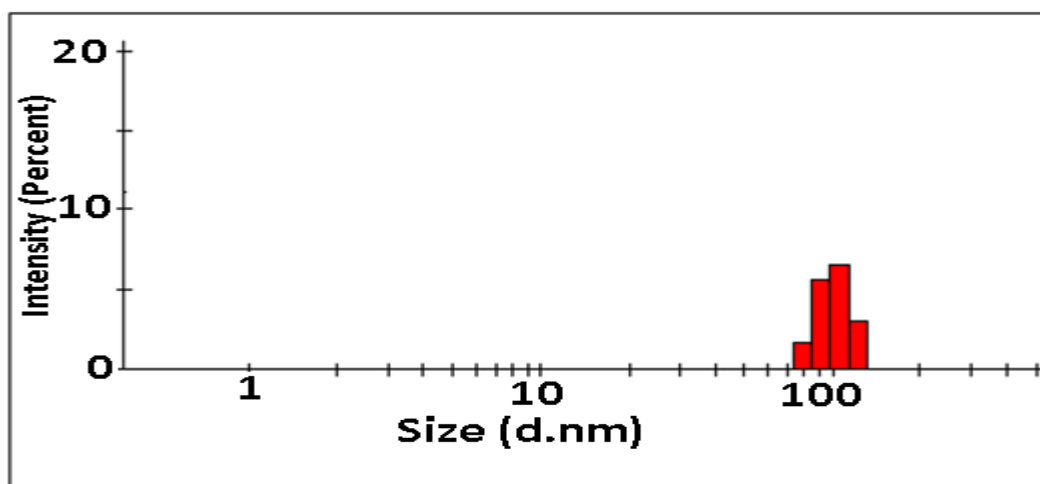
**(a)**



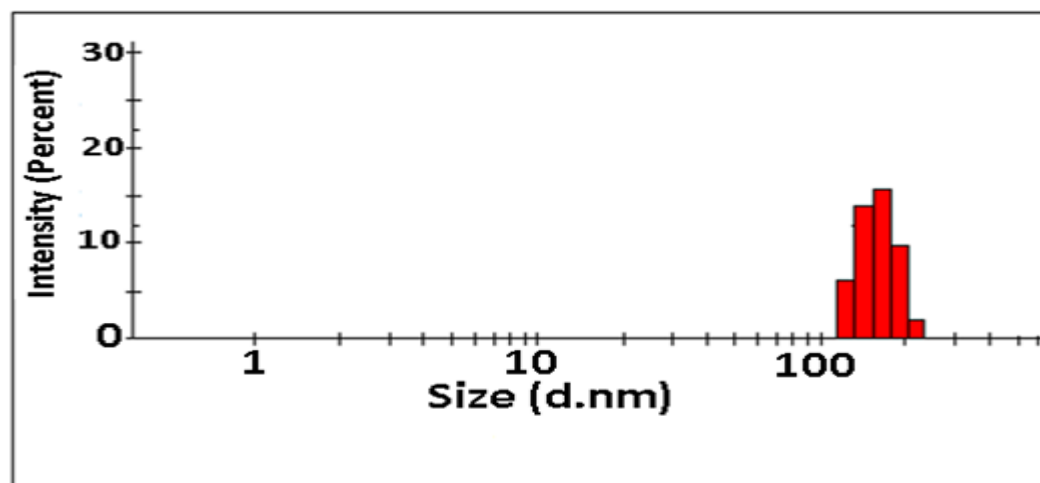
**(b)**

**Figure-25. Morphology and size of nanogel C-PLM-NG at pH 7.4 (a) at pH 5.5 (b)**

Further, the dynamic light scattering measurements of the C-PLM-NG reveal particle size around 115 nm at pH 7.4 and 190 nm at pH 5.5 substantiating the pH sensitive swelling of C-PLM-NG (Figure-26).



(a)



(b)

Figure-26. DLS measurement of C-PLM-NG at pH 7.4 (a) at pH 5.5 (b)

The surface charge analysis of PLM-NG and C-PLM-NG revealed surface charge of -6.79 and 28 mv respectively (Figure-27 and 28).

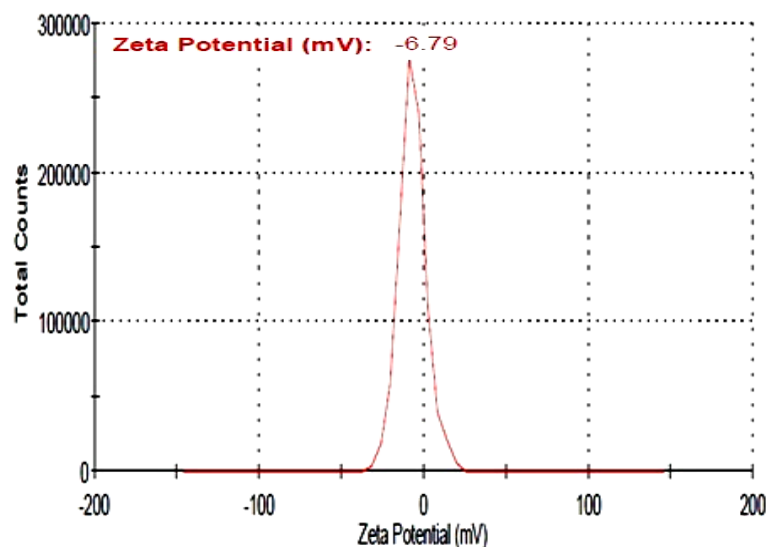


Figure-27. Surface charge analysis of PLM-NG

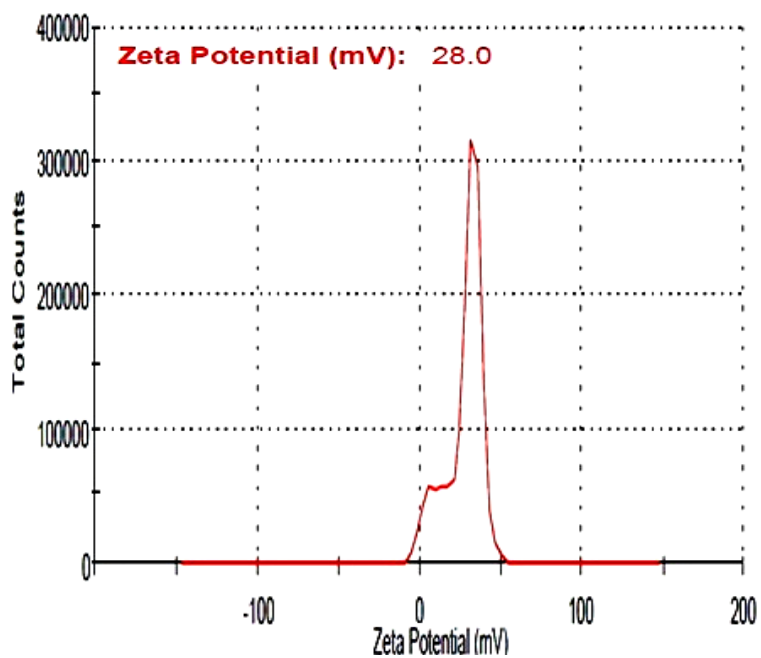


Figure-28. Surface charge analysis of C-PLM-NG

#### 4.1.6. Evaluation on cytocompatibility, hemolytic potential and cellular uptake and imaging capability of PLM and C-PLM-NG

Cytotoxicity is a major drawback associated with current fluorescent agents used for biomedical applications. Hence, the cytocompatibility of PLM-NG and C-PLM-NG nanogels was evaluated using MTT assay. PLM-NG exhibited good cell viability over a different range of concentrations revealing cytocompatibility (Figure-29 and 30).

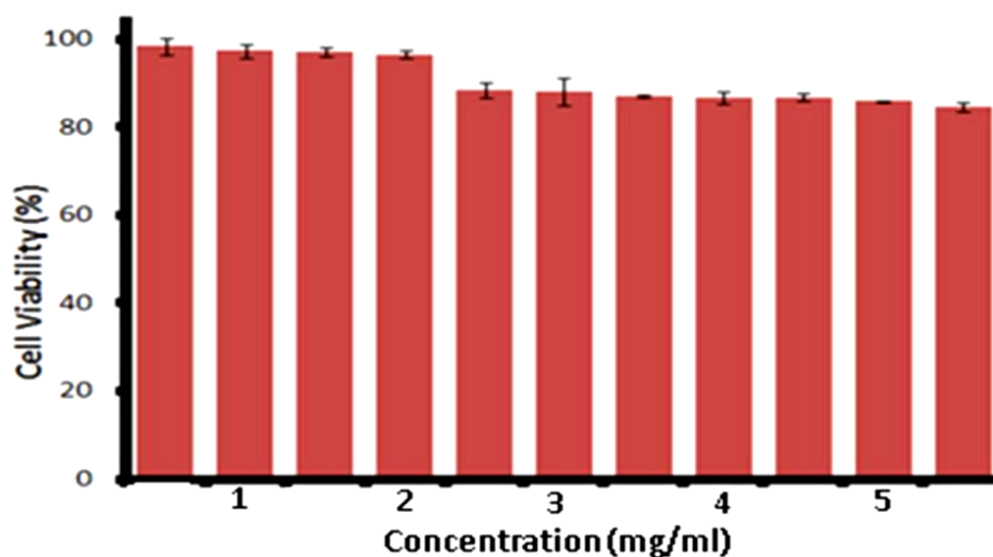
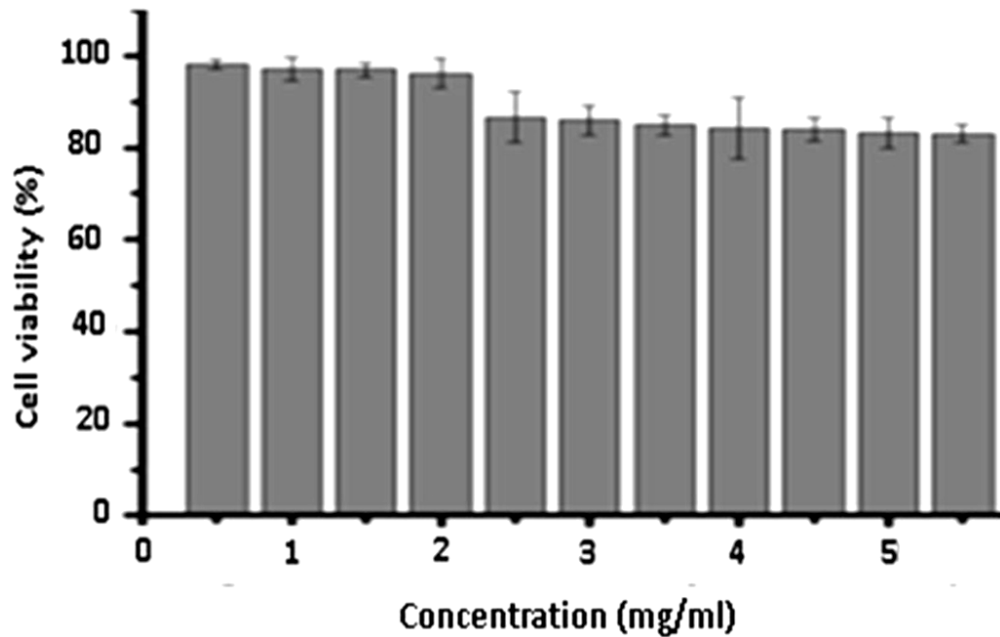


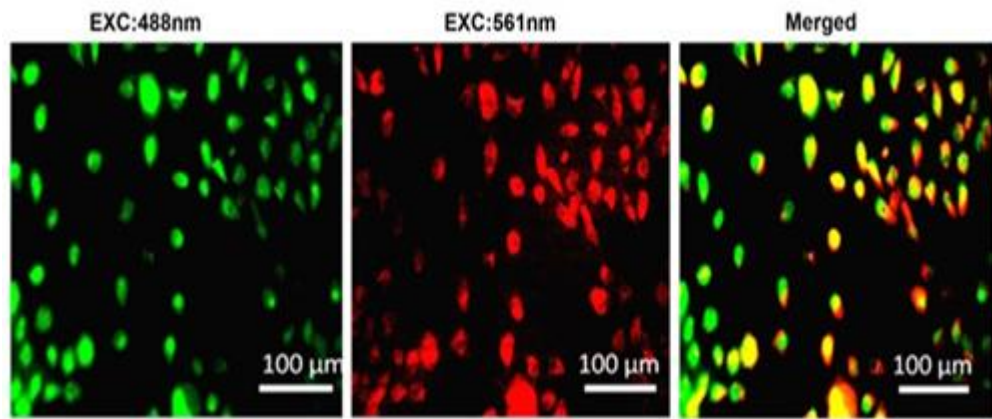
Figure-29. MTT assay showing the cell viability of the PLM-NG at different concentrations (500-6000 µg/ml). Data represents Mean±SD (n=3)



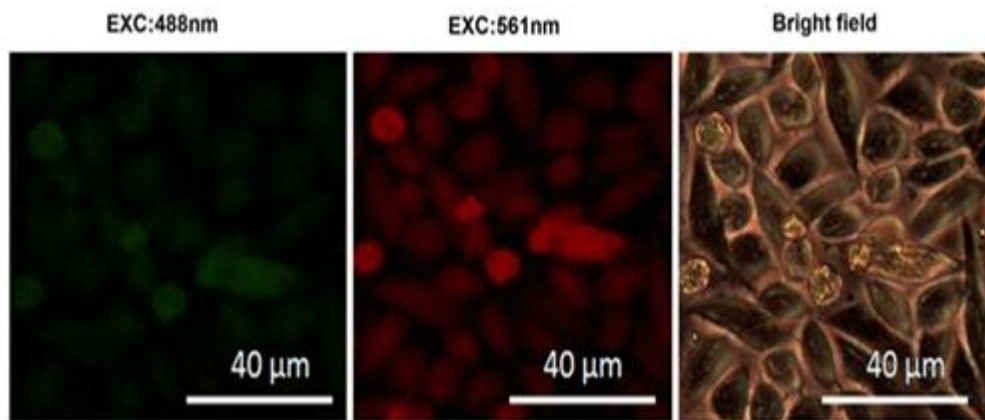
**Figure-30. MTT assay showing the cell viability of the C-PLM-NG at different concentrations (500-6000  $\mu\text{g/ml}$ ). Data represents Mean $\pm$ SD (n=3)**

Furthermore, hemolysis is another major challenge for blood contact devices. The hemolytic potential of the nanogels were evaluated according to ISO standards. Hemolysis studies have revealed hemolytic percentage of 0.12 and 0.03 for PLM-NG and C-PLM-NG nanogels respectively.

The cellular imaging capability of the PLM-NG nanogel was evaluated using L929 fibroblast and Hela cell lines. The cellular uptake images of PLM-NG in L929 and Hela cell demonstrated dual emissions (green and red) at excitation wavelengths 488 nm (green) and 561 nm (red) respectively (Figure-31). Similar observations were also noted for C-PLM-NG on Hela cell line (Figure-32).



**(a)**



**(b)**

**Figure-31. Cellular uptake of PLM-NG in L929 cells (a) HeLa cells (b)**

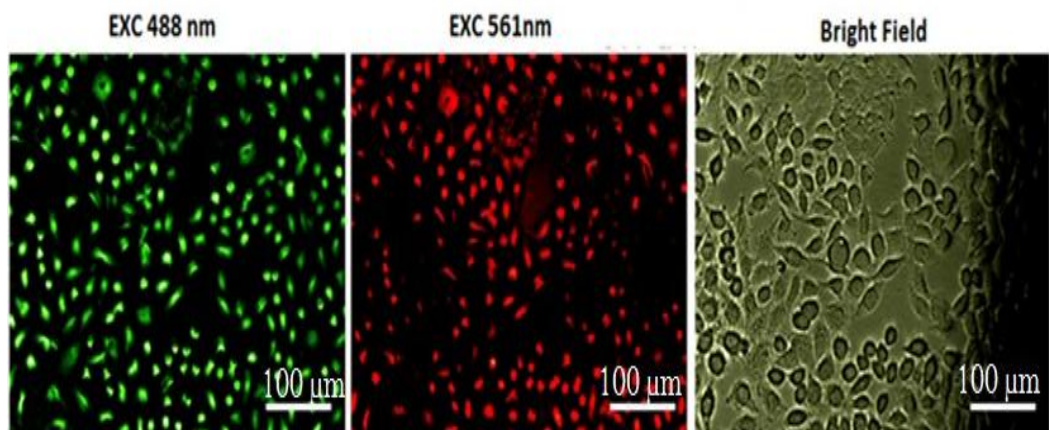


**Figure-32. Cellular uptake of C-PLM-NG in HeLa cells**

#### 4.1.7. Evaluation of the therapeutic potential of C-PLM-NG

DOX is loaded inside the nanogel during the preparation of nanogel. The drug loading efficiency is found to be 80% for C-PLM-NG. The studies on pH sensitive swelling of nanogel and release of DOX revealed 15% release in normal physiological pH; but in intracellular acidic pH 5.5, the release of DOX significantly increased to 48%. From the release profile of DOX, it is evident that the present nanogel exhibits favorable pH dependent drug release kinetics (Figure-33). MTT assay on Hela cell line with the nanogel loaded with DOX reveal low cell viability; the observed decrease in cell viability is attributed to the release of this anticancer drug from the C-PLM-NG (Figure-34). This result suggests the good therapeutic potential of C-PLM-NG.

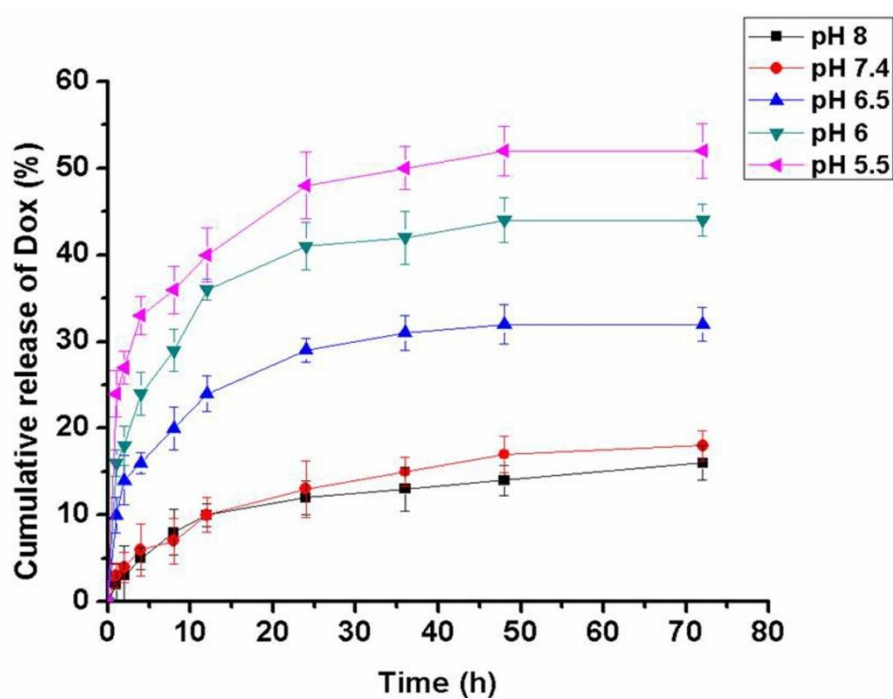


Figure-33. pH Sensitive release of doxorubicin from C-PLM-NG

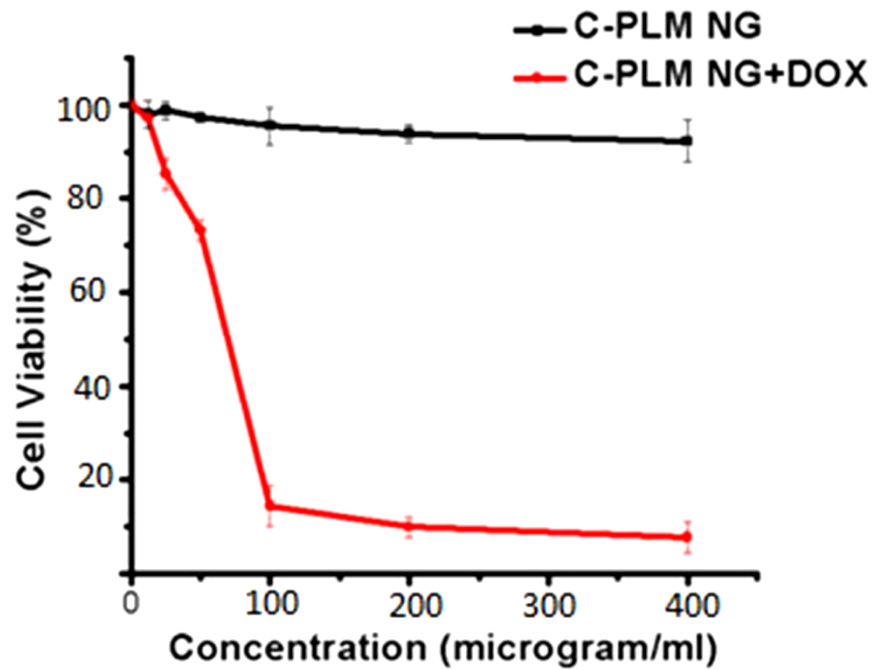
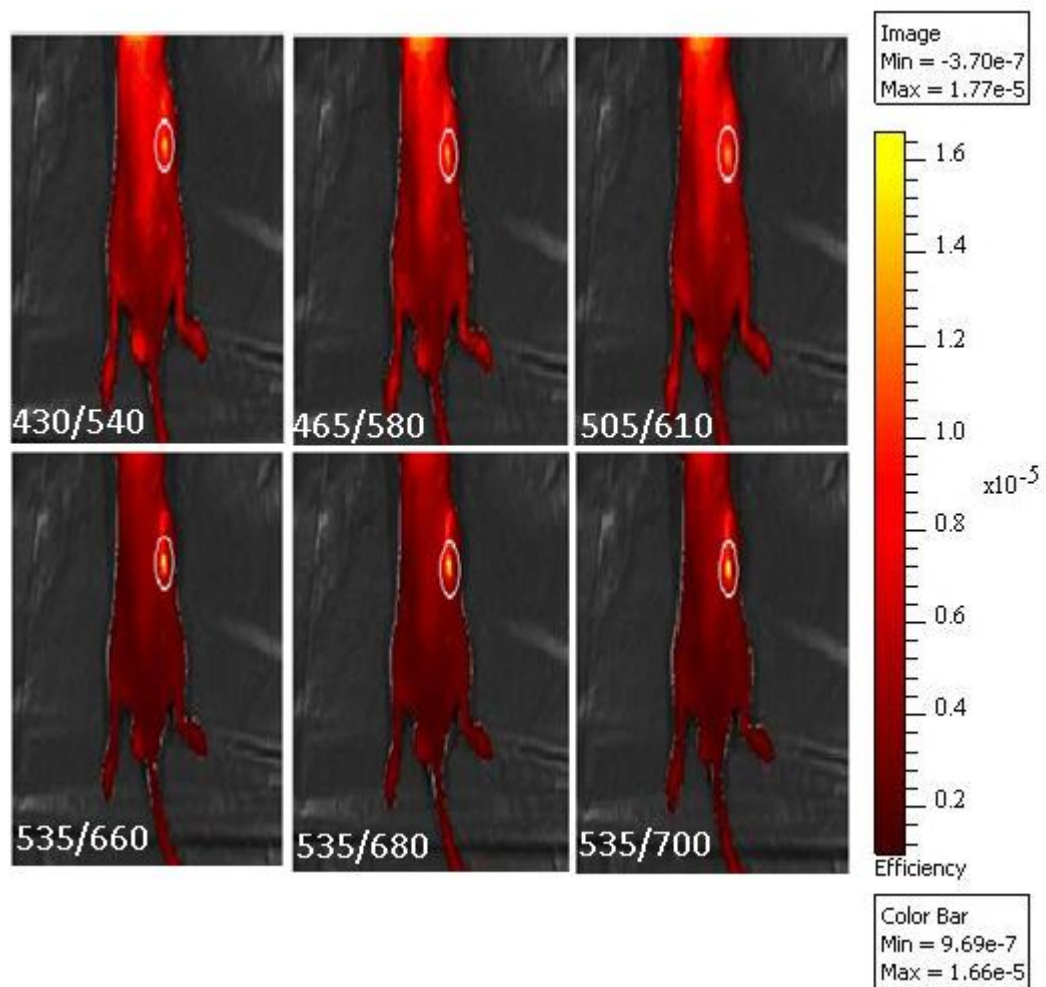


Figure-34. Cell viability C-PLM-NG and doxorubicin-loaded C-PLM-NG.

#### 4.1.8. Evaluation of the bioimaging capability of C-PLM-NG

The efficacy of C-PLM-NG for bioimaging is assessed using mice model. The excitation wavelength, which offers the emission at near IR region with relatively higher intensity, is chosen. The images of the subcutaneously injected nanogel for excitations (430, 465, 505 and 535 nm) and emissions (540, 580, 610, 660, 680 and 700 nm) are collected using filters. The images of the subcutaneously injected nanogel in mice are given in figure 35.



**Figure-35. Images of the subcutaneously injected nanogel on mice for different excitations (The circled area shows the position of injected area and the inset shows the different excitation and emission wavelengths used for imaging)**

Since the excitation wavelength of 535 nm offers emission at near IR region with relatively higher intensity, the images for the near IR emission was captured using different emission filters. The processed images captured for the near IR emission at 660 nm - 700 nm for the excitation at 535 nm are also given in Figure-36

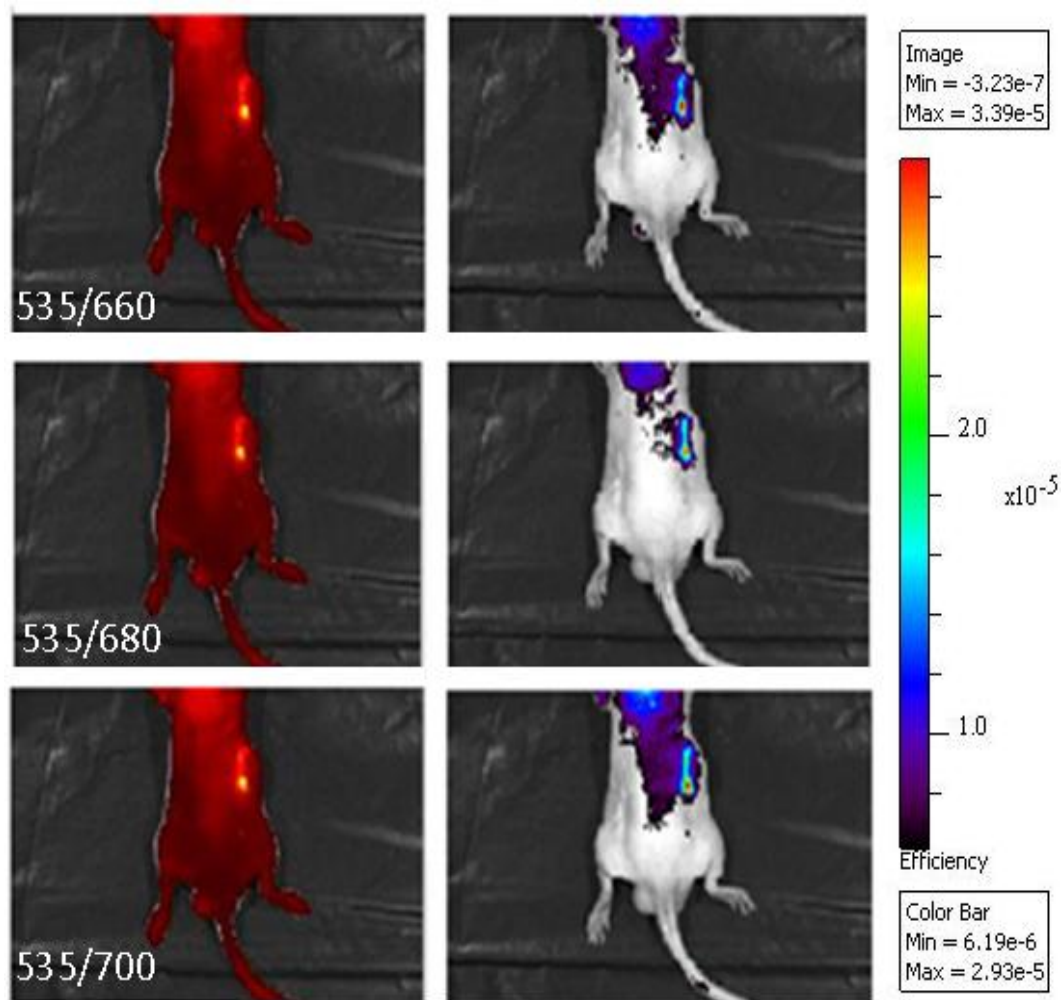
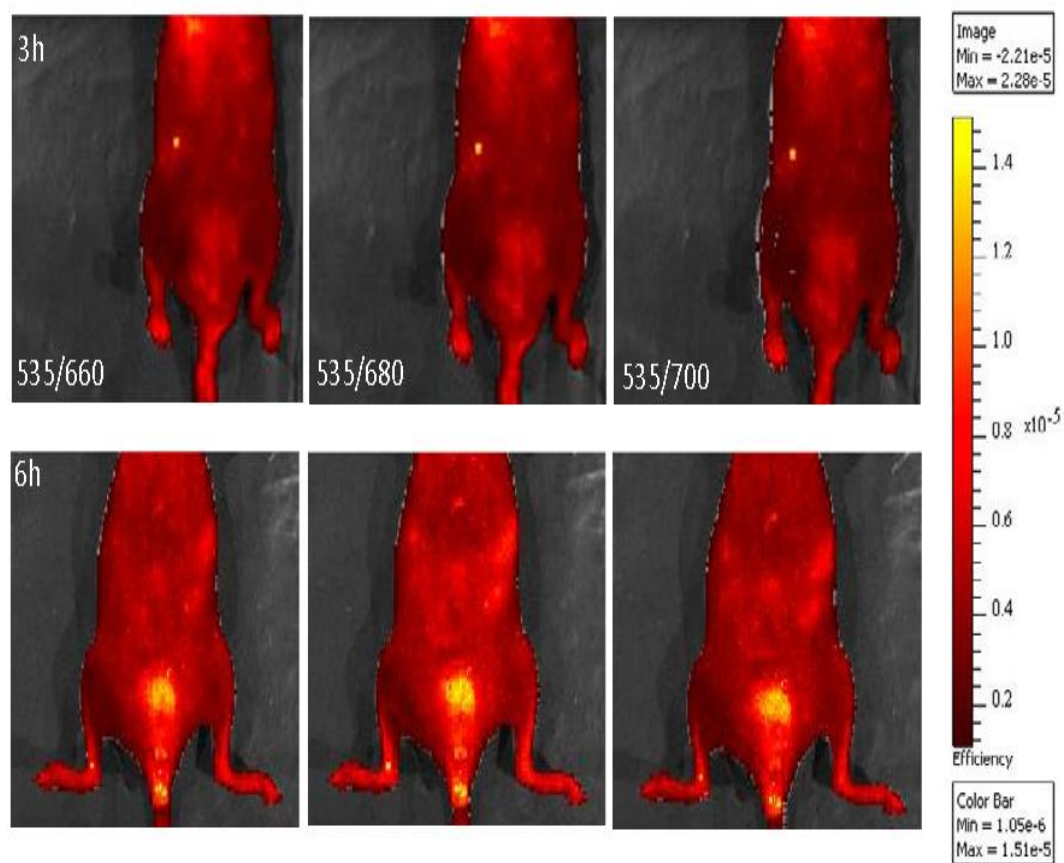


Figure-36. Processed near IR fluorescent images of mice using C-PLM-NG

#### 4.1.9. Evaluation of the bioimaging, biodistribution and biocompatibility of C-PLM-NG

It is necessary that any biomaterial after performing its intended function should be metabolized or excreted from the body without creating any toxicological problems. Hence, biodistribution and clearance mechanism of C-PLM-NG from the body of mice was also studied. C-PLM-NG injected in the mice through tail vein revealed a spot like signal from liver region after 3 h post injection (Figure-37). After 6 h post injection, signal from liver region disappeared and a strong visible signal appeared from urinary bladder and urine.



**Figure-37. Biodistribution of intravenously injected nanogel in mice (Inset shows the excitation and emission wavelengths detected with cut off filters)**

*Ex vivo* imaging of organs with C-PLM-NG on mice carried out at 3 h and 24 h of post injection offered further insight on biodistribution. After 3 h post injection, imaging of the carcass after opening the abdomen and thorax with organs *in situ* revealed signals from liver especially from the gall bladder as well as urinary bladder (Figure-38).

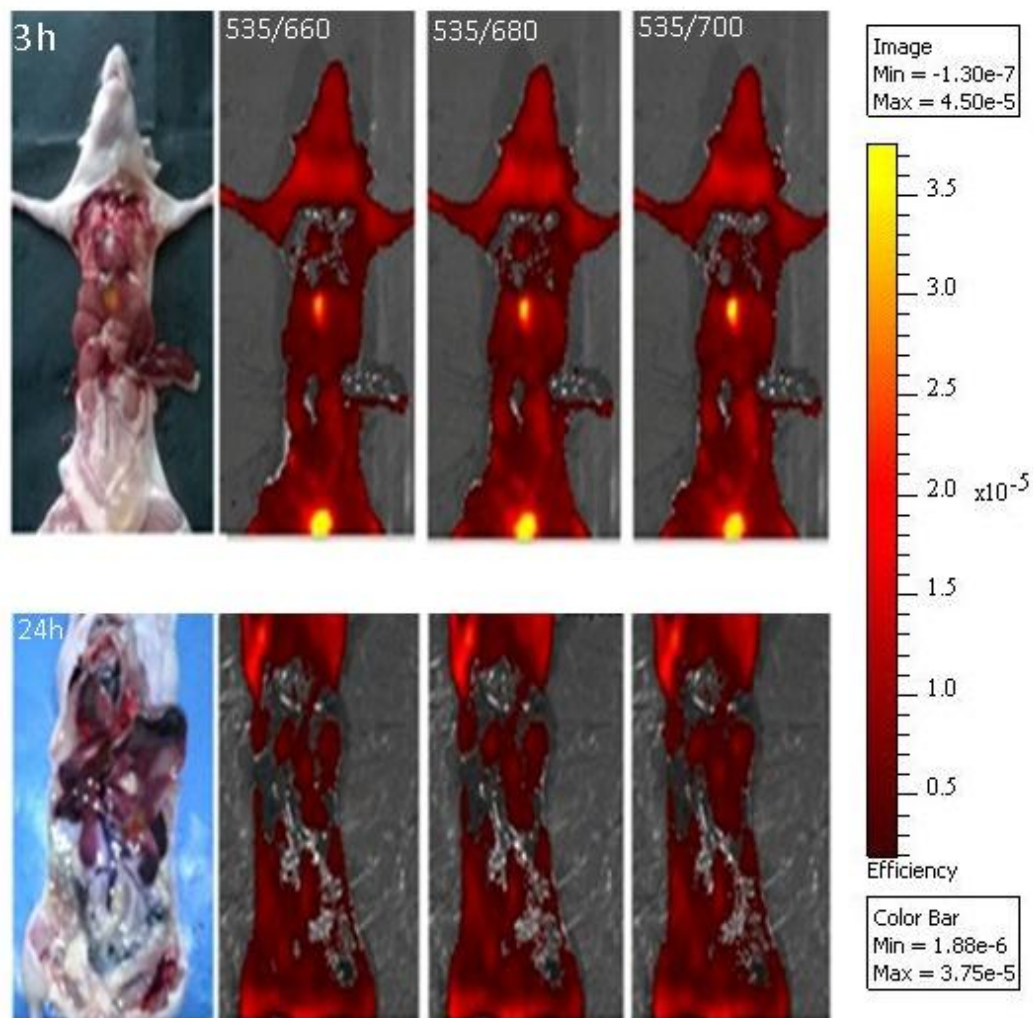


**Figure-38. *Ex vivo* imaging of carcass of mice after 3 h and 24 h post injection depicting biodistribution (Inset shows the excitation and emission used)**

The dissected organs liver, kidney and heart at 3h time were also imaged. Very strong fluorescent signal appeared from kidney and liver while no fluorescence from heart (Figure-39).

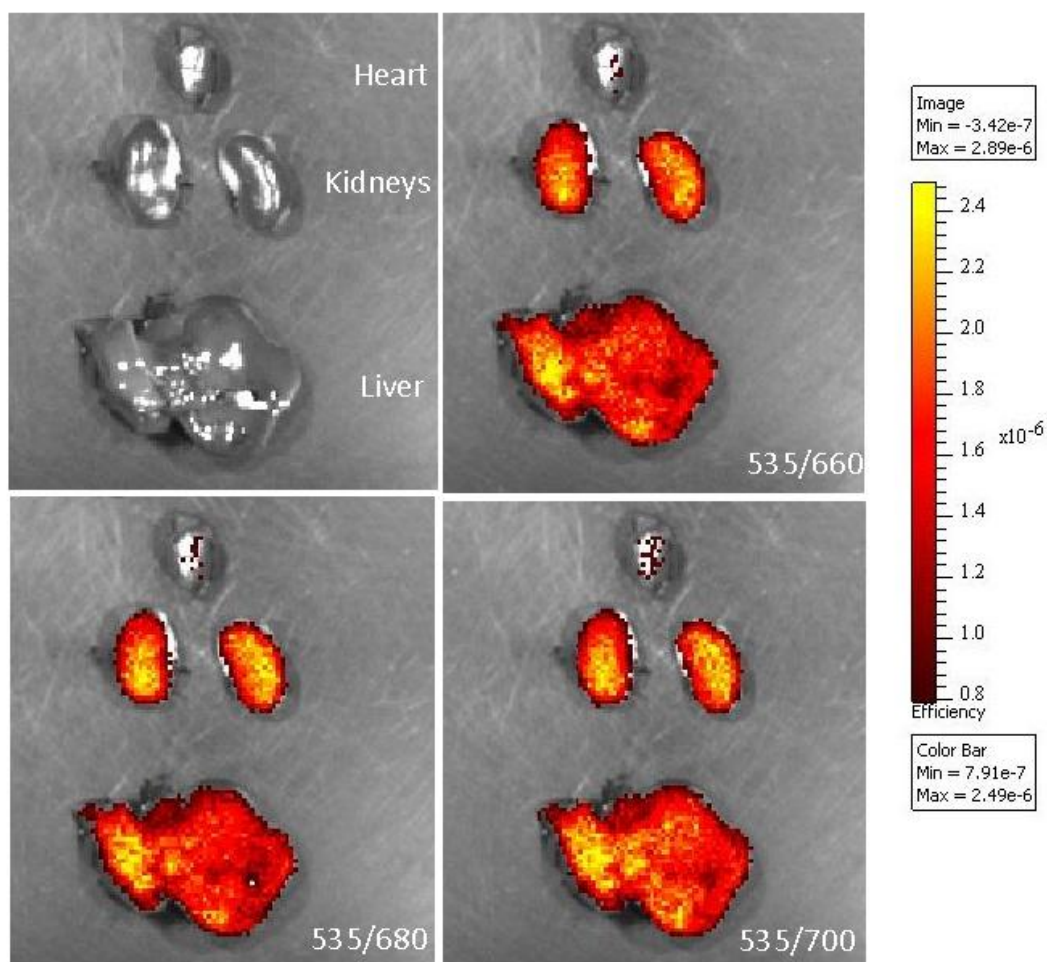


**Figure-39. Ex vivo imaging of different organs of mice after 3 h and 24 h post injection depicting biodistribution (Inset shows the excitations and emissions)**

Evaluation of toxicity profile of the nanoparticles is very critical for biomedical applications. Hence, the histopathological evaluation of the heart, liver and kidney were carried out. The histopathological analysis revealed normal tissue morphology without any significant change or signs of necrosis (Figure-40).

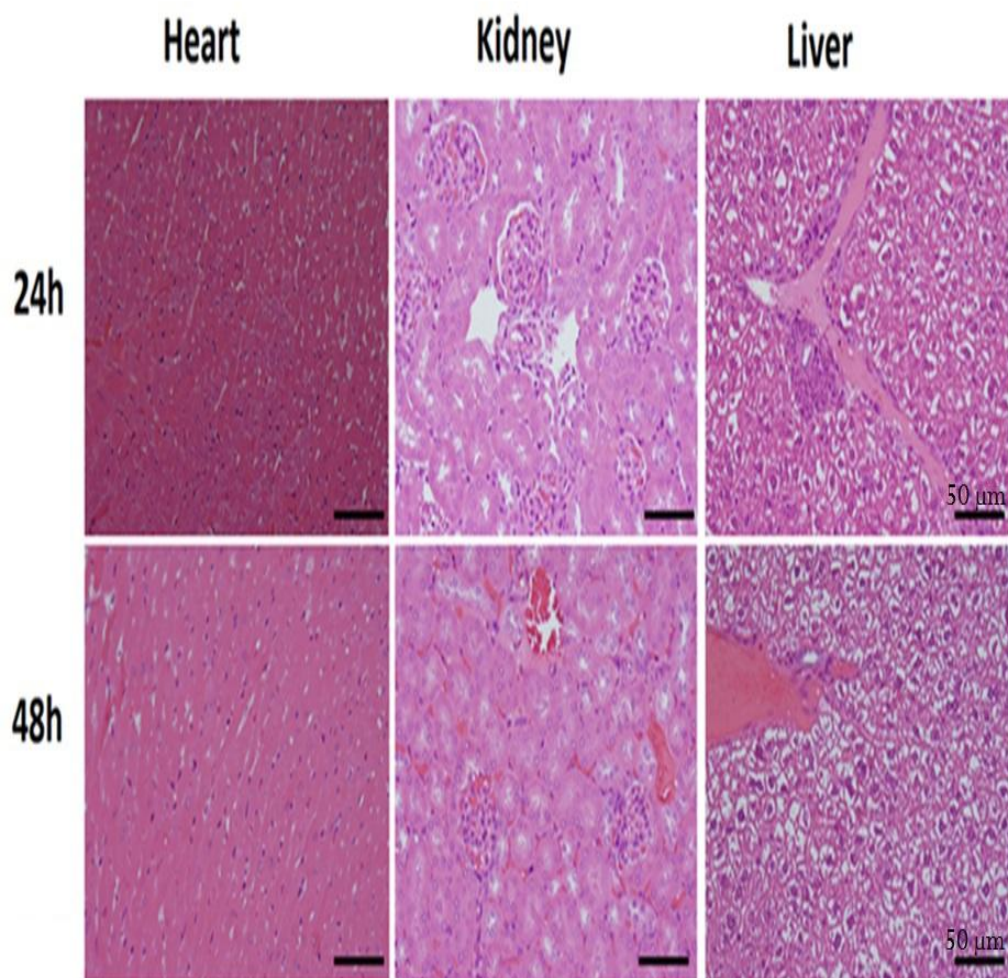


**Figure-40. H&E stained images of organs of mice at 24 h and 48 h post injection**

Lymph node imaging is an important tool for differentiating the benign and malignant nodes. With the present studies, the tracking of migration of nanogel to axillary lymph nodes of mice is accomplished with the fluorescence from axillary lymph nodes as shown in Figure- 41.

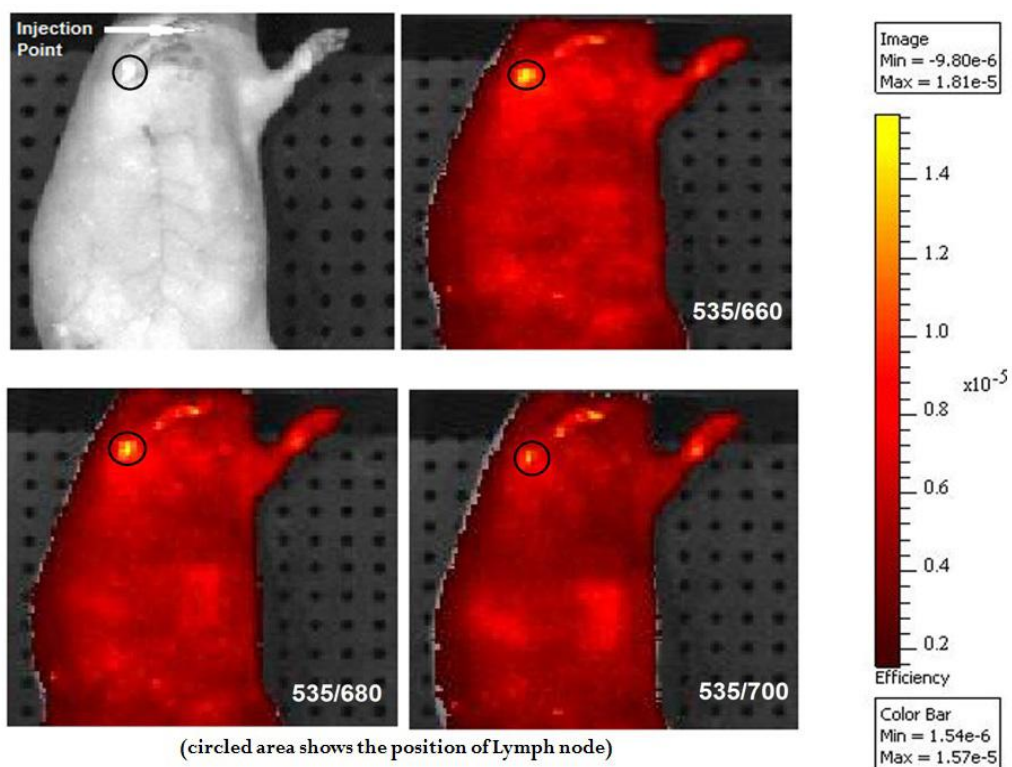


**Figure-41.**Lymph node imaging of a mice using C-PLM-NG (Inset shows the excitation and emission wavelengths detected with cut off filters)

## 4.2. Studies on magneto-fluorescent nanogel for theranostic applications

### 4.2.1. Synthesis of photoluminescent PEG-Maleic acid-Glycine (PMG) comacromer

Photoluminescent PMG comacromer was synthesized by condensation polymerization of PEG, maleic acid and glycine as given in the reaction scheme in Figure- 42.

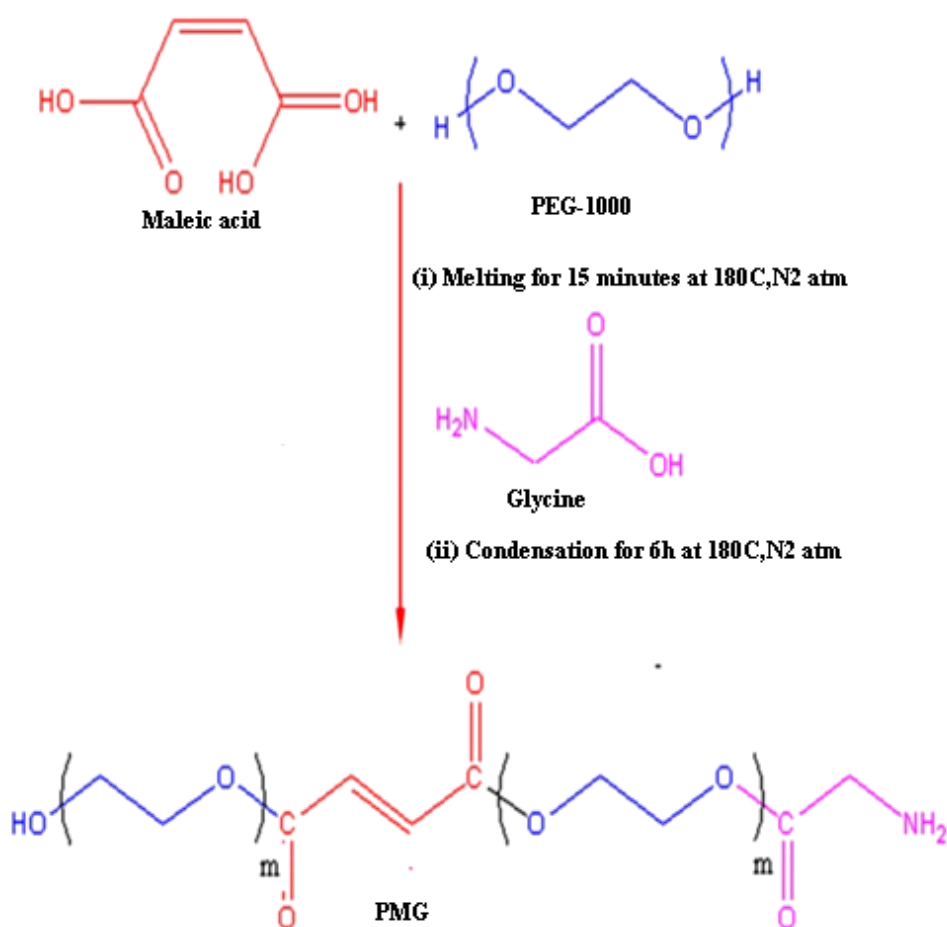


Figure-42. Synthesis of the photoluminescent PMG comacromer

#### 4.2.2. Structural evaluation of PMG comacromer

The structure of the synthesized PMG comacromer was evaluated using FTIR and proton NMR spectroscopy. FTIR spectrum of the comacromer (Figure-43) reveals peaks at  $3390\text{ cm}^{-1}$  (-OH stretching vibrations of PEG),  $1644\text{ cm}^{-1}$  (C=C stretching of CH=CH- bond of maleic acid),  $1352\text{ cm}^{-1}$  (C-C and C-O stretching of ester linkages) and  $1078\text{ cm}^{-1}$  (C-N stretching vibrations of glycine) suggesting the formation of comacromer. The structure of the synthesized comacromer was confirmed through proton NMR spectral analyses of comacromer (Figure-44).  $^1\text{H}$  NMR spectrum shows peaks at 6.8 ppm (double bonds CH=CH of maleic acid), 4.7 ppm (-NH groups of glycine) and 3.4 ppm (-CH<sub>2</sub> groups from PEG).

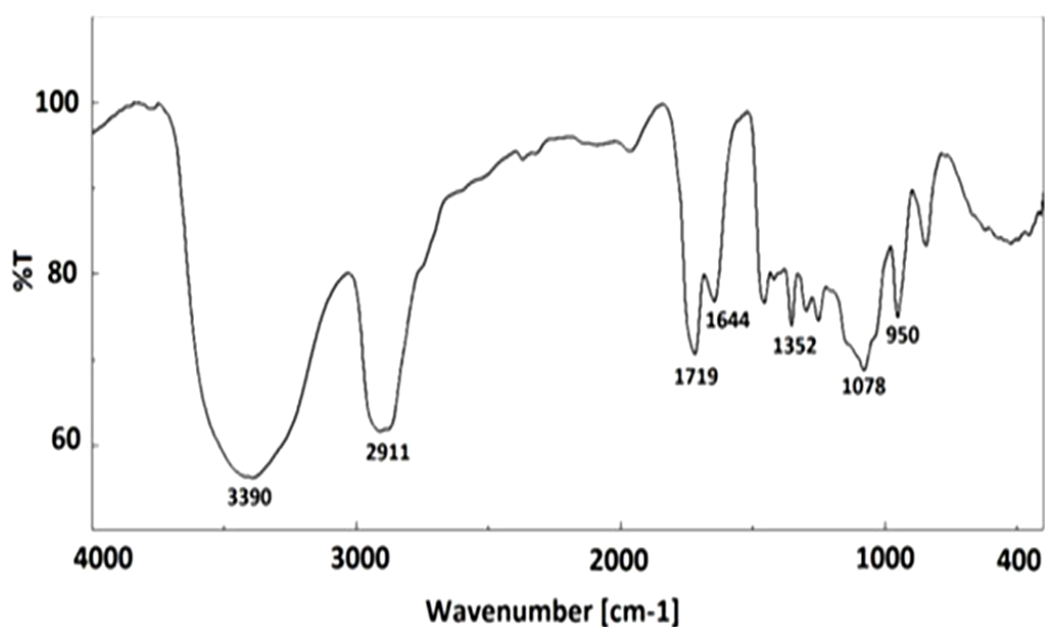
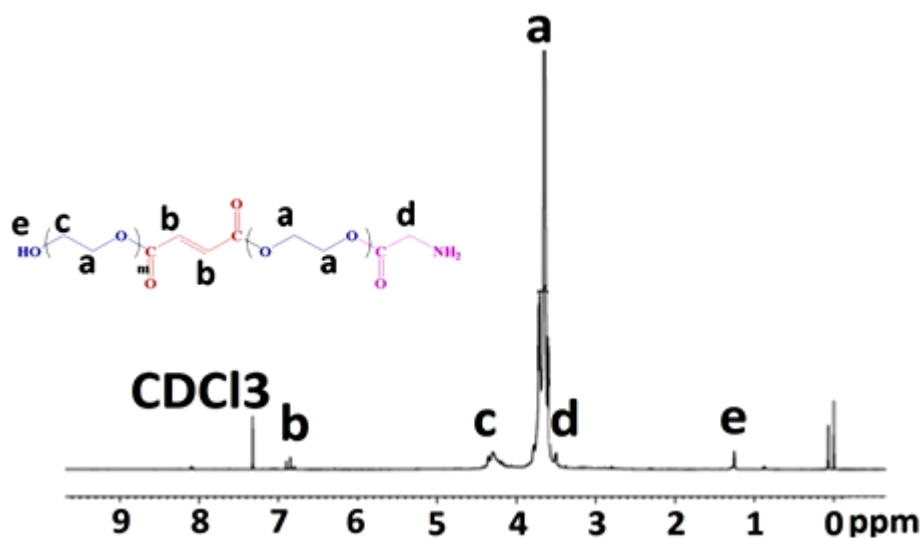


Figure-43. FTIR spectral analyses of the photoluminescent PMG comacromer



**Figure-44.** <sup>1</sup>H NMR spectral analyses of the photoluminescent PMG comacromer

The molecular weight of the comacromer is Mn 3344, Mw 3637 and polydispersity index of 1.09.

#### **4.2.3. Evaluation of the photoluminescence properties of the PMG comacromer**

The comacromer PMG has displayed excitation wavelength dependent fluorescence characteristics. It exhibited multiple emissions (543 nm-893 nm) when excited with different excitation wavelengths (480-800 nm) (Figure-45). Further, the 3 dimensional photoluminescence contour plot demonstrated the visible to near IR fluorescence emission characteristics of the comacromer (Figure-46).

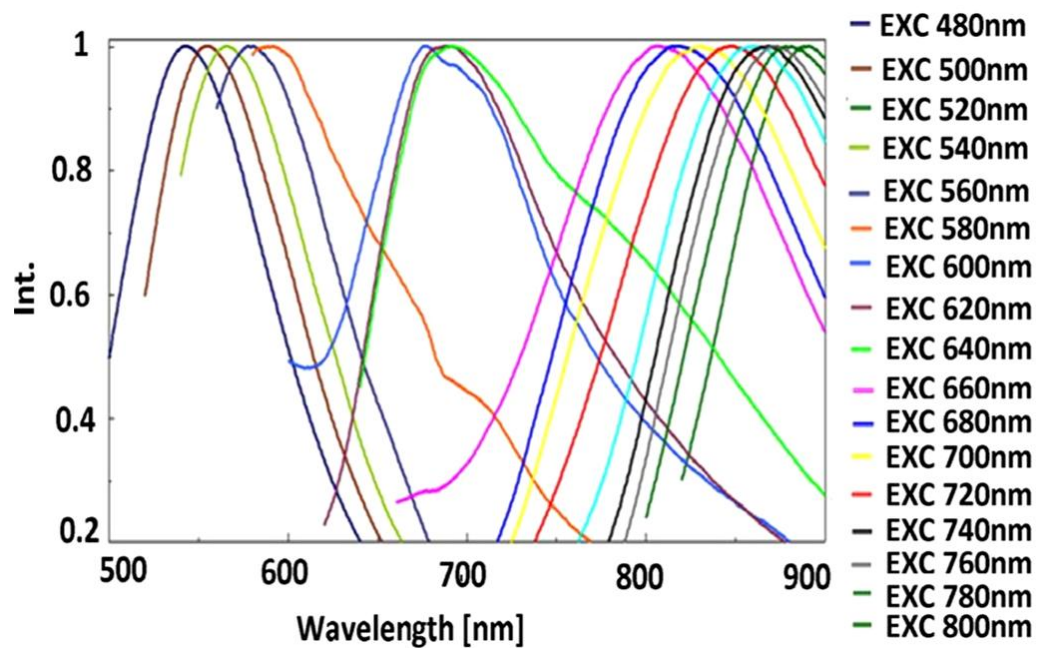


Figure-45. Excitation wavelength dependent photoluminescent spectra of the PMG comacromer under aqueous conditions at different excitations (480-800nm)

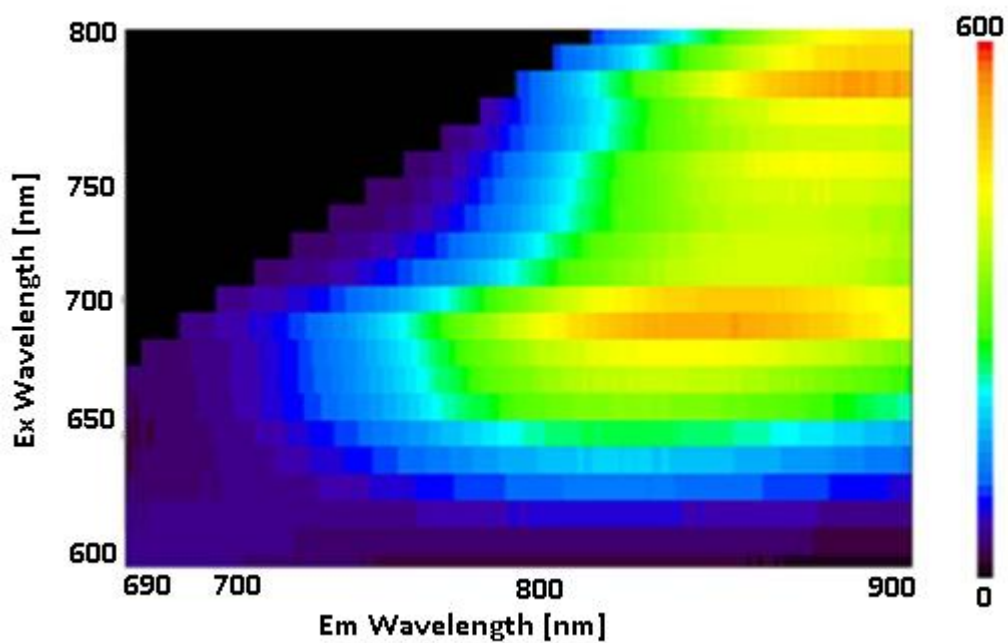


Figure-46. Three dimensional photoluminescence contour plot of the PMG comacromer

It is very important for any fluorophores to have fluorescent lifetime values to be in the order of nanoseconds for efficient bioimaging. The fluorescent lifetime of the comacromer was evaluated. The comacromer was followed a diexponential decay pathway with fluorescent lifetime of 8 nanoseconds (Figure-47).The photostability analysis of the comacromer has revealed good photostability when continuously irradiated for a period of 30 min (Figure-48).

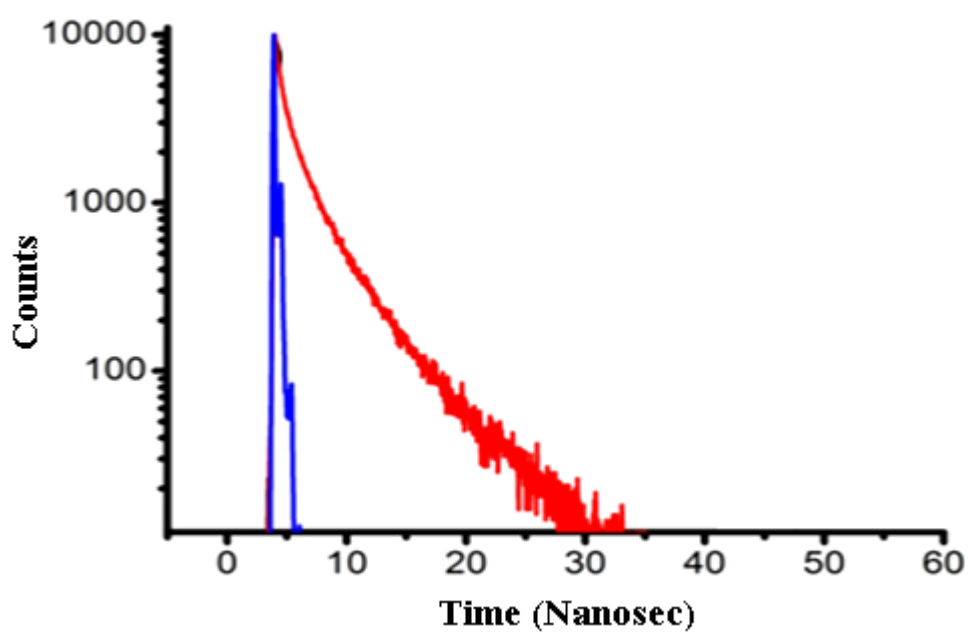


Figure-47. Photoluminescence life time of PMG comacromer

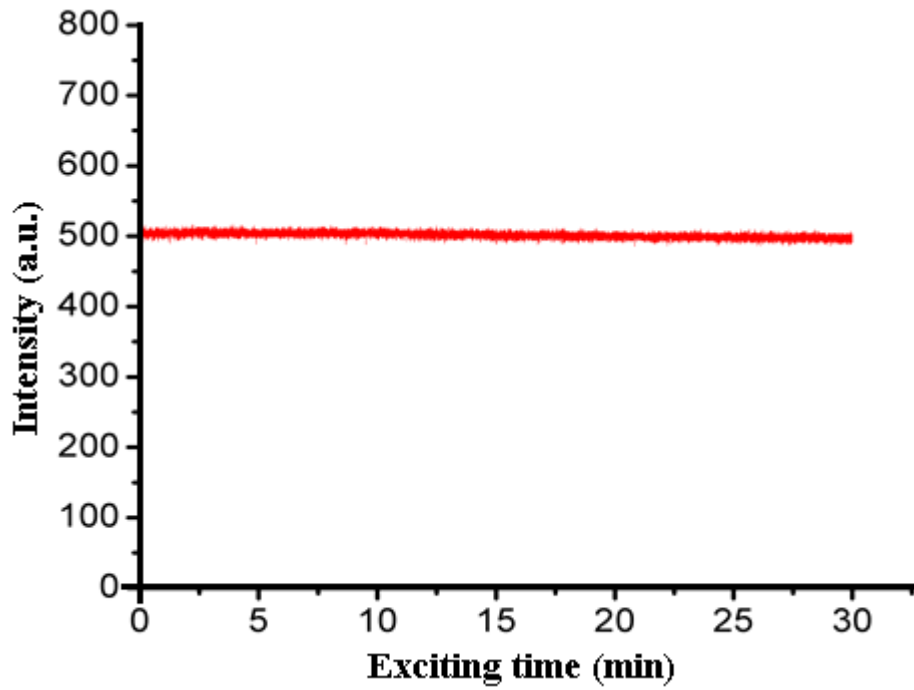


Figure-48. Photostability graph of the comacromer

#### 4.2.4. Synthesis of magneto-fluorescent nanogel (C-SPION-NG)

A magnetofluorescent nanogel was synthesized by the *in situ* incorporation of superparamagnetic iron oxide nanoparticles during the crosslinking of the PMG comacromer with dimethylaminoethyl methacrylate (DMEMA) as given in the reaction scheme in Figure-49.

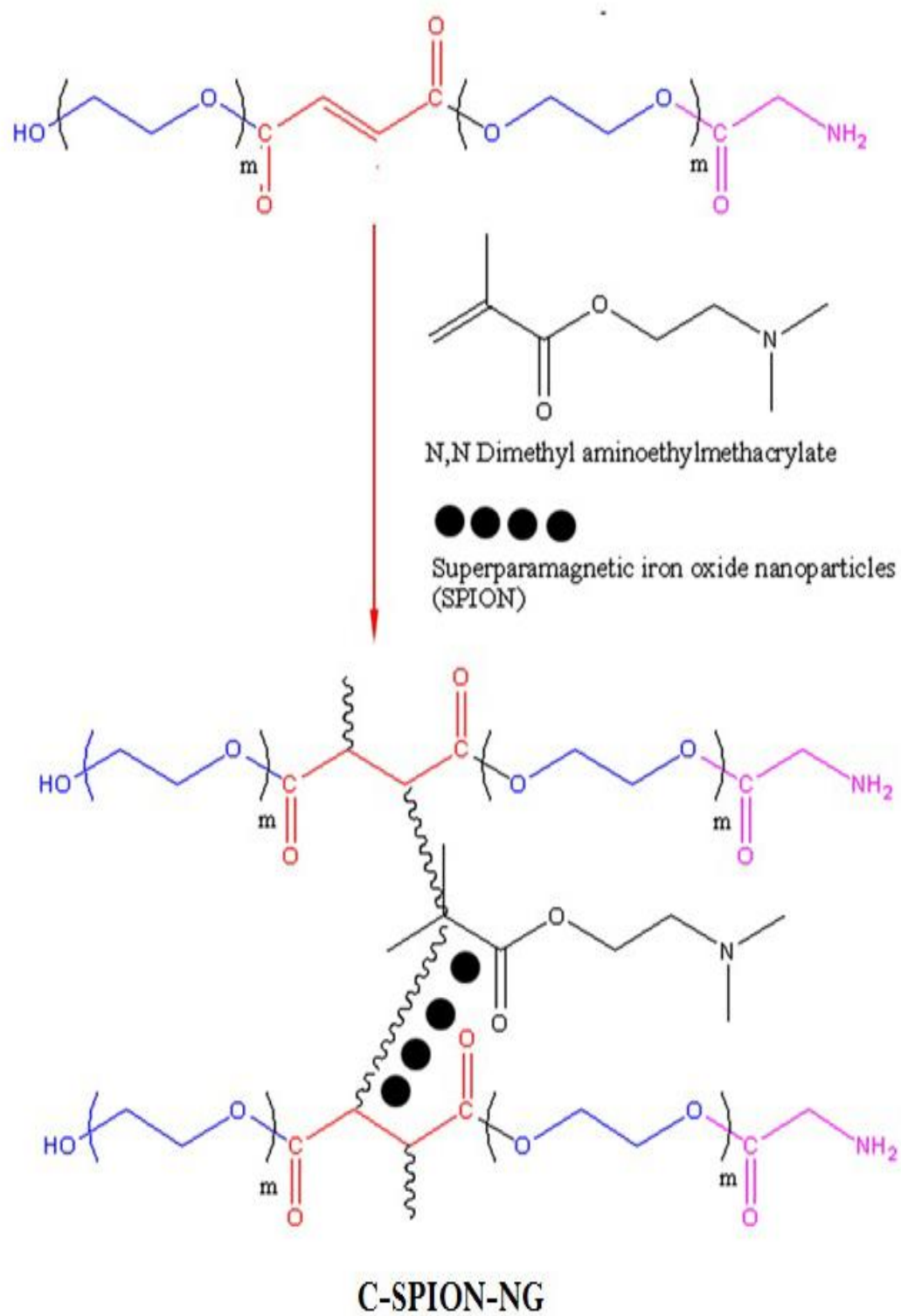
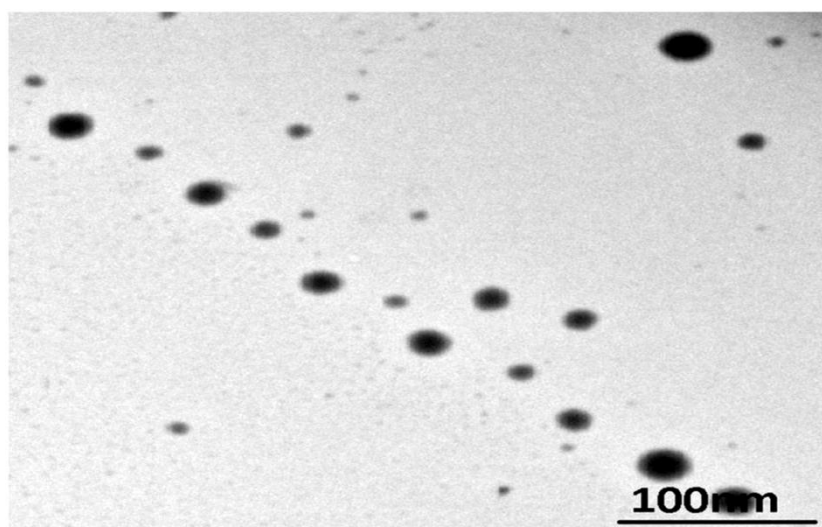


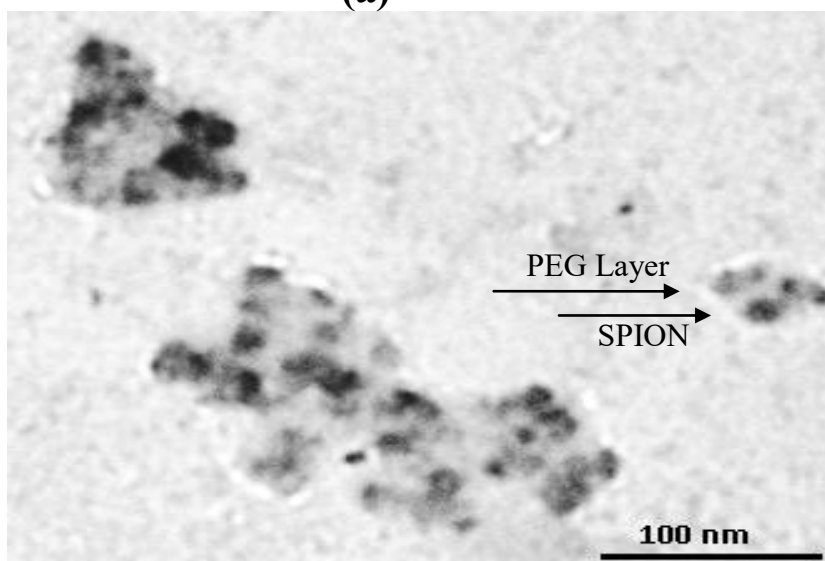
Figure-49. Synthesis scheme of magneto-fluorescent nanogel (C-SPION-NG)

#### 4.2.5. Evaluation of size,morphology and surface charge of C-SPION-NG

The TEM images of C-SPION reveal spherical shape with particle size around 10 nm in size (Figure-50a).The C-SPION-NG shows core-shell morphology with SPION core and PEG shell. The average particle size of C-SPION-NG was found to be 80 nm (Figure-50b). Thus, TEM observation suggests the successful formation of C-SPION-NG.



(a)



(b)

Figure-50. TEM images of C-SPION (a) C-SPION-NG (b)

The hydrodynamic size of the C-SPION and C-SPION-NG measured through DLS analysis revealed average particle size of 25 nm and 100 nm respectively (Figure-51a and 51b).

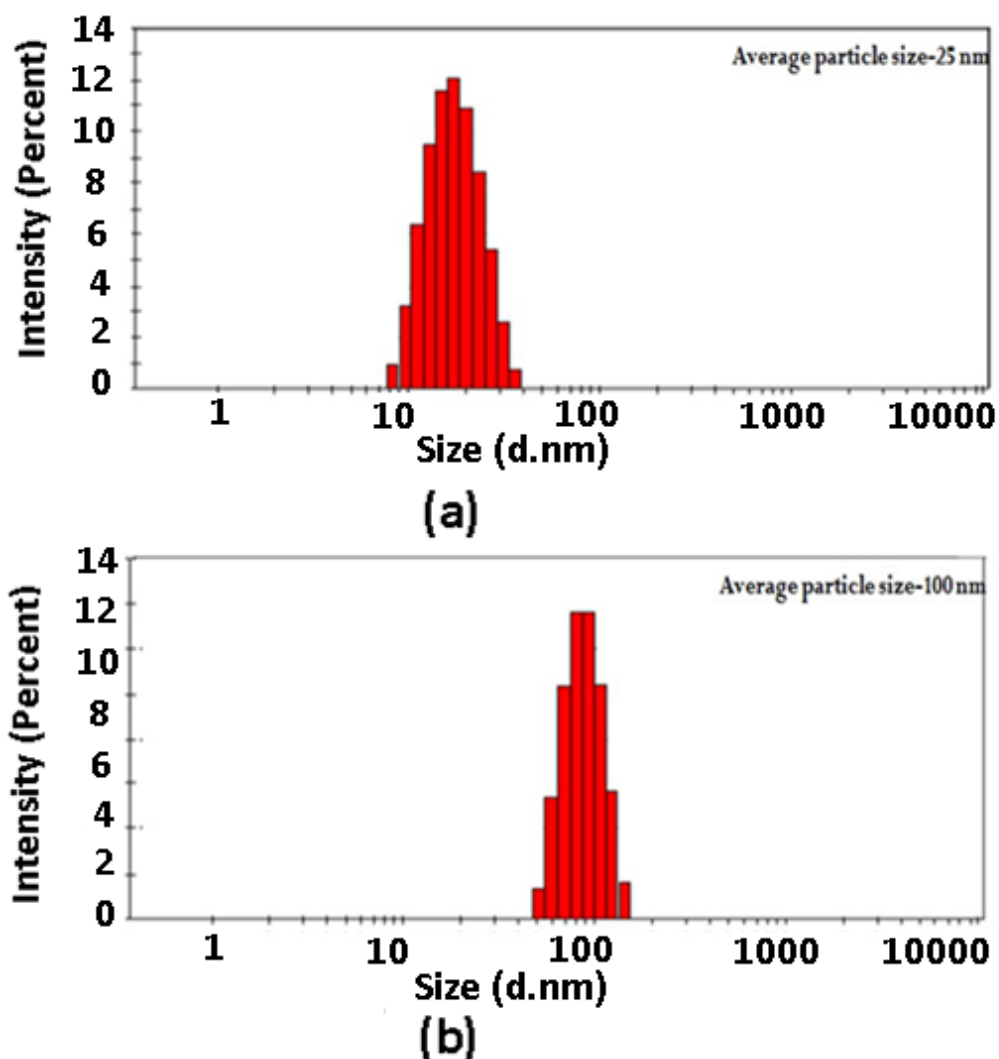
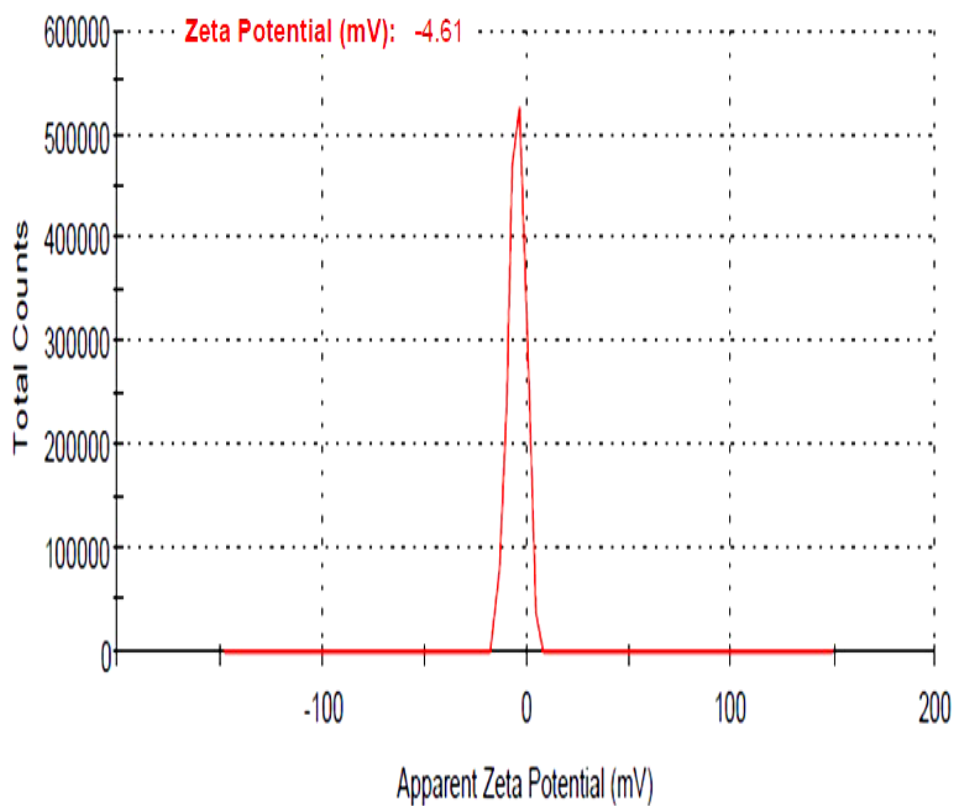


Figure-51. DLS histogram of C-SPION (a), C-SPION-NG

The zeta potential measurements of C-SPION-NG reveal surface charge of -4.61mv (Figure- 52).



**Figure-52. Zeta potential measurement of C-SPION-NG**

#### **4.2.6. Evaluation of the magneto-fluorescent characteristics of C-SPION-NG**

The EDAX analysis of C-SPION-NG revealed the presence of different elements, carbon, nitrogen, oxygen and iron (Figure-53). The analysis of magnetic separation of nanogel revealed comparable magnetic separation for both bare C-SPION and C-SPION-NG (Figure-54).

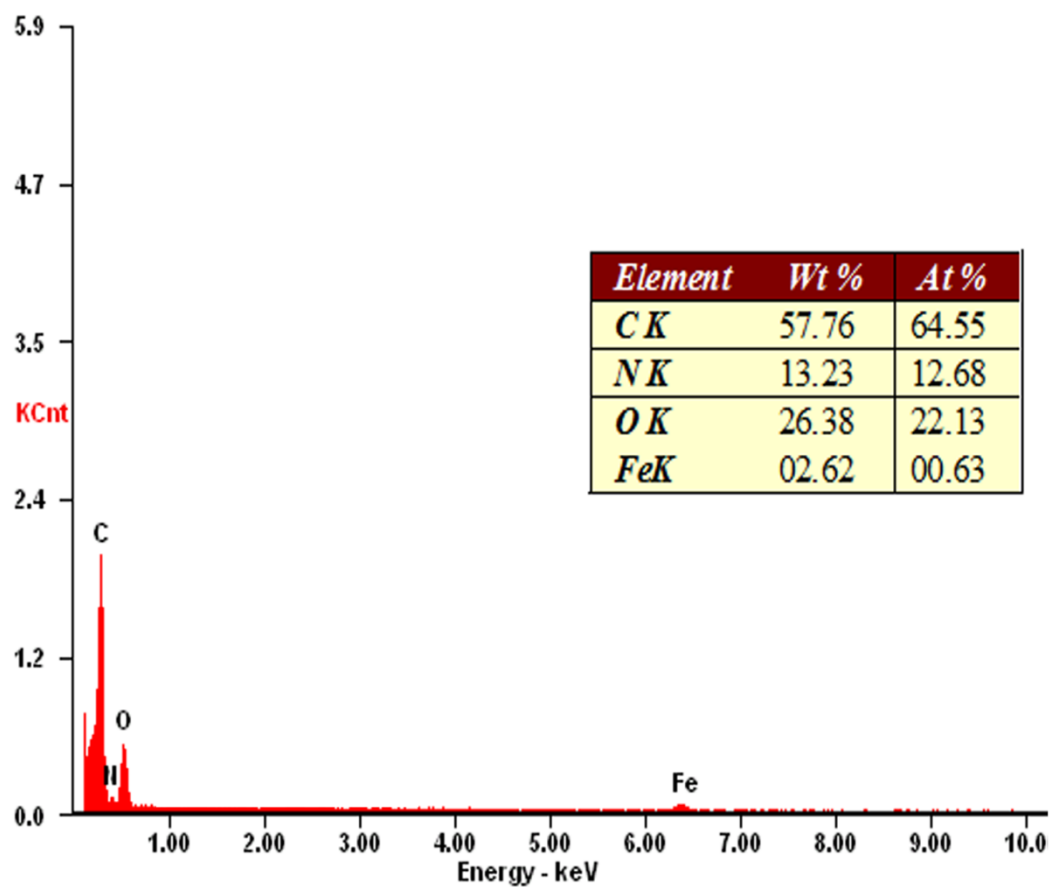


Figure-53. EDAX spectrum of C-SPION-NG

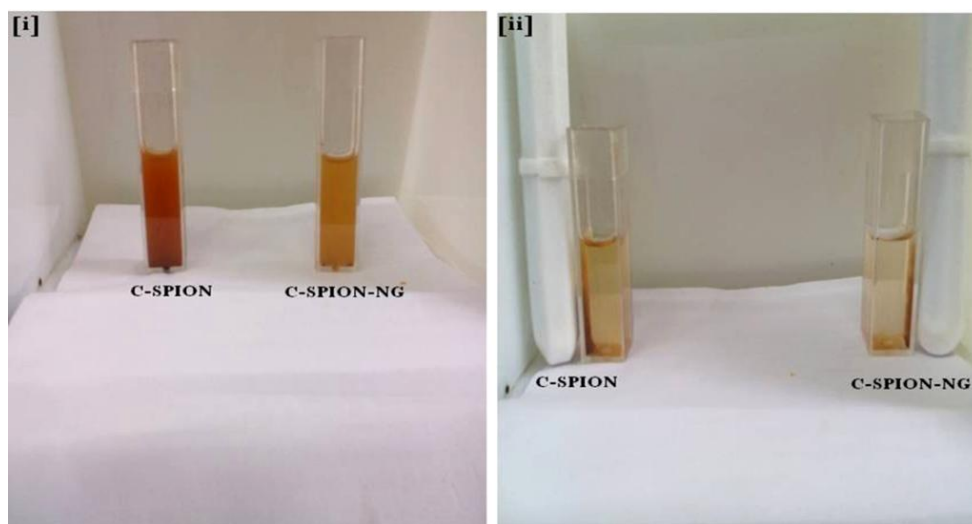
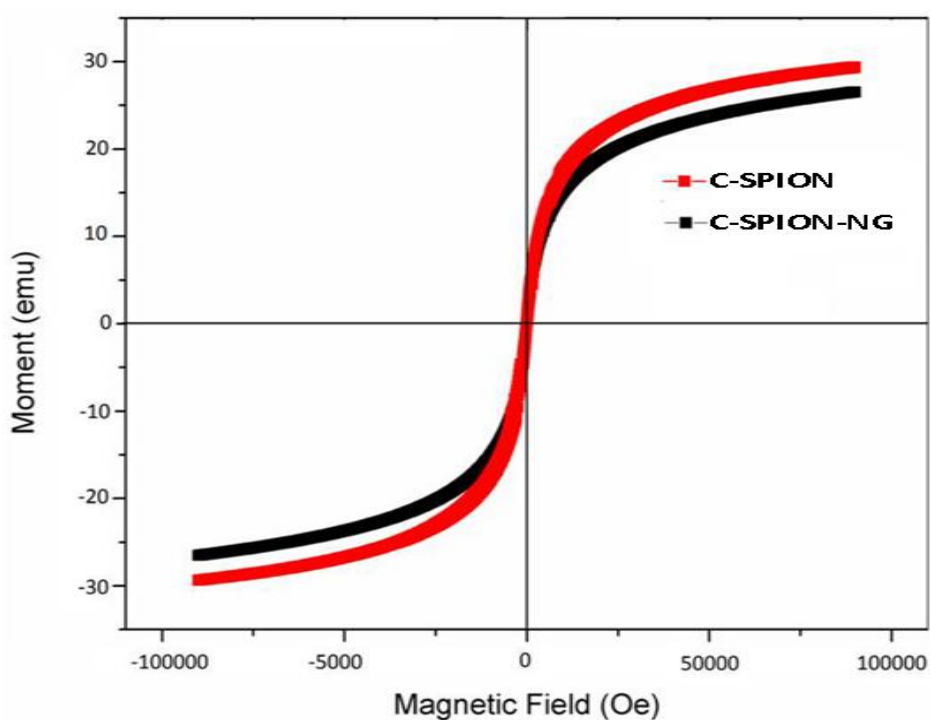


Figure-54. C-SPION and C-SPION-NG in the absence of magnetic field (i), in the presence of magnetic field (ii)

The magnetic property of C-SPION and C-SPION-NG was further evaluated through vibrating sample magnetometer (VSM) analysis. Both C-SPION and C-SPION-NG displayed superparamagnetic behaviour with magnetic saturation around 28 and 25 emu/g respectively (Figure-55). The C-SPION-NG also exhibited excitation wavelength dependent fluorescence (530-860 nm) when excited with different excitation wavelengths (500-800 nm) (Figure-56).



**Figure-55.VSM graph of C-SPION (a) and C-SPION-NG (b)**

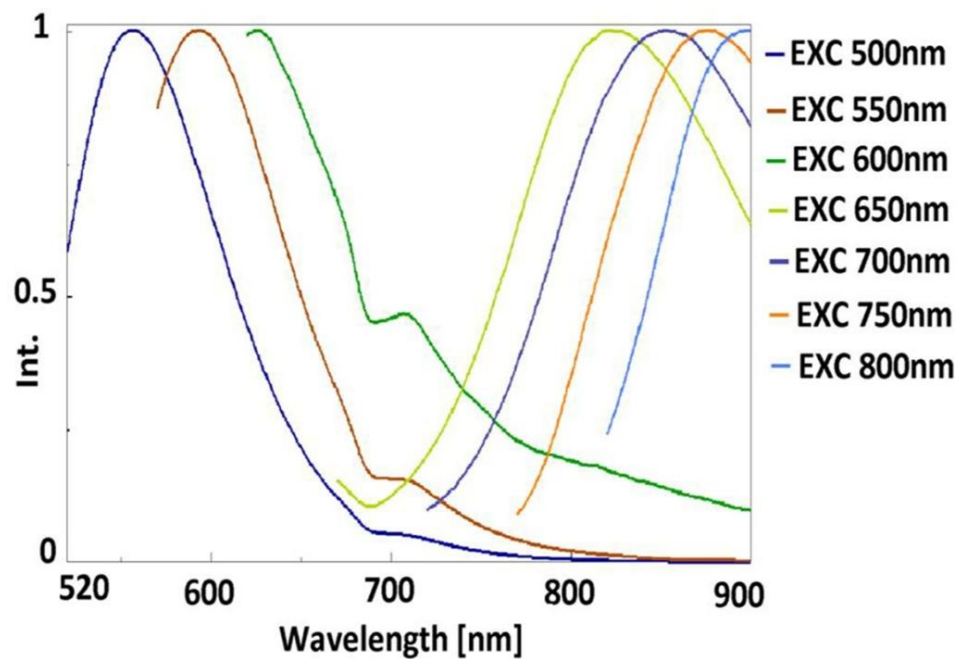


Figure-56. Excitation wavelength dependent photoluminescent spectra of the C-SPION-NG under aqueous conditions at different excitations (500-800nm)

C-SPION-NG under UV light showed bright green fluorescent emission. Once a magnetic field was applied, good magnetic separation of fluorescent particles towards the side of magnet occurred (Figure-57).

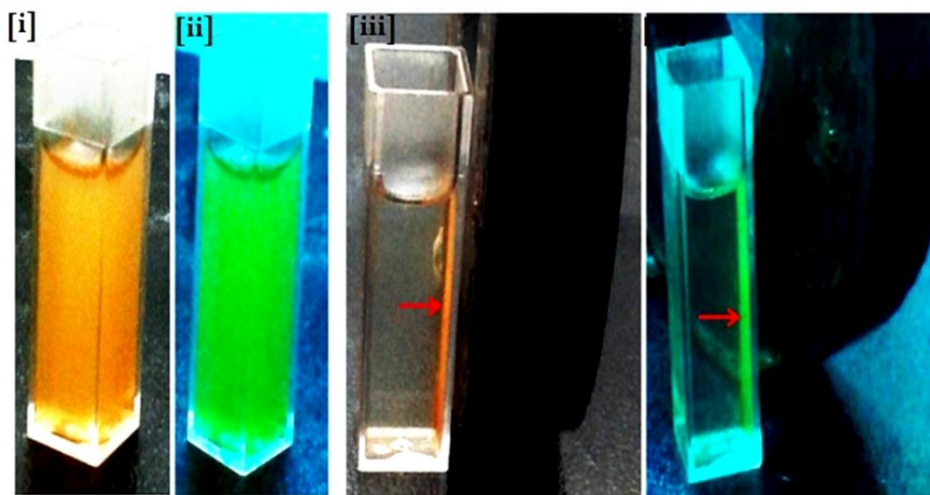


Figure-57. C-SPION-NG under normal light (i), under UV light (ii), C-SPION-NG under magnetic field (iii), C-SPION-NG under UV light and magnetic field (iv)

#### 4.2.7. Evaluation of the cyto compatibility, hemolytic potential and cellular uptake of C-SPION-NG

The cytocompatibility of both C-SPION and C-SPION-NG was studied using MTT assay. It was found that the C-SPION-NG maintained good cell viability over different range of concentrations ranging from 250-4000  $\mu\text{g}$  when compared to bare C-SPION (Figure-58).

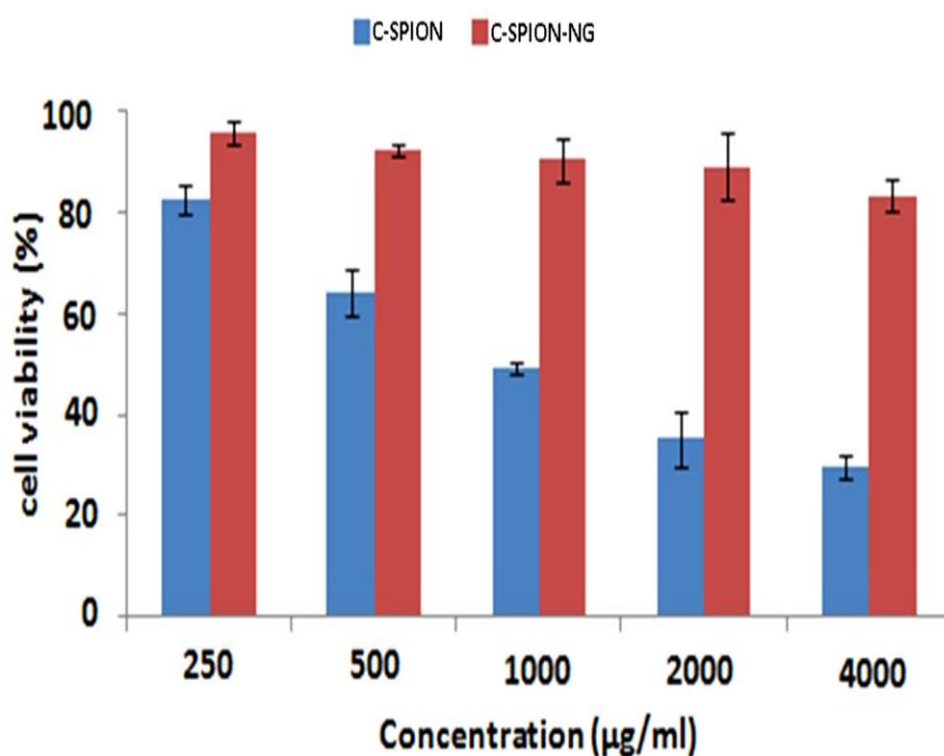
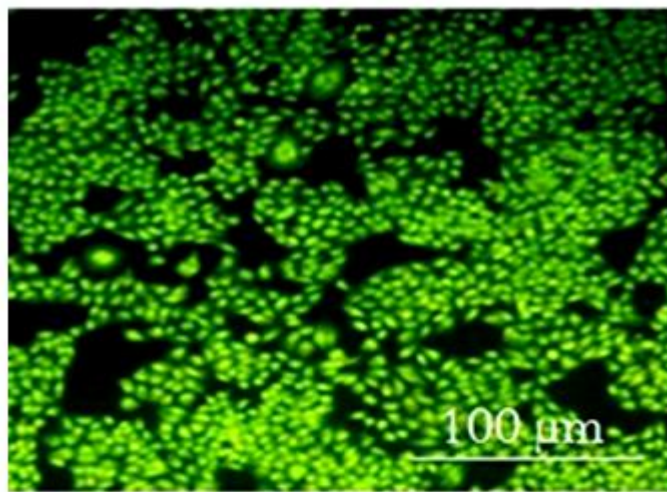
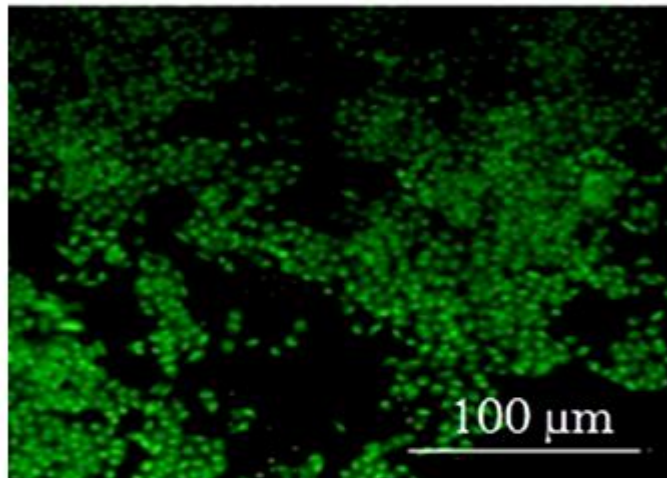


Figure-58. Cellular viability of SPION and C-SPION-NG having different concentrations (250-4000 $\mu\text{g}$ ). Data represents Mean $\pm$ SD (n=3)

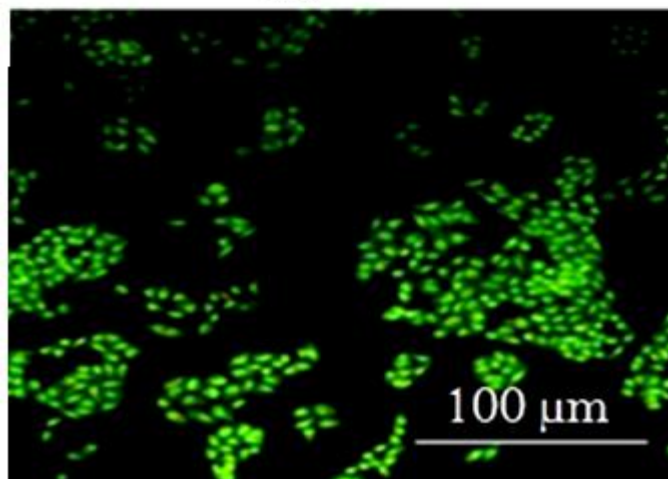
The cytocompatibility of C-SPION-NG was further evaluated with the help of live dead assay. Two different concentrations of C-SPION-NG (500 and 1000  $\mu\text{g}$ ) incubated with Hela cells exhibited predominant green emissions representing the live and viable cells (Figure-59).



(a)



(b)



(c)

**Figure-59.** Live dead assay of C-SPION-NG. Hela cells as control (a), cells treated with 500  $\mu\text{g}$  of C-SPION-NG (b), cells treated with 1000  $\mu\text{g}$  of C-SPION-NG (c)

The cell cycle analysis was evaluated further to prove the cytocompatibility of C-SPION-NG. The cell cycle analysis of C-SPION-NG (500 and 1000  $\mu\text{g}$ ) treated and untreated control samples exhibited comparable cell population especially in the G0/G1 phase (55.4 % for control and 54.6 % and 51.2% for the two tested concentrations of C-SPION-NG) (Figure-60).

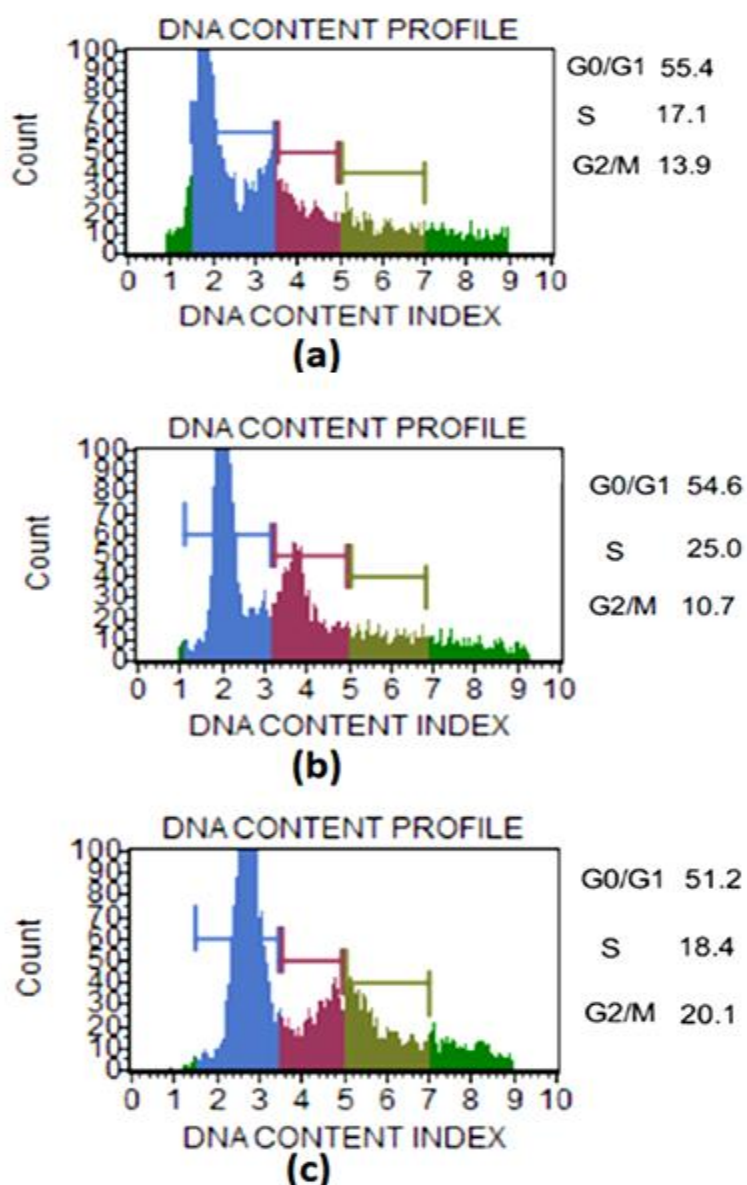


**Figure-60.** Cell cycle analysis of C-SPION-NG. Hela cells as control (a), cells treated with 500  $\mu\text{g}$  of C-SPION-NG (b) cells treated with 1000  $\mu\text{g}$  of C-SPION-NG (c)

The hemolysis studies of C-SPION-NG have shown low hemolytic percentage of 0.03 with appearance of colorless supernatant as given in Figure-61. The low percentage of hemolysis exhibited by the C-SPION-NG suggests the hemocompatibility of C-SPION-NG.

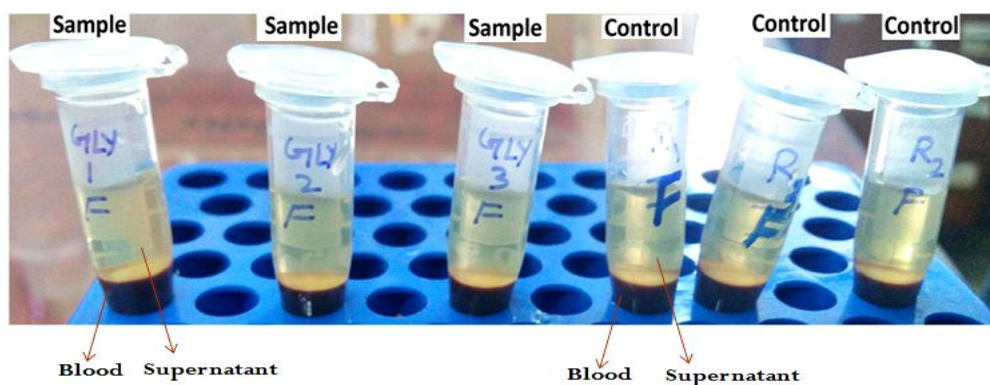


**Figure-61. Hemolysis assay of C-SPION-NG**

The cellular uptake of C-SPION-NG was evaluated with the help of Prussian blue staining. The C-SPION-NG having 2 different concentrations (500 and 1000  $\mu\text{g}$ ) internalized inside the cells were visualized as blue spots inside the cells (Figure-62).

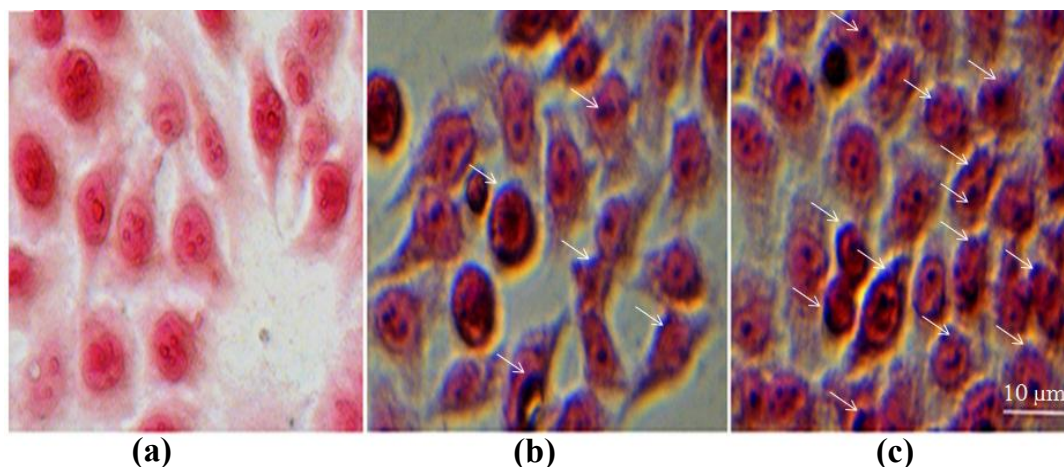


**Figure-62. Prussian blue staining of HeLa cells incubated with C-SPION-NG. Control HeLa cells (a), cells treated with 500  $\mu\text{g}$  of C-SPION-NG (b) cells treated with 1000  $\mu\text{g}$  of C-SPION-NG (c) (the blue spots shows iron present inside the cells)**

#### 4.2.8. Evaluation of the theranostic potential of C-SPION-NG

The C-SPION-NG displayed dual emissions (green and red) from HeLa cell under different excitation wavelengths (Figure-63). Thus, it was evident that the synthesized C-SPION-NG can be used for cancer cell imaging.

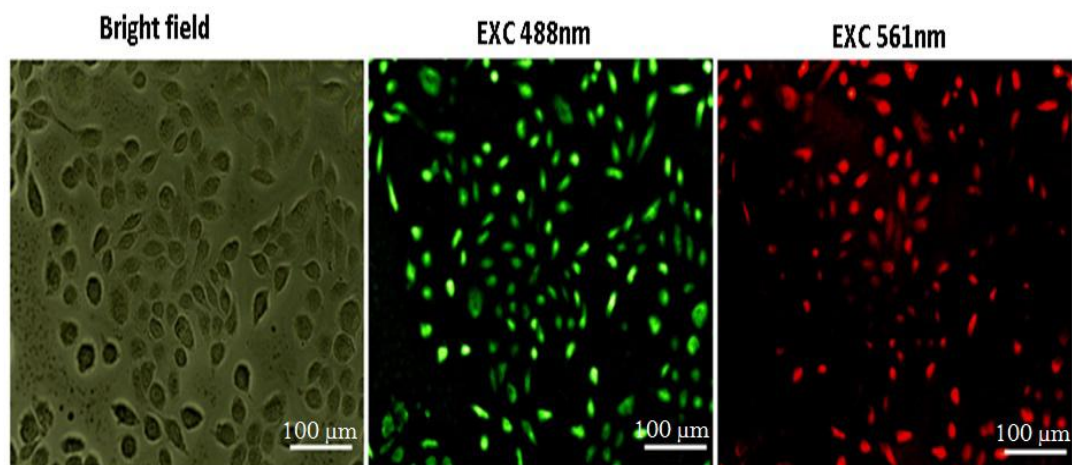
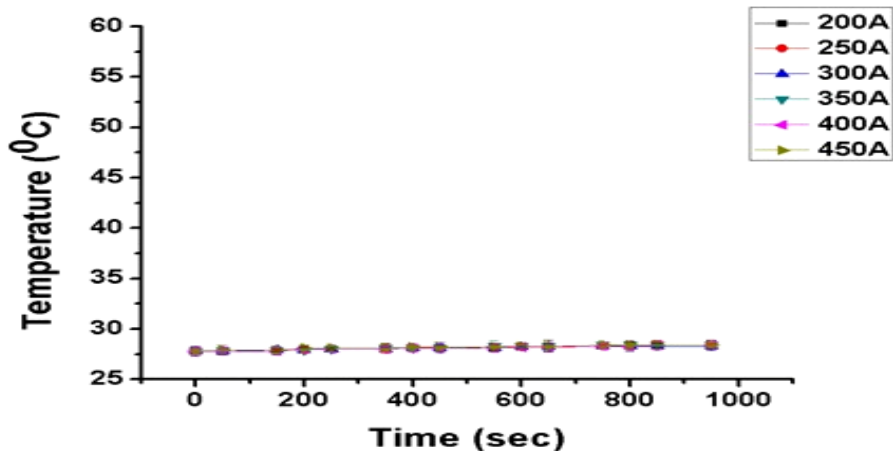
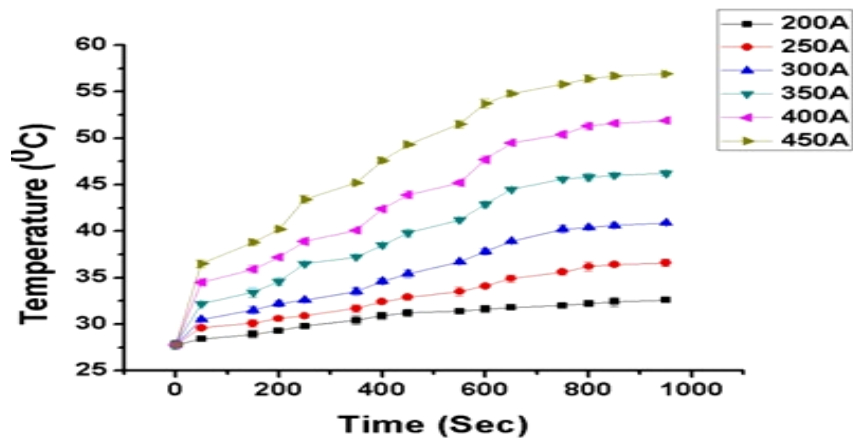


**Figure- 63: Fluorescent microscope images showing uptake in HeLa cells with C-SPION-NG (b).Observed with FITC filter and Texas red filter**

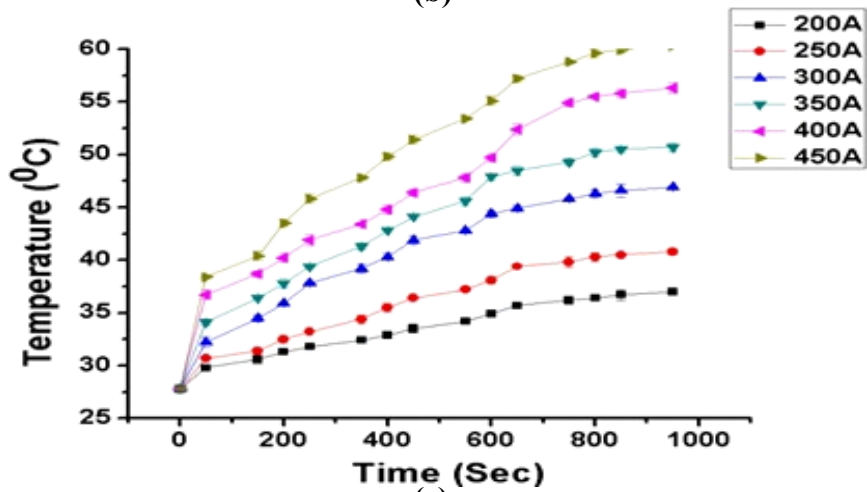
The therapeutic potential of C-SPION-NG was evaluated through the magnetic hyperthermia studies. The temperature generation efficiency of this probe was studied by analyzing the magnetic hyperthermia capability of C-SPION-NG. The C-SPION-NG having 2 different concentrations (2 mg/ml and 4 mg/ml) were checked for temperature generation capability under alternating magnetic field. C-SPION-NG has generated temperature 56<sup>0</sup> and 61<sup>0</sup>C for the concentrations 2 mg/ml and 4 mg/ml respectively. The distilled water, which is used as the control, has not increased temperature beyond 27<sup>0</sup> C under alternating magnetic field (Figure-64).



(a)



(b)

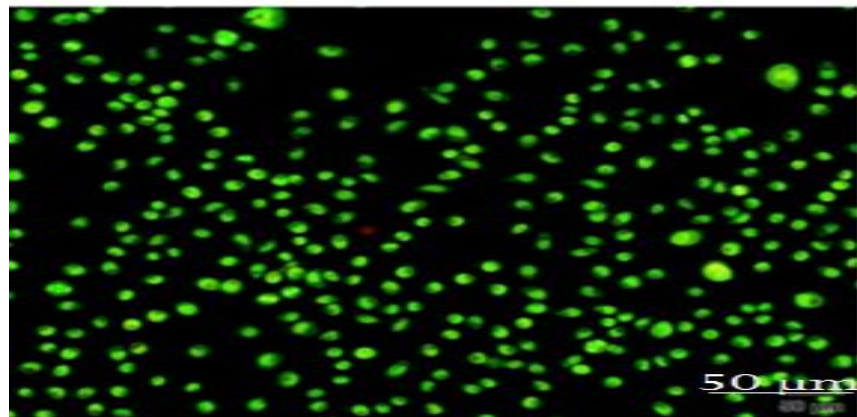


(c)

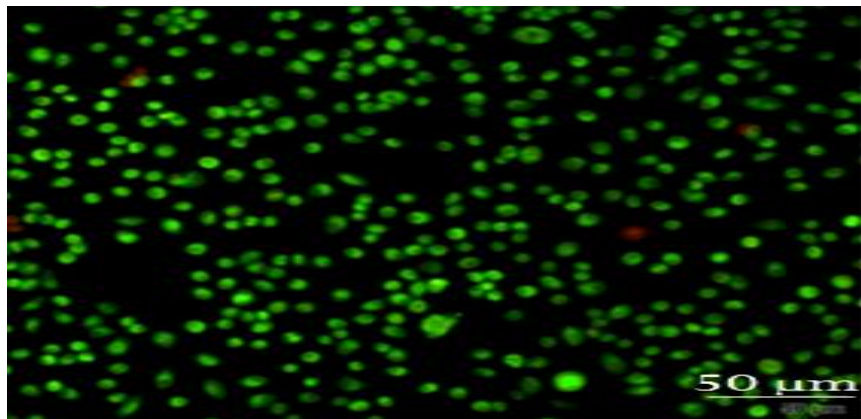
Figure-64. Magnetic hyperthermia curves of distilled water (a),  
2 mg/ml C-SPION-NG (b), 4mg/ml C-SPION-NG (c)

The magnetic hyperthermia capability of C-SPION-NG was demonstrated through live dead assay. The C-SPION-NG incubated cells treated with

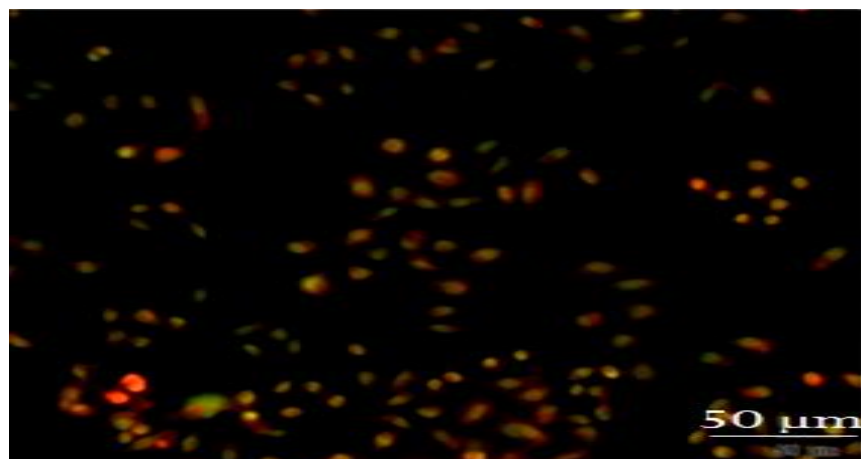
alternating magnetic field has shown significant cell death, where as the untreated cells were showing significant cell viability (Figure-65).



(a)



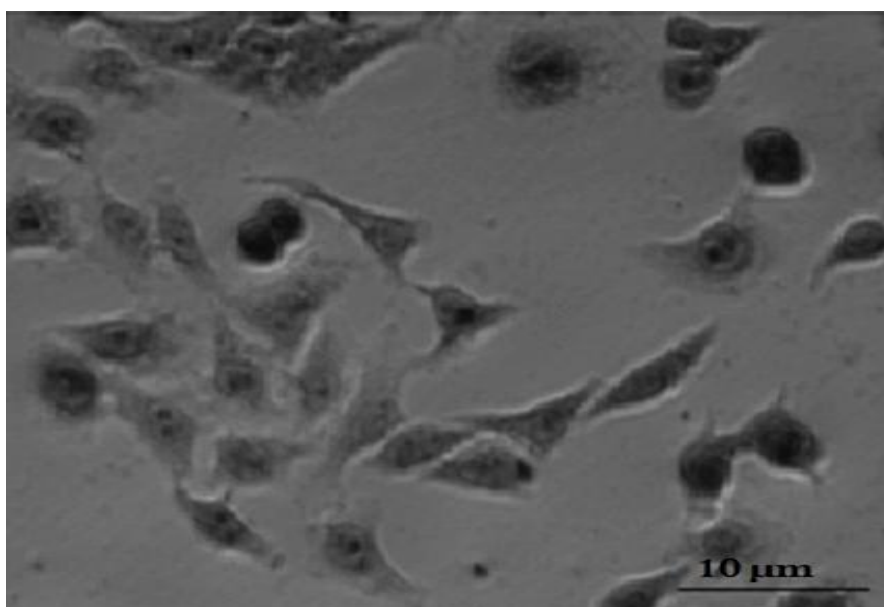
(b)



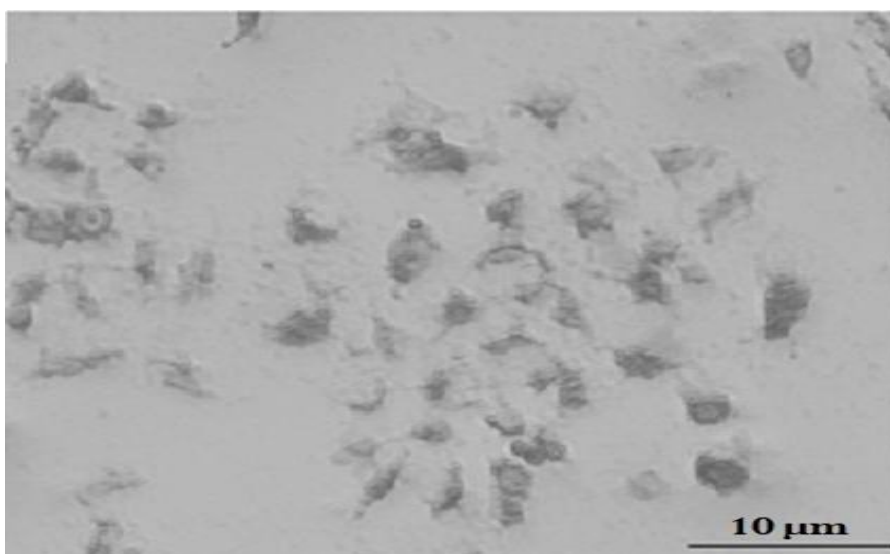
(c)

**Figure-65. Live dead assay of magnetic hyperthermia treated HeLa cells. Control HeLa cells (a), HeLa cells incubated with C-SPION-NG without alternating magnetic field (b), HeLa cells incubated with C-SPION-NG with alternating magnetic field (c)**

The phase contrast images of the hyperthermia-treated cells have shown irregular morphology when compared to the normal cells, which clearly suggests the therapeutic potential of the synthesized C-SPION-NG (Figure- 66).



(a)



(b)

**Figure-66. Phase contrast microscope images of control HeLa cells (a), HeLa cells treated with alternating magnetic field (b)**

#### 4.2.9. Evaluation of the bioimaging, biodistribution and biocompatibility of C-SPION-NG

The EDF property of the C-SPION-NG was exploited for bioimaging. The subcutaneously injected C-SPION-NG in mice has shown very interesting excitation wavelength dependent near IR emission (Figure-67).

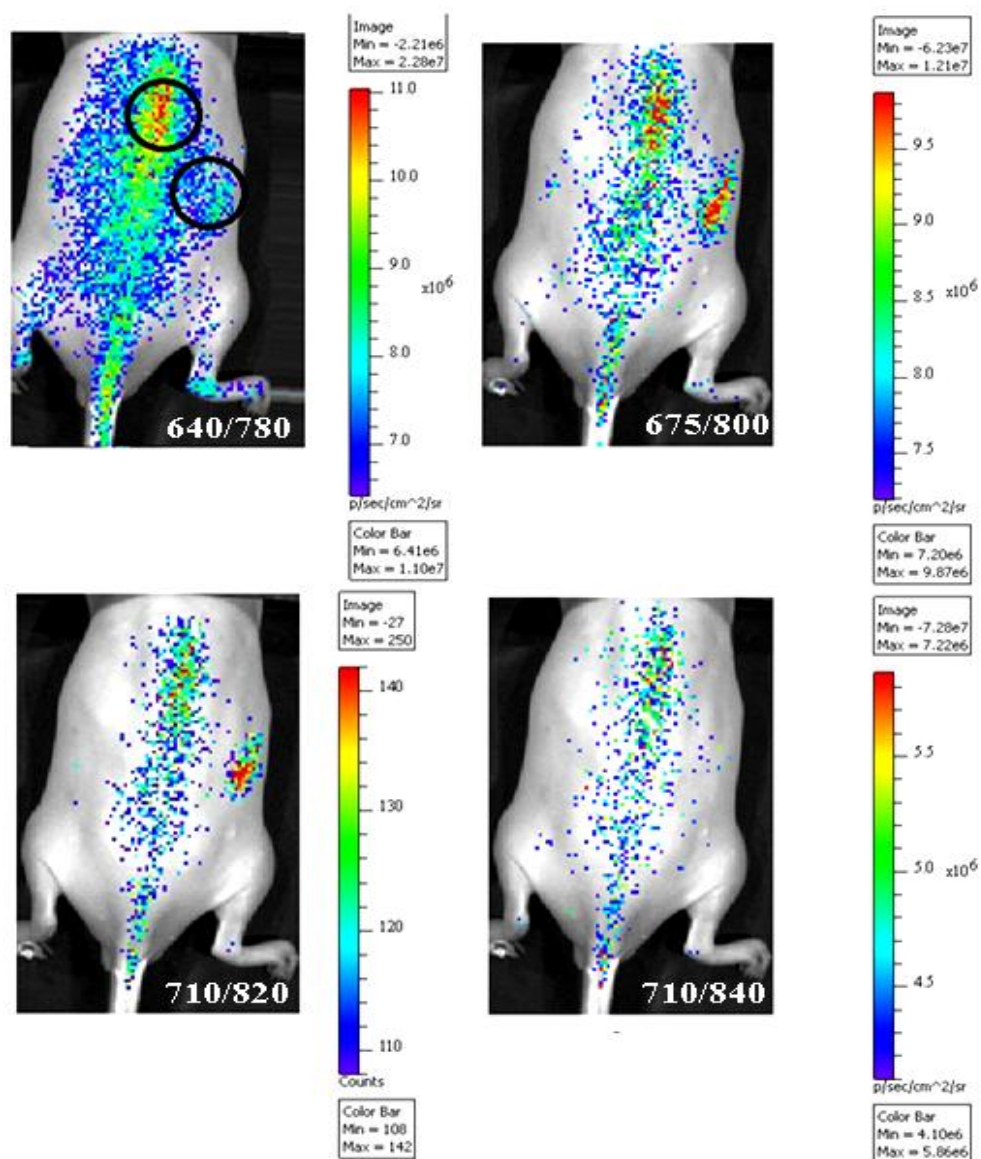
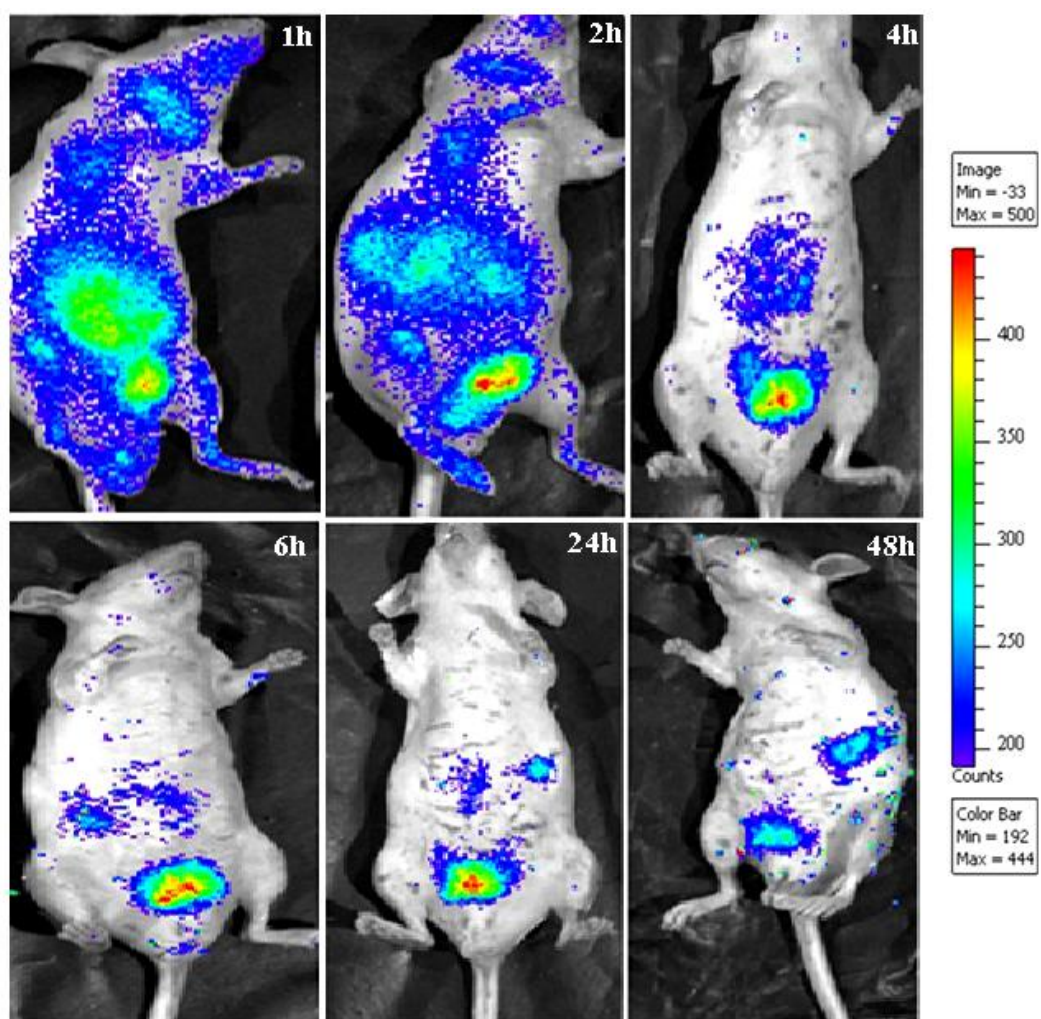


Figure-67. *In vivo* fluorescence bioimaging capability of mice using different excitation and emission wavelengths (the circled areas show the position of injected area and bottom of images shows the excitation and emission wavelengths used)

Different excitations (640,675 and 710nm) were used and emissions at near IR region (780,800,820 and 840 nm) were captured. The studies on biodistribution in mice with C-SPION-NG revealed gradual decrease of fluorescence signals from the animal body during 48 h and complete removal of the nanogel after 48h from the body (Figure-68).



**Figure-68. Biodistribution of intravenously injected C-SPION-NG in mice at different time points (the excitation/ emission used for imaging is 675/800 nm)**

The histopathology evaluations of organs such as liver, heart and kidney carried out revealed nontoxic profile of C-SPION-NG with normal tissue morphology (Figure-69).

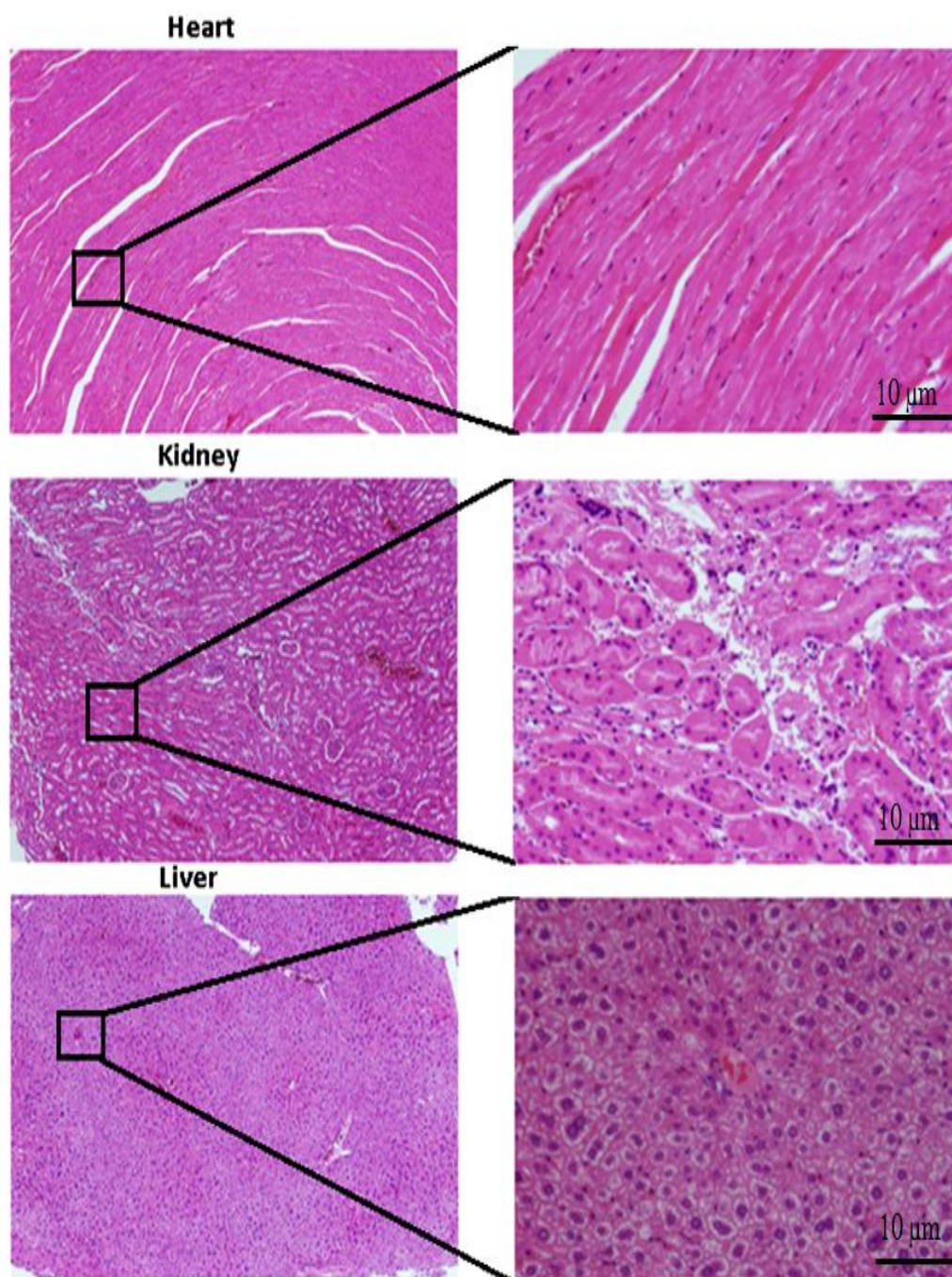


**Figure-69. H&E stained images of organs of mice at 48h post injection**

### ***4.3 Studies on actively targeted nanogel for theranostic applications***

#### **4.3.1. Preparation and structural characterization of photoluminescent comonomer PEG-Maleic acid-benzoic acid (PMB) and octreotide conjugated nanogel (PMB-OctN)**

A targeted nanogel, PMB-OctN, based on photoluminescent comonomer (PMB), diethyleneglycoldimethacrylate and octreotide was designed for theranostic applications. The scheme of the synthesis of PMB-OctN is given in Figure-70. The PMB comonomer was synthesized by polycondensation reaction of PEG, maleic acid and 4-aminobenzoic acid. The unconjugated nanogel (PMB-N) was synthesized by crosslinking the photoluminescent comonomer with diethyleneglycoldimethacrylate. The octreotide conjugated nanogel (PMB-OctN) was prepared by coupling carboxylic acid groups which are available on the PMB-N with the amino groups of octreotide via EDC coupling reaction.

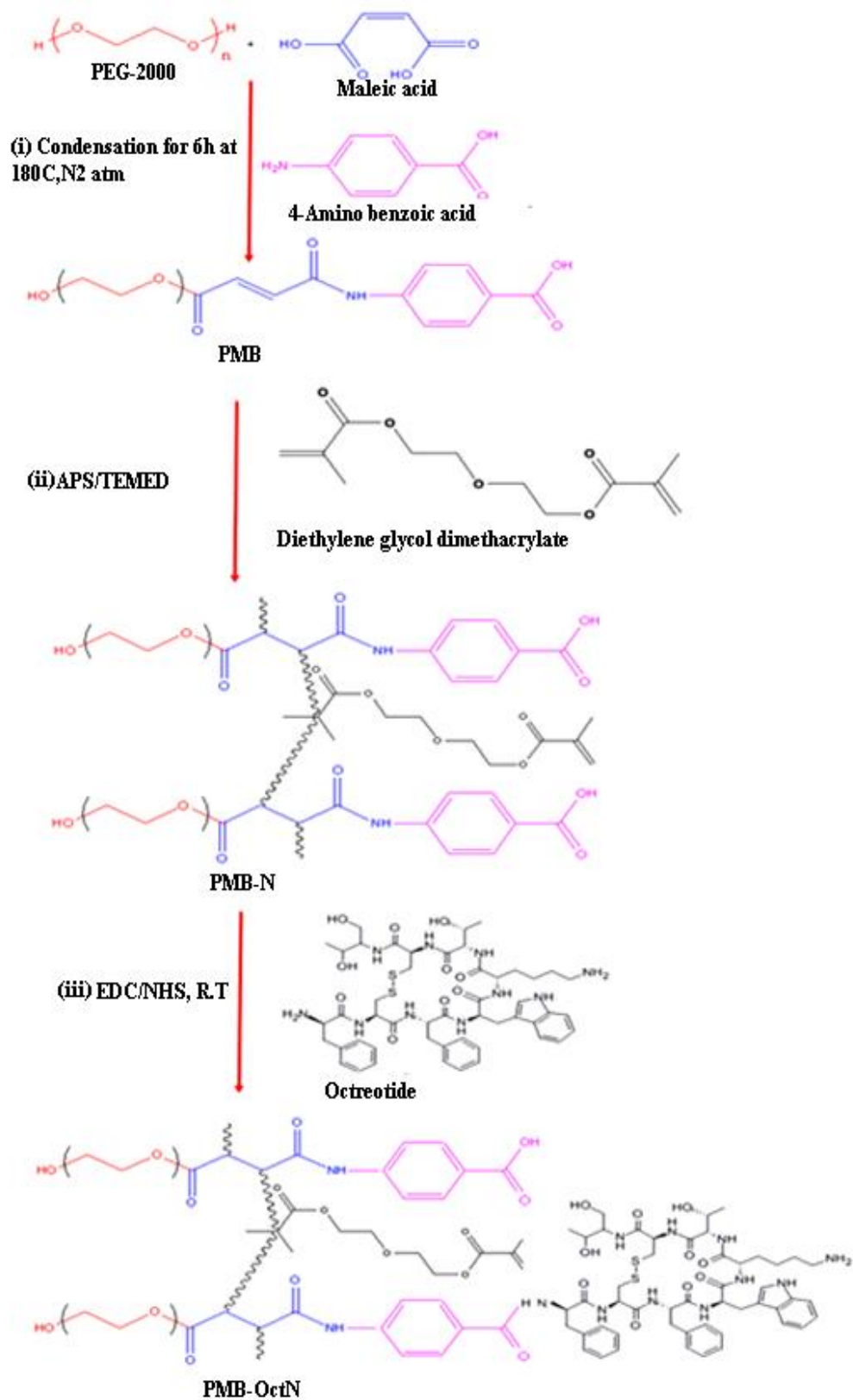
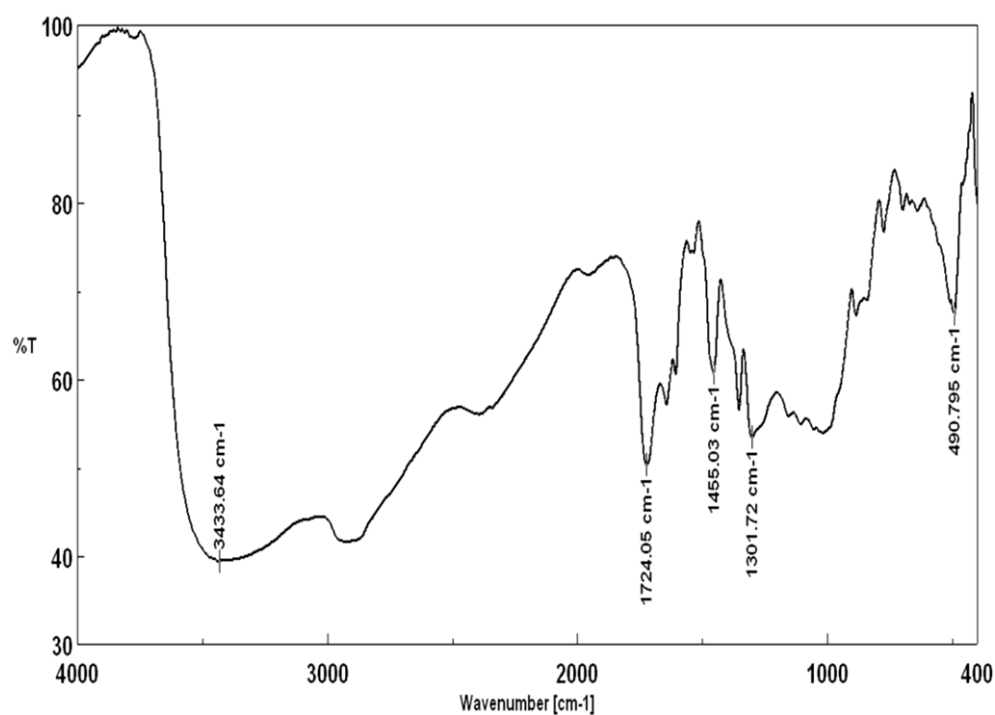
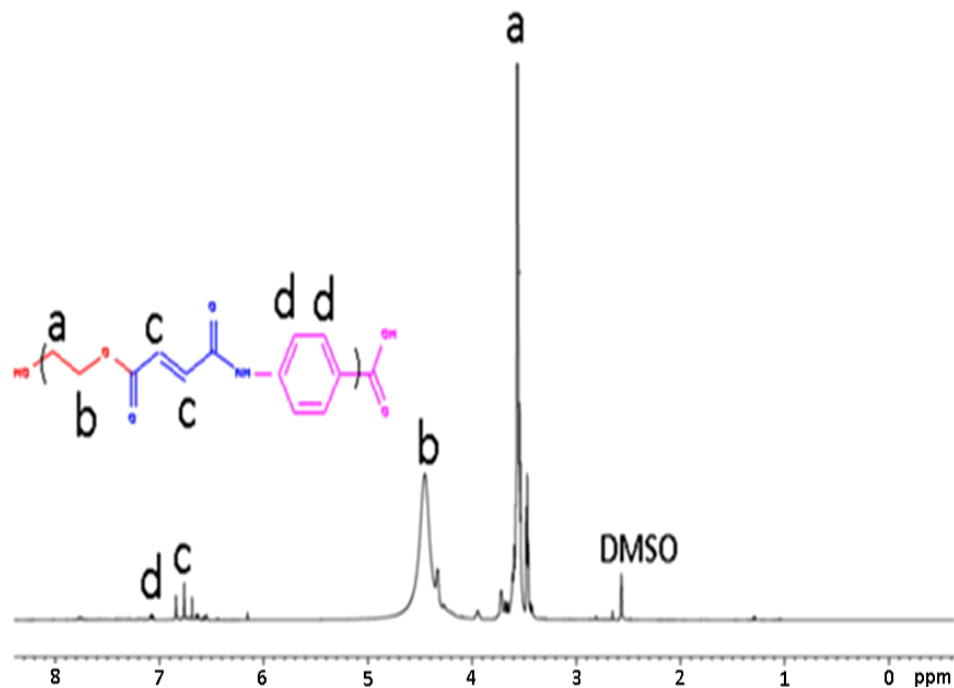


Figure-70. Synthesis scheme of photoluminescent comacromer (PMB) and octreotide-conjugated nanogel (PMB-OctN)

The structure of photoluminescent comacromer, PMB was evaluated with FTIR spectrum (Figure-71). The spectral analysis reveals peaks at  $3433\text{ cm}^{-1}$  (-OH stretching vibrations of PEG),  $1724\text{ cm}^{-1}$  (ester linkages (O-C=O) of the PMB),  $1644\text{ cm}^{-1}$  (C=C stretching of CH=CH- bond of maleic acid units of PMB),  $1455\text{ cm}^{-1}$  (aromatic C=C stretching vibrations of aminobenzoic acid units of PMB) and  $1352\text{ cm}^{-1}$  (C-C and C-O stretching of ester linkages).  $^1\text{H}$  NMR spectral analysis was carried out to confirm the structure of PMB (Figure-72).  $^1\text{H}$  NMR spectrum of PMB reveals peaks at 7.2 ppm (aromatic protons of aminobenzoic acid units of PMB), 6.8 ppm (double bonds CH=CH of maleic acid units of PMB), and 3.4 ppm (-CH<sub>2</sub> groups from PEG units of PMB). Thus, FTIR and proton NMR spectra substantiated the formation of PMB comacromer.



**Figure-71. FTIR Spectral analyses of the PMB comacromer**



**Figure-72.  $^1\text{H}$  NMR spectra Spectral analyses of the PMB comacromer**

The molecular weight of the comacromer, PMB is  $M_n$  3294,  $M_w$  4393 and polydispersity index of 1.33. Thus, molecular weight analysis of the comacromer reveals the macromeric nature of the synthesized comacromer.

The FTIR spectrum of octreotide conjugated nanogel, PMB-OctN reveals strong peak at  $1641\text{ cm}^{-1}$  for  $-\text{N}-\text{H}-$  bond and additional band at  $1025\text{--}1200\text{ cm}^{-1}$  for C-N stretch of  $\text{NH}_2$  groups and at  $800\text{ cm}^{-1}$  for N-H bend of  $\text{NH}_2$  groups along with  $1718\text{ cm}^{-1}$  (O-C=O linkages of the PMB-N) and  $2916\text{ cm}^{-1}$  ( $-\text{CH}_2$  groups of PEG units of the PMB-N) (Figure-73).

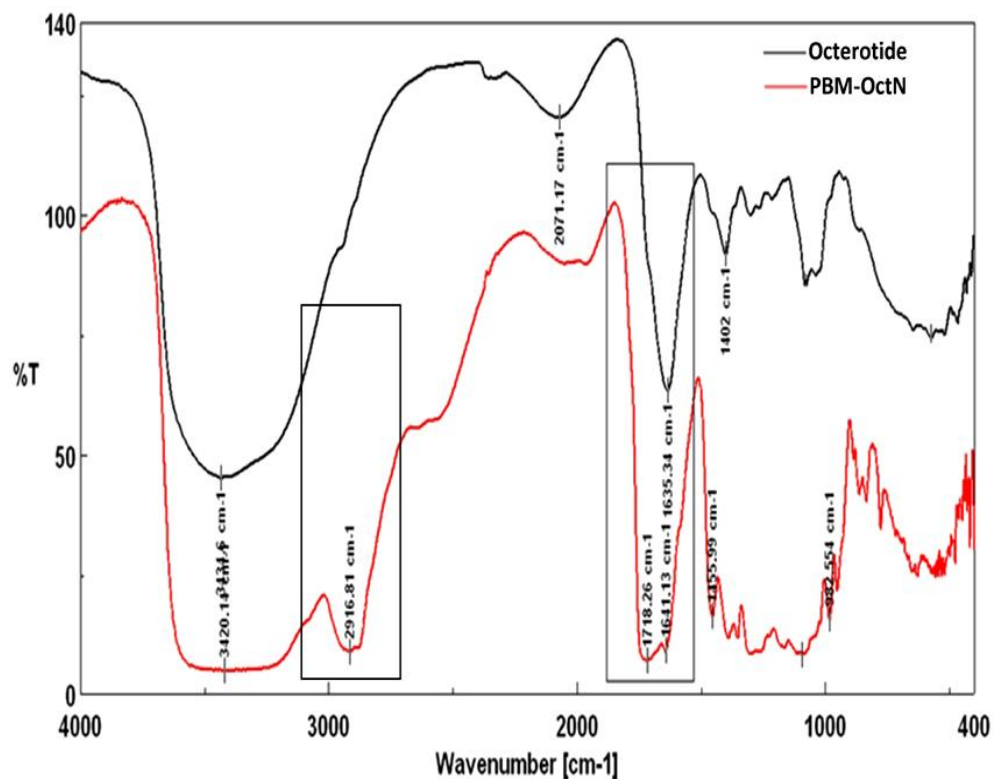


Figure-73. FTIR spectra of the octreotide and PMB-OctN

#### 4.3.2. Evaluation of the photoluminescence properties of the PMB comacromer

The PMB comacromer has displayed excitation wavelength dependent fluorescence characteristics. The comacromer exhibited multiple emissions (534 nm-825 nm) when excited with different excitation wavelengths (460-800 nm) (Figure-74). The three dimensional photoluminescent contour plots substantiated the visible to near IR emission characteristics of the comacromer (Figure-75).

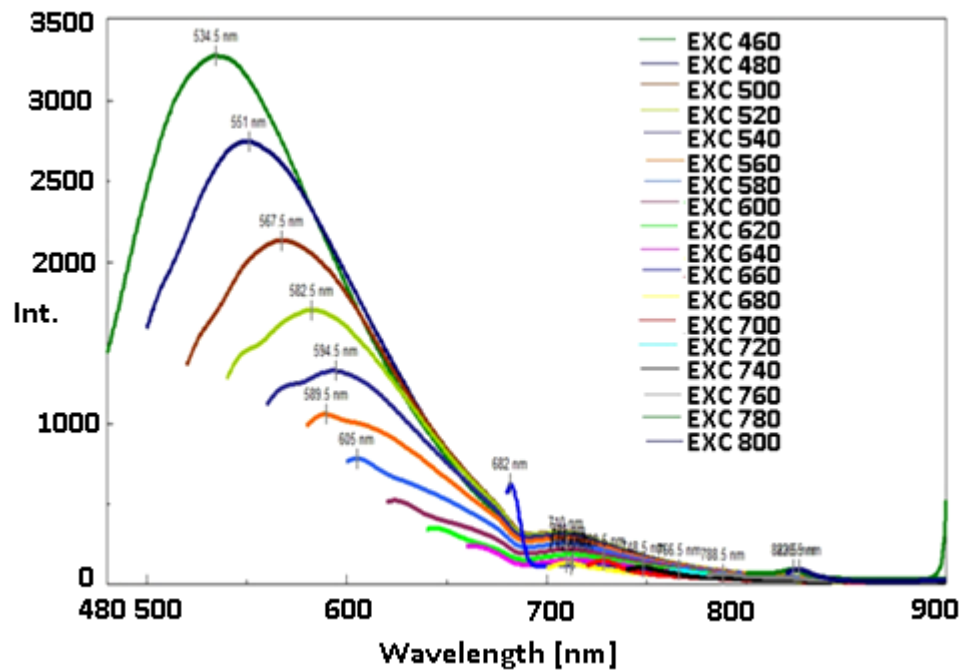


Figure-74. Excitation wavelength dependent photoluminescent spectra of the PMB under aqueous conditions at different excitations on visible region (460-800nm)

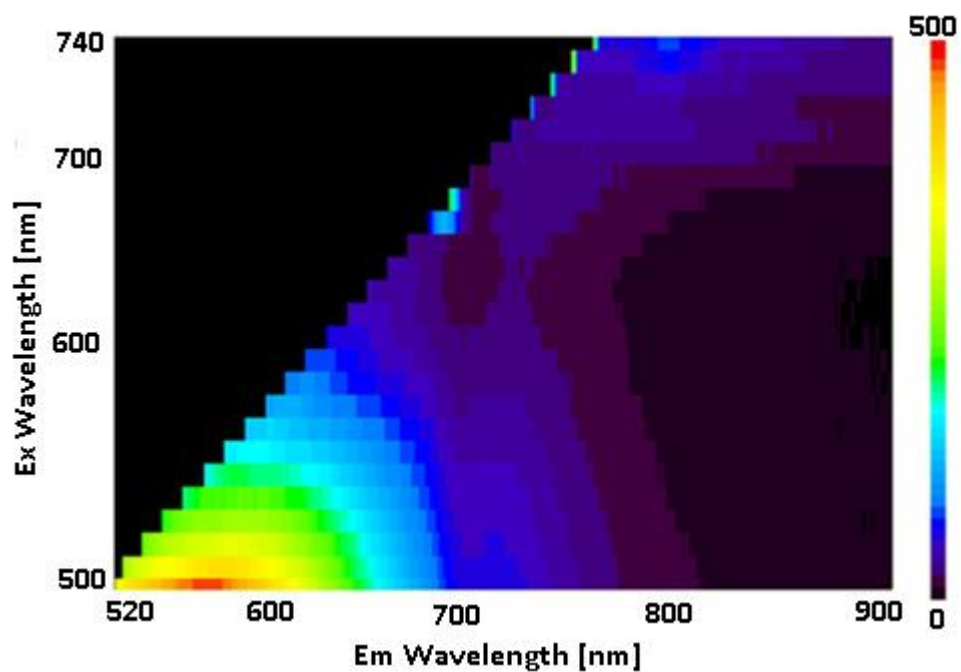


Figure-75. Three dimensional photoluminescent contour plot of the PMB

The fluorescent lifetime of the PMB was evaluated. The PMB was following a diexponential decay pathway with fluorescent lifetime value of 8

nanoseconds (Figure-76). The photostability of the PMB was evaluated. The synthesized PMB exhibited good photostability without any significant decrease in fluorescence intensity for a period of 30 minutes continuous irradiation (Figure-77).

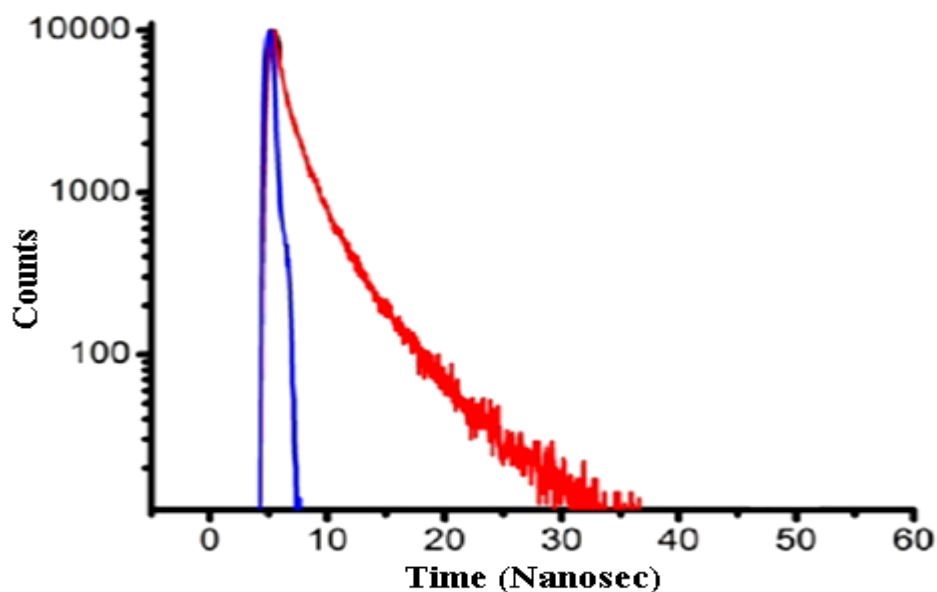


Figure-76. Photoluminescence life time of PMB ( $\lambda_{\text{ext}}$  : 440 nm &  $\lambda_{\text{emiss}}$  : 540 nm)

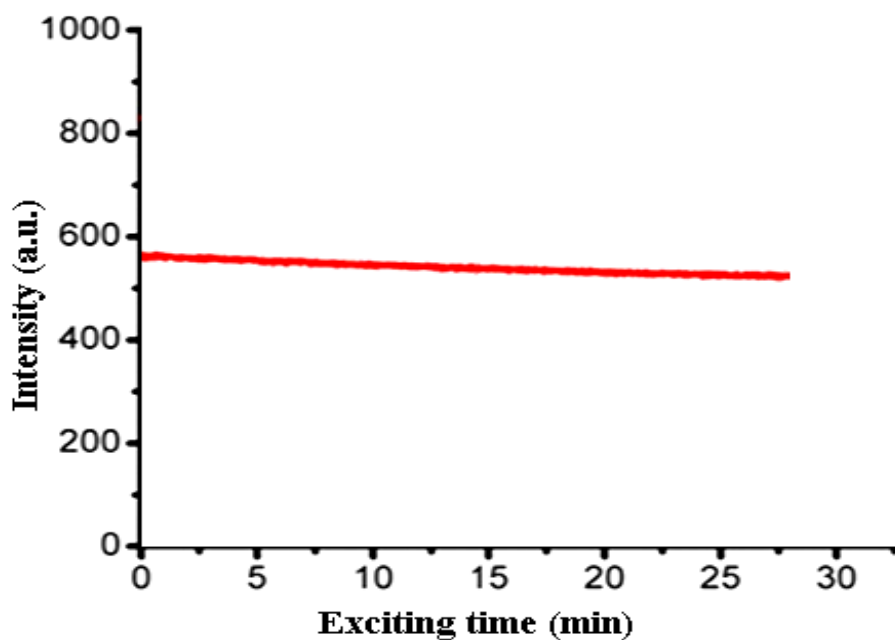


Figure-77. Photostability graph of the PMB ( $\lambda_{\text{ext}}$  : 420 nm &  $\lambda_{\text{emiss}}$  : 525 nm)

### 4.3.3. Evaluation of size, morphology and surface charge of PMB-OctN

The conjugated nanogel PMB-OctN was spherical in shape with average particle size around 110 nm (Figure-78a). The dynamic light scattering measurements of the PMB-OctN revealed average hydrodynamic size of 145 nm (Figure-78b).

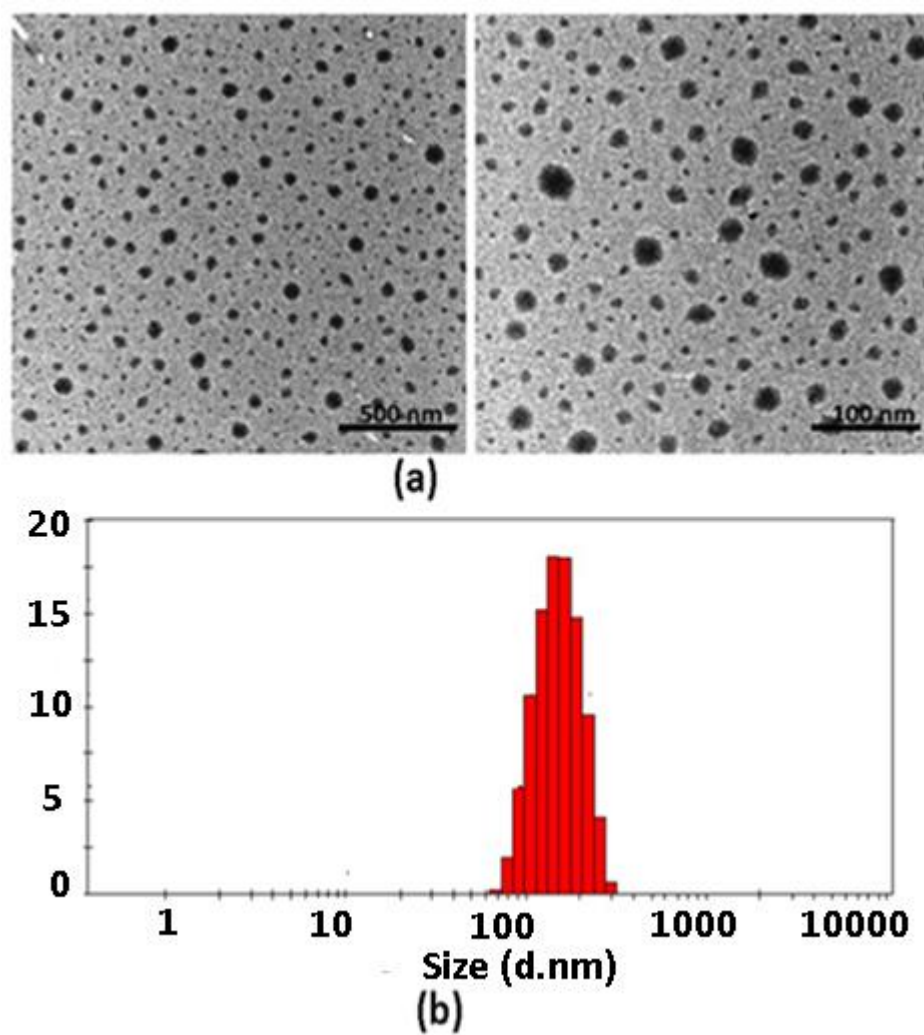
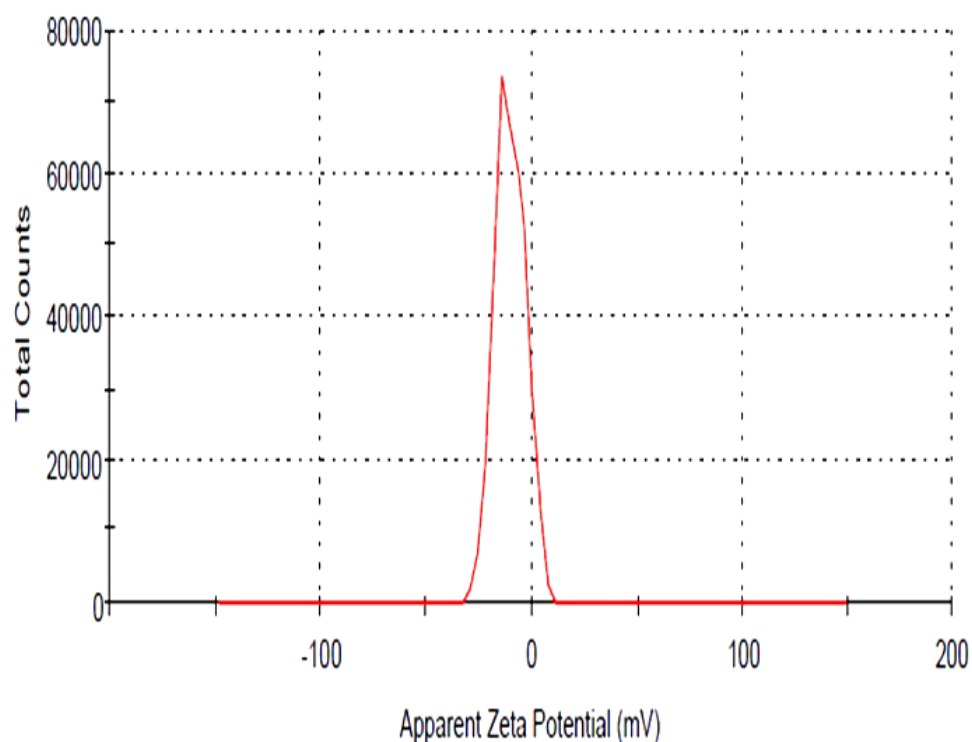


Figure-78. Transmission electron microscope (TEM) images of PMB-OctN (under different magnifications) (a), Dynamic light scattering (DLS) histogram of PMB-OctN (b)

The surface charge of the PMB-OctN measured through zeta potential measurement has shown a negative charge of -9 mv (Figure-79).



**Figure-79. Zeta potential measurement of PMB -OctN**

#### **4.3.4. Evaluation of drug release, therapeutic capability and hemolytic potential of PMB-OctN**

Doxorubicin was loaded inside the PMB-OctN. The loading efficiency was found to be 78 % for PMB-OctN. The studies on the drug release profile of the PMB-OctN reveal steady drug release and reached up to 50% within 48 h followed by a sustainable release of DOX till 120 h (Figure-80). The MTT assay has shown that the PMB-OctN is non-toxic at different concentrations ranging from 1000-4000  $\mu\text{g/ml}$  (Figure-81). The PMB-OctN loaded with doxorubicin having similar concentrations of PMB-OctN show decreased cell viability; this

trend of decreasing cell viability continues with increase in PMB-OctN concentration.

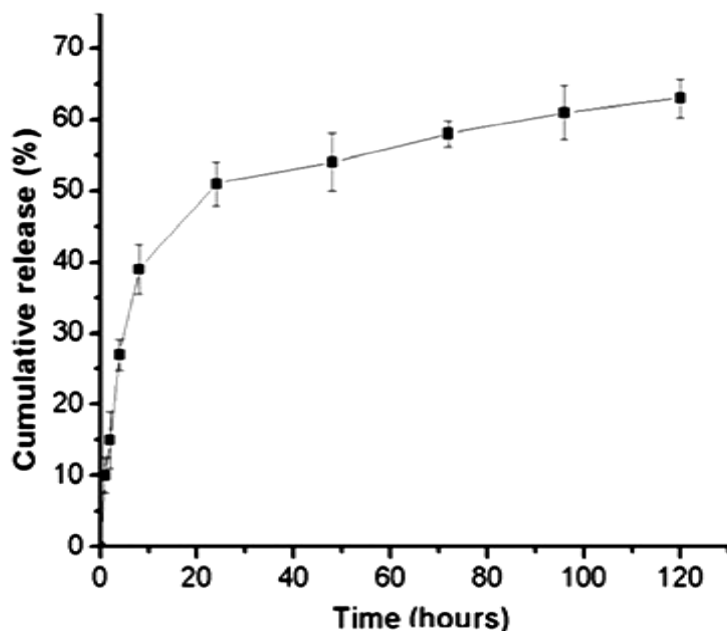


Figure-80. Doxorubicin release profile from PMB-OctN

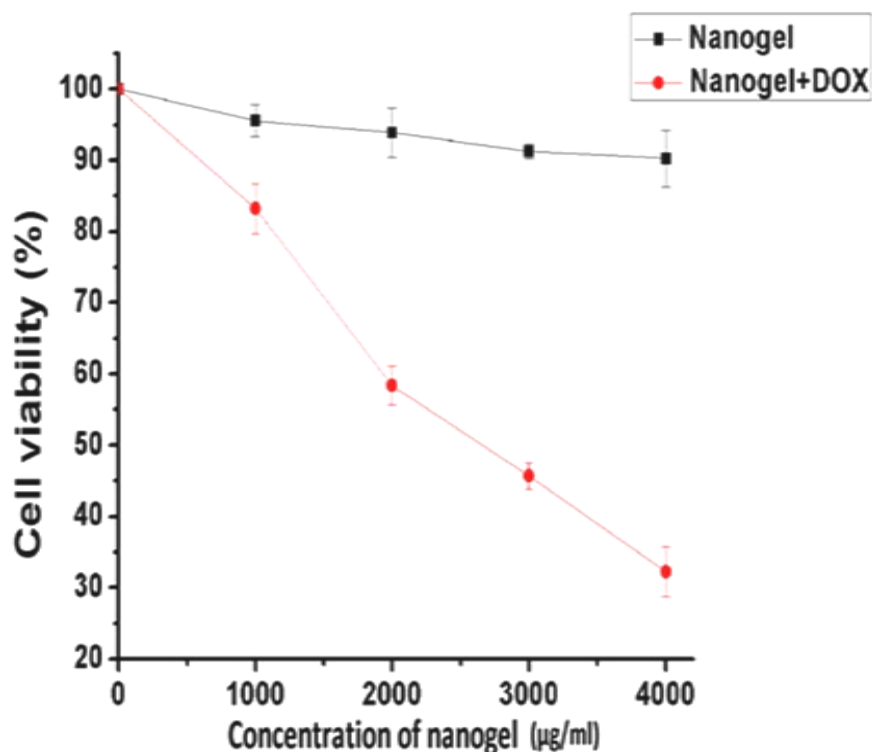
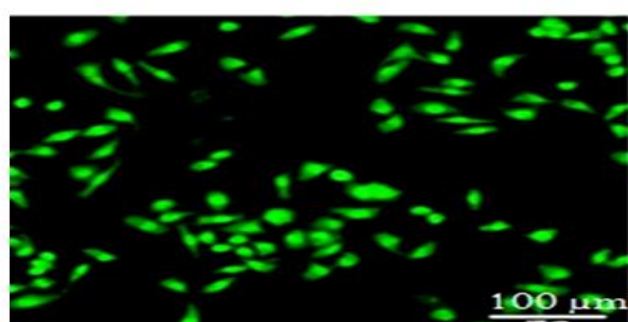
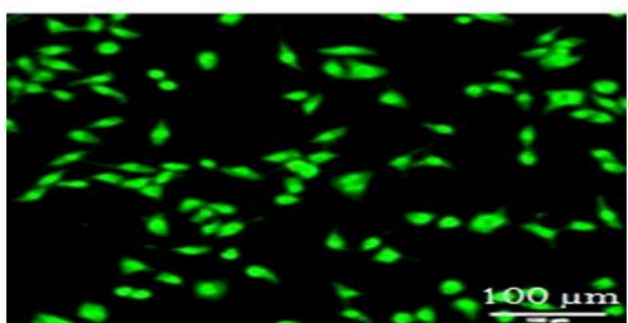


Figure-81. Cell viability of PMB-OctN and doxorubicin-loaded PMB-OctN

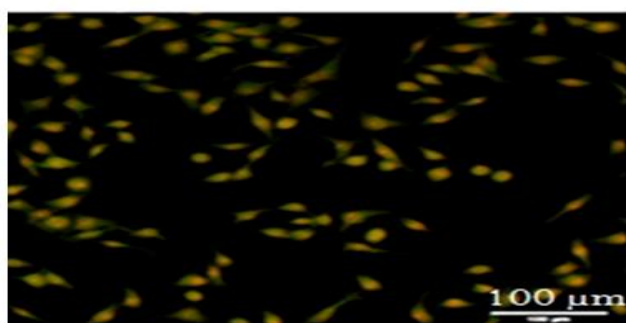
The cell apoptotic activity of the PMB-OctN in the presence and absence of doxorubicin was further evaluated through live dead cell analysis. The PMB-OctN loaded with doxorubicin has shown significant apoptotic activity and resulted in orange fluorescence from the cells suggesting the apoptotic death of cancer cells (Figure-82). The PMB-OctN without doxorubicin has shown comparable viable green fluorescing cells as that of the untreated control group.



(a)



(b)



(c)

**Figure-82.** Live dead assay of PMB -OctN and doxorubicin-loaded PMB -OctN. Untreated HeLa cells as control (a), HeLa cells treated with PMB -OctN (b), HeLa cells treated with doxorubicin-loaded PMB -OctN (c)

From the cell cycle analysis, it is evident that the PMB-OctN without doxorubicin showed cell proliferation comparable to that of untreated control group (Figure-83). The PMB-OctN loaded with doxorubicin show cell cycle arrest especially in the population of the G2/M phase. The cell population in the G2/M phase of the PMB-OctN loaded with doxorubicin is significantly lower when compared to PMB-OctN without doxorubicin and untreated control group.

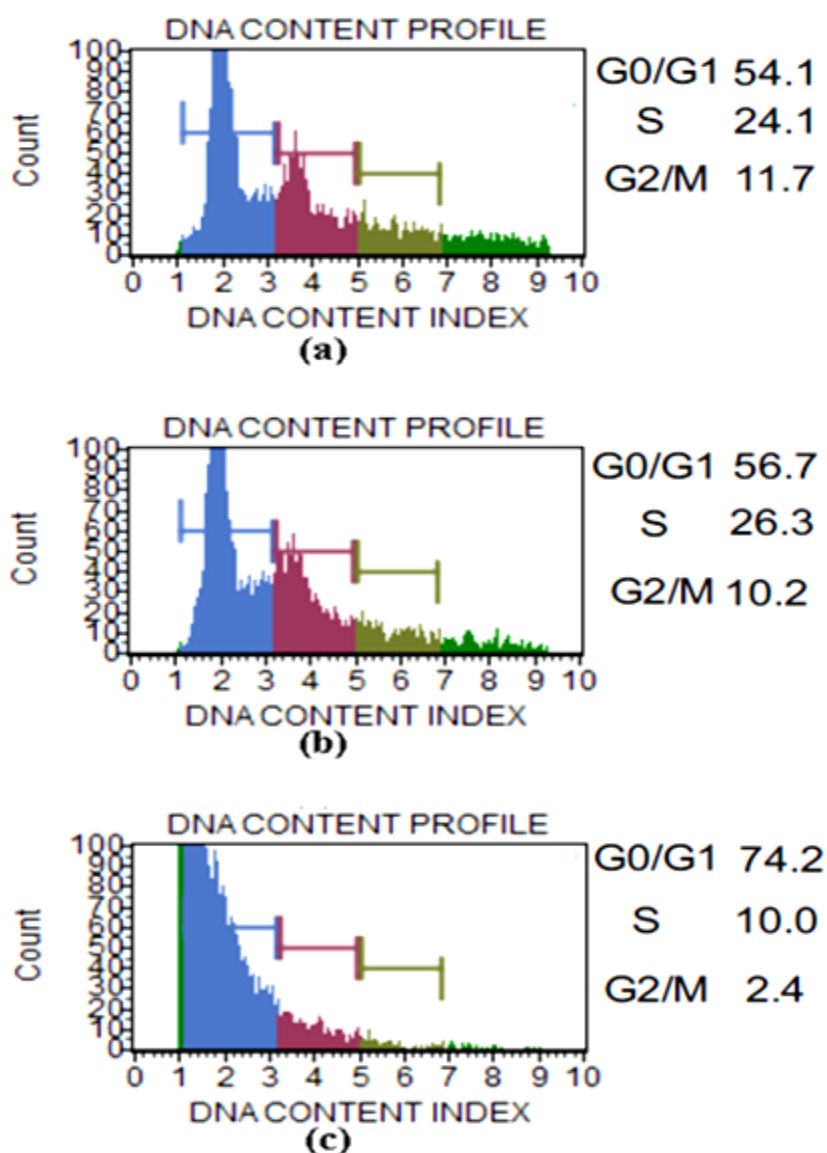


**Figure-83.** Flow cytometric analysis of PMB -OctN. Hela cells as control (a), cells treated with PMB -OctN (b) cells treated with doxorubicin-loaded PMB -OctN (c)

The hemolysis studies of PMB-OctN have shown low hemolytic percentage of 0.03 with appearance of colorless supernatant as given in Figure-84. The low percentage of hemolysis exhibited by the PMB-OctN suggests the hemocompatibility of PMB-OctN.

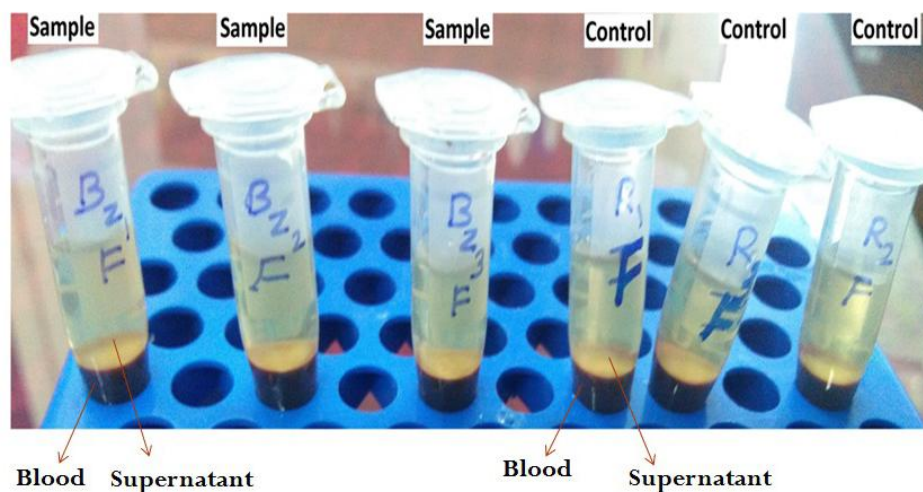


**Figure-84. Hemolysis assay of PMB-OctN**

#### **4.3.5. Evaluation of the targetting capability of PMB-OctN**

The targetting capability of the PMB-OctN has been demonstrated through comparing the cellular uptake of PMB-OctN and PMB-N (Figure-85). The excitation wavelength dependent fluorescence emission characteristic of the PMB-OctN has been used for imaging cancer cells. The nanogel displayed dual emission characteristics (emission) when excited under different excitation wavelengths. The emission is observed more significantly with PMB-OctN.

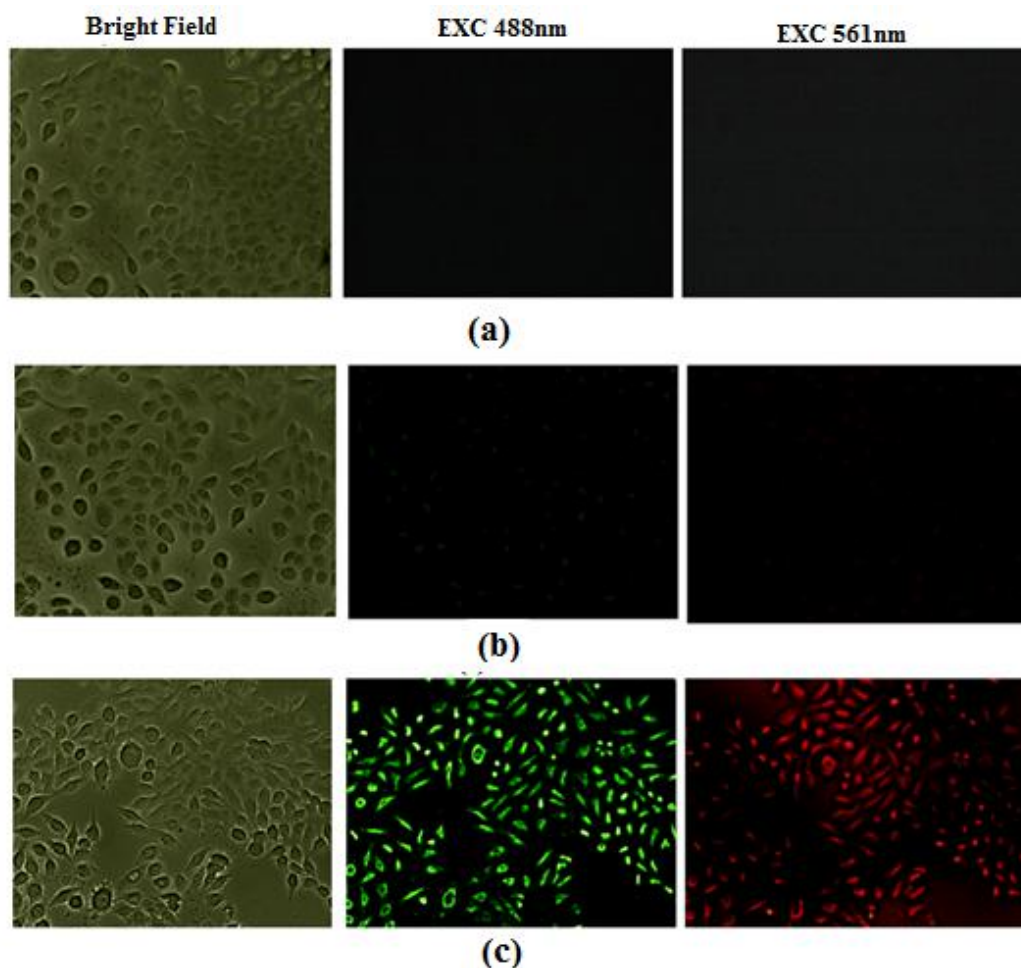


**Figure-85. Fluorescent microscope images showing uptake comparison in HeLa cells with PMB -N and PMB-OctN. HeLa cells as control (a) cells treated with PMB-N (b), cells treated with PMB-OctN (c).Observed with FITC filter and Texas red filter**

#### **4.3.6. Evaluation of the bioimaging capability of PMB-OctN**

The *in vivo* fluorescence bioimaging of the PMB-OctN carried out on mice demonstrated with near IR imaging at 700 and 720 nm under two different excitation wavelengths 640 and 675 nm (Figure-86).

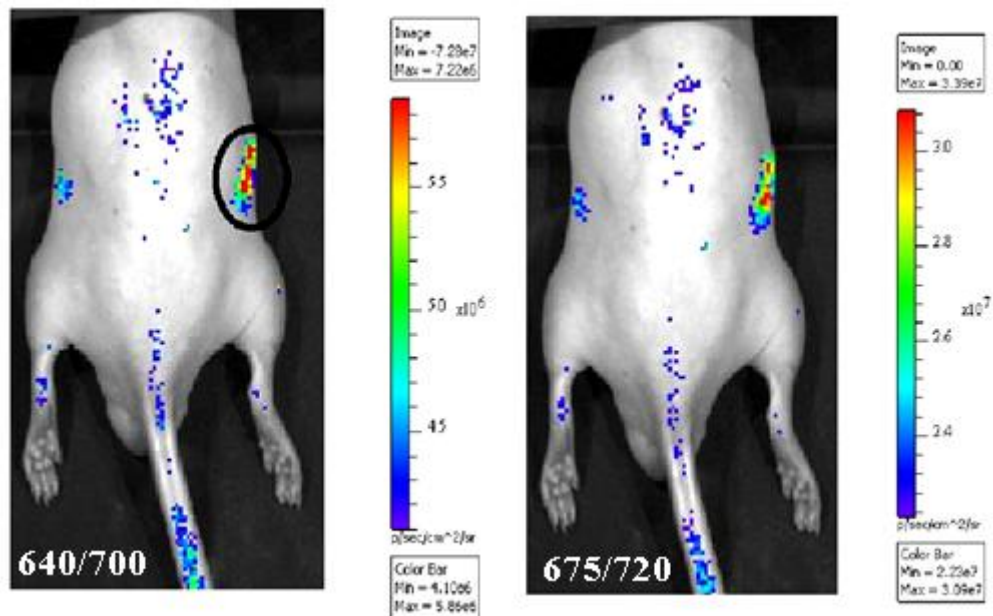


**Figure-86. *In vivo* fluorescence bioimaging of PMB-OctN in mice using different excitation and emission wavelengths (the inset of each image shows excitation and emission used; the circled areas show the position of injected area)**

#### **4.3.7. Evaluation of the biodistribution and biocompatibility of PMB-OctN**

The studies on biodistribution of injected octreotide conjugated nanogel, PMB-OctN revealed progressive decrease of fluorescent signals from the mice body with time and disappear completely after 96 h (Figure-87). The persistence of fluorescence signals till 96h suggested the extended circulation lifetime of the PMB-OctN.

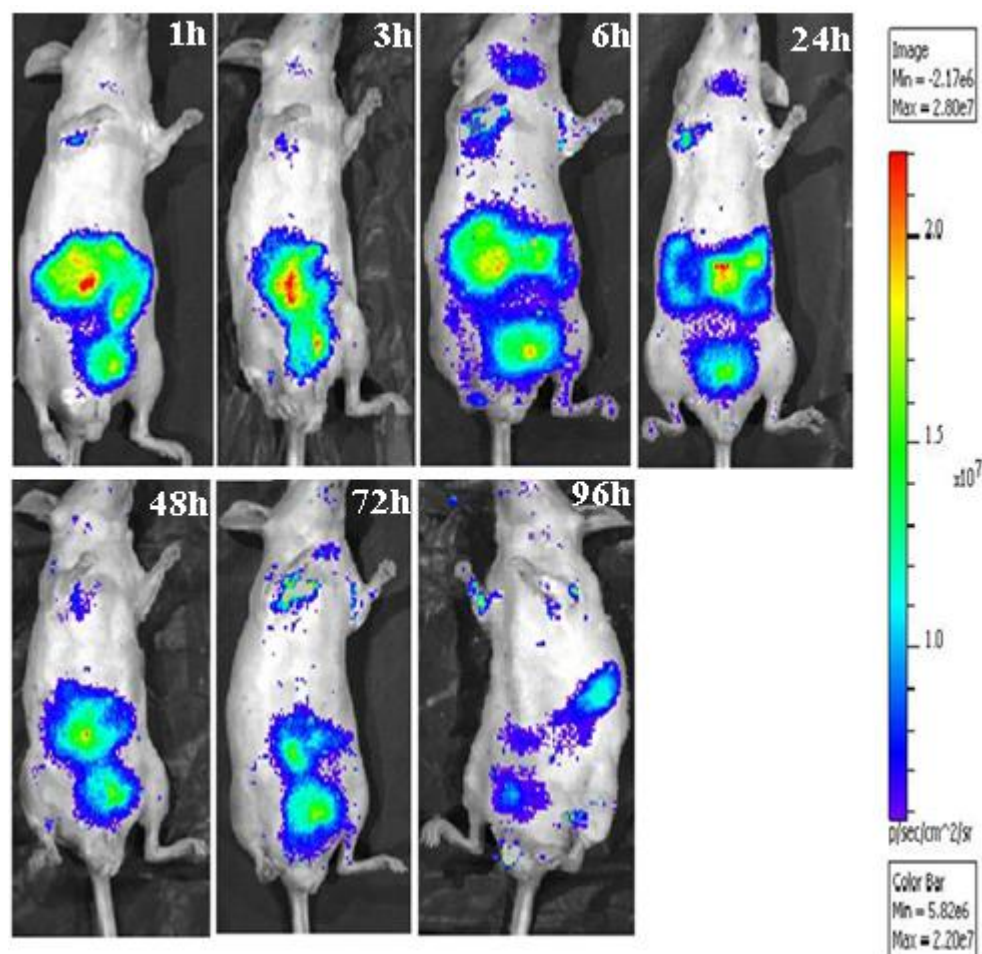
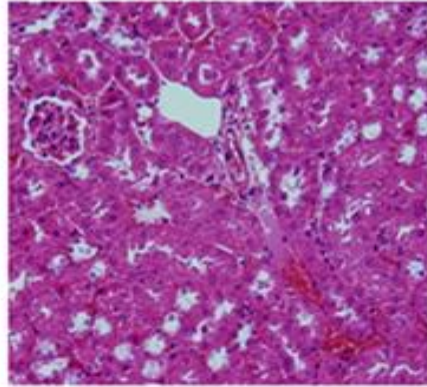


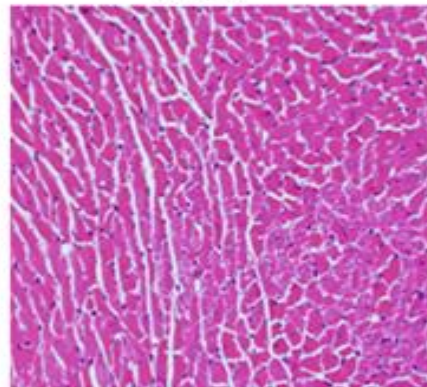
**Figure-87. Biodistribution of intravenously injected PMB-OctN in mice**

The histopathological evaluations of organs liver, heart and kidney were carried out to study the toxicity profile of the PMB-OctN. The tissue sections of organs, heart, liver and kidney revealed normal tissue morphology without any signs of necrosis (Figure-88). The tissue sections of liver reveal normal sinusoids, portal triads and central vein. The tissue sections of heart section reveals visible striations in the myocardium with centrally placed nuclei. The cortical and medullary areas in the kidneys appeared with normal glomeruli, tubules and blood vessels.

**Kidney**



**Heart**



**Liver**

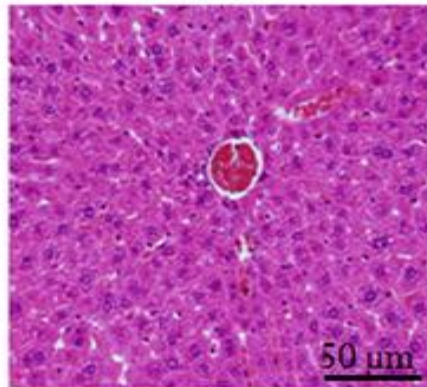


**Figure-88.H&E stained images of organs of mice at 96h post injection of PMB-OctN**

## **Chapter 5**

### **Discussion**

*This chapter comprises of three sections. First section deals with the synthesis and theranostic properties of passively targeted nanogels. The second section deals with the synthesis and theranostic properties of magneto-fluorescent nanogel endowed with innate near IR emissions and magnetic properties. The third section deals with the synthesis and theranostic properties of actively targeted octreotide conjugated nanogel endowed with innate near IR emissions. The discussion on the synthesis and characterisation of three different photoluminescent comacromers and nanogels, studies on near IR emission characteristics, cytocompatibility, therapeutic and cellular imaging capability of the nanogels are presented.*

#### ***5.1. Studies on passively targeted nanogels for theranostic applications***

##### **5.1.1. Synthesis of photoluminescent PPF-PEG-glycine (PLM) and PPF-PEG-citric acid-glycine (C-PLM) comacromers**

Polypropylene fumarate (PPF) is unsaturated polyester which is widely used for bone tissue engineering applications (Jayabalan et al., 2001). PEG is a FDA approved polyol, which imparts useful properties to materials such as protein resistance, low toxicity and immunogenicity (Zhang et al., 2002). Glycine

is an essential amino acid, which has also been used for synthesizing biocompatible polymer derivatives. In the present study an aliphatic photoluminescent comacromers (PLM and C-PLM) are synthesized with excitation wavelength dependent fluorescence (EDF) characteristics by one pot poly-condensation reaction. PLM is synthesized by the polycondensation reaction of PPF, PEG and glycine. C-PLM is synthesized by the polycondensation reaction of PPF, PEG, citric acid and glycine. The crosslinkable double bonds on PPF component of both PLM and C-PLM comacromers undergo crosslinking in the formation of fluorescent nanogels.

### **5.1.2. Structural evaluation of PLM and C-PLM comacromers**

The FTIR spectra of PLM and C-PLM comacromers confirm the successful formation of the comacromers (Figure-8). The characteristic peak of fumarate of the comacromers reveals the crosslinkable double bond to form nanogels. The peak of hydroxyl groups reveals the hydrophilic nature of the comacromers. The ester bands present in the comacromer reveals the presence of multiple ester carbonyl groups present in the comacromers. The  $^1\text{H}$  NMR spectra of PLM and C-PLM have shown different chemical shift values corresponding to the PEG, PPF, citric acid and glycine components present in the comacromers (Figure-9). Thus taken together, both FTIR and proton NMR spectra suggested the formation of the comacromers.

The molecular weight analysis of PLM and C-PLM reveals the macromeric nature of the comacromers.

### **5.1.3. Evaluation of the photoluminescence properties of the PLM and C-PLM comonomers**

Excitation dependent photoluminescence (EDF) is an interesting phenomenon exhibited by carbon-based nanoparticles, which show color tunable photoluminescent properties with different excitation and emission ranges. Carbon based nanoparticles such as graphene (Tang et al., 2012), graphite (Sun et al., 2006), carbon nanotubes (Zhou et al., 2007), and pyromellitic diimide nanowire (Zhang et al., 2010) have been reported with EDF phenomenon. These nanomaterials endowed with EDF characteristics, show a unique property of shift in emission wavelength towards longer wavelength region with increase in excitation wavelength. Some of the important mechanisms suggested for this intriguing phenomenon are incomplete solvation of the excited state (Irimpan et al., 2007), size distribution of the nanocrystallites (Huang et al., 2008) and level splitting by doped ions (Li et al., 2003). Although many mechanisms have been proposed, the phenomenon of EDF is still unclear. EDF enabled fluorophore can be excited with different wavelength to generate fluorescence red-shifted from visible to near IR. Unlike the conventional fluorophores such as organic dyes and quantum dots in which fluorescence tuning can be accomplished only through composition or size change, fluorophores exhibiting EDF can be tuned from visible to near IR region without the change of composition or size (Cushing et al., 2014). This type of excitation dependent near IR emissions is highly beneficial for bioimaging due to the absence of auto fluorescence observed in the near IR region (650-900nm) (Pansare et al., 2012). These unique features of EDF

render them wide applications such as bioimaging, biosensing and FRET ratiometric sensing.

In the present study, the comacromers PLM and C-PLM exhibited EDF property with different excitations and emissions (Figures-10,11,12,13). PLM and C-PLM exhibited emissions ranging from visible to near IR region when excited with different wavelengths. The fluorescence emission at near IR region is particularly important as they have very high tissue penetration with lack of autofluorescence.

Lack of photostability is one of the major disadvantages with organic dyes such as indocyanine green, which is widely used for bioimaging applications (Luo et al., 2011). The comacromers, PLM and C-PLM exhibited photostability without undergoing photo bleaching (Figures-14,15 and Table-1). This shows the advantage of the present comacromers when compared with organic dyes.

Photoluminescence life time value exhibited by both PLM and C-PLM is higher in comparison with that of most of the endogenous fluorophores [except phenylalanine (7 ns) and protophorphyrin IX (up to 15 ns)] which exhibit autofluorescence in tissues (Berezin et al., 2010) (Figures-16,17). The stokes shift value (120nm) exhibited by both PLM and C-PLM comacromers are higher in comparison with that of organic dye, perylene (40 nm) (Stopel *et al.*,2014) (Figures-18,19). The higher stokes shift reduces the chance of spectral overlapping which makes bioimaging more efficient (Table-1).

#### **5.1.4. Investigation on the photoluminescence properties of the analogues comacromers**

To unravel the photoluminescence behavior of the comacromers, the photoluminescent property of the analogues of PLM viz PEG-P and PEG-G is investigated. Interestingly, both the PEG-P and PEG-G exhibited photoluminescent characteristics (Figure-20). It is worth to note that PLM comprises of condensation products between CTPPF and PEG, and PEG and glycine. Since we have observed fluorescent behavior with the PLM analogues, PEG-P and PEG-G, we conclude that the observed EDF behavior of the PLM system is due to synergistic effect of both of these analogues. UV absorption spectral analysis of PEG-P and PEG-G also proves this observation (Figure-21a). The PEG-M comacromer also exhibited fluorescent characteristics (Figure-21b). If we take both PEG-M and PEG-G, both of the comacromers exhibited EDF characteristics with PEG as common unit having multiple carbonyl groups. Polyesters, in general, contain multiple number of carbonyl groups in their backbone which causes several electronic transitions like  $n-\pi^*$ , where  $n$  denotes the excited electrons of the unshared electron pairs available on the oxygen and  $\pi^*$  denotes the excited electron which goes to the anti-bonding orbital of oxygen-carbon double bond of carbonyl groups. Even though polyesters comprise of several electronic transitions, fluorescence phenomenon is not often associated with these transitions.

Unlike general polyesters, PLM has exhibited a unique excitation-dependent fluorescence (EDF) phenomenon. Environment surrounding any chromophore may influence its fluorescent properties. Therefore, polyethylene

glycol units that are connected to the carbonyl groups of PLM may influence the emissive properties of carbonyl chromophores inside the PLM. It is reported that electrophilic carbonyl groups undergo a stabilizing interaction with nucleophilic groups such as oxygen known as  $n-\pi^*$  interactions or Buergi-Dunitz interaction, these interactions can influence the photo physical properties of chromophores (Choudhary et al., 2012). These  $n-\pi^*$  interactions involve delocalization of lone pair electron (n) of the nucleophilic donor to the acceptor carbonyl groups anti-bonding orbital ( $\pi^*$ ). In macromolecules like proteins, such  $n-\pi^*$  interactions or Buergi-Dunitz interactions are reported (Fufezan et al., 2010). Here in the case of PLM, multiple number of nucleophilic oxygen atoms of PEG can interact with the electrophilic ester carbonyl groups ( $O\dots C=O$  interactions). Since PLM contains multiple number of  $O-C=O$  bonds, number of  $n-\pi^*$  interactions is numerous for the present material which may confer the material the unique property of EDF. Similar EDF phenomenon is reported with monoacylglycerol cluster chromophores in which  $OH\dots CO$  ( $n-\pi^*$ ) interactions between the ester carbonyl groups and protons of the alcohol are responsible factor for exhibiting EDF phenomenon (Lee et al., 2013).

#### **5.1.5. Preparation of PLM-NG and C-PLM-NG nanogels and evaluation of size,morphology and surface charge of nanogels**

For the smart theranostic nanocarrier, the particle size and shape should be optimum to favour prolonged blood circulation, to avoid renal clearance, and to avoid capture by the reticuloendothelial system (RES). It should also have required surface chemistry to avoid the systemic-level processes (such as opsonisation) and to enhance the cellular-level processes (such as cell uptake).

With PLM-NG, the PLM comonomer is crosslinked with acrylic acid (Figure – 22). With PC-LM-NG, the C-PLM comonomer is crosslinked with a pH sensitive tertiary amino group bearing crosslinker N,N dimethylaminoethyl methacrylate (DMEAMA) (Figure-23).

PLM-NG has smooth spherical geometry with average particle size from 180 nm (TEM measurements) (Figure-24a). The dynamic light scattering measurements has also revealed average particle size around 210 nm (Figure-24b). The observed smooth spherical geometry of PLM-NG nanogel makes it suitable for efficient cellular internalization. It has been reported that spherical nanoparticles induce higher cellular uptake with minimal cell membrane disruption (Sharifi et al., 2014). The C-PLM-NG exhibits pH sensitive swelling property. The C-PLM-NG has particle size around 100-115 nm and 180-190 nm at pH 7.4 (physiological) and 5.5 (intracellular acidic condition of cancer cells) respectively (Figure-25,26). Therefore, the optimum particle size of the C-PLM-NG is more favourable for prolonged blood circulation and to avoid renal clearance and to avoid capture by the reticuloendothelial system (RES) as reported elsewhere (Petros R.A, 2010).

The observed pH sensitive swelling behavior of C-PLM-NG can be attributed to the tertiary amino group of the crosslinker that undergoes protonation and causes subsequent swelling in acidic environment due to increase in the ion osmotic pressure with polymer solvation (Oishi et al., 2010). The observed pH sensitive swelling behavior of C-PLM-NG is comparable with that of pH sensitive nanogels prepared with PEG having polymerizable vinyl benzyl groups and DMEMA (Hayashi et al., 2004). The high dispersion stability exhibited by both

PLM-NG and C-PLM-NG can be attributed to PEG chains present on the nanogels (Otsuka et al., 2003).

The surface charge analysis of PLM-NG revealed negative surface charge of PLM-NG, which can be attributed to the anionic acrylic acid crosslinker, used to prepare the nanogel. The positive charge exhibited by the C-PLM-NG can be attributed to the cationic DMEMA crosslinker (Figures-27,28).

#### **5.1.6. Evaluation on cytocompatibility, hemolytic potential and cellular imaging capability of PLM and C-PLM-NG**

The cytocompatibility exhibited by PLM-NG and C-PLM-NG can be attributed to the presence of the hydrophilic PEG units present on the nanogels (Figures-29,30). PEGylation significantly improves the biocompatibility of nanoparticles. The appreciable cell viability, above 80% observed for 5 mg/ml is comparatively better than that observed with wavelength-tunable photoluminescent carbon dots for 500 µg/ml (Liu et al., 2015). The hemolytic percentage exhibited by PLM-NG and C-PLM-NG is lesser than the acceptable value of 5% according to ISO standards. The observed low hemolytic percentage of C-PLM-NG when compared to the PLM-NG can be attributed to the positive surface charge of the C-PLM-NG which reduces the interaction with positively charged RBC membrane (Yildirim et al.,2013). Thus hemolysis studies suggest the good hemocompatibility of the present nanogels.

The cellular uptake images of PLM-NG and C-PLM-NG in L929 and HeLa cells demonstrated cellular imaging capability (Figures-31,32). The observed total intracellular distribution of C-PLM-NG is consistent with that of polyacrylic acid

based nanogels, which are believed to overcome cellular barriers and enter intracellular regions due to optimal size and bending of the plasma membrane as reported by Chen et al (Chen et al., 2010). The enhanced cellular uptake of the C-PLM-NG is attributed to the favourable surface chemistry introduced by the crosslinker DMEMA which can undergo protonation in acidic pH and also due to the positive surface charge (28 mv) of the C-PLM-NG. Albanese et al (Albanese et al., 2012) have reported that cell uptake is enhanced by the the cationic surface charges of nanoparticles due to increased electrostatic interactions with cell membranes. It is anticipated that the cationic character of the C-PLM-NG may induce adsorption of serum protein and subsequent clearance by the immune system (opsonisation) in a *in vivo* conditions. However, C-PLM-NG may not induce opsonisation as the present nanogel is comprised with PEG with molecular weight 300. Nanoparticles having PEG units provide steric barrier against protein adsorption and remain undetectable by the immune system (Papahadjopoulos et al., 1991). The inherent EDF characteristics associated with C-PLM NG enabled cellular imaging of Hela cells with multi emissions. The observed multi color illuminations of cells with PLM-NG and C-PLM-NG are comparable with that of carbon dots having EDF emissions (Mehta et al., 2014).

#### **5.1.7. Evaluation of the therapeutic potential of C-PLM-NG**

The high drug loading capability exhibited by the C-PLM-NG can be attributed to the higher water content present inside the nanogel. The higher water content makes more space for drug loading which confers high drug loading capability. The release profile of DOX from the C-PLM-NG exhibits favorable pH dependent drug release kinetics (Figure-33). The observed pH dependent drug

release kinetics can be attributed to the pH sensitive swelling behavior of C-PLM-NG. At lower pH, DMAEMA crosslinker with tertiary amino group having pka value 7.8 protonates. This causes the subsequent swelling of the nanogel at lower pH and swelling driven release of the loaded drug from the core of the nanogel. The observed release of DOX from C-PLM-NG is comparable to that of chitin-poly (L-lactic acid) composite nanogel reported for liver cancer (Arun raj et al., 2014).

The decreasing cellular viability of doxorubicin loaded C-PLM-NG can be attributed to the release of this anticancer drug from the C-PLM-NG in to the intracellular region (Figure-34). As the nanogel concentration increases, the doxorubicin content also increases. This causes the observed concentration dependent cytotoxic effects of doxorubicin loaded C-PLM-NG.

#### **5.1.8. Evaluation of the bioimaging, biodistribution and biocompatibility of C-PLM-NG**

The EDF property of the C-PLM-NG enables bioimaging of the present nanogels by collecting different emissions (540, 580, 610, 660, 680 and 700 nm) for excitations (430, 465, 505 and 535 nm) (Figure-35). The excitation at wavelength 535 nm offers emission at near IR region 660 nm - 700 nm with relatively higher intensity. The processed images captured for the near IR emission at 660 nm - 700 nm reveal efficient biomaging with the present C-PLM-NG without any auto fluorescence (Figure-36). Moreover, as the emission of the present nanogel lies in the Near IR region, imaging of deep tissue is highly feasible with the present C-PLM-NG.

The *in vivo* biodistribution of C-PLM-NG without causing any systemic toxicity is an essential requirement for a theranostic agent. C-PLM-NG injected in the mice through tail vein revealed distribution of nanogel in different organs with time. A spot like signal has been observed from liver region after 3 h post injection which disappeared after 6 h post injection. A strong visible signal appeared from urinary bladder (Figure-37). The high accumulation of C-PLM-NG on excretory organs, liver and kidney suggests that C-PLM-NG can be cleared easily by the body. *Ex vivo* imaging of the carcass at 24 h post injection revealed no signals from the animal body suggesting that the material is eliminated from the animal without any toxicological concerns (Figures-38,39).

The histopathological analysis after the *in vivo* imaging studies with C-PLM-NG revealed normal sinusoids, portal triads and central vein of liver (Figure-40). The heart section has visible striations in the myocardium with centrally placed nuclei. Both the cortical and medullary areas in the kidneys appeared normal with no visible abnormalities to glomeruli, tubules and blood vessels histologically. Thus, histopathological analysis revealed that the C-PLM-NG does not elicit any acute toxicological response *in vivo*. The lymph node imaging capability of C-PLM-NG suggests the potential of C-PLM-NG for sentinel lymph node mapping, which is vital in cancer biopsy C-PLM-NG (Figure-41).

## ***5.2. Studies on magneto-fluorescent nanogel for theranostic applications***

### **5.2.1. Synthesis of photoluminescent PEG-Maleic acid-Glycine (PMG) comacromer**

The preparation of magneto-fluorescent nanogel is accomplished with synthesis of comacromer (PMG) with excitation wavelength dependent fluorescence (EDF) characteristics by the polycondensation reaction of PEG, maleic acid and glycine (Figure-42). The FTIR spectrum of PMG comacromer confirms the formation of the comacromer (Figure-43). The characteristic peak of double bond of the comacromer reveals the crosslinking ability of the comacromer to form nanogel. The characteristic peak of hydroxyl groups reveals the hydrophilic nature of the comacromer. The characteristic ester bands present in the comacromer reveal the presence of multiple ester carbonyl groups present in the comacromer. The  $^1\text{H}$  NMR spectrum has shown different chemical shift values corresponding to the PEG, maleic acid, and glycine components present in the comacromer (Figure-44). Thus taken together, both FTIR and  $^1\text{H}$  NMR spectra suggested the formation of the comacromer. The molecular weight analysis of PMG comacromer reveals the macromeric nature of the comacromer.

### **5.2.2. Evaluation of the photoluminescence properties of the PMG comacromer**

The PMG comacromer has displayed excitation wavelength dependent fluorescence characteristics (Figure-45,46). The observed fluorescence behaviour of the comacromer from visible to near IR region is comparable to that of recently

reported fluorescent carbon dots with tunable photoluminescence (Hu et al., 2015). In the case of these fluorescent carbon dots, fluorescence emission is observed from 400-710 nm, but the present comacromer has shown longer near IR emissions. The tuning of fluorescence emission of these carbon dots to near IR region is accomplished only through the usage of different dehydrating agents. But, in the case of present fluorescent comacromer, no such reagents are needed to shift the fluorescence emission to near IR region. The fluorescence lifetime of the PMG comacromer is of the order of nanoseconds which makes bioimaging more efficient (Figure-47). The photostability analysis suggested the good photostability of the comacromer without any photobleaching property (Figure-48). Thus, it is evident that the comacromer displayed favourable photoluminescent properties such as multiple emissions that includes both visible and near IR, good photostability and fluorescent lifetime.

### **5.2.3. Preparation of magneto-fluorescent nanogel C-SPION-NG and evaluation of size,morphology and surface charge of nanogels.**

The synthesis of magneto-fluorescent nanogel, C-SPION-NG, involves crosslinking reaction between PEG-M-GL and DMEMA crosslinker followed by *in situ* coating of SPION by electrostatic interaction between the negatively charge citrated SPION with cationic DMEMA unit of the polymer (Figure-49). With different crosslinkers such as methacrylic acid, acrylic acid and DMEMA, anionic crosslinkers doesn't facilitate the formation of magneto-fluorescent nanogel. Only when the cationic DMEMA crosslinker is used, it resulted in the formation of stable magneto-fluorescent nanogel. The formation of present stable magneto-fluorescent nanogel C-SPION-NG is attributed to the crosslinking

reaction between PEG-M-GL and DMEMA crosslinker and electrostatic interaction between anionic citric acid modified SPION and cationic DMEMA unit of the polymer resulting in the formation of stable nanogel with C-SPION core and PEG corona. It has been already reported that for gene delivery applications, negatively charged DNA fragments can form stable nanocomplexes through electrostatic forces of attraction between polycations (Wakebayashi et al., 2004).

Uzun et al. has reported highly crosslinked polymeric hydrogel by crosslinking DMEMA and ethylene glycol dimethacrylate (EGDMA) in presence of gamma radiations (Uzun *et al.*, 2003). In the present nanogel, similar to the above system, the free radical catalysed-DMEMA/PEG-M-GL/water mixture has resulted into crosslinked polymeric gels with PEG chains conferring improved gelation characteristics and dispersion stability.

The TEM and DLS analyses of C-SPION-NG reveals nanogel with C-SPION core and PEG corona with average particle size of 80 nm and hydrodynamic size of 100 nm (Figure-50,51). PEG modification imparts good biocompatibility, circulation lifetime and internalization efficiency to nanoparticles as reported by Zhang et al. (Zhang et al., 2002). C-SPION-NG has surface charge of -4.61mv (Figure-52). C-SPION-NG, which contains DMEMA crosslinker may undergo protonation and negative-to-positive charge conversion under prolonged incubation in medium and promote cell uptake as reported by Jin-Zhi Du et al. (Jin-Zhi Du et al., 2010).

#### **5.2.4. Evaluation of the magneto-fluorescent characteristics of C-SPION-NG**

The elemental analysis of C-SPION-NG substantiates the presence of iron present in the nanogel (Figure-53). The magnetic separation and vibrating sample magnetometer (VSM) analysis of bare C-SPION and C-SPION-NG shows the successful retention of magnetic properties of the SPION inside the nanogel (Figure-54). The observed magnetic saturation of C-SPION-NG, 25 emu/g, is found to be higher than the recently reported polyacrylic acid- iron oxide based nanogels having magnetic saturation value of 20 emu/g (Chen et al., 2015) (Figure-55).

The fluorescence behaviour of C-SPION-NG, with emissions from 530 nm to 860 nm for different excitation wavelengths (500-800 nm) also suggests that the nanogel retained the EDF property of the PMG comonomer (Figure-56). It is very crucial to determine whether the synthesized nanogel is able to retain both magnetic as well as fluorescent characteristics. The appearance of the C-SPION-NG under UV light clearly shows the magneto-fluorescence characteristics of C-SPION-NG (Figure-57). The observed magneto-fluorescent characteristics are comparable to that of recently reported Fe<sub>3</sub>O<sub>4</sub>-CdSe core shell magneto-fluorescent nanocarriers (Chen et al., 2014).

#### **5.2.5. Evaluation on cytocompatibility, hemolytic potential and cellular uptake of C-SPION-NG**

Cytotoxicity is the major drawback faced by the SPION when used for biomedical applications. However, the cytocompatibility studies (MTT assay)

show that the C-SPION-NG maintained cell viability when compared to bare C-SPION (Figure-58). It has already reported that iron oxide nanoparticles when coated with PEG or dextran elicited the least reactive oxygen species generation inside the cells and reduced the cytotoxicity of bare iron oxide nanoparticles (Yu et al., 2012). Hence, the observed cytocompatibility of C-SPION-NG can be attributed to the presence of biocompatible fluorescent PEG layer around the iron oxide nanoparticles. The live dead assay substantiated the cytocompatibility of C-SPION-NG (Figure-59). Monitoring a cell's ability to proliferate is critical for assessing a cell's health during toxicity studies. The cell cycle analysis clearly substantiated that the C-SPION-NG is not creating any cell cycle arrest, which leads to the apoptosis of cells (Figure-60). Hence, it is evident that the synthesized C-SPION-NG exhibited cytocompatibility.

The interaction of nanoparticles with the blood may cause the lysis of the red blood cells, which causes the hemoglobin to be released to the supernatant, which makes the supernatant red in color. The hemolysis study of C-SPION-NG has shown colorless supernatant which suggested that the nanogel does not cause significant hemolysis (Figure-61). The hemolytic percentage exhibited by C-SPION-NG is lesser than the acceptable value of 5% according to ISO standards. Thus, hemolysis studies suggest the good hemocompatibility of the synthesized nanogel.

It is very important for any nanoparticles to have good cellular internalization to perform the theranostic functions efficiently. The cellular uptake studies revealed the internalization of the C-SPION-NG in Hela cells in spite of the negative surface charge of -4.61 mv, which is not very very low (Figure-62).

The appreciable cell uptake may be attributed to the protonation of DMEMA crosslinker and conversion of negative-to-positive charge under prolonged incubation in the medium as reported by Jin-Zhi Du et al. (Jin-Zhi Du et al., 2010).

#### **5.2.6. Evaluation of the theranostic potential of C-SPION-NG**

The objective of combining the fluorescent comonomer with magnetic iron oxide nanoparticles is to exploit the fluorescence properties of the comonomer for diagnostics and the magnetic hyperthermia capability of iron oxide nanoparticles for therapy and thereby accomplishing the theranostic capabilities. Hence, the theranostic capability of the C-SPION-NG is evaluated. The diagnostics potential is evaluated through fluorescence imaging and therapeutic potential of C-SPION-NG is evaluated through the magnetic hyperthermia. The dual color emission of C-PLM-NG from HeLa cells revealed the good diagnostic potential of the synthesized nanogel (Figure-63). The magnetic hyperthermia measurements have revealed the temperature generating capability of C-SPION-NG required for the lysis of cancer cells (Figure-64). The observed temperature generation capability of C-SPION-NG under the magnetic field is comparable with that of the PEGylated superparamagnetic clusters for theranostic applications (Hayashi et al., 2013). The C-SPION-NG exhibited good therapeutic capability by inducing the lysis of cancer cells by generating heat inside the cells as demonstrated by the live dead assay (Figure-65) and phase contrast images of the hyperthermia-treated cells (Figure-66). It is already reported that when the temperature inside a cancer cells becomes more than 42<sup>0</sup>C, the cells encounters DNA damage which will lead to apoptosis of cancer cells

(Harmon et al., 1990). Hence, the generated heat above 42<sup>0</sup>C can be efficiently used for killing cancer cells. Thus, it is evident that the C-SPION-NG displays both therapeutics and diagnostics potential within a single domain.

#### **5.2.7. Evaluation of the bioimaging, biodistribution and biocompatibility of C-SPION-NG**

The bioimaging studies revealed that C-SPION-NG has good fluorescent imaging capability at 800 and 820 nm revealing good fluorescence bioimaging capability (Figure-67). The observed near IR imaging capability of C-SPION-NG around 800 nm is comparable to that of widely used near IR emitting indocyanine green dyes (Alander et al., 2012). The studies on biodistribution demonstrated sufficient circulation lifetime and elimination from the body after performing its intended function without causing toxicity (Figure-68). Even though the size of the synthesized C-SPION-NG (80 nm) is large enough to surpass renal clearance, the fluorescent signals from the bladder region of the mice has suggested the renal clearance of the synthesized C-SPION-NG. The observed renal clearance of C-SPION-NG can be attributed to the crosslinked comacromer containing PEG units in the nanogel and strong and stable electrostatic interaction with SPION. The coating material present on the iron oxide nanoparticles has a profound effect on the renal clearance of iron oxide nanoparticles (Wahajuddin *et al.*,2012). Bourrinet *et al* has reported renal elimination of Ferumoxtran-10 (iron oxide core coated with low molecular weight dextran) having particle size of 30 nm. The study has shown that 22% of the particles are eliminated through urine and feaces (Bourrinet *et al.*,2006). Weissleder *et al* has reported renal elimination of AMI-25 (dextran coated superparamagnetic iron oxide nanoparticles) with size of 120 nm.

The study revealed nearly 25% elimination of AMI-25 through urine and faeces (Weissleder *et al.*,1989). These reports suggest that the coating material has a significant impact on the renal clearance of the iron oxide nanoparticles irrespective of the other physico-chemical characteristics. In the present system, the nanogel with strong and stable electrostatic interaction with SPION favours the renal clearance of the nanogel similar to that observed with the dextran coated-SPION [Ferumoxtran and AMI-25].

The PEG chains present in the crosslinked comonomer nanogel prevents the interaction of serum proteins with the nanogel by virtue of its steric effects and confers good stability (Castillo *et al.*, 2015).The PEGylation on C-SPION-NG decreases the interaction of the nanoparticles with opsonising proteins present in the blood and that confers more circulation lifetime to the C-SPION-NG. The histopathology analysis reveal normal tissue morphology of sinusoids, portal triads and central vein with liver, visible striations in the myocardium with centrally placed nuclei with heart and cortical and medullary areas in the kidneys (Figure-69). Taken together, the synthesized C-SPION-NG has shown promising near IR bioimaging capability and biodistribution without any *in vivo* tissue toxicity.

### ***5.3. Studies on actively targeted nanogel for theranostic applications***

#### **5.3.1. Synthesis and characterisation of photoluminescent comacromer PEG-Maleic acid-Benzoic acid (PMB) and octreotide conjugated nanogel (PMB-OctN)**

In the present study, the nanogel, PMB-OctN with excitation wavelength dependent fluorescence (EDF) characteristics is prepared using aliphatic photoluminescent comacromer (PMG) which is synthesized by the polycondensation reaction of PEG, maleic acid and 4-aminobenzoic acid followed by crosslinking the photoluminescent comacromer (PMB) with diethylene glycoldimethacrylate (PMB-N) (Figure-70). The targeting of the nanogel is carried out by conjugating the octreotide on the surface of the fluorescent PMB-N nanogel using the carbodiimide mediated coupling reaction between the carboxyl groups of the nanogel with the amino groups on the octreotide. The unsaturated double bonds present in the PMB comacromer is crosslinked with diethylene glycol dimethacrylate (DEGDMA) to prepare nanogel (PMB-N).

Somatostatin is a peptide hormone composed of 14 amino acids, which are used for cancer therapeutics. Somatostatin receptors are over expressed in neuroendocrine tumors that can be exploited for active targeting and there by achieving site specific delivery of the drug at tumor region (Strowski *et al.*,2008), (Hoyer *et al.*,1995). Octreotide is a somatostatin (natural growth hormone) analogue that has highest affinity for somatostatin receptors that are over expressed in tumors (Lelle *et al.*,2015). Octreotide formulations are usually labeled with radioactive indium-111. After reaching the tumor site, this indium

labeled octreotide can visualize tumors and kills them by emitting radiations. Hence, it is evident that the octreotide-based formulations have good theranostic potential.

The FTIR spectrum of aliphatic photoluminescent comacromer (PMG) confirms the formation of the comacromer (Figure-71). The characteristic peak of fumarate double bond of the comacromer reveals the crosslinking ability of the comacromer to form nanogel. The characteristic peak of hydroxyl groups reveals the hydrophilic nature of the synthesized comacromer. The characteristic ester bands present in the comacromer reveals the presence of multiple ester carbonyl groups present in the comacromers. The  $^1\text{H}$  NMR spectrum has shown different chemical shift values corresponding to the PEG, maleic acid and 4- aminobenzoic acid components present in the comacromer (Figure-72). Thus taken together, both FTIR and proton NMR spectra analyses suggested the formation of the comacromer. The molecular weight analysis of PMG comacromer reveals the macromeric nature of the synthesized comacromer.

The infrared spectrum of PMB-OctN reveals the spectral responses of amino and carboxyl groups of the octreotide, which confirmed the octreotide conjugation on PMB-N (Figure-73). In addition to these bands, the PMB-OctN also displayed ester carbonyl groups and methylene groups of PMB comacromer. These results suggested the successful conjugation of octreotide with PMB-N.

### **5.3.2. Evaluation of the photoluminescence properties of the PMB comacromer**

The fluorescence emission of the PMB comacromer spanned from visible to near IR region demonstrating the excitation wavelength dependent fluorescence

characteristics (Figure-74,75). The fluorescence lifetime of the PMB comacromer is higher than the widely used cyanine dyes having fluorescence lifetime of one nanosecond (Berezin et al., 2010) (Figure-76). The photostability evaluations have revealed the good photostability of the PMB comacromer without undergoing photobleaching (Figure-77). Thus, the synthesized PMB displayed favourable properties such as multiple fluorescence emissions, good fluorescent lifetime and photostability suitable for bioimaging.

### **5.3.3. Preparation and evaluation of size,morphology and surface charge of PMB-OctN**

The TEM analysis of the octreotide-conjugated nanogel (PMB-OctN) reveals the formation of spherical and non-aggregated nanoparticles (Figure-78). The good dispersion stability exhibited by PMB-OctN can be attributed to PEG chains present on the nanogels (Otsuka et al., 2003). PMB-OctN nanogel is spherical in shape with average particle size around 110 nm and average hydrodynamic size of 145 nm and negative surface charge of -9 mv (Figure-79). The optimum hydrodynamic size of 145 nm is also more favourable for prolonged blood circulation without early renal clearance and capture by the reticuloendothelial system (RES) in *in vivo* conditions as reported elsewhere (Petros R.A, 2010). The negative surface charge of the PMB-OctN can be attributed to the abundant surface carboxyl groups present in the PMB-OctN.

#### **5.3.4. Evaluation of drug release, therapeutic capability and hemolytic potential of PMB-OctN**

Theranostic capability of a haemocompatible nanogel is assessed by drug loading and release potential of nanogel for therapy. The PMB-OctN has high drug loading potential, which is attributed to the higher water content present on PMB-OctN, which creates more space for drug loading. The high drug loading efficiency of the PMB-OctN is comparable to that of the recently reported polyglycidol based nanogels (Lockhart et al., 2016). The observed sustainable release profile of doxorubicin from the PMB-OctN can be explained based on the electrostatic interaction between the anionic DEGDMA and cationic doxorubicin (Figure-80). The electrostatic attraction between anionic DEGDMA and cationic doxorubicin confers high drug loading potential. Hence, the nanogel-drug interaction is strong which prevents the leakage of the drug. The nanogel on contact with solutions, drug release from the nanogel is governed by slow diffusion controlled drug release kinetics. This causes the observed trend of slow and sustainable release of the loaded drug from PMB-OctN. Hence, the drug release reveals sustainable release of doxorubicin sufficient for generating optimal therapeutic response desirable for chemotherapy. The observed sustainable release of doxorubicin from the PMB-OctN is comparable to that of recently reported hyaluronic acid and pluronic F127 polymer based nanogel for controlled delivery of doxorubicin (Gurav et al., 2016).

The therapeutic response of the loaded drug from the nanoparticles is important to ensure the success of chemotherapy. The PMB-OctN loaded with doxorubicin having similar concentrations of PMB-OctN showed decreased cell

viability; this trend of decreasing cell viability with increase in concentration of doxorubicin is due to the increase of cumulative availability of doxorubicin as the concentration of the doxorubicin loaded-PMB-OctN increases (Figure-81). The observed cell apoptotic activity of the doxorubicin loaded-PMB-OctN is comparable to that of polymeric vesicles loaded with doxorubicin (Yang et al., 2010). The live dead studies suggests that the PMB-OctN itself is nontoxic (Figure-82); when it is combined with an anticancer drug, it can generate optimal therapeutic response needed for killing cancer cells. The observed cell cycle arrest of doxorubicin loaded PMB-OctN refers the successful delivery of doxorubicin from the polymeric carrier in to the nuclei of cancer cells, which causes the cell death as reported by Yang *et al* (Yang et al., 2011) (Figure-83). It is already reported that doxorubicin can cause cell cycle arrest, which will lead towards apoptotic cell death (Siu et al., 1999).

The hemolysis study of PBM-OctN has shown colorless supernatant which suggests that the nanogel does not cause significant hemolysis (Figure-84). The hemolytic percentage exhibited by PBM-OctN is lesser than the acceptable value of 5% according to ISO standards. Thus, hemolysis studies suggest the hemocompatibility of the synthesized nanogels.

### **5.3.5. Evaluation of the targetting capability of PMB-OctN**

The targeting capability of any drug formulations significantly reduces the chances of systemic side effects. The cellular uptake of the present PMB-OctN in Hela cells has demonstrated the targeting capability of the PMB-OctN (Figure-85). The faster and significant internalization of PBM-OctN suggests the targeted

entry of these nanoparticles on cancer cells. Yang et al. has reported similar internalization and cytotoxicity with HeLa cells for the targeted polypeptide conjugated CdSe nanogels (Yang et al., 2014). The faster internalization of PMB-OctN can be attributed to the somatostatin receptor mediated endocytosis on HeLa cells. Moreover, the internalization of the PMB-OctN in HeLa cells in spite of the negative surface charge of -9 mV, may be attributed to the conversion of negative-to-positive charge under prolonged incubation in the medium as reported by Jin-Zhi Du et al. (Jin-Zhi Du et al., 2010).

### **5.3.6. Evaluation of the bioimaging, biodistribution and biocompatibility of PMB-OctN**

The in vivo bioimaging studies reveal the good near IR imaging capability with good signal intensity (Figure-86). The studies on biodistribution PMB-OctN revealed progressive decrease of fluorescent signals from the mice body with time and disappear completely after 96 h (Figure-87). The observed high circulation lifetime of the PMB-OctN can be explained by the three important factors such as composition, size and surface charge of the PMB-OctN. The PMB-OctN is comprised with multiple PEG polymer chains resembling a bottle brush. Hence, the availability of PEG chains in the PMB-OctN is adequate to confer the stealth effect to the PMB-OctN and remain undetectable by the immune system, which ultimately reduces the process of opsonisation of the nanogel by macrophages (Knop et al., 2010, Papahadjopoulos et al., 1991). Nanogels with PEGylated layer having high density PEG coating (molecular weight of 2000-10000 D) can effectively reduce opsonisation and provide extended circulation lifetime to PEGylated nanogels (Perry et al., 2012).

Size and surface charge also plays a crucial role in determining the circulation lifetime of the nanoparticles. It has been reported that PEGylated nanoparticles having negative or neutral surface charge reduced plasma protein adsorption and therefore have extended circulation lifetime (Alexis et al., 2008). The present PEGylated PMB-OctN has negative surface charge of -9 mv. Hence, its interaction with opsonising proteins in the blood will be very less and thus provides more circulation lifetime to the PMB-OctN. Thus, the present *in vivo* bioimaging studies suggest that the PMB-OctN has good bioimaging capability with sufficient circulation lifetime required to perform the theranostic function.

The histopathological evaluations of organs liver, heart and kidney are carried out to study the toxicity profile of the PMB-OctN. The tissue sections of liver revealed normal sinusoids, portal triads and central vein (Figure-88). The tissue sections of heart section revealed visible striations in the myocardium with centrally placed nuclei. The cortical and medullary areas in the kidneys appeared with normal glomeruli, tubules and blood vessels. These results suggested the biocompatibility of PBM-OctN.

## **Chapter-6**

### **Summary and Conclusions**

Theranostic nanomedicine is an emerging important area in biomedical research. Nanocarriers have greater role in theranostic nanomedicine especially for the treatment of cancer. Polymer-based fluorescent theranostic nanoparticles have great diversity in terms of compositional, structural and morphological characteristics as well as diagnostic and targeting modalities. However, they have major drawbacks such as possible leaching of the fluorophores from the polymer back bone, decreased diagnostic capability after linking with the polymer and toxicity. Therefore, the nanogels with inherent excitation wavelength dependent photoluminescence in near IR (NIR) region are highly essential for bioimaging as the tissue penetration of NIR is maximum with minimal auto fluorescence from the body. Moreover, the nanogels should have optimum particle size and shape to favour prolonged blood circulation and to avoid renal clearance and also to avoid capture by the reticuloendothelial system (RES).

Therapeutic agents, which can deliver the drug at the targeted tumor site either by passive or active mode, are essential to ensure the safety and efficacy of the therapeutic agent. The passive mode of targeting the tumor site and tumor-

specific accumulation of drug (enhanced permeability and retention (EPR) effect), can be accomplished with the stimuli responsive character of the nanocarrier. Magneto-fluorescent nanocarriers which combine the optical and magnetic properties have great scope for theranostic applications. The site-specific delivery of the drug molecule at the target site can be accomplished by surface functionalization of nanogels with active targeting ligands.

Therefore the present studies were designed for the development of biocompatible comonomers with inherent EDF in NIR region, polymeric nanogels with stimuli responsive and EDF characteristics for passive targeted delivery, polymeric magneto-fluorescent nanogels and octreotide based targeted polymeric nanogels with EDF characteristics for the site-specific delivery for the treatment of cancer.

In the first part of the study, the passively targeted theranostic nanogels (PLM-NG and C-PLM-NG) were developed and evaluated its theranostic potential. Two fluorescent comonomers based on PEG, PPF, glycine (PLM) and PEG, PPF, citric acid and glycine (C-PLM) were prepared. The comonomers exhibited excitation wavelength dependent fluorescence (EDF) with emissions ranging from visible to near IR mediated by the  $n-\pi^*$  interactions between electrophilic ester carbonyl groups and nucleophilic oxygen atoms of PEG ( $O\dots C=O$  interactions).

Nanogels (PLM-NG and C-PLM-NG) synthesized from PLM and C-PLM comonomers by crosslinking with acrylic acid and N, N dimethylaminoethylmethacrylate (DMEAMA) also exhibited near IR emission

properties. The optimum particle size of the C-PLM-NG, [100 nm at pH 7.4 (physiological) and 180 nm 5.5 (intracellular acidic condition of cancer cells)] is more favourable for prolonged blood circulation and to avoid early renal clearance and also to avoid capture by the reticuloendothelial system. The C-PLM-NG exhibited pH sensitive swelling property and caionic surface charge required for stimuli responsive character for drug release. The enhanced cellular uptake of the C-PLM-NG is attributed to the favourable surface chemistry introduced by the crosslinker DMEMA which undergoes protonation in acidic pH and the positive surface charge of the C-PLM-NG. The C-PLM-NG may not induce opsonisation as the present nanogel is comprised with PEG, which provides steric barrier against protein adsorption and remain undetectable by the immune system.

The inherent EDF characteristics associated with C-PLM NG enabled cellular imaging of Hela cells with multiemissions which are comparable with that of carbon dots. The innate near IR emission capability of the nanogel was exploited for bioimaging. The bioimaging, biodistribution and histopathology studies on C-PLM-NG in mice revealed near IR emission and elimination from the body without causing any toxicity at 24 h post injection. The lymph node imaging with C-PLM-NG have demonstrated the potential of sentinental lymph node mapping in cancer biopsy. To best of our knowledge, there are no reports on the development of polymeric nanogel with innate near IR emissions for drug delivery and bioimaging.

The second part of the study focused on the development of a hybrid magneto-fluorescent nanogel. The PMG comacromer synthesized with PEG,

maleic acid and glycine (PMG) also exhibited EDF properties with emissions ranging from visible to near IR. Magneto-fluorescent nanogel, C-SPION-NG, synthesized by the *insitu* incorporation of citric acid capped super paramagnetic iron oxide nanoparticles (C-SPION) exhibited appreciable magnetic and fluorescence properties with magnetic saturation of 25 emu/g and fluorescence emission at 530-860 nm.

C-SPION-NG has average particle size of 80 nm and surface charge of -4.61mv. C-SPION-NG, which contains DMEMA crosslinker can undergo protonation and negative-to-positive charge conversion under prolonged incubation in physiological medium. The C-SPION-NG shows core-shell morphology with SPION core and PEG shell. Therefore, the presence of PEG in the shell of C-SPION-NG may not favour opsonisation *in vivo*. The PEG layer formed over the magnetic nanoparticles has improved the cytocompatibility of bare magnetic nanoparticles. The cytocompatibility studies of C-SPION-NG exhibited improved cytocompatibility when compared to bare iron oxide nanoparticles. The appreciable cell uptake of C-SPION-NG may be attributed to the protonation of DMEMA crosslinker and conversion of negative-to-positive charge under prolonged incubation in the medium.

The present hybrid nanogel has demonstrated magnetic hyperthermia on cervical cancer cells and the fluorescence capability. The biodistribution and histopathology studies in mice revealed near IR emission and elimination from the body without causing any toxicity at 24 h post injection.

The third part of the present study focused on the development of an actively targeted nanogel prepared with a photoluminescent comacromer based on

PEG, maleic acid and 4-aminobenzoic acid (PMB). The PMB comonomer exhibited EDF properties with emissions ranging from visible to near IR similar to C-PLM and PMG comonomers. The octreotide conjugated targeted nanogel, PMB-OctN nanogel synthesized from the PMB comonomer by crosslinking with diethyleneglycoldimethacrylate (DEGDMA) and conjugated with octreotide exhibited high drug loading capability with sustainable drug release profile. PMB-OctN nanogel was spherical in shape with average particle size around 110 nm and average hydrodynamic size of 145 nm and negative surface charge of -9 mv. The optimum hydrodynamic size of 145 nm is also more favourable for prolonged blood circulation without early renal clearance and capture by the reticuloendothelial system (RES) in *in vivo* conditions. The appreciable cell uptake of PMB-OctN nanogel may be attributed to the conversion of negative-to-positive charge under prolonged incubation in the medium.

The studies on the drug release profile of the synthesized PMB-OctN reveal steady drug release and reached up to 50% within 48 h followed by a sustainable release of DOX till 120 h. The cytocompatibility studies of PMB-OctN tested on cervical cancer cells have revealed that the nanogel itself is non-toxic but when is combined with an anticancer drug it elicits good therapeutic response suitable for the lysis of cancer cells. The PMB-OctN exhibited faster and more cellular internalization when compared to non-targeted nanogel. The biodistribution studies revealed that the designed nanogel exhibited longer circulation lifetime of 48 h and normal tissue morphology without any signs of necrosis desirable for theranostic applications.

In conclusion the present polymeric nanogel with stimuli responsive and EDF characteristics for passive targeted delivery C-PLM NG, polymeric magneto-fluorescent nanogel, C-SPION-NG and octreotide based targeted polymeric nanogel PMB-OctN with EDF characteristics for the site-specific delivery are promising candidates for theranostic applications especially for the treatment of cancer. Comparatively, among the present nanogels, the octreotide conjugated targeted nanogel PMB-OctN has better properties such as cytocompatibility and appreciable cellular intake, longer circulation lifetime, active targeting capability, good near IR imaging capability, sustainable drug release profile and good therapeutic capability.

### ***6.1. Future prospects***

Theranostic nanoparticles should have good functional performance with biocompatibility. The present nanogel PMB-OctN has promising potential in theranostic nanomedicine. The design of multifunctional theranostic nanogels by conjugating the present nanogel with other theranostic nanoparticles such as gold nanoparticles, quantum dots and carbon nanotubes can impart multifunctional performance with biocompatibility. These multifunctional nanogels can combine multiple therapeutic and diagnostic capabilities in a single nanoparticles framework. The future work also involves the design of polymeric nanogels with varying stimuli responsive units such as disulfide, acetal or ketal groups that can respond to multiple stimuli such as temperature and pH to trigger the drug release at cancer cells.

The fabrication of smart nanogel using advanced techniques such as particle replication in non wetting template (PRINT) methods can give nanogels with precisely controlled morphology and size suitable for theranostic applications. The future study also involves the evaluation of the candidate nanogel on tumor model, product safety evaluation and clinical translation of the designed nanogel.

## References

- Albanese A, Tang PS, Chan WC (2012) The effect of nanoparticle size, shape, and surface chemistry on biological systems. *Annu Rev Biomed Eng.*; 14: 1-16.
- Aguilar-Castillo BA, Santos JL, Luo H, et al (2015) Nanoparticle stability in biologically relevant media: influence of polymer architecture. *Soft Matter* 11:7296–7307.
- Alander JT, Kaartinen I, Laakso A, et al (2012) A Review of Indocyanine Green Fluorescent Imaging in Surgery. *Int J Biomed Imaging* 2012:1–26.
- Alexis F, Pridgen E, Molnar LK, Farokhzad OC (2008) Factors Affecting the Clearance and Biodistribution of Polymeric Nanoparticles. *Mol Pharm* 5:505–515.
- Allison RR (2014) Photodynamic therapy: oncologic horizons. *Future Oncol Lond Engl* 10:123–124.
- Allison RR, Bagnato VS, Sibata CH (2010) Future of oncologic photodynamic therapy. *Future Oncol* 6:929–940.
- Andrä W, Nowak H (2006) Front Matter. In: *Magn. Med.* Wiley-VCH Verlag GmbH & Co. KGaA, pp I–XXIII
- Arunraj TR, Sanoj Rejinold N, Ashwin Kumar N, Jayakumar R (2014) Bio-responsive chitin-poly(l-lactic acid) composite nanogels for liver cancer. *Colloids Surf B Biointerfaces* 113:394–402.
- Asadian-Birjand M, Bergueiro J, Wedepohl S, Calderón M (2016) Near Infrared Dye Conjugated Nanogels for Combined Photodynamic and Photothermal Therapies. *Macromol Biosci* 16:1432–1441.
- Asokan A, Cho MJ (2002) Exploitation of Intracellular pH Gradients in the Cellular Delivery of Macromolecules. *J Pharm Sci* 91:903–913.
- Ballou B, Ernst L, Waggoner A (2005) Fluorescence Imaging of Tumors In Vivo. *Curr Med Chem* 12:795–805.
- Bañobre-López M, Teijeiro A, Rivas J (2013) Magnetic nanoparticle-based hyperthermia for cancer treatment. *Rep Pract Oncol Radiother* 18:397–400.
- Bauhuber S, Hozsa C, Breunig M, Göpferich A (2009) Delivery of Nucleic Acids via Disulfide-Based Carrier Systems. *Adv Mater* 21:3286–3306.

- Beeran AE, Fernandez FB, Nazeer SS, et al (2015) Multifunctional nano manganese ferrite ferrofluid for efficient theranostic application. *Colloids Surf B Biointerfaces* 136:1089–1097.
- Berezin MY, Achilefu S (2010) Fluorescence Lifetime Measurements and Biological Imaging. *Chem Rev* 110:2641–2684.
- Billinton N, Knight AW (2001) Seeing the Wood through the Trees: A Review of Techniques for Distinguishing Green Fluorescent Protein from Endogenous Autofluorescence. *Anal Biochem* 291:175–197.
- Bourrinet P, Bengele HH, Bonnemain B, et al (2006) Preclinical Safety and Pharmacokinetic Profile of Ferumoxtran-10, an Ultrasmall Superparamagnetic Iron Oxide Magnetic Resonance Contrast Agent: *Invest Radiol* 41:313–324.
- Busquets MA, Estelrich J, Sánchez-Martín MJ (2015) Nanoparticles in magnetic resonance imaging: from simple to dual contrast agents. *Int J Nanomedicine* 1727.
- Campbell RB (2007) Battling tumors with magnetic nanotherapeutics and hyperthermia: turning up the heat. *Nanomed* 2:649–652.
- Candiani G, Pezzoli D, Ciani L, et al (2010) Bioreducible Liposomes for Gene Delivery: From the Formulation to the Mechanism of Action. *PLoS ONE* 5:e13430.
- Caravan P, Ellison JJ, McMurry TJ, Lauffer RB (1999) Gadolinium(III) Chelates as MRI Contrast Agents: Structure, Dynamics, and Applications. *Chem Rev* 99:2293–2352.
- Castano AP, Demidova TN, Hamblin MR (2005) Mechanisms in photodynamic therapy: part two—cellular signaling, cell metabolism and modes of cell death. *Photodiagnosis Photodyn Ther* 2:1–23.
- Chang H-I, Yeh M-K (2012) Clinical development of liposome-based drugs: formulation, characterization, and therapeutic efficacy. *Int J Nanomedicine* 7:49–60.
- Chen O, Riedemann L, Etoc F, et al (2014) Magneto-fluorescent core-shell supernanoparticles. *Nat Commun* 5:5093.
- Chen Y, Nan J, Lu Y, et al (2015) Hybrid Poly(acrylic acid) Nanogels for Theranostic Cancer Treatment. *J Biomed Nanotechnol* 11:771–779.
- Chen Y, Wilbon PA, Zhou J, et al (2013) Multifunctional self-fluorescent polymer nanogels for label-free imaging and drug delivery. *Chem Commun Camb Engl* 49:297–299.

- Chen Y, Zheng X, Qian H, et al (2010) Hollow Core–Porous Shell Structure Poly(acrylic acid) Nanogels with a Superhigh Capacity of Drug Loading. *ACS Appl Mater Interfaces* 2:3532–3538.
- Cheng R, Feng F, Meng F, et al (2011) Glutathione-responsive nano-vehicles as a promising platform for targeted intracellular drug and gene delivery. *J Controlled Release* 152:2–12.
- Chiang W-H, Ho VT, Chen H-H, et al (2013) Superparamagnetic Hollow Hybrid Nanogels as a Potential Guidable Vehicle System of Stimuli-Mediated MR Imaging and Multiple Cancer Therapeutics. *Langmuir* 29:6434–6443.
- Chicheł A, Skowronek J, Kubaszewska M, Kanikowski M (2007) Hyperthermia – description of a method and a review of clinical applications. *Rep Pract Oncol Radiother* 12:267–275.
- Cho H, Stuart JM, Magid R, et al (2014) Theranostic immunoliposomes for osteoarthritis. *Nanomedicine Nanotechnol Biol Med* 10:619–627.
- Choudhary A, Kamer KJ, Raines RT (2012) A conserved interaction with the chromophore of fluorescent proteins. *Protein Sci Publ Protein Soc* 21:171–177.
- Cushing SK, Li M, Huang F, Wu N (2014) Origin of Strong Excitation Wavelength Dependent Fluorescence of Graphene Oxide. *ACS Nano* 8:1002–1013.
- David B, Yusuf M, Mark M, Brian L, Daniel K, Scott T, Malik J, Marry S, Jeffrey M (2015) <sup>99m</sup>Tc-depreotide tumour uptake in patients with non-Hodgkin's lymphoma. *Nucl Med Commun* 25:839-843
- Davis ME, Chen Z (Georgia), Shin DM (2008) Nanoparticle therapeutics: an emerging treatment modality for cancer. *Nat Rev Drug Discov* 7:771–782.
- Davis SS, Wilding EA, Wilding IR (1993) Gastrointestinal transit of a matrix tablet formulation: comparison of canine and human data. *Int J Pharm* 94:235–238.
- Devadasu VR, Bhardwaj V, Kumar MNVR (2013) Can Controversial Nanotechnology Promise Drug Delivery? *Chem Rev* 113:1686–1735.
- Dolmans DEJGJ, Fukumura D, Jain RK (2003) TIMELINE: Photodynamic therapy for cancer. *Nat Rev Cancer* 3:380–387.
- Dougherty TJ, Gomer CJ, Henderson BW, et al (1998) Photodynamic therapy. *J Natl Cancer Inst* 90:889–905.
- Dougherty TJ, Grindey GB, Fiel R, et al (1975) Photoradiation therapy. II. Cure of animal tumors with hematoporphyrin and light. *J Natl Cancer Inst* 55:115–121.

- Elsabahy M, Heo GS, Lim S-M, et al (2015) Polymeric Nanostructures for Imaging and Therapy. *Chem Rev* 115:10967–11011.
- Fang J, Nakamura H, Maeda H (2011) The EPR effect: Unique features of tumor blood vessels for drug delivery, factors involved, and limitations and augmentation of the effect. *Adv Drug Deliv Rev* 63:136–151.
- Fang J-Y, Wen C-J, Zhang, et al (2012) Theranostic liposomes loaded with quantum dots and apomorphine for brain targeting and bioimaging. *Int J Nanomedicine* 1599.
- Farokhzad OC, Langer R (2009) Impact of Nanotechnology on Drug Delivery. *ACS Nano* 3:16–20.
- Foster FS, Lockwood GR, Ryan LK, et al (1993) Principles and applications of ultrasound backscatter microscopy. *IEEE Trans Ultrason Ferroelectr Freq Control* 40:608–617.
- Fufezan C (2010) The role of Buergi-Dunitz interactions in the structural stability of proteins. *Proteins* 78:2831–2838.
- Gao W, Chan JM, Farokhzad OC (2010) pH-Responsive Nanoparticles for Drug Delivery. *Mol Pharm* 7:1913–1920.
- Geraldes CFGC, Laurent S (2009) Classification and basic properties of contrast agents for magnetic resonance imaging. *Contrast Media Mol Imaging* 4:1–23.
- Gerweck LE (2006) Tumor pH controls the in vivo efficacy of weak acid and base chemotherapeutics. *Mol Cancer Ther* 5:1275–1279.
- Grayson SM, Fréchet JMJ (2001) Convergent Dendrons and Dendrimers: from Synthesis to Applications. *Chem Rev* 101:3819–3868.
- Greish K (2010) Enhanced permeability and retention (EPR) effect for anticancer nanomedicine drug targeting. *Methods Mol Biol Clifton NJ* 624:25–37.
- Guo J, Hong H, Chen G, et al (2014) Theranostic Unimolecular Micelles Based on Brush-Shaped Amphiphilic Block Copolymers for Tumor-Targeted Drug Delivery and Positron Emission Tomography Imaging. *ACS Appl Mater Interfaces* 6:21769–21779.
- Guo M, Mao H, Li Y, et al (2014) Dual imaging-guided photothermal/photodynamic therapy using micelles. *Biomaterials* 35:4656–4666.
- Gurav DD, Kulkarni AS, Khan A, Shinde VS (2016) pH-responsive targeted and controlled doxorubicin delivery using hyaluronic acid nanocarriers. *Colloids Surf B Biointerfaces* 143:352–358.

- Harmon BV, Corder AM, Collins RJ, et al (1990) Cell Death Induced in a Murine Mastocytoma by 42–47°C Heating *in Vitro* : Evidence that the Form of Death Changes from Apoptosis to Necrosis Above a Critical Heat Load. *Int J Radiat Biol* 58:845–858.
- Hawker CJ, Frechet JMJ (1990) Preparation of polymers with controlled molecular architecture. A new convergent approach to dendritic macromolecules. *J Am Chem Soc* 112:7638–7647.
- Hayashi H, Iijima M, Kataoka K, Nagasaki Y (2004) pH-Sensitive Nanogel Possessing Reactive PEG Tethered Chains on the Surface. *Macromolecules* 37:5389–5396.
- Hayashi K, Nakamura M, Sakamoto W, et al (2013) Superparamagnetic Nanoparticle Clusters for Cancer Theranostics Combining Magnetic Resonance Imaging and Hyperthermia Treatment. *Theranostics* 3:366–376.
- Henderson BW, Dougherty TJ (1992) How Does Photodynamic Therapy Work?. *Photochem Photobiol* 55:145–157.
- Hoyer D, Bell GI, Berelowitz M, et al (1995) Classification and nomenclature of somatostatin receptors. *Trends Pharmacol Sci* 16:86–88.
- Hu S, Trinchì A, Atkin P, Cole I (2015) Tunable Photoluminescence Across the Entire Visible Spectrum from Carbon Dots Excited by White Light. *Angew Chem Int Ed* 54:2970–2974.
- Huang YM, Zhai B, Zhou F (2008) Correlation of excitation-wavelength dependent photoluminescence with the fractal microstructures of porous silicon. *Appl Surf Sci* 254:4139–4143.
- Irimpan L, Krishnan B, Deepthy A, et al (2007) Excitation wavelength dependent fluorescence behaviour of nano colloids of ZnO. *J Phys Appl Phys* 40:5670.
- Jayabalan M, Thomas V, Rajesh PN (2001) Polypropylene fumarate/phloroglucinol triglycidyl methacrylate blend for use as partially biodegradable orthopaedic cement. *Biomaterials* 22:2749–2757.
- Jin-Zhi Du, Tian-Meng Sun, Wen-Jing Song, Juan Wu, and Jun Wang (2010), A Tumor-Acidity-Activated Charge-Conversional Nanogel as an Intelligent Vehicle for Promoted Tumoral-Cell Uptake and Drug Delivery, *Angew. Chem. Int. Ed.* 49, 3621 –3626
- Jones M-C, Leroux J-C (1999) Polymeric micelles – a new generation of colloidal drug carriers. *Eur J Pharm Biopharm* 48:101–111.
- Kabanov AV, Vinogradov SV (2009) Nanogels as Pharmaceutical Carriers: Finite Networks of Infinite Capabilities. *Angew Chem Int Ed* 48:5418–5429.

- Kelkar SS, Reineke TM (2011) Theranostics: combining imaging and therapy. *Bioconjug Chem* 22:1879–1903.
- Kim J -w. (2006) Cancer's Molecular Sweet Tooth and the Warburg Effect. *Cancer Res* 66:8927–8930.
- Knop K, Hoogenboom R, Fischer D, Schubert US (2010) Poly(ethylene glycol) in Drug Delivery: Pros and Cons as Well as Potential Alternatives. *Angew Chem Int Ed* 49:6288–6308.
- Konan YN, Gurny R, Allémann E (2002) State of the art in the delivery of photosensitizers for photodynamic therapy. *J Photochem Photobiol B* 66:89–106.
- Krasia-Christoforou T, Georgiou TK (2013) Polymeric theranostics: using polymer-based systems for simultaneous imaging and therapy. *J Mater Chem B* 1:3002
- Labib A, Lenaerts V, Chouinard F, et al Biodegradable Nanospheres Containing Phthalocyanines and Naphthalocyanines for Targeted Photodynamic Tumor Therapy. *Pharm Res* 8:1027–1031.
- Lam T, Pouliot P, Avti PK, et al (2013) Superparamagnetic iron oxide based nanoprobe for imaging and theranostics. *Adv Colloid Interface Sci* 199–200:95–113.
- Lammers T, Kiessling F, Hennink WE, Storm G (2010) Nanotheranostics and image-guided drug delivery: current concepts and future directions. *Mol Pharm* 7:1899–1912.
- Lanza GM, Wickline SA (2001) Targeted ultrasonic contrast agents for molecular imaging and therapy. *Prog Cardiovasc Dis* 44:13–31.
- Lee K-M, Cheng W-Y, Chen C-Y, et al (2013) Excitation-dependent visible fluorescence in decameric nanoparticles with monoacylglycerol cluster chromophores. *Nat Commun* 4:1544.
- Lee R-S, Lin C-H, Aljuffali IA, et al (2015) Passive targeting of thermosensitive diblock copolymer micelles to the lungs: synthesis and characterization of poly(N-isopropylacrylamide)-block-poly( $\epsilon$ -caprolactone). *J Nanobiotechnology*.
- Lelle M, Kaloyanova S, Freidel C, et al (2015) Octreotide-Mediated Tumor-Targeted Drug Delivery via a Cleavable Doxorubicin–Peptide Conjugate. *Mol Pharm* 12:4290–4300.
- Li GH, Zhang Y, Wu YC, Zhang LD (2003) Wavelength dependent photoluminescence of anodic alumina membranes. *J Phys Condens Matter* 15:8663–8671.

- Li W, Zheng C, Pan Z, et al (2016) Smart hyaluronidase-activated theranostic micelles for dual-modal imaging guided photodynamic therapy. *Biomaterials* 101:10–19.
- Li Y, Li Y, Zhang X, et al (2016) Supramolecular PEGylated Dendritic Systems as pH/Redox Dual-Responsive Theranostic Nanoplatfoms for Platinum Drug Delivery and NIR Imaging. *Theranostics* 6:1293–1305.
- Liu H, He Z, Jiang L-P, Zhu J-J (2015) Microwave-Assisted Synthesis of Wavelength-Tunable Photoluminescent Carbon Nanodots and Their Potential Applications. *ACS Appl Mater Interfaces* 7:4913–4920.
- Liu J, Levine AL, Mattoon JS, et al (2006) Nanoparticles as image enhancing agents for ultrasonography. *Phys Med Biol* 51:2179–2189.
- Lockhart JN, Beezer DB, Stevens DM, et al (2016) One-pot polyglycidol nanogels via liposome master templates for dual drug delivery. *J Controlled Release*. doi: 10.1016/j.jconrel.2016.07.013
- Luan L, Ding L, Zhang W, et al (2013) A naphthalocyanine based near-infrared photosensitizer: Synthesis and in vitro photodynamic activities. *Bioorg Med Chem Lett* 23:3775–3779.
- Lucky SS, Soo KC, Zhang Y (2015) Nanoparticles in Photodynamic Therapy. *Chem Rev* 115:1990–2042.
- Luk BT, Fang RH, Zhang L (2012) Lipid- and Polymer-Based Nanostructures for Cancer Theranostics. *Theranostics* 2:1117–1126.
- Luo S, Zhang E, Su Y, et al (2011) A review of NIR dyes in cancer targeting and imaging. *Biomaterials* 32:7127–7138.
- Ma Y, Mou Q, Wang D, et al (2016) Dendritic Polymers for Theranostics. *Theranostics* 6:930–947.
- Maeda H, Wu J, Sawa T, et al (2000) Tumor vascular permeability and the EPR effect in macromolecular therapeutics: a review. *J Control Release* 65:271–284.
- Malam Y, Loizidou M, Seifalian AM (2009) Liposomes and nanoparticles: nanosized vehicles for drug delivery in cancer. *Trends Pharmacol Sci* 30:592–599.
- Mallidi S, Wang B, Mehrmohammadi M, et al (2009) Ultrasound-based imaging of nanoparticles: From molecular and cellular imaging to therapy guidance. *IEEE*, pp 27–36
- Manry D, Yang J (2011) Size optimization of biodegradable fluorescent nanogels for cell imaging. *J.High School Res* 2: 12

- Mason WT (1999) *Fluorescent and Luminescent Probes for Biological Activity: A Practical Guide to Technology for Quantitative Real-Time Analysis*. Academic Press
- Matai I, Sachdev A, Gopinath P (2015) Self-Assembled Hybrids of Fluorescent Carbon Dots and PAMAM Dendrimers for Epirubicin Delivery and Intracellular Imaging. *ACS Appl Mater Interfaces* 7:11423–11435.
- Mehta VN, Jha S, Singhal RK, Kailasa SK (2014) Preparation of multicolor emitting carbon dots for HeLa cell imaging. *New J Chem* 38:6152–6160.
- Meng F, Hennink WE, Zhong Z (2009) Reduction-sensitive polymers and bioconjugates for biomedical applications. *Biomaterials* 30:2180–2198.
- Moghimi SM, Hunter AC, Murray JC (2001) Long-circulating and target-specific nanoparticles: theory to practice. *Pharmacol Rev* 53:283–318.
- Mornet S, Vasseur S, Grasset F, Duguet E (2004) Magnetic nanoparticle design for medical diagnosis and therapy. *J Mater Chem* 14:2161.
- Murgia S, Bonacchi S, Falchi AM, et al (2013) Drug-Loaded Fluorescent Cubosomes: Versatile Nanoparticles for Potential Theranostic Applications. *Langmuir* 29:6673–6679.
- Nagahama K, Sano Y, Kumano T (2015) Anticancer drug-based multifunctional nanogels through self-assembly of dextran–curcumin conjugates toward cancer theranostics. *Bioorg Med Chem Lett* 25:2519–2522.
- Oishi M, Nagasaki Y (2010) Stimuli-responsive smart nanogels for cancer diagnostics and therapy. *Nanomed* 5:451–468.
- Oleinick NL, Evans HH (1998) The photobiology of photodynamic therapy: cellular targets and mechanisms. *Radiat Res* 150:S146–156.
- Oleinick NL, Morris RL, Belichenko I (2002) The role of apoptosis in response to photodynamic therapy: what, where, why, and how. *Photochem Photobiol Sci Off* 1:1–21.
- Ormond A, Freeman H (2013) Dye Sensitizers for Photodynamic Therapy. *Materials* 6:817–840.
- Otsuka H, Nagasaki Y, Kataoka K (2003) PEGylated nanoparticles for biological and pharmaceutical applications. *Adv Drug Deliv Rev* 55:403–419.
- Papahadjopoulos D, Allen TM, Gabizon A, Mayhew E, Matthey K, Huang SK, et al. (1991) Sterically stabilized liposomes: improvements in pharmacokinetics and antitumor therapeutic efficacy. *Proc Natl Acad Sci U S A*. 88: 11460-4.

- Pansare VJ, Hejazi S, Faenza WJ, Prud'homme RK (2012) Review of Long-Wavelength Optical and NIR Imaging Materials: Contrast Agents, Fluorophores, and Multifunctional Nano Carriers. *Chem Mater* 24:812–827.
- Pansare VJ, Hejazi S, Faenza WJ, Prud'homme RK (2012) Review of Long-Wavelength Optical and NIR Imaging Materials: Contrast Agents, Fluorophores, and Multifunctional Nano Carriers. *Chem Mater* 24:812–827.
- Panyam J, Dali MM, Sahoo SK, et al (2003) Polymer degradation and in vitro release of a model protein from poly(d,l-lactide-co-glycolide) nano- and microparticles. *J Controlled Release* 92:173–187.
- Panyam J, Labhasetwar V (2003) Biodegradable nanoparticles for drug and gene delivery to cells and tissue. *Adv Drug Deliv Rev* 55:329–347.
- Park JS, Yang HN, Woo DG, et al (2013) Poly(N-isopropylacrylamide-co-acrylic acid) nanogels for tracing and delivering genes to human mesenchymal stem cells. *Biomaterials* 34:8819–8834.
- Park JS, Yi SW, Kim HJ, et al (2016) Sunflower-type nanogels carrying a quantum dot nanoprobe for both superior gene delivery efficacy and tracing of human mesenchymal stem cells. *Biomaterials* 77:14–25.
- Perry JL, Reuter KG, Kai MP, et al (2012) PEGylated PRINT Nanoparticles: The Impact of PEG Density on Protein Binding, Macrophage Association, Biodistribution, and Pharmacokinetics. *Nano Lett* 12:5304–5310.
- Petros RA, DeSimone JM. (2010) Strategies in the design of nanoparticles for therapeutic applications. *Nat Rev Drug Discov.* 9: 615-27.
- Portnoy E, Vakruk N, Bishara A, et al (2016) Indocyanine Green Liposomes for Diagnosis and Therapeutic Monitoring of Cerebral Malaria. *Theranostics* 6:167–176.
- Quan S, Wang Y, Zhou A, et al (2015) Galactose-based Thermosensitive Nanogels for Targeted Drug Delivery of Idoazomycin Arabinofuranoside (IAZA) for Theranostic Management of Hypoxic Hepatocellular Carcinoma. *Biomacromolecules* 16:1978–1986.
- Rajput G, Majmudar F, Patel J, et al (2010) Stomach-specific mucoadhesive microsphere as a controlled drug delivery system. *Syst Rev Pharm* 1:70.
- Riehemann K, Schneider SW, Luger TA, et al (2009) Nanomedicine--challenge and perspectives. *Angew Chem Int Ed Engl* 48:872–897.
- Rizzitelli S, Giustetto P, Cutrin JC, et al (2015) Sonosensitive theranostic liposomes for preclinical in vivo MRI-guided visualization of doxorubicin release stimulated by pulsed low intensity non-focused ultrasound. *J Controlled Release* 202:21–30.

- Rümenapp C, Gleich B, Haase A (2012) Magnetic nanoparticles in magnetic resonance imaging and diagnostics. *Pharm Res* 29:1165–1179.
- Rushton M, Morash R, Larocque G, et al (2015) Wellness Beyond Cancer Program: Building an effective survivorship program. *Curr Oncol* 22:419.
- Schafer FQ, Buettner GR (2001) Redox environment of the cell as viewed through the redox state of the glutathione disulfide/glutathione couple. *Free Radic Biol Med* 30:1191–1212.
- Schmaljohann D (2006) Thermo- and pH-responsive polymers in drug delivery. *Adv Drug Deliv Rev* 58:1655–1670.
- Sharifi S, Behzadi S, Laurent S, et al (2012) Toxicity of nanomaterials. *Chem Soc Rev* 41:2323–2343.
- Sharma A, Sharma US (1997) Liposomes in drug delivery: Progress and limitations. *Int J Pharm* 154:123–140.
- Singh R, Lillard JW (2009) Nanoparticle-based targeted drug delivery. *Exp Mol Pathol* 86:215–223.
- Siu WY, Yam CH, Poon RY. (1999) G1 versus G2 cell cycle arrest after adriamycin-induced damage in mouse Swiss3T3 cells. *FEBS Lett* 461:299–305.
- Stephen ZR, Kievit FM, Zhang M (2011) Magnetite Nanoparticles for Medical MR Imaging. *Mater Today Kidlington Engl* 14:330–338.
- Stopel MHW, Blum C, Subramaniam V (2014) Excitation Spectra and Stokes Shift Measurements of Single Organic Dyes at Room Temperature. *J Phys Chem Lett* 5:3259–3264.
- Strowski MZ, Blake AD (2008) Function and expression of somatostatin receptors of the endocrine pancreas. *Mol Cell Endocrinol* 286:169–179.
- Su S, Wang H, Liu X, et al (2013) iRGD-coupled responsive fluorescent nanogel for targeted drug delivery. *Biomaterials* 34:3523–3533.
- Sun Y-P, Zhou B, Lin Y, et al (2006) Quantum-sized carbon dots for bright and colorful photoluminescence. *J Am Chem Soc* 128:7756–7757.
- Tang L, Ji R, Cao X, et al (2012) Deep Ultraviolet Photoluminescence of Water-Soluble Self-Passivated Graphene Quantum Dots. *ACS Nano* 6:5102–5110.
- Torchilin VP (2005) Recent advances with liposomes as pharmaceutical carriers. *Nat Rev Drug Discov* 4:145–160.
- Uzun C, Hassnisaber M, Şen M, Güven O (2003) Enhancement and control of cross-linking of dimethylaminoethyl methacrylate irradiated at low dose rate

- in the presence of ethylene glycol dimethacrylate. *Nucl Instrum Methods Phys Res Sect B Beam Interact Mater At* 208:242–246.
- Vaupel P (2004) Tumor microenvironmental physiology and its implications for radiation oncology. *Semin Radiat Oncol* 14:198–206.
- Vijayan VM, Komeri R, Victor SP, Muthu J (2015) Photoluminescent PEG based comacromers as excitation dependent fluorophores for biomedical applications. *Colloids Surf B Biointerfaces* 135:243–252.
- Vinogradov SV, Bronich TK, Kabanov AV (2002) Nanosized cationic hydrogels for drug delivery: preparation, properties and interactions with cells. *Adv Drug Deliv Rev* 54:135–147.
- Virgolini I, Traub T, Novotny C, et al (2002) Experience with Indium-111 and Yttrium-90-Labeled Somatostatin Analogs. *Curr Pharm Des* 8:1781–1807.
- Wahajuddin, Arora (2012) Superparamagnetic iron oxide nanoparticles: magnetic nanoplatforms as drug carriers. *Int J Nanomedicine* 3445.
- Wakebayashi D, Nishiyama N, Itaka K, et al (2004) Polyion Complex Micelles of pDNA with Acetal-poly(ethylene glycol)-poly(2-(dimethylamino)ethyl methacrylate) Block Copolymer as the Gene Carrier System: Physicochemical Properties of Micelles Relevant to Gene Transfection Efficacy. *Biomacromolecules* 5:2128–2136.
- Wang C, Ravi S, Martinez GV, et al (2012) Dual-purpose magnetic micelles for MRI and gene delivery. *J Controlled Release* 163:82–92.
- Wang D, Zhao T, Zhu X, et al (2015) Bioapplications of hyperbranched polymers. *Chem Soc Rev* 44:4023–4071.
- Wang Z, Niu G, Chen X (2014) Polymeric Materials for Theranostic Applications. *Pharm Res* 31:1358–1376.
- Weissleder R, Stark DD, Engelstad BL, et al (1989) Superparamagnetic iron oxide: pharmacokinetics and toxicity. *AJR Am J Roentgenol* 152:167–173.
- Wolfbeis OS (2015) An overview of nanoparticles commonly used in fluorescent bioimaging. *Chem Soc Rev* 44:4743–4768.
- Wu C, Chiu DT (2013) Highly Fluorescent Semiconducting Polymer Dots for Biology and Medicine. *Angew Chem Int Ed* 52:3086–3109.
- Wu W, Shen J, Banerjee P, Zhou S (2011) Water-dispersible multifunctional hybrid nanogels for combined curcumin and photothermal therapy. *Biomaterials* 32:598–609.
- Xie J, Lee S, Chen X (2010) Nanoparticle-based theranostic agents. *Adv Drug Deliv Rev* 62:1064–1079.

- Xing T, Mao C, Lai B, Yan L (2012) Synthesis of Disulfide-Cross-Linked Polypeptide Nanogel Conjugated with a Near-Infrared Fluorescence Probe for Direct Imaging of Reduction-Induced Drug Release. *ACS Appl Mater Interfaces* 4:5662–5672.
- Xu C, Sun S (2013) New forms of superparamagnetic nanoparticles for biomedical applications. *Adv Drug Deliv Rev* 65:732–743.
- Xu W, Ling P, Zhang T (2013) Polymeric Micelles, a Promising Drug Delivery System to Enhance Bioavailability of Poorly Water-Soluble Drugs. *J Drug Deliv* 2013:1–15.
- Xu X, Jian Y, Li Y, et al (2014) Bio-Inspired Supramolecular Hybrid Dendrimers Self-Assembled from Low-Generation Peptide Dendrons for Highly Efficient Gene Delivery and Biological Tracking. *ACS Nano* 8:9255–9264.
- Yang H-M, Oh BC, Kim JH, et al (2011) Multifunctional poly(aspartic acid) nanoparticles containing iron oxide nanocrystals and doxorubicin for simultaneous cancer diagnosis and therapy. *Colloids Surf Physicochem Eng Asp* 391:208–215.
- Yang J, Yao M-H, Wen L, et al (2014) Multifunctional quantum dot–polypeptide hybrid nanogel for targeted imaging and drug delivery. *Nanoscale* 6:11282–11292.
- Yang X, Grailer JJ, Rowland IJ, et al (2010) Multifunctional SPIO/DOX-loaded wormlike polymer vesicles for cancer therapy and MR imaging. *Biomaterials* 31:9065–9073.
- Yildirim A, Ozgur E, Bayindir M (2013) Impact of mesoporous silica nanoparticle surface functionality on hemolytic activity, thrombogenicity and non-specific protein adsorption. *J Mater Chem B* 1:1909.
- Yu M, Huang S, Yu KJ, Clyne AM (2012) Dextran and Polymer Polyethylene Glycol (PEG) Coating Reduce Both 5 and 30 nm Iron Oxide Nanoparticle Cytotoxicity in 2D and 3D Cell Culture. *Int J Mol Sci* 13:5554–5570.
- Zhang H, Ma Y, Xie Y, et al (2015) A Controllable Aptamer-Based Self-Assembled DNA Dendrimer for High Affinity Targeting, Bioimaging and Drug Delivery. *Sci Rep* 5:10099.
- Zhang H, Xu X, Ji H-F (2010) Excitation-wavelength-dependent photoluminescence of a pyromellitic diimide nanowire network. *Chem Commun* 46:1917–1919.
- Zhang M, Li XH, Gong YD, et al (2002) Properties and biocompatibility of chitosan films modified by blending with PEG. *Biomaterials* 23:2641–2648.

- Zhang Y, Kohler N, Zhang M (2002) Surface modification of superparamagnetic magnetite nanoparticles and their intracellular uptake. *Biomaterials* 23:1553–1561.
- Zhou J, Booker C, Li R, et al (2007) An Electrochemical Avenue to Blue Luminescent Nanocrystals from Multiwalled Carbon Nanotubes (MWCNTs). *J Am Chem Soc* 129:744–745.
- Zhu H, Li Y, Qiu R, et al (2012) Responsive fluorescent Bi<sub>2</sub>O<sub>3</sub>@PVA hybrid nanogels for temperature-sensing, dual-modal imaging, and drug delivery. *Biomaterials* 33:3058–3069.
- Zhu J, Zheng L, Wen S, et al (2014) Targeted cancer theranostics using alpha-tocopheryl succinate-conjugated multifunctional dendrimer-entrapped gold nanoparticles. *Biomaterials* 35:7635–7646.

### *List of Publications*

1. **Vineeth M. Vijayan**, R. Komeri, S.P. Victor, Jayabalan Muthu, Photoluminescent PEG based comacromers as excitation dependent fluorophores for biomedical applications, *Colloids Surf. B Biointerfaces*. 135 (2015) 243–252. doi:10.1016/j.colsurfb.2015.07.027. (I.F. 4.152)
2. **Vineeth M. Vijayan**, Sachin Shenoy, S.P. Victor, Jayabalan Muthu, stimuli responsive nanogel with innate near IR emission capabilities for drug delivery and bioimaging, *Colloids Surf. B Biointerfaces*, 146, (2016), 84-96 (I.F. 4.152)
3. **Vineeth M. Vijayan**, Jayabalan Muthu, Stimuli responsive nanogel for colon cancer theranostic applications, *Front. Bioeng. Biotechnol.* 4 (2016). doi:10.3389/conf.FBIOE.2016.01.01359
4. **Vineeth M. Vijayan**, Sachin Shenoy, S.P. Victor, Jayabalan Muthu. PEGylated iron oxide nanogel for potential for theranostic applications (Under review in *Polymer journal*) (I.F. 3.6)
5. **Vineeth M. Vijayan**, Sachin shenoy, S.P., Jayabalan Muthu. Octerotide-conjugated fluorescent PEGylated polymeric nanogel for theranostic applications (Under review in *Material Science and Engineering C*) (I.F.3.5)
6. **Vineeth M. Vijayan**, Jayabalan Muthu. Polymeric nanoparticles for theranostic nanomedicine (Review article communicated to *Journal of Polymer for advanced technologies*.) (I.F. 2)
7. Girija seetharaman, Adarsh Kallar, **Vineeth M Vijayan**, Muthu Jayabalan, Sivaram Selvam, Design, Preparation and Characterization of pH-Responsive

Prodrug Micelles with Hydrolyzable Anhydride Linkages for Controlled Drug Delivery (Just accepted manuscript in Journal of Colloids and interfaces,2017) (I.F. 3.8) (doi.org/10.1016/j.jcis.2016.12.070)

8. Sunita Prem Victor, Willi paul, **Vineeth M Vijayan**, Remya Komeri, Jayabalan Muthu and Chandra P Sharma. Theranostic nanoplatfoms based on neodymium doped hydroxyl appetite for colon specific drug delivery applications, 145 (2016),539-547 (I.F. 4.152)

9. Sunita prem Victor, **Vineeth M Vijayan**, Remya Komeri, Sivaram Selvam and Jayabalan Muthu Covalently Crosslinked Hydroxyapatite-Citric Acid Based Biomimetic Polymeric Composites for Bone Applications. Journal of bioactive and compatible polymers, (2015).30:524-540 (I.F. 2.5)

10. Sunita Prem Victor, Jibin Kunnupuarathu, Gayathri Devi, Remya Komeri, **Vineeth M Vijayan**, Jayabalan Muthu. Design and characterisation of biodegradable macroporous hybrid inorganic-organic polymer for orthopedic applications.(Under revision in Material science and Engineering C) (I.F. 3.45)

## *Conference Proceedings*

1. **Vineeth M Vijayan** and M Jayabalan. PEGylated Stimuli Responsive Nanogels for Cancer Therapy (Poster presentation). Material research society of India (MRSI) Annual meeting on February 24 – 26, 2015 at Rajasthan, India.
2. **Vineeth M Vijayan** and M Jayabalan. PEGylated Excitation Dependent Fluorescence Enabled Polymeric Nanogels for Combined Drug delivery and Bioimaging Applications (Oral presentation), International symposium on Photonics Applications and Nanomaterials on October 28-30, 2015, Thiruvananthapuram, India.
3. **Vineeth M Vijayan** and M Jayabalan. Smart Polymeric Nanogel for Near IR imaging and drug delivery (Oral presentation), Kerala science congress on January 28-30,2016 Mallapuram, India
4. **Vineeth M Vijayan** and M Jayabalan. Magneto-fluorescent nanogel for Diagnostic applications (Poster presentation), BITERM conference on April 15-17, 2016, IIT Delhi.
5. **Vineeth M Vijayan** and M Jayabalan. PEGylated Polymeric nanogels for theranostic applications (Oral presentation), MACRO conference on January 8-11,2017, Thiruvananthapuram.

## *CURRICULUM VITAE*

### **Education**

01/2014 – Present: Ph D Scholar at Sree Chitra Tirunal Institute for Medical Sciences and Technology, Biomedical Technology Wing, Polymer Division, Trivandrum, Kerala, India.

Advisor: Dr. M.Jayabalan

03/2013 – 12/ 2013: Project Assistant at Sree Chitra Tirunal Institute for Medical Sciences and Technology, Biomedical Technology Wing, Polymer Division, Trivandrum, Kerala, India.

Advisor: Dr. M.Jayabalan

10/2010 – 10/ 2012: Masters of Science in Chemistry, University of Kerala, India

06/2006 – 06/2009: Bachelors of Science in Chemistry, University of Kerala, India

Home Address

Sivasakthi House

Plavila

Thirumala PO

Thiruvananthapuram-695006

Ph: 9633555419

Email: vineethvm076@gmail.com